Alma Mater Studiorum – Università di Bologna

DOTTORATO DI RICERCA IN

CHIMICA

XXX Ciclo

Settore Concorsuale: 03/A1

Settore Scientifico Disciplinare: CHIM/12

FIELD AND LABORATORY STUDIES

TO EVALUATE THE INFLUENCE OF WET&DRY

ATMOSPHERIC DEPOSITIONS ON WEATHERING STEEL

Presentata da: Lara Nobili

Coordinatore Dottorato

Prof. Aldo Roda

Supervisore

Dr. Elena Bernardi

Co-Supervisore

Prof. Ivano Vassura

Esame finale anno 2018

"Che cosa c'è, che cosa c'è, che cosa c'è di meglio

che trovarsi

nel proprio naufragio?"

Verde, Lo Stato Sociale,

colonna sonora del film "*Gli Asteroidi*"

Agli Asteroidi e alle Persone più belle

che la vita mi ha permesso di incontrare

su questo meraviglioso pianeta

Dea, Chiara Bea, Dani y Jenifer

Table of Contents

I

Abstract

In this work, an innovative perspective was applied to study the effect that atmospheric depositions have on material corrosion. The influence of different atmospheric conditions on corrosion process was investigated using weathering steel (WS) both in natural exposures and laboratory tests.

Specifically, the influence that different start time of material exposure and consequently different atmospheric conditions could have on the early stage of corrosion was evaluated by means of WS field exposures in terms of colour measurements, surfaces characterization, ions amount contained in the patina and corrosion rates. To achieve the maximum information and highlight possible correlations, all the significant variables were processed by Principal Component Analysis (PCA).

Additionally, by means of the application of Design of Experiment as chemometric tool, laboratory tests (alternate immersion accelerated ageing tests) were performed on WS to evaluate the interaction among particulate matter inorganic anions and to investigate in more realistic conditions the influence of different amounts and proportions of chlorides, sulphates and nitrates on corrosion rate and metal release, underlining also competitive and synergic interactions between them. As well, through this approach it was possible to directly relate and predict the trend of the measured response factors within an experimental domain that represents different atmospheric compositions and build models that take into account also possible changes in the concentration of pollutants of growing interest.

Lastly, in order to further investigate the action of particulate matter on different kind of materials and on differently oriented surfaces, a new developed device (called "Deposition Box") to sample dry deposition was tested and validated through SEM/EDS analysis combined with the freeware software ImageJ. "Deposition Box" allows achieving reproducible samples of particulate matter (PM) dry deposits and to sample also fine particles $(0.4 - 5 \ \mu m^2)$ making the study of dry deposits less tricky.

Chapter 1

Introduction

Air pollutants such as SO_2, NO_x and O_3 are directly involved in chemical reactions that lead to corrosion of materials. Even if it is known that the acid gas SO_2 is one of the worst factors affecting the corrosion process, nowadays, due to the recent environmental regulations, the lower atmospheric levels of SO_2 induce to consider the contribution of other pollutants to the decay mechanisms.

Specifically, the increase in the relative concentrations of NO_x and Particulate Matter (PM) with respect to SO_2 focus the attention towards the study of the effects of these species that some studies in literature indicate to play a significant role in the corrosion process.

In addition, the atmospheric composition and thus the presence of a specific combination of aggressive ions can induce a certain effect on the material decay, especially during the early stage of the corrosion process, when the material begins its outdoor exposition.

In order to study this phenomenon, weathering steel, a material that was already studied through accelerated ageing tests and natural exposures, was employed in this work, exploiting the former knowledge achieved about it and its peculiar features.

Weathering steel (WS) is a low-alloyed steel, with a carbon content of less than 0.2 wt%, which shows higher corrosion resistance and tensile strength than the traditional carbon steel. Actually, due to its composition containing small amounts of alloying elements such as Cu, Cr, Mn, Ni and P, weathering steel shows an enhanced corrosion resistance related to the spontaneously development, after long-term environmental exposure, of an adherent and compact layer of corrosion products known as patina. In addition to its self-healing and protective ability, patina plays an important aesthetic role for its attractive appearance that provides to this material a special value in artistic and architectural fields.

According to the literature, the composition, stability and consequently the protective ability of the patina are strongly influenced by several factors, including exposure conditions and environmental surroundings. Thus, the presence and the amount of contaminants can induce a specific aesthetic damage and decay of WS. In order to evaluate the effect of different conditions in terms both of aggressive pollutant species

present and of environmental parameters (such as temperature, relative humidity, rainfalls and wind), sheltered and unsheltered field exposures were performed in the urban-coastal site of Rimini, Italy. Three different one-year campaigns were planned to start in different time of the year (summer, winter and spring) to subject WS samples to different condition and atmospheric compositions since the beginning of their exposure. Once withdrawn, samples were characterized through surface analysis (XRD and SEM-EDS) and to destructive or semi-destructive tests (i.e. ions extraction from the patina and pickling).

Moreover, it is also necessary to consider that changing in atmospheric pollutants concentrations can lead not only to increase the relevance of PM among contaminants but can also lead to a change in the amount and proportion of aggressive ions that can deposit on the surfaces, in dissolved or particulate form, as a consequence of wet & dry depositions. Considering the complexity of the environmental matrices, this study focus on the investigation of the action of main inorganic anions contained in atmospheric depositions (chlorides, sulphates and nitrates) in relation to their concentration and to possible synergic effects.

Therefore, besides field exposures, alternate immersion accelerated ageing tests were performed to deeply investigate the effect of the selected anions. Specifically, in order to simulate real conditions and to investigate the potential interactions among the anions, not only ions pure solutions have been considered but also different mixtures of chlorides, sulphates and nitrates, choosing the range of concentrations so as to represent both mild and quite aggressive atmospheres.

To this purpose, the Design of Experiment (DoE) was applied as chemometric tool. Essentially, besides data analysis and their representation, multivariate methods can also be used as powerful and useful tools during the planning and the optimization stage of an experimental procedure. Specifically, in order to achieve the maximum knowledge and high-quality information through the minimum number of experiments, experimental design can be performed as a replacement for the classical univariate OVAT – one variable at a time approach. In this study, a Full Factorial Design was applied and all the variables considered relevant and significant for the system (in this case the ions concentrations) were varied at the same time within a selected experimental domain based on a defined matrix plan. Additionally, once the experiments have been performed, by means of DoE is possible to acquire also predictive information about the factors monitored in the entire experimental range, building and validating models. Thus,

experimental design allows to extend the information about the system moving from a local to a global level of knowledge.

To completely characterize the corrosion process, at the end of the tests, WS surfaces were analysed by X-Ray Diffraction (XRD) and Scanning Electron Microscopy (SEM), metal release in the ageing solutions was quantified through Atomic Absorption Spectroscopy (AAS) and corrosion rates were calculated.

The whole surface characterization of the aged samples was performed at Centro Nacional de Investigaciones Metalúrgicas - Consejo Superior de Investigaciones Científicas (CENIM - CSIC) in Madrid, under the supervision of Professor Manuel Morcillo Linares.

This work allowed to obtain further and more complete comprehension of the behaviour of atmosphere characterized by different levels of aggressiveness. Especially, interesting considerations were achieved focusing the attention on pollutants of growing interest, among those arises particulate matter.

Lastly, during this work, another important issue initiates to acquire relevance. As mentioned before, PM could play an active role in corrosion process through its wet and dry deposition. Although the wet and dry contributions are generally considered equally important, the majority of the works presents in literature focus on wet deposition because it is much easier to measure and evaluate than the contribution of dry deposition.

As matter of fact, even considering different exposure methods, achieve samples of dry deposits is still a challenging task due to the difficulties related to the reproducibility of these samples and therefore to achieve affordable measures of PM dry deposition fluxes. They can strongly depend not only on the atmospheric factors (such as winds, sampling height, temperature) but also on the sampler geometry, on the sampling surfaces characteristics and orientations and on other several mechanisms that take part in the deposition process (i.e. Brownian diffusion, gravitational sedimentation, extreme meteorological events).

In order to obtain representative and reproducible samples of dry deposits, a new sampler designed and developed by the research group of Professor E. Bolzacchini from the University of Milano Bicocca was validated in this work of thesis and the results are presented in Appendix A. The sampler is named "Deposition Box" and makes the dry

deposition sampling reproducible, by avoiding particles removal mechanisms (i.e. rainfall, wind) that, for their inner nature, cannot be standardised. Sampler validation was achieved through the evaluation of size distribution of deposits obtained during several different campaigns performed both on surrogate (aluminium foils and PTFE filters) and real surfaces (marbles). A new developed methodology of validation based on the processing of SEM images of the samples through the freeware software ImageJ was applied.

Therefore, this work allowed to move deeply in the study of environmental factors that influence atmospheric corrosion of weathering steel and to achieve a better and functional understanding of their interaction, enclosing the attention to pollutant species that reach high relevance in the present atmospheric composition and to the development of new methodology to simplify their future investigation.

Chapter 2

Atmospheric corrosion

2.1   General aspects of corrosion

As stated by the international standard [1], the term corrosion is used with the purpose to indicate all the effects developed by the interaction between a material and the environment or conditions to which it is exposed. This interaction spontaneously leads to a decay of the material followed by a change in its chemical-physical properties and a subsequent loss of functionality.

The usual interpretation of the term is related to an attack on a metallic material caused by reaction with its environment. Nowadays, however, the concept is used in a broader sense to extend the evaluation to each kind of material, not exclusively to metals [2].

There are three primary reasons for concern about the study of corrosion: safety, economics and conservation [3]. This statement acquires even more value and significance taking into account that material corrosion is a natural and unstoppable process. However, a good understanding of the phenomenon and an exhaustive investigation of the variables involved may help to control and reduce the decay process and moreover may provide the necessary knowledge to develop protective systems (such as coatings or inhibitors) or to identify the best practices and condition for the exposure of materials and to elaborate a proper procedure for their maintenance.

Corrosion can be considered an unstoppable process due to the natural tendency of the elements that constitute materials to return to their most thermodynamically stable state. Considering the nature of the process, corrosion can be divided in two main groups [2, 4]:

- ▪ *Dry corrosion* often called high-temperature corrosion because this process requires high temperature to occur in reasonable time. Dry corrosion consists of an oxidation process that takes place when the acting corrosive environment involves only dry gases. The mechanism associated to this phenomenon follows a chemical behaviour, for this reason, dry corrosion category is ruled by the laws of thermodynamics and chemical kinetics related to heterogenic reactions.

- ▪ *Wet corrosion*, on the other hand, represents basically the major part of the natural cases of corrosion because containing water environments are involved.

Wet corrosion is an electrochemical process driven from the result of a typical galvanic system in which an *anodic reaction* (the oxidation reaction) and a *cathodic reaction* (the reduction reaction) take place. Thus, wet corrosion is ruled by the thermodynamics and kinetics of electrochemistry.

Due to its importance and its large incidence, in this work only wet corrosion will be taken into account. The following section is going to focus on the electrochemical nature of this process.

2.1.1 Wet corrosion

When the metallic material is placed in environments containing water, it undergoes to an electrochemical process described as *galvanic* cells system (**Figure 2.1**).
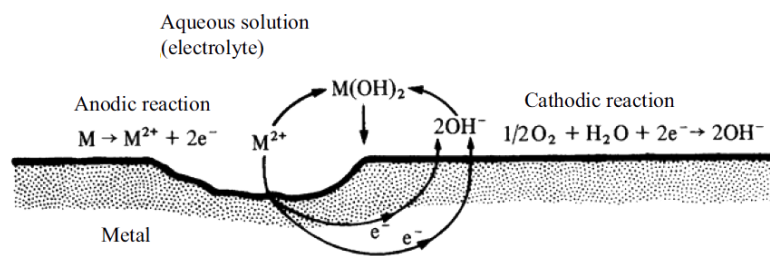
Figure 2.1: Scheme of wet corrosion of a bivalent metal M contained in an electrolyte with oxygen [2].

Galvanic system is composed by two reactions. In the anodic reaction (oxidation) a metal M is dissolved in solution as ions M^{n+}. Conversely, the cathodic reaction uses the moving and available electrons to reduce one or more specie present in the environment, for instance in **Figure 2.1** is reported the reduction of oxygen, while, in acidic solutions, the cathodic reaction may involve the reduction of hydrogen ion.

During this process it is necessary the presence of a conducting liquid – an electrolyte – in contact with the metal. In fact, the metal takes advantage of its conductivity to drive the electrons released by the anodic reaction to the cathodic area, where they can be involved in the reduction process. Anyhow, the electrical circuit is closed by the ion conduction through the electrolyte.

Generally, an electrolyte is defined as a solvent with dissolved species, the solutes, which are present into their positively or negatively charged forms. The most usual solvent in

corrosion is water, which appears to be a good solvent for most solutes due to its large dipole moment.

Basically the conductivity of water is only $\kappa = 6 \times 10^{-8}\ \Omega^{-1} \cdot cm^{-1}$ but it is increased by the concentration in solution of species like acids, bases and dissolved salts and by their charge and mobility [5].

2.1.2 Morphology of corrosion

Corrosion is often associated only to rusting and tarnishing phenomenon but actually corrosion damages occur in several other forms. Therefore corrosion is also classified [6] as:

- *General corrosion* or *uniform attack,* which is a process that involves the entire surface of the material and that represents the most common and well known form of corrosion. During this kind of decay a great loss of material can be achieved. Anyway, uniform corrosion is not considered extremely dangerous due to its easy predictability and thus controllability.

- *Pitting corrosion*, conversely, is a form of extremely local corrosion and it is considered the most dangerous form due to its relatively difficulty to be detected and due to its autocatalytic behaviour. Generally, this type of corrosion is encouraged by the presence of corrosive species, such as chlorides or sulphates and lead to the formation of cavities – *pits* – that can expand from the surface to the inside of the material, even hidden by the outer rust layer. Several differences in the morphologies of the cavities form can be also detected. Specifically, deep pits can be obtained if the attack is confined to a relatively small and fixed area of the material acting as the anode. Otherwise, shallow pits are achieved when the area of attack is larger and not so deep.

- *Crevice corrosion* that is another type of localized corrosion that occurs in proximity of crevice area, namely confined spaces characterized by a limited access of fluids from the environment.

- *Contact* or *galvanic corrosion* can arise when two metal, generally one nobler than the other, are placed with the surfaces in contact.

- *Intergranular corrosion*, which represents a localized attack at the grain boundaries of a metal. As result, loss of strength and ductility are observed in the

8

metal. Through a rapid and deep penetration into the metal, this type of attack often causes catastrophic failures.

Among the corrosion categories introduced, it can be noticed that some types of corrosion depict a very fast and dangerous process. Several years ago, the National Institute of Standards and Technology estimated that the annual cost of corrosion in the United States was in the range of $9 billion to $90 billion [3]. These figures were confirmed and expanded ($276 billion per year [7]) by various technical organizations, including the World Corrosion Organization (WCO) and the National Association of Corrosion Engineers [8].

In order to achieve a good estimation, all the possible contribution attributable to corrosion have been considered: corrosion of highways and bridges from deicing chemicals, atmospheric corrosion of steel fences and various outdoor structures (buildings, bridges, towers, ships and so on) and innumerable other constructions exposed to the atmospheric environment.

A further noteworthy fact is that was also estimated that the cost of protection against atmospheric corrosion absorbs approximately the 50% of the total cost of all corrosion-protection methods.

These figures highlight the importance of the investigation of corrosion phenomenon and especially the study of atmospheric corrosion that is introduced in the following paragraph.

2.1.3 Atmospheric corrosion

Atmospheric corrosion generally refers to a specific electrochemical corrosion process that can occur in outdoor or indoor environments on a specific material. Thus, all types of corrosion (introduced in the previous section) may take place depending on the material considered and on the contaminants present. Specifically, as mentioned before, this work is focused on the study of outdoor atmospheric corrosion of weathering steel.

As described more in detail in the next section, many parameters used to describe the atmospheric corrosion process are related to climatology, such as rainfalls, speed and direction of the wind, humidity, and so on.

The most important factor in atmospheric corrosion is by far the presence of a thin-film electrolyte that may form on metallic surfaces when they are exposed to a critical level of humidity. Thinner is the film, more it can show aggressive properties due to the high concentration reach by the species contained in it, especially in condition of sequential wetting and drying. In the presence of thin-film electrolytes, atmospheric corrosion proceeds following the general and galvanic wet corrosion mechanism described in section 2.1.1 [9].
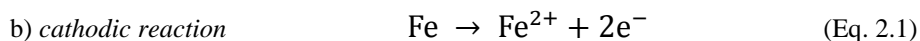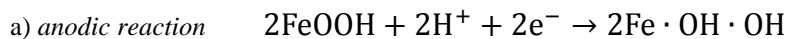
The first stage of interaction between the metal and the atmosphere is the instant reaction of water vapour with the solid. This stage is thus defined *wetting of the dry surface* and it is really fast (it occurs within a small fraction of a second).

Considering weathering steel atmospheric corrosion, water may bond with the metal either in molecular form, bonding with the oxygen atom to the metal and in association with a net transfer of charge from water to the metal, or in dissociated form, where the driving force of the process is the consecutive formation of metal-oxygen or metal-hydroxyl bonds. Hence, surface hydroxyl groups are generated (**Figure 2.2**) [10].
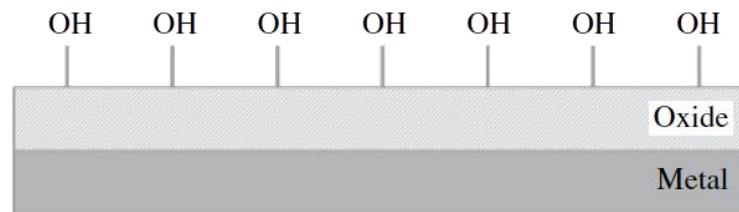
Figure 2.2: Schematic representation of surface hydroxyl groups on a metal oxide surface [10].

During this stage, the electrochemical process mainly comprehends the cathodic reaction of the metal in the rust layer to balance the anodic dissolution of iron, according to:

a) *anodic reaction* $\quad 2FeOOH + 2H^+ + 2e^- \rightarrow 2Fe \cdot OH \cdot OH$

b) *cathodic reaction* $\quad\quad\quad Fe \rightarrow Fe^{2+} + 2e^- \quad\quad\quad$ (Eq. 2.1)

While the cathodic O_2 reduction reaction is much slower than the anodic iron dissolution.

Once the available and reducible FeOOH have been used, O_2 reduction reaction becomes the predominant cathodic process and determining also the rate of the metal dissolution. As a consequence of the presence of rust layer pores filled with electrolytes, the O_2

diffusion rate is quite small and consequently also the rate of metal dissolution is not high.

This represents the second stage or the stage of *wet surface*.

Lastly, also a third stage can be observed and defined as *drying-out of the surface*. In the alternation of wet and dry cycles, the latter stage induce an increase of the rate of O_2 diffusion due to the thinning of the electrolyte film towards the inner surface of the rust layer. During this step, corrosion rate is very high. Besides being involved in the main cathodic reduction reaction, O_2, can also re-oxidize the reduced Fe^{2+} produced during the first stage (equation 2.2).

$$2Fe \cdot OH \cdot OH + \frac{1}{2}O_2 \rightarrow 2FeOOH + H_2O \qquad \text{(Eq. 2.2)}$$
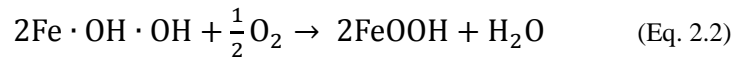
As main result, the high corrosion rate of the last stage suggests that this stage dominate the entire metal loss of the whole wet-dry cycle [10, 11].

2.1.4 Effect of the exposure parameters

As mentioned earlier, several factors rule atmospheric corrosion.

Besides the general microclimate definition of the atmosphere of exposure that is going to be introduced in the following section 2.2, it is also important to consider the specific environmental characterization of the test site (microclimate definition). Therefore, temperature, relative humidity, direction and speed of the wind, solar radiation, rainfalls amount and time of wetness have to be measured and considered. Moreover, also the presence and the concentration of atmospheric pollutants have to be taken into account.

Despite of levels of humidity causing dew and condensation represent always undesirable factors for corrosion, water in the form of rain do not always induce an increase in corrosion. Conversely, rain may wash away atmospheric pollutants, which have been deposited on the surface or dilute their presence in the electrolyte film [9].

However, considering the dependence of corrosion process from the electrolyte film formed on the material surface, some general consideration can be expressed considering the single influence of temperature and relative humidity.

Specifically, temperature may affect corrosion both promoting or moderating the process. Actually, considering the electrochemical nature of the process, an increase in temperature is directly related to an increase in kinetic rate of the process. On the other hand, high temperatures cause the evaporation of the electrolyte and thus reduce the solubility of oxygen.

Concerning the electrolyte, another important parameter that has to be considered is its thickness. As a consequence of a high thickness, the diffusion of oxygen is reduced causing a decrease in the corrosion rate. Thus, in order to reach the adequate thickness (that is assumed at about 150 µm), the critical humidity value has to be exceeded [10]. Airborne gases and particles not only modify the chemistry of the liquid layer, but they also retain the liquid layer at the surface due to their hygroscopicity. When the relative humidity reaches a certain critical value, the phase reaches its deliquescence point, prompting the absorption of water until a saturated solution is achieved [10].

A parameter as widely used as largely discussed is Time of Wetness (TOW) [12 – 14], which has the aim to estimate the period of time during which the atmospheric conditions leading to the creation of the electrolyte film occur. The adopted and standardized [15] definition of TOW is the time during which the temperature is above 0°C while the relative humidity exceeds or is equal to 80%. Thus, TOW is arbitrarily defined and depends on the chosen critical temperature and relative humidity. As a rule, corrosion occurs when temperature ranges between -4 °C and 0°C, and even lower, depending on the metal [16]. On the other hand, corrosion rates rapidly rise at a relative humidity higher than 70% or even at lower humidity values if SO_2 is present [17]. Consequently, TOW determines the duration of the electrochemical corrosion process and when the mass transport and charge transfer occur [18].

2.2 The composition of atmosphere

In order to properly study atmospheric corrosion and obtain the better understanding of the processes, it is essential to acquire maximum knowledge about atmospheres chemical composition and its chemical-physical properties.

N_2 (~ 78 mol%), O_2 (~ 21 mol%), Ar (~ 0.9 mol%) and water vapour (0 ~ 5 mol%) mainly constitute earth atmosphere. However, a multitude of trace gases with concentrations ranging from $\mu mol \cdot mol^{-1}$ to $fmol \cdot mol^{-1}$ are also present in atmosphere (**Table 2.1**). While the concentration of the major species (especially N, O) is almost unvaried, the concentration of the trace compounds can substantially vary from one site to another and from one season to another [4].

Table 2.1: Average composition of natural atmospheres [4].

Main Components (mol%)		Trace Elements (ppm)			
Nitrogen	78.1	CO_2	380	NO	0.3
Oxigen	20.9	Rare gases	30	NH_3	< 0.1
Water vapour	0 ~ 5	CH_4	2	SO_2	10^{-3}
Argon	0.93	H_2	0.5	NO_x	10^{-3}

Each chemical compound owns a specific *atmospheric lifetime* that can vary from few seconds and to more than 1000 years. Among the short-lived ones, some extremely reactive species are present and characterized by a high oxidation capacity. The most remarkable oxidizing compound is the *hydroxyl radical* (OH·), even though its lifetime in atmosphere is less than one second [19].

Among the main components of atmosphere, oxygen owns an active oxidative role in atmospheric corrosion, water acts as the electrolyte and lastly the highly soluble CO_2 contributes to the acidification of the liquid layer.

Generally, as stated by ISO 9223 [15], atmospheres can be divided in four different major categories due to the different corrosion behaviour that materials show in these environments:

- *Rural,* is an unpolluted or slightly polluted atmosphere and generally an area characterized by very dry climatic conditions; thus, a kind of atmosphere that leads to really low corrosion.

- *Urban* is a recent extension of the three original categories (rural, industrial and marine) introduced to indicate atmospheres affected by a medium pollution grade directly associated to road traffic, vehicular fuel burning and domestic heating.

- *Industrial*, which includes a higher grade of pollution than urban sites originated by the presence of industries. As better described below, sulphur dioxide and nitrogen oxide, as combustion products, are typical pollutants related to these atmospheres.

- *Marine* associated to all the coastal areas that have proved to be potentially aggressive for metallic materials due to corrosive species present (such as chlorides and sulphates, see section 2.3.4). The amount of these pollutants is directly proportional to the distance from the shore: the closer to the shore, the grater is their deposition and thus the corrosive effect.

As proposed by the European Environment Agency (EEA) [20, 21], this categorization may also be clarified considering as a criteria the distance from large pollution sources, such as cities and vehicular traffic and obtaining:

	Distance from large pollution sources
Natural background	> 50 km
Rural background	10 ~ 50 km
Near city background	3 ~ 10 km
Urban background	< 2500 vehicles/day within a radius of 50 m

2.3   Air pollutants

As mentioned before, atmospheric corrosion is a process that, among several factors, is strictly affected by the contaminant species present and their concentration. Environmental contaminants may be originated by natural sources (defined *primary contaminants*) or by further reaction on which the primary contaminants are involved to produce *secondary contaminants*.

All the species may affect materials through direct or indirect mechanism and produce a change for instance in the electrolyte film formation or in the local pH value. Contaminants can deposit both as wet and dry species: dry deposition accounts for approximately 70% while wet deposition for the remaining 30% [4].

For that reason, atmospheric contaminants and their characteristic reactions are briefly described in the next sections.

2.3.1 Sulphur dioxide (SO_2)

The most important of the atmospheric corrosive gases may be represented by sulphur dioxide (SO_2) [10]. SO_2 formation is mainly related to anthropogenic sources; specifically it is formed during the combustion of all the fossil fuels that contain sulphur. It is also emitted during metal smelting process.

Thus, SO_2 gas tends to reflect the level of industrialization of a specific region. Conversely to other typical industrial emissions (such as CO_2 and NO_2), sulphur emissions are more easily catchable, as a matter of fact, the latest technological improvements allow many regions to control and reduce their emissions. Despite of in main developed countries, both total emission and pollutant concentration have drastically decreased, in some developing countries where coal is the major source of energy, the reduction is less remarkable [22]. China and Eastern Europe tend to keep the highest emission fluxes even though both in USA and in Europe the average of SO_2 atmospheric concentration has decreased in the past decades. Specifically, the United States Environmental Protection Agency (EPA) states that national trend in sulphur dioxide levels has been reduced of about 72% from 2000 and 2016 (**Figure 2.3**) [23]. A similar situation is also accounted for Europe: in the last air quality report [24], the European Environment Agency (EEA) expresses that SO_2 levels have decreased since

2000 of approximately 60-70% (**Figure 2.4**) due to recent environmental regulations [25].
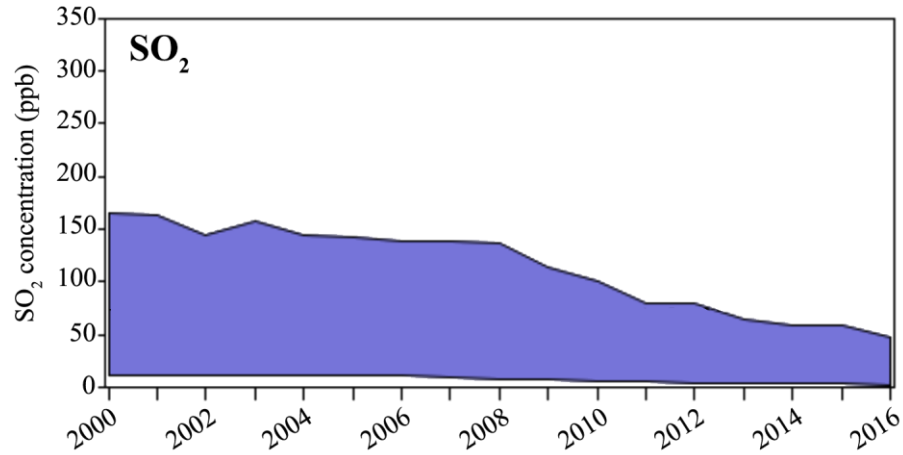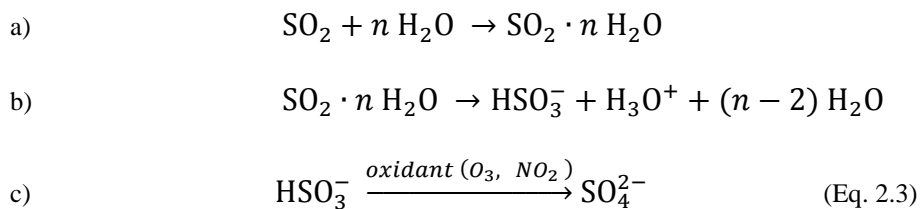

Figure 2.3: Decreasing in SO_2 atmospheric concentrations during the last decades in United States. *(Modified from [23])*
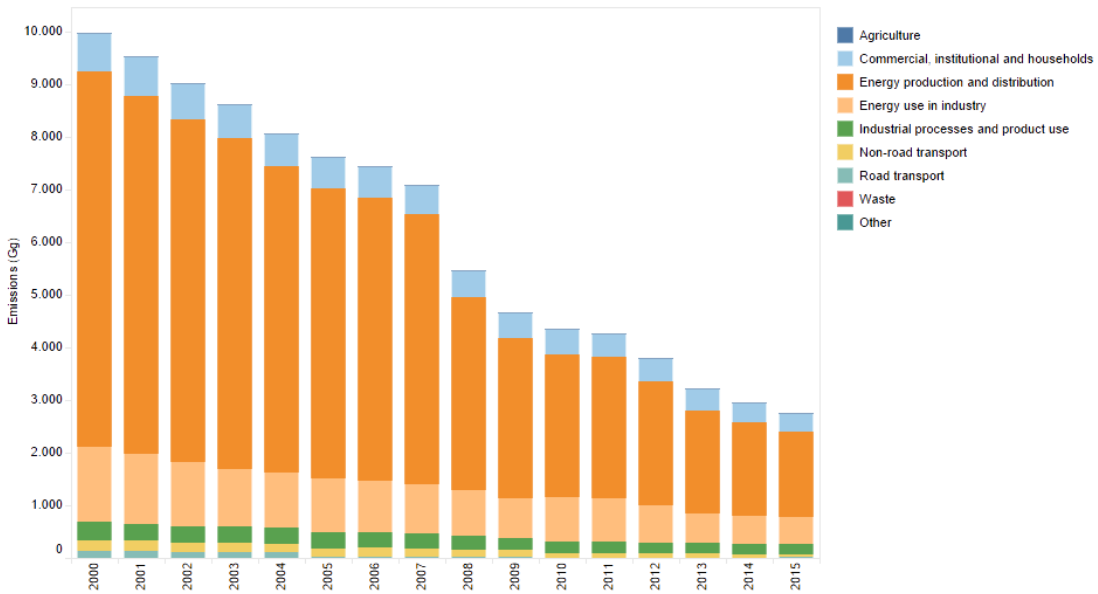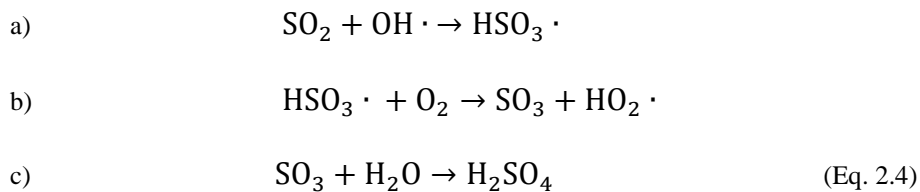

Figure 2.4: Decreasing in SO_2 emission during the last decades in Europe (EU-28). Different pollutant emission sources are highlighted. *(Modified from [26])*

Due to its moderate solubility in water, SO_2 is significantly absorbed into aerosol particles and oxidized into the sulphate ion (SO_4^{2-}) according to the following steps gathered in equation 2.3:

a) $$SO_2 + n\,H_2O \rightarrow SO_2 \cdot n\,H_2O$$

b) $$SO_2 \cdot n\,H_2O \rightarrow HSO_3^- + H_3O^+ + (n-2)\,H_2O$$

c) $$HSO_3^- \xrightarrow{oxidant\,(O_3,\ NO_2)} SO_4^{2-}$$ (Eq. 2.3)

Basically, an identical process occurs when SO_2 run into a material surface by deposition. Especially, through wet deposition of water dissolved SO_2, the sulphate ions formed can reach the surface and accelerate its decay reducing the critical value of relative humidity and thus encouraging water condensation. The critical relative humidity varies as function of both pollutant and material considered [3].

Additionally, in gas phase, this molecule is reasonably reactive towards hydroxyl radicals so the process described in equation 2.4 is carried on leading to the formation sulphuric acid (H_2SO_4) and thus to acid rains [10, 21], which can induce an acidification of the aqueous layers.

a) $$SO_2 + OH \cdot \rightarrow HSO_3 \cdot$$

b) $$HSO_3 \cdot + O_2 \rightarrow SO_3 + HO_2 \cdot$$

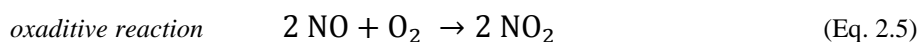c) $$SO_3 + H_2O \rightarrow H_2SO_4 \qquad \text{(Eq. 2.4)}$$

Lastly, also by dry deposition sulphur compounds (mainly in SO_2 form) can reach the materials and are adsorbed by the surface. Besides indoors, dry depositions are considered predominant in highly polluted areas, especially if they are close to the emission sources.
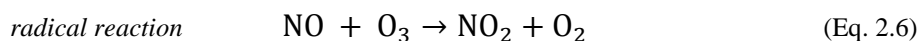
2.3.2 Nitrogen oxides

Less recognized as corrosion promoters are nitrogen oxides NO and NO_2, which are also products of combustion (mainly NO form) and specifically, in urban areas, their major source is related to vehicles traffic. Thus, high concentration levels of NO_x are typical of industrial and urban areas. As a result, behind historic records of nitrogen oxides it raises a pattern that reflects the development in energy exploitation and in the use of fuels burned by vehicles [10].
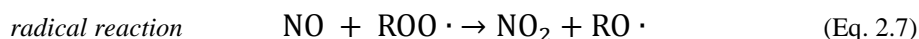
Likewise the sulphur oxides, NO_x can be oxidized to nitric acid (HNO_3) according to one of the processes described in the following equations:
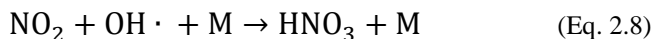
oxaditive reaction $\quad$ $$2\,NO + O_2 \rightarrow 2\,NO_2 \qquad \text{(Eq. 2.5)}$$

or

radical reaction $\quad$ $$NO + O_3 \rightarrow NO_2 + O_2 \qquad \text{(Eq. 2.6)}$$

or during the day

$$\textit{radical reaction} \qquad NO + ROO\cdot \rightarrow NO_2 + RO\cdot \qquad \text{(Eq. 2.7)}$$

to induce the formation of NO_2 species that can be further oxidized according to

$$NO_2 + OH\cdot + M \rightarrow HNO_3 + M \qquad \text{(Eq. 2.8)}$$

In equation 2.8, which is the principal sink for NO_x during the daytime, M represents an inert molecule capable of absorbing the excess molecular energies. Nitric acid is removed by atmosphere in about 1 week through dry and wet deposition. Therefore, likewise sulphur oxides, nitrogen oxides also lead to the formation of acid rains and consequently to the acidification of materials surfaces. As mentioned before (see section 2.1.3), corrosion, especially from the electrochemical point of view, is strongly related to the pH of the medium that can strongly influence also the presence of aggressive species in the wet layer.

Additionally, once NO is converted to NO_2, a number of collateral reactions are available and are directly related to the presence of sunlight. Actually, during the day, NO rapidly reaches equilibrium with NO_2 through the cycle presented in equation 2.9 – 2.10.

$$NO + O_3 \rightarrow NO_2 + O_2 \qquad \text{(Eq. 2.9)}$$

and

$$NO_2 + O_2 + M \xrightarrow{h\nu} NO + O_3 + M \qquad \text{(Eq. 2.10)}$$
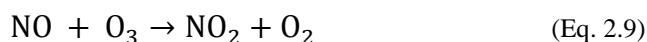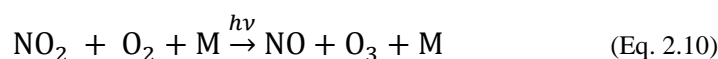
On the other hand, during the night, when the sunlight radiation is no longer present, nitrogen oxides appears only in NO_2 form due to the accomplishment of only reaction 2.9. During night hours, NO_2 is oxidized to NO_3 only as consequence of the ozone action (equation 2.6). Then, the formed NO_3 species react with NO_2 to produce N_2O_5, which immediately combines with water on particles and cloud droplets to form nitric acid that will be released by the evaporation of cloud water [19, 27, 28].

Nitric acid and ozone (described in details in the following paragraph) both show a seasonal trend with a maximum during the brightest time of the year and a minimum during the darkest one.

For what concern their trend in atmospheric concentrations, in the last years, nitrogen oxides levels have been decreased too, even if showing a slower improvement compared
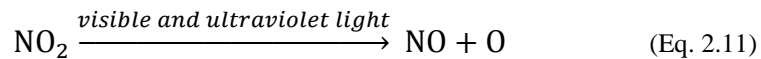
to SO_2 achievements (see **Figure 2.5**). Actually, emissions of nitrous oxides more than halved while SO_2 emission decreased of 90%, since 1990.
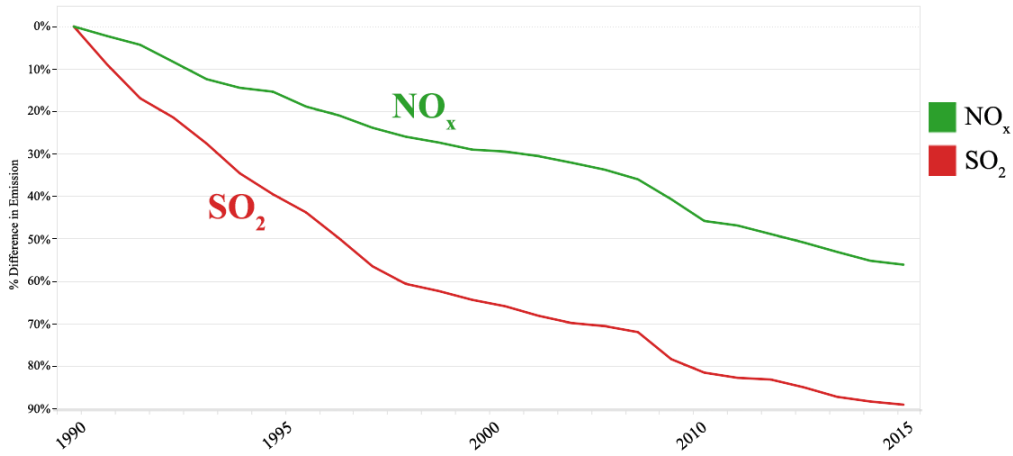
Figure 2.5: Percentage of decreasing of the NO_x emission compared to SO_2 ones during the last years (since 1990) measured in Europe (EU-28). *(Adapted from [26])*
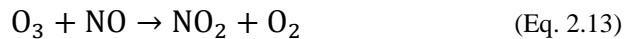
2.3.3 Ozone (O_3)

In troposphere, ozone concentrations are clearly related to the emission of nitrogen oxides, as shown in the previous paragraph and described by equation 2.11 – 2.13.

$$NO_2 \xrightarrow{\textit{visible and ultraviolet light}} NO + O \qquad \text{(Eq. 2.11)}$$

and

$$O + O_2 + M \rightarrow O_3 + M \qquad \text{(Eq. 2.12)}$$

then

$$O_3 + NO \rightarrow NO_2 + O_2 \qquad \text{(Eq. 2.13)}$$

As shown in equation 2.13, ozone tropospheric levels are sensitive to the presence of NO: for instance, near highways where NO is abundantly produced and it reaches high concentrations, a depletion of O_3 can be observed. On the other hand, due to the presence of volatile organic compounds (VOCs) in atmosphere, O_3 levels increase during the day, especially during summer months, when conditions of high solar radiation, elevated temperatures and almost absence of winds are registered [29].

Actually, the reactions reported in equation 2.11 – 2.13 describe an equilibrium among the species, where their concentrations do not vary much.

In some tropical and mid latitude cities the average of ozone have doubled or tripled in respect to the level measured two or three decades ago [30]. In Europe, in spite of a large emission reduction of ozone precursors obtained by air quality policies, a significant reduction in O_3 concentrations was not yet observed, making at present this secondary pollutant one of the most problematic pollutant for Europe, in association with particulate matter (PM), better introduced in section 2.3.5 [29].

Moreover, as stated by Screpanti et al. [31], ozone concentration in Italy, especially in zones where the climate is less cold and the sunlight radiation is higher, reaches very high levels (~ 45 ppb, yearly average). O_3 levels increase especially in the period between May and July and during the hours of daylight (from 10.00 a.m. to 6.00 p.m.) [32]. Moreover, the residence time of ozone in atmosphere, that is in the order of a few days, is long enough to allow its propagation also at large distances [33].

Besides affecting human health and damage vegetation, ozone can also affect materials, including cultural heritage sites, mainly through a synergic interaction with other pollutants. Lastly, as confirmed also by the results obtained by ICP Materials [28], even though the level of the main pollutants such as SO_2 have decreased, corrosion rates measured for several tested materials increase. Thus, it may suggest taking into account other pollutants, especially O_3 and PM, which nowadays can play a more important role than in the past.

2.3.4 Chlorides

Although in literature a large part of the analytical attention has been focused on sulphur compounds, chlorides are one of the most aggressive species towards corrosion process [10]. Specifically, similar to SO_4^{2-} ions, also Cl^- are present in hygroscopic salts, which are species that promote chemical condensation of moisture in the air and simultaneously decrease the protection of the corrosion product layer.

Commonly, the main source of chlorides is sea spray. For this reason, their amount is strongly affected by several factors; first of all, the distance from the seacoast has to be considered, even though Cl^- concentration varies largely from seacoast to seacoast and season to season. Secondly, the direction and the strength of prevailing winds should not be overlooked, also considering that through winds chlorides are carried straight to

materials surfaces where can be transported across the rust film, thus they can directly attack the underlying bulk metal [6]. Morcillo et al. [34] described the relation between "saline wind" (i.e. certain marine wind directions) and the variation in salinity, so the change in chlorides content. Specifically, for each site considered a prevalent direction can be determined that most contribute to the enrichment of marine aerosol from the sea to the land. Moreover, above a critical velocity close to 3 m · s^{-1} coastal atmospheric salinity remarkably increased, depending on the persistence in hours of the critical conditions.

Anyway, the presence of chlorides is often detected also far from the seashores due to the possible alternative origin of chlorides from human activities such as road deicing, coal burning and incinerators. Chlorides are also one of the constituents (mainly in in NaCl salt form) of particulate matter (as described in the following section).
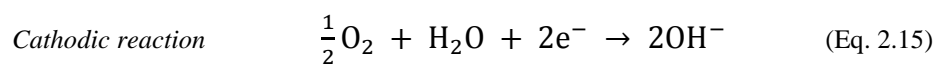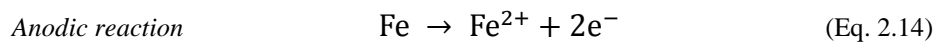
Airborne salinity refers to the content of gaseous and suspended salt in the atmosphere. Since the salt directly deposited on the material surface affects the corrosion, the airborne salinity is measured in terms of deposition rates (mg · m^{-2} · day^{-1}). Several methods have been employed to determine the contamination of atmosphere induced by chlorides carried by aerosol. For instance, the "*wet candle method*" [35] is relatively simple but brings some disadvantages over, mainly overestimating the salinity: actually, wet candle also collects particles of dry salt that might not deposit otherwise. Thus, it provides an indication of the salinity of the atmosphere rather than the contamination of the exposed metal surface. Chlorides levels can also be measured in terms of concentration of the dissolved salt in rainwater or in bulk deposition.

As described in section 3.4.3, chlorides compete with OH^{-} to bond the metal surface and they are particularly favourite if the surfaces present irregularities, roughness or if the rust layer is discontinued [36, 37]. Once the chlorides have been adsorbed on the substrate, an oxidative anodic reaction induces the formation of soluble compound that can easily dissolved in water solutions and penetrate in interstitial spaces. What is here described represents the beginning of *pitting corrosion* (**Figure 2.6**), one of the most aggressive forms of corrosion [4] due to its propensity to propagation.
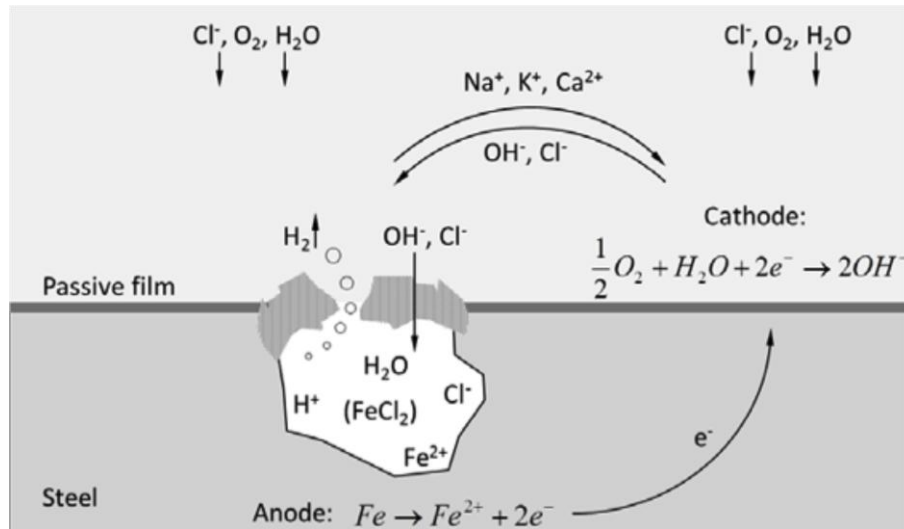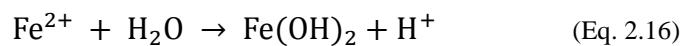
Figure 2.6: *Pitting* corrosion scheme highlighting the effect of chlorides in the process, when pH is higher than 3. *(Adapted from [38])*

In fact, pitting corrosion is a localized accelerated dissolution of metal that takes place as a result of the breakdown of the protective passive film present on the material surface. Specifically, when chlorides are dissolved in water, a particular background may be established inside the areas where the film is damaged, called also *cavities* or *pits*. Afterward, pits act like nuclei for the amplification of the process. Together with an increase in chloride ions concentration, pH within the cavities tend to significantly decrease due to the metal hydrolysis reaction expressed in equation 2.16:

$$\text{Anodic reaction} \qquad\qquad Fe \rightarrow Fe^{2+} + 2e^- \qquad\qquad \text{(Eq. 2.14)}$$

$$\text{Cathodic reaction} \qquad \frac{1}{2}O_2 + H_2O + 2e^- \rightarrow 2OH^- \qquad \text{(Eq. 2.15)}$$

therefore

$$Fe^{2+} + H_2O \rightarrow Fe(OH)_2 + H^+ \qquad\qquad \text{(Eq. 2.16)}$$

Subsequently, the hydrolysis described in equation 2.16 encourages the penetration and diffusion of chlorides in the cavity to achieve a charge balance.

It is noteworthy consider also that pits often appear to be rather small at the surface but may own larger cross-section area deeper, hidden under surface deposit and/or corrosion products and causing an unseen perforation and leakage [39].

Another influence of the presence of chlorides that should not be overlooked is related to the steel corrosion. As well described in the following section 3.4.2, rust layers on iron and steel generally includes different oxides and hydroxides. Specifically, FeOOH may own several crystal forms. Apparently its β-FeOOH (known as *akaganeite*) is originated only in determined condition, among which emerges also a relevant concentration of chlorides required.

2.3.5 Particulate matter (PM)

Particulate matter (PM) is a complex matrix constituted by a mixture of solid particles and liquid droplets (aerosols) in air, which vary in size and composition depending on the location and time. PM consists of several species, including elemental or black carbon (BC) and organic carbon (OC) compounds, sulphates, nitrates, trace metals, soil particles and sea salt [40, 41]. PM size ranges in a wide interval; considering PM characterized by an aerodynamic diameter less than 10 μm, four different fractions can be distinguished:

- ≤ 10 μm, namely PM_{10} or also denoted as *coarse particles*

- ≤ 2.5 μm, namely $PM_{2.5}$ or also denoted as *fine particles*

- ≤ 0.1 μm, namely $PM_{0.1}$ or also denoted as *ultrafine particles*

- ≤ 0.05 μm, namely $PM_{0.05}$ or also denoted as *nanoparticles*

The early Vernon's experiment [42] expressed the importance of atmospheric dust, besides the well-known hazard for human health [29, 43], on the corrosion process. The role of PM in the decay process is remarkably enhanced in the last decades, due to a change of atmospheric composition in terms of pollutants concentration. According to [24], **Figure 2.7** shows the increase in Europe of the PM relative concentration respect to other pollutants, especially respect to sulphur dioxide and nitrogen oxide.
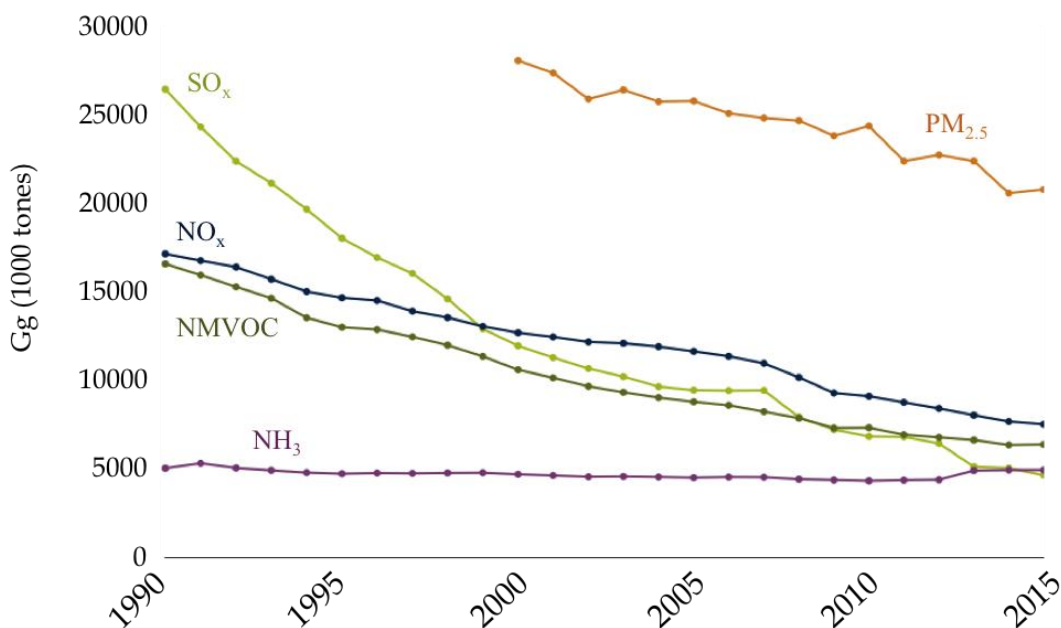
Figure 2.7: Emissions of the main air pollutants in Europe during 1990-2015.
(Adapted from [23])

In terms of source origin, PM can be present in atmosphere because it is directly emitted (*primary* aerosol) from natural or anthropogenic sources or formed in the atmosphere from a series of gaseous combustion by-products such as VOCs (volatile organic compounds), NH_3, SO_x and NO_x (*secondary* aerosol). Secondary PM is particularly sensitive also to the reaction of gaseous compounds with O_3, OH· and other reactive species [41]. Secondary aerosol is also responsible for long-range transport of sulphur and nitrogen.

As a result to its sensitiveness towards geographical and time variables, PM is a complex mixture subjected to high multiplicity in terms of composition. Moreover, changing in the atmospheric composition can lead to change the amount and the proportion of aggressive ions that composed the chemical fractions of PM. Mainly, the *water-soluble* fraction of PM contains water-soluble compounds such as nitrates, sulphates, chlorides and ammonium in different proportion according to the site considered and the seasons [44]. In **Table 2.2** are reported the annual average concentration (in ppm, that in solutions corresponds to mg · L^{-1}) of chlorides, nitrates and sulphates determined in bulk deposition – labelled with '*' – or rains – labelled with '♦' – in different geographical areas and representing mild atmospheres [45 – 50]. It should be specified that in presence of more aggressive atmospheres, this species can also reach higher values [51].

Table 2.2: Annual average concentration of chlorides, nitrates and sulphates.

Annual Average Concentration (ppm)	Years	B / R	Ref.	Cl^-	NO_3^-	SO_4^{2-}
Atehns, Greece	2001-02	◆	[34]	5.01	3.7	11.85
Cadriano, Italy	2009-13	*	[35]	5.42	15	10.56
Madrid, Spain	2009-13	*	[36]	0.17	0.21	0.4
Milan, Italy	2009-13	*	[36]	0.33	1.79	1.2
Stockholm, Sweden	2009-13	*	[36]	0.3	0.76	0.4
Shangdianzi, China	2007	◆	[37]	0.92	6.33	10.47
Hedo, Japan	2004	◆	[38]	23.9	0.6	5.1
Brisbane, Australia	2007-08	*	[39]	23.76	10	9.31

PM can be removed from the atmosphere through three principal mechanisms [52], thus they also represent the ways in which PM can deposit on the surfaces of materials:

- *Wet deposition* that takes place during rain events.

- *Dry deposition*, which occurs in absence of precipitation and that is ruled by several factors (see section A.1).

- *Occult deposition* that takes into account water droplets deposited by the interception of fog, mist or clouds; although this contribute can reach a significant role in specific case, it is generally negligible in urban sites.

The samplers used to evaluate atmospheric deposition can be differentiated into various categories depending on which depositions are interested to collect: *dry*, in absence of rain, *wet*, collected only during rain and *bulk*, where wet and dry deposition are collected together

Moreover, PM can act on materials through a direct or an indirect mechanism. In the latter case, it can promote the adsorption of corrosive gases, such as SO_2, carrying those gases from the atmosphere directly to the metals surface and prompting in this way its corrosion.

On the other hand, the hygroscopic behaviour (i.e. deliquescence and adsorption of water on the particles surface) of NaCl, $(NH_4)_2SO_4$, Na_2SO_4 and NH_4NO_3 particles promotes the growth of aerosol particles and thus changes their chemical reactivity [53]. Therefore, in contact with metallic surfaces, PM can significantly influence corrosion rate forming an electrolyte on the metal due to its hygroscopic nature. Actually, when metallic surfaces

become contaminated with hygroscopic salts, their surfaces can be wetted at a lower value of relative humidity. For instance, the presence of magnesium chloride ($MgCl_2$) on a metallic surface can make it wet at 34% RH while sodium chloride (NaCl) on the same surface requires 77% RH to create the same effect [54].

2.3.6 Other pollutants

Lastly, in this section are concisely described some other pollutants, which have a minor effect on the corrosion process [10].

Hydrogen sulfide has largely natural sources by the degradation of organic sulphuric compounds. Nevertheless, anthropogenic process similar to the natural ones can provoke H_2S emissions. Even if its water solubility is slight, hydrogen sulfide (H_2S) can dissolve following equation 2.17 and originating HS^-, which is a corrosive agent.

$$H_2S \ (g) \rightarrow \ H_2S \ (aq) \rightarrow H^+ + HS^- \qquad \text{(Eq. 2.17)}$$
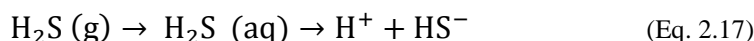
Ammonia is the only base among the common atmospheric gases. Besides its presence in the natural ecosystems, the global NH_3 cycle is ruled by the anthropogenic sources especially from agriculture through, animal excrements, synthetic fertilizers and burning biomass. The high solubility of NH_3 induces its loss to water-covered aerosol particles and cloud droplets causing substantial variations in its atmospheric concentrations. Moreover, equilibrium with the ammonium cation NH_4^+ occurs due to its water solubility; this reaction is followed by a local increase in pH.

$$NH_3 + \ H_2O \ \rightarrow NH_4^+ + OH^- \qquad \text{(Eq. 2.18)}$$
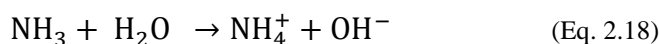
Then, through the combination with oxidized sulphur dioxide, ammonium cation is generally converted in $(NH_4)_2SO_4$ or acid ammonium sulphates (such as NH_4HSO_4 or $(NH_4)_3H(SO_4)_2$).

CO_2 is a natural constituent of the atmosphere acting in a balanced cyclic pattern that involves vegetation, oceans and some photochemical reactions. However, CO_2 is also emitted by anthropogenic activities (especially in North America, Europe and China) due to the combustion of fossil fuels and during the manufacture of cements. Carbon dioxide is an unreactive species in the atmosphere, so it has a long atmospheric lifetime. Due to

its solubility in water it can be absorbed and thus dissociate producing carbonic acid according to:

$$CO_2 \text{ (g)} \rightarrow CO_2 \text{ (aq)} \xrightarrow{H_2O} H^+ + HCO_3^- \qquad \text{(Eq. 2.19)}$$
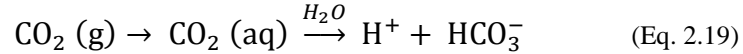
Lastly, another slightly aggressive atmospheric pollutant is carbon monoxide. It is not specifically aggressive towards metallic materials. The major source of CO is methane oxidation followed by technological processes (combustion and industrial processes), biomass burning, and the oxidation of non methane hydrocarbons. In troposphere, where it is consumed by OH·, CO has a chemical lifetime of about 30 – 90 days, it reaches the highest concentration during spring and it is predominately present in the northern hemisphere [40].

2.4 Corrosivity of the atmospheres

Metals, protective coatings and other materials are subjected to deterioration when exposed to atmospheric environments even in mild conditions. Pollution just increases and influences materials decay and corrosion rates. Thus, in order to select the right materials, propose a protective system and reduce cost damages, a good knowledge concerning atmosphere of exposure is required. Subsequently, this information and understandings were gradually included in several international standards [55].

ISO 9223 [15] provides a useful classification of outdoor atmospheric environments on the basis of their corrosivity due to Cl^- (S_{dep}) and SO_2 (P_{dep}) depositions and time of wetness (TOW $- \tau$), as shown in **Table 2.3**. TOW is estimated as the time during which relative humidity is greater than 80% and temperature is higher than 0 °C.

Table 2.3: Atmospheric corrosivity classification based on Cl^- and SO_2 depositions and TOW values.

τ Time of Wetness $h \cdot a^{-1}$	Corrosivity Levels	Cl^- Deposition rates $mg \cdot m^{-2} \cdot d^{-1}$	Corrosivity Levels	SO_2 Deposition rates $mg \cdot m^{-2} \cdot d^{-1}$	Corrosivity Levels
$\tau \leq 10$	τ_1	$S_{dep} \leq 3$	S_0	$P_{dep} \leq 4$	P_0
$10 < \tau \leq 250$	τ_2	$3 < S_{dep} \leq 60$	S_1	$4 < P_{dep} \leq 24$	P_1
$250 < \tau \leq 2500$	τ_3	$60 < S_{dep} \leq 300$	S_2	$24 < P_{dep} \leq 80$	P_2
$2500 < \tau \leq 5500$	τ_4	$300 < S_{dep} \leq 1500$	S_3	$80 < P_{dep} \leq 200$	P_3
$5500 < \tau$	τ_5				

When atmospheres show level above those reported in **Table 2.3**, the extreme category CX is used to indicate their aggressiveness. From the classifications based on Cl$^-$ and SO$_2$ depositions and TOW, corrosivity categories directly related to corrosion rates can be correlated and derived. **Table 2.4** reports the estimation of corrosivity categories (C1 – C5) based on corrosion rates for each material such as carbon steel, zinc, copper and aluminium.

Table 2.4: Corrosivity categories for different materials based on corrosion rates related to the first year of their exposure [15].

Corrosivity Category	r_{corr} **Carbon steel** corrosion rate $g \cdot m^{-2} \cdot a^{-1}$	r_{corr} **Zinc** corrosion rate $g \cdot m^{-2} \cdot a^{-1}$	r_{corr} **Copper** corrosion rate $g \cdot m^{-2} \cdot a^{-1}$	r_{corr} **Aluminium** corrosion rate $g \cdot m^{-2} \cdot a^{-1}$
C1	$r_{corr} \leq 10$	$r_{corr} \leq 0.7$	$r_{corr} \leq 0.9$	*negligible*
C2	$10 < r_{corr} \leq 200$	$0.7 < r_{corr} \leq 5$	$0.9 < r_{corr} \leq 5$	$r_{corr} \leq 0.6$
C3	$200 < r_{corr} \leq 400$	$5 < r_{corr} \leq 15$	$5 < r_{corr} \leq 12$	$0.6 < r_{corr} \leq 2$
C4	$400 < r_{corr} \leq 650$	$15 < r_{corr} \leq 30$	$12 < r_{corr} \leq 25$	$2 < r_{corr} \leq 5$
C5	$650 < r_{corr} \leq 1500$	$30 < r_{corr} \leq 60$	$25 < r_{corr} \leq 50$	$5 < r_{corr} \leq 10$

Therefore, preliminary assessment of decay caused by environment on materials can be achieved through the estimation of corrosivity category and defining in this way a sort of standardized environment to which an object is exposed. It is a noteworthy fact that not all the facts defining the corrosion process are included in the corrosivity category estimation [56]; for instance, other environmental parameters, such as precipitations, velocity and direction of wind and sunlight [57] are not taken into account for the corrosivity classification. Specifically, some discrepancies can be noticed for carbon steel due to the presence of alloying elements that affect the corrosion resistance (see section 3.3). For that reason, once again, it is remarked the inevitable need to apply a multivariate tool able to consider all the variables that affect the system to achieve a better understanding of the system in analysis and not to neglect any element.

2.5   Methodologies for the study of corrosion

Considering how the lifetime of a material is affected by the environmental conditions, the study of material atmospheric corrosion and the characterization of the corrosion products formed in different exposure conditions represent a really valuable knowledge to better understand the behaviour of this phenomenon [58]. Therefore, developed advanced technologies looking at the corrosion control and investigating atmospheric corrosion mechanism turns out to be advantageous also to achieve a reduction of the costs related to decay of materials.

Due to the influence of many parameters, corrosion in natural outdoor or indoor environment is a complex process that can be studied by means of field tests. However, considering the large number of variables that can influence the exposure and in order to guarantee the comparison between the results achieved, field tests require to be standardized. The outdoor exposure site should be characterized by uniform conditions of a specific environment and it should be located in such a way that sources of emission can be avoided. Additionally, samples should be exposed facing south in the northern hemisphere while the opposite orientation is required in the southern hemisphere [59]. Furthermore, the main environmental parameters (such as temperature, relative humidity, wind direction and speed, precipitations) should be measured as well as the content of the atmospheric pollutants species (such as chlorides, sulphur dioxide and any other gas and/or particle of interest) [59].

Several studies employed natural field exposures to study the corrosion process of steels, especially to evaluate the composition and the protective ability of the rust layer formed on the material investigated in this work, i.e. weathering steel (later described in section 3.4) [28, 60 – 63] and to relate the corrosion products formed to different environments: especially to marine [64 – 66] and urban or industrial [66 – 69] atmospheres.
Moreover, specific attention was paid to the study of the effect of the main atmospheric pollutants such as SO_2, NO, O_3, chlorides and particulate matter [70 – 72].

Nevertheless, natural atmospheric exposure tests show the disadvantage of being costly and time-consuming. Even if the main steps forward in the study of atmospheric corrosion arise from natural exposures, atmospherics tests can take about 10 – 20 years or more. Therefore, researchers were encouraged also to use accelerated laboratory tests to

study the performance of materials towards different environments and the mechanisms of their decay [73].

Actually, in order to perform more systematic studies of the parameters that influenced corrosion, laboratory tests are frequently used. By applying laboratory tests, single parameters can be studied and varied under controlled conditions. Obviously, considering the reduction of the variables acting in a controlled process, the representativeness of these tests may be reasonably questioned. A comprehensive study [74], in which the corrosion effects of nickel have been compared in the field and laboratory tests, can answer to this issue. In both natural exposures and laboratory tests, same or similar corrosion products were formed. Even if each metal behaves in a unique way, the results obtained for nickel are encouraging and suggest that the same corrosion process takes place in both exposures.

Among the several accelerated cyclic corrosion tests that have been used for weathering steel investigation, only few have been designed and performed according to the standard. Basically, these tests consist of a sequence of a wetting and a drying stage performed with different characteristics (such as temperature, relative humidity, drying conditions, the duration of each step or of the whole test and the number of cycles to be performed) by different researchers.

In 1966, the Belgian Centre for Corrosion Study developed a wet and dry method (CEBELCOR test) based on repeated cycles of immersion (12 min) in a saline solution and the subsequent drying phase (42 min) [75]. This cyclic test has been used to simulate different acting atmospheres by changing the ageing solutions. By means of CEBELCOR test, Calero et al. [76] simulated the formation of multi-layered rust on carbon steel in marine atmospheres using as weathering solution a 3.5 % NaCl solution. The effect of chlorides on steels was studied by laboratory tests also by Garcìa et al. [77] to compare the rust products formed on weathering and carbon steels and by Xiao [78] to follow the evolution of akaganeite in rust layers.

Additionally, alternate wet/dry tests were used also to investigate the effects of other pollutants on weathering steel corrosion [79, 80]; specifically, Montoya et al. [81] verify the possibility to apply both Kesternich test (used to simulate SO_2 polluted atmospheres)

and Prohesion test (that simulates marine atmosphere) on weathering steel and they point out some analogies between experimentation in field and in the laboratory.

The effects of other parameters were evaluated by means of laboratory tests: Cheng et al. [82] studied the influence of Ni as alloying element in weathering steel simulating its exposition in marine atmosphere.

Chiavari et al. [83] investigated the behaviour of weathering steel with different surface finish both in stagnant and run-off conditions using as weathering solution a solution prepared on the basis of the chemical composition and concentrations found in bulk deposition samples collected in Rimini, Italy. Artificial weathering simulating stagnant condition was performed through alternate immersion test while, in order to simulate run-off conditions, a dropping test was employed. In this test, the weathering solution is periodically dropped onto a surface of specimens and then collected to be analysed. Specimens were 45° inclined and mounted on Teflon supports. As a result, the high metal release found suggests the need of field exposures to investigate possible effects on the environment.

Thus, considering the complementary information that can be achieved by applying both experimentations, in order to obtain a better understanding of the phenomenon investigated, both natural field exposures and alternate immersion accelerated ageing test (Wet/Dry) were performed in this work.

Chapter 3

Steel

The terms *iron* and *steel* are often confusing in the common vision due to the fact that *steel* is the word used to describe almost all the alloys of iron (ferrous alloys), where the iron is the prime constituent and its percentage is always higher than 95% [84, 85]. Ferrous alloys are produced in larger quantities than any other metal type. They are widely used due to three factors: the earthly high abundance of iron-containing compounds; the relative low cost of extraction, alloying and fabrication techniques; mechanical and physical properties that make ferrous alloys extremely versatile. A taxonomic classification of metal alloys is presented in **Figure 3.1**.
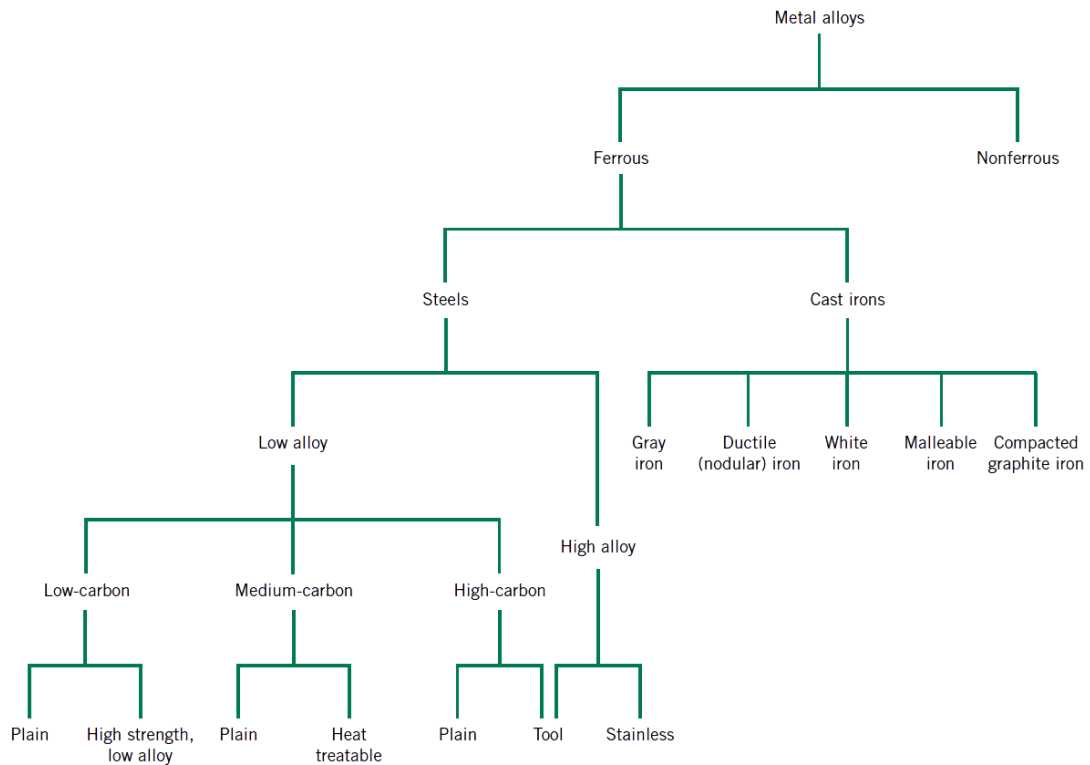
Figure 3.1: Scheme of classification for the various ferrous alloys [84].

Therefore, considering the main role played in metal alloys, investigate the nature of solid iron is a good starting point to understand what steel is. Actually the material investigated in this work is weathering steel (see the following section 3.4) that is a family of low-carbon steels.

3.1 Pure iron

Pure iron undergoes several phase changes. At atmospheric pressure, iron exists in three different allotropic forms (**Figure 3.2**) [86]:

- α – iron, or *ferrite*, which consists of a crystal structure where at each corner and in the middle of a cube it presents an atom of iron; this crystal structure is called a body-centered cubic (BCC) structure, and the geometric arrangement of atoms is often called a BCC lattice.
 This iron phase is stable below 912°C.

- γ iron, or *austenite*, that presents a structure called face-centered cubic (FCC) where the atoms lie on the corners of a cube as well as one atom lie in the centre of each cube face. The ferrite-to-austenite (α-to-γ) transformation is accompanied by a volume change. The density of austenite is 2% higher than ferrite, which means that the volume per atom of iron is less in austenite.
  Austenite is stable between 912 °C and 1394 °C.

- δ iron, or again *ferrite*, which shows the same BCC structure of α – iron.
  This structure is stable between 1394 °C and 1536 °C.

Above 1536 °C, iron is present in liquid amorphous form (L).
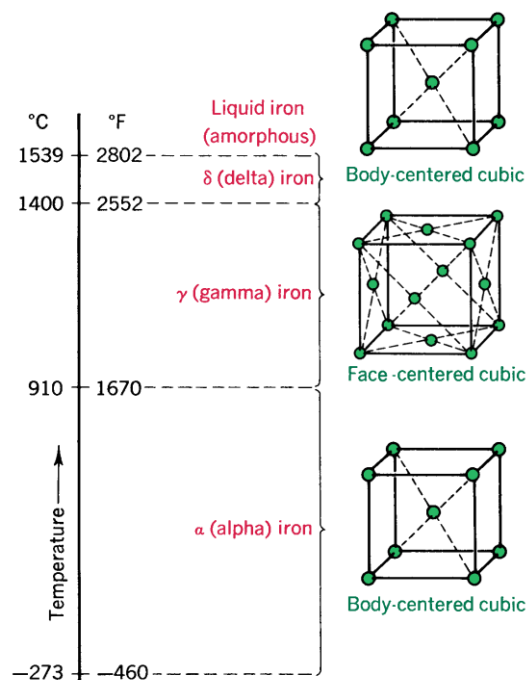
Figure 3.2: The three different allotropic forms of iron at atmospheric pressure as function of the temperature. *(Modified from [86])*

3.2　Carbon steels

The most common steels are carbon steels, which may contain up to 1.5% of carbon and generally speaking they can be subdivided into the following categories on the basis of the carbon content [76]:

- Up to 0.30% of C   ➢ *Mild steel* or *Low-carbon steel*

- 0.30 ~ 0.60% of C   ➢ *Medium-carbon steel*

- 0.60 ~ 1.00% of C   ➢ *Hard steel* or *High-carbon steel*

- Free-machining grades

Carbon is the most important single alloying element in steel due to its directly relevance on the steel mechanical properties. For instance, the strength and hardness of the alloy are raised as the carbon content is increased. Many other alloying elements are considered largely on the basis of their effects on the iron-carbon system.

The basic principle of alloying and thus of the formation of carbon steels is associated to the formation of a solid interstitial solution, where iron acts like the solvent and the carbon (or the alloying element) acts as the solute (or as an interstitial impurity). Thus, an extremely relevance is hold by the solubility of the alloying element considered inside each allotropic forms of iron and also the related phase diagrams [84]. Specifically, in **Figure 3.3** a portion of the iron – carbon phase diagram is shown. Along the left vertical axes the diagram presents all the polymorphic transformation of pure iron. Along the x axis is reported the content of carbon (wt%). The boundary of the composition axis of **Figure 3.3** is fixed to 6.70 wt% of C due to fact that at this concentration iron carbide, or *cementite* (Fe_3C) is formed. In practice, the carbon percentage in steel ranges from 0.002% to 2.1%; above this value, alloys are called cast iron and will not be considered here. Thus, the more appropriate label for **Figure 3.3** would be iron-iron carbide diagram because only iron-rich portions of iron-carbon system are here considered.
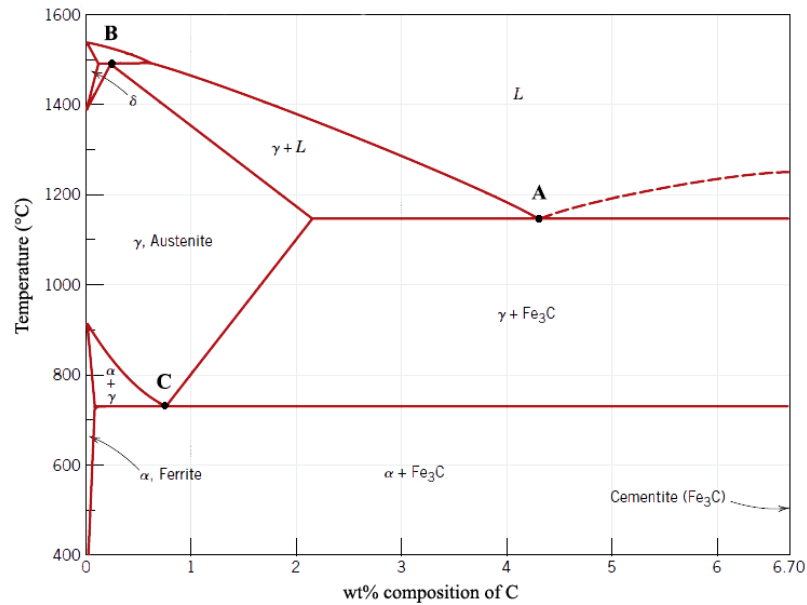
Figure 3.3: A portion of the iron-carbon phase diagram.
(Adapted from84])

Each α, γ and δ allotropic phase can behave as solvent for carbon to give different interstitial solutions: $α – ferrite$, $δ – ferrite$ and *austenite* when carbon is included in $γ –$ iron.

As interstitial impurity, carbon can have a specific maximum solubility for each allotropic form considered. Due to the shape and size of its interstitial position, in BCC structure of $α – ferrite$ only small concentration of carbon are soluble and the maximum solubility measured at 727 °C is 0.022 wt%. Despite its low concentration, carbon significantly influences the mechanical properties of both $α$ and $δ – ferrite$. Conversely, the solubility of carbon measured at 1147 °C in austenite is approximately 100 times greater (2.14 wt%) due to the larger octahedral sites of the FCC structures.

Mechanical and chemical-physical properties of steel are strictly related to the carbon percentage presents in the alloy. Specifically, *mild steels* (0.05 ~ 0.30 wt% of C), due to their microstructures, are relatively soft and weak but really malleable, ductile and tough; in addition, they are also machinable and weldable so suitable for a lot of application including structural shapes, sheets used in pipelines, buildings and bridges.

Medium-carbon steels (0.30 ~ 0.60 wt% of C) are most often used in tempered condition and they improve their ductility and strength after heat treatments.

High-carbon steels (normally 0.60 ~ 1.40 wt% of C) are the hardest and yet ductile among carbon steels. These steels are used as cutting tools and as dies to form and shape other materials.

3.3 Effect of alloying elements

Alloying elements are used primarily to increase the hardenability of the steels. In fact, when they are added to iron-carbon alloys, its phase diagram will change and the three transactions, called A, B and C in **Figure 3.3**, slightly shift. Specifically, these three transactions refer to phase transformation [85]:

A. *Eutectic transformation*

The eutectic reaction involves a liquid phase that, upon cooling, is transformed into two solid phases at a characteristic temperature.

For what concern iron-carbon alloys, this transformation occurs at T = 1148 °C and wt% of C equal to 4.3% and can be represented as (equation 3.1):

$$L \rightarrow Austenite + Cementite \qquad \text{(Eq. 3.1)}$$
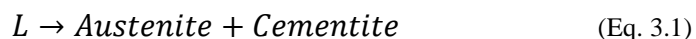
B. *Peritectic transformation*

During this process, upon cooling, a liquid and one solid phase are transformed in another solid phase.

For what concern iron-carbon alloys, this transformation occurs at T = 1495 °C and wt% of C equal to 0.17% and can be represented as (equation 3.2):

$$L + \delta - Ferrite \rightarrow Austenite \qquad \text{(Eq. 3.2)}$$

C. *Eutectoid transformation*

For what concern iron-carbon alloys, this transformation occurs at T = 723 °C and wt% of C equal to 0.8% and can be represented as (equation 3.3):

$$Austenite \rightarrow \alpha - ferrite + Cementite \qquad \text{(Eq. 3.3)}$$
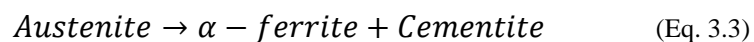
Phase transformation usually involves alteration of the material microstructure, which directly influences its mechanical properties and resistance towards the corrosion [84]. Thus, metals, such as manganese, nickel, chromium, vanadium, tungsten, molybdenum are usually added to obtain specific properties; for instance [6, 87, 88]:

- **Manganese**, which acts in a three-fold manner: it promotes the hardenability and the tensile strength of the steel; it prevents the formation of iron sulphide inclusions and assists in deoxidation of the steel.

- **Silicon** is a filler metal used as a deoxidizer and it tends to strengthen the alloy.

- **Copper** is beneficial to atmospheric corrosion resistance when it is present in amounts exceeding 0.20%, despite of it moderate tendency to segregate.

- **Phosphorus**, that generally is considered as an undesirable impurity, can be added in low-alloy steel to improve both strength and corrosion resistance.

- **Chromium** is added for remarkably increasing the hardenability of the steel and for its great improvement in corrosion resistance. Cr is a really powerful alloying element in steel.

- **Nickel** is frequently used to improve steel toughness at low temperature and if it is combined with chromium, Ni produces alloy steels with greater hardenability, higher impact strength and greater fatigue resistance.

3.4   Weathering Steel

This study is mainly focused on the investigation of the atmospheric corrosion of a specific low-alloyed steel called *weathering steel*, which will be mentioned in the following sections with the 'WS' acronym. WS are steels, which contain less than 3 ~ 5 wt% of metals such as Cu, P, Cr, Ni and Si, as alloying elements [10]. Due to their composition, during field exposure, an adherent, compact and protective layer of corrosion product is formed on their surface causing a lag in further corrosion. In the 1920s several steel companies and technical committees started specific outdoor studies during which it was recognized that the addition of small quantities of other alloying elements (especially copper) to the alloy provided an increase in the atmospheric corrosion resistance and, on the other hand, an enhancement in the strength of the steel [22].

Weathering steels were originally developed by U.S. Steel Corporation in 1933 and their invention inadvertently created the classification of *high-strength low-alloy* (HSLA) steels. Since their first commercialization branded as COR-TEN to indicate their high corrosion resistance and tensile strength, the use of WS has spread to the entire world,

thus tested and exposed to different environmental conditions and consequently it has undergone to several changes in composition and many variant have been developed. Specifically, the latest version available on the market is based on the Fe – Cu – Cr – Ni – P system that represents the basis for the American Society for Testing and Materials (ASTM) standard series [89 – 93] listed in **Table 3.1**.

Table 3.1: Composition of weathering steel according to the standards (*Modified from [10]*).

	C	Si	Mn	P	S	Cu	Cr	Ni
CORTEN	~0.10	0.50–1.00	0.10–0.30	0.10–0.20	—	0.20–0.50	0.50–1.50	
1940 CORTEN	≤0.12	0.25–0.75	0.20–0.50	0.07–0.15	≤0.05	0.25–0.55	0.30–1.25	≤0.65
USS CORTEN A	≤0.12	0.25–0.75	0.20–0.50	0.07–0.15	≤0.05	0.25–0.55	0.50–1.25	≤0.65
USS CORTEN B	≤0.19	0.30–0.65	0.80–1.25	≤0.04	≤0.05	0.25–0.40	0.40–0.65	≤0.40
USS CORTEN B-QT	≤0.19	0.30–0.65	0.80–1.25	≤0.04	≤0.05	0.25–0.40	0.40–0.65	≤0.40
USS CORTEN C	≤0.19	0.30–0.65	0.80–1.35	≤0.04	≤0.05	0.25–0.40	0.40–0.70	≤0.40
ASTM A242 (M)	≤0.15	—	≤1.00	≤0.15	≤0.05	≤0.20	—	—
ASTM A588 A	≤0.19	0.30–0.65	0.80–1.25	≤0.04	≤0.05	0.25–0.40	0.40–0.65	<0.40
ASTM A588 B	≤0.20	0.15–0.50	0.75–1.35	≤0.04	≤0.05	0.20–0.40	0.40–0.70	≤0.50
ASTM A588 C	≤0.15	0.15–0.40	0.80–1.35	≤0.04	≤0.05	0.20–0.50	0.30–0.50	0.25–0.50
ASTM A588 D	0.10–0.20	0.50–0.90	0.75–1.25	≤0.04	≤0.05	≤0.30	0.50–0.90	—
ASTM A588 K	≤0.17	0.25–0.50	0.50–1.20	≤0.04	≤0.05	0.30–0.50	0.40–0.70	≤0.40

Nowadays, three main types of WS are commercialized on the market in function of their different performances:

- **Cor-Ten A** that is usually employed in architectural applications and shows an excellent corrosion resistance, about 5 ~ 8 times higher than carbon steel. Commonly is also known as *phosphorous Cor-Ten* because contains higher amount of P (0.07 ~ 0.015%) than the other commercialized WS.

- **Cor-Ten B** was specially designed with a percentage of P lower than 0.04% to avoid weld cracking of plates, at the expense of its corrosion resistance (only 4 times higher than CS).

- **Cor-Ten C**, which is the latter type introduced to the market and it was developed to accomplish higher mechanical resistance without losing corrosion resistance (that is kept comparable to those of Cor-Ten B). It appears specifically suitable for application that involves stressed structure.

As introduced, the main advantage in the WS use regards its technical properties. Actually, compared to carbon steel, WS exhibits enhanced mechanical properties that establish also a development in terms of safety concern and economic benefits. Above all, however, the major advantage is related to the improved corrosion resistance in different types of atmosphere, as shown in **Figure 3.4**.
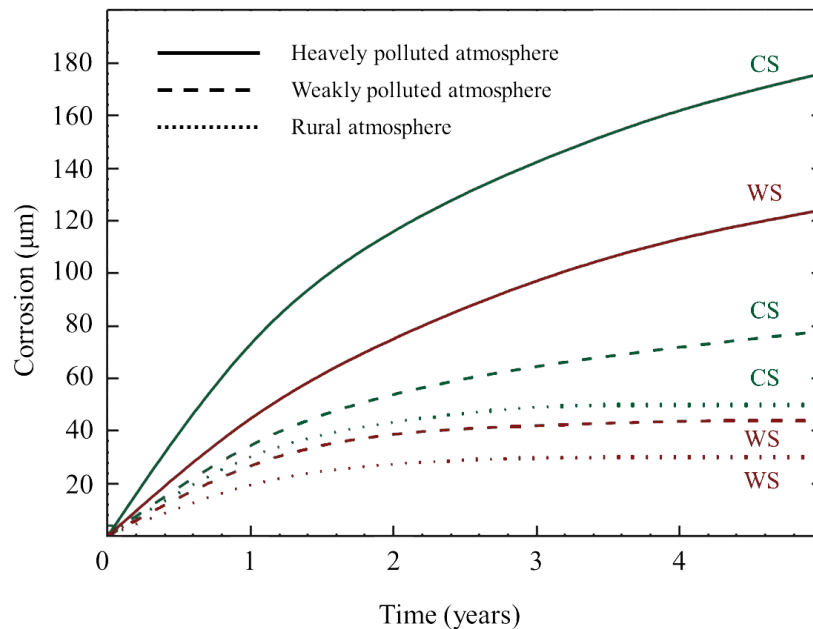
**Figure 3.4**: Comparison of the corrosion trend of WS and CS exposed in different atmospheres [94].

The special features and performance of WS are associated to the formation of a compact protective layer called *patina* composed of a mixture of iron compounds, specifically, of iron oxides and hydroxides [73]. More considerations and details concerning the mechanism of passivation of WS are expressed in section 3.4.2.

3.4.1 Art and architectural application

Investigating and studying WS gain even more importance considering that, besides the initial concept of the engineers who developed it, this material has fascinated and raised the interest of many artist and architects coming from the entire world.

Behind a less expensive and mechanically improved material, WS also owns special aesthetic features especially after its atmospheric exposure. Due to the composition of its alloy, WS exhibits unique chromatic properties, which are constantly evolving in function of the time flowing and depending on the surroundings. This may suggest a direct connection between the colour shown by the patina of the material and the exposure

conditions subjected. As shown in **Figure 3.5**, the alloy changes its colour turning from yellowish to dark-brown, acquiring a warmer and welcoming aspect [95].

1969   1973   1991   2007

4 yr elapsed   22 yr elapsed   38 yr elapsed
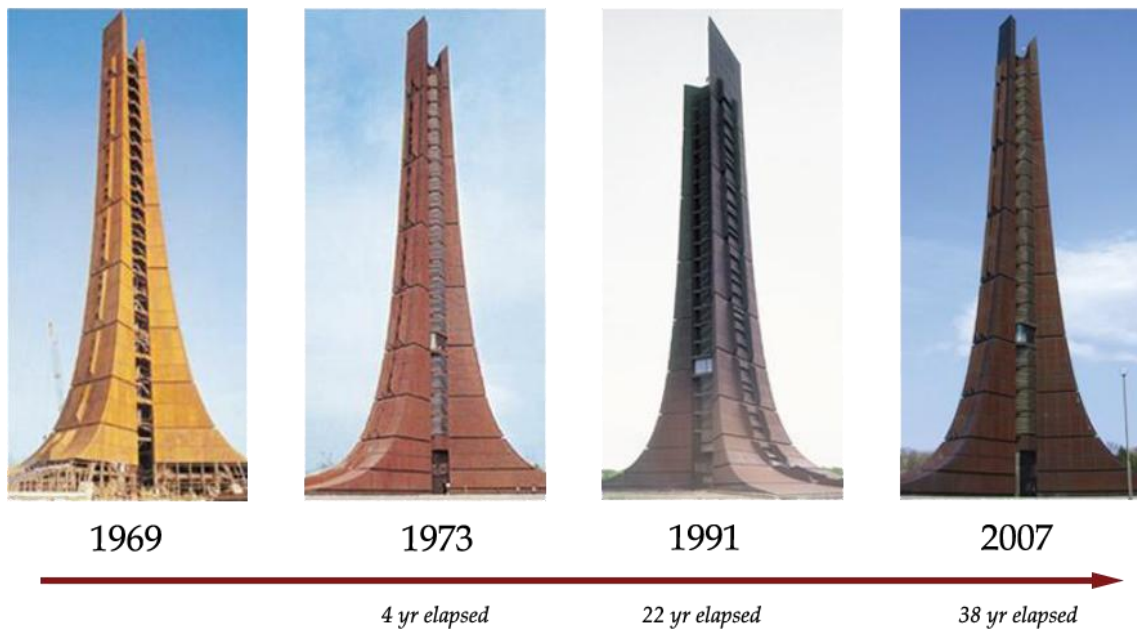
Figure 3.5: Several photos of the centennial memorial tower of Hokkaido, Sapporo taken from 1969, when it was under construction, to 2007 [99].

Thanks to its ability to change appearance over the time, WS gained popularity and the appellative of "*living material*". Specifically, after its exposure, WS showed different coloured regions due to its mechanism of autopassivation (section 3.4.2). The change of colour from yellow to dark-brown is related to the growth of a patina composed by a mixture of iron oxides and oxy-hydroxides on the surface of WS [95, 96]. Altobelli Antunes et al. [97] demonstrated that it is possible to associate the colour of the oxide to its particular phase. Red oxides showed Raman spectra typical of lepidocrocite (γ-FeOOH), while the Raman spectra of yellow oxides correspond to a mixture of lepidocrocite and goethite (γ-FeOOH).

WS is widely used in construction or modernization of each kind of buildings (such as towers, museums or art galleries, churches, universities and schools), especially combined with other kind of materials like glass, wood and cement (**Figure 3.6 – 3.10**).

Figure 3.6: New School of Architecture, Royal Institute of Technology – KTH
(Tham & Videgard, Stockolm, 2015).
© Ãke Eison Lindman
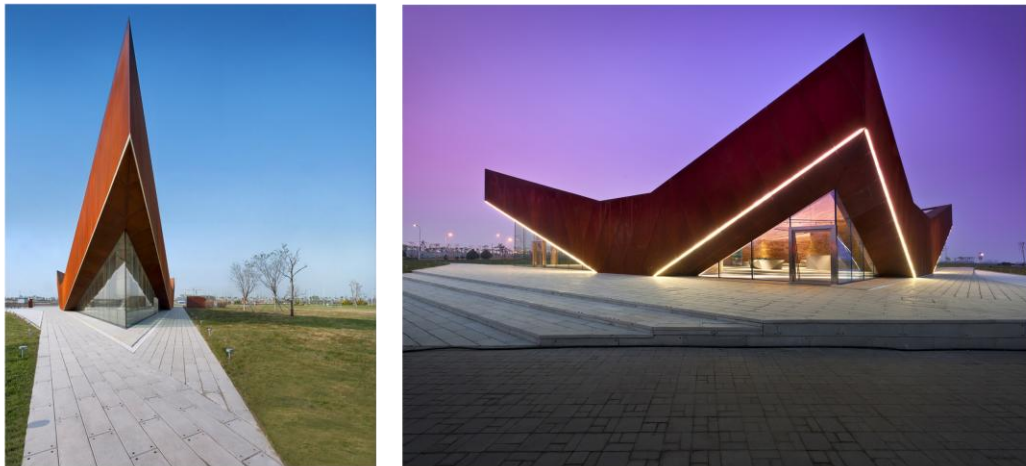
Figure 3.7: Vanke Triple V Gallery (Ministry of Design, Tianjin, 2011).
© CI&A Photography Edward Hendricks

Figure 3.8: Parish church of Santa Monica de Rivas (Vicens & Ramos, Madrid, 2009).
© archdaily.com

41

Figure 3.9: The Flour Storage (HG Arhitektuur, Tallinn, 2008).
© Martin Siplane

Figure 3.10: Vlooyberg Tower (Close to Bone, Tielt-Winge, 2015).
© Kris Van den Bosch

Additionally, besides buildings and towers, WS finds extensively application also in urban and metropolitan installations with the aim of modernize and renovate urban spaces and to generate an aesthetical enrichment (**Figure 3.13 – 3.14**) but also with practical and functional purpose (**Figure 3.11 – 3.12**).
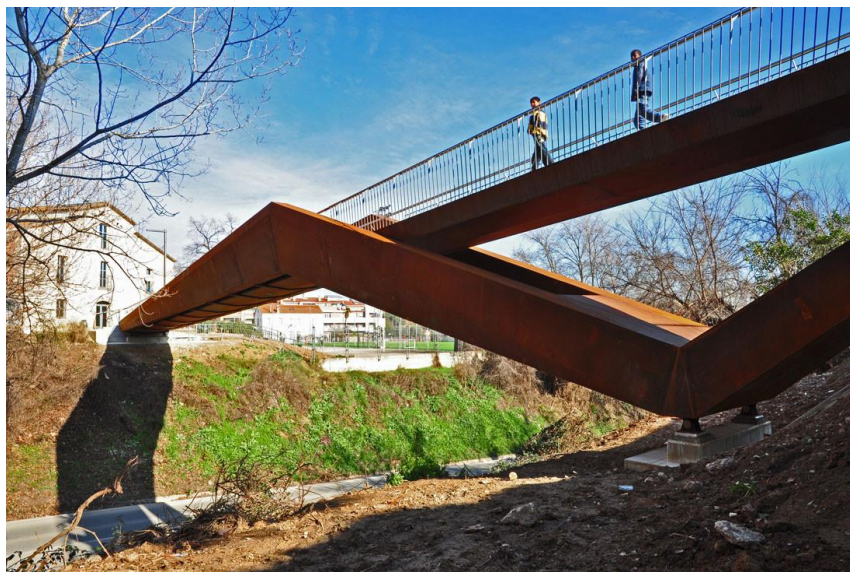
Figure 3.11: Can Gili Footbridge (Alfa Polaris, Granollers, 2010).
© Xavier Font

Figure 3.12: Craigieburn Bypass (Tonkin Zulaikha Greer, Melbourne's Freeway, 2005).
© Peter Hyatt

Figure 3.13: "Monumento al Cine" (José Carralero, Ponferrada, 2011).
© Pablo Gomèz

Figure 3.14: "Angel of North" (Sir Antony Gormley, Gateshead, 1998).
© SFT Photography

Lastly, special features of WS have stimulates and exhorted artists from everywhere to face with the new challenge of working with this material, embracing also its concept value finely related to its distinctiveness. The indivisibility occurring between WS and the time and the place in which it is housed makes each artwork realized with this material belonging only to a specific and unique place and time. Many sculptors rising from international sphere gather the occasion to work with Cor-Ten, as shown in Figure **3.12 – 3.25**.

Richard Serra is an American performance artist and sculptors who realizes his pieces of art starting from WS sheets shaped to accomplish a mixture of convex and concave surfaces that convey in the spectator a sense of lightweight movement and gentle flow (**Figure 3.15 – 3.16**).
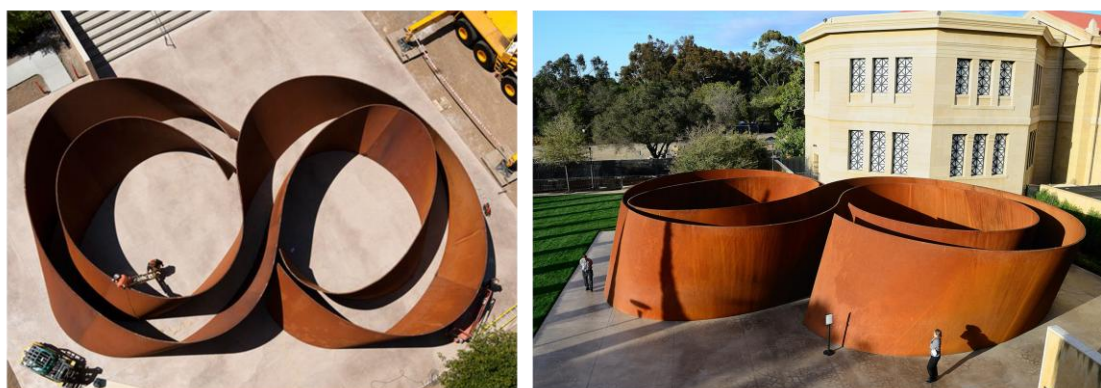
Figure 3.15: "Sequence" (Richard Serra, Cantor Center for Visual Arts at Stanford University, California, USA, 2011).
© https://slyder24.wordpress.com

Figure 3.16: "Vortex" (Richard Serra, Modern Art Museum of Forth Worth, Texas, USA, 2002).
© Modern Art Museum of Fort Worth

Bernard Venet, on the other hand, uses weathering steel to obtain sculptures composed by arched or angular structures, depicting a slight balance between man and environment (**Figure 3.17 – 3.18**).

Figure 3.17: 88.5 Arc x 8 (Bernar Venet, Gibbs Farm, Kaipara Harbour, New Zealand, 2012).
© Bernar Venet Foundation

Figure 3.18: a) 219.5° Arc x 28 and b) Two Indeterminate Lines, both exposed in a temporary exhibition (November 2015 – February 2016) at the Cultural Center and Art museum square of Hong Kong (Bernar Venet, Hong Kong, 2011).
© De Sarthe Gallery

Among these authors, one contemporary Italian author is Mauro Staccioli, whose artworks are constituted by simple geometric shapes that create a perfect frame for the outstanding landscapes (**Figure 3.19 – 3.22**).

Figure 3.19: "Primi Passi" (Mauro Staccioli, Piancorboli, Volterra, Italy, 2009).
© Studio Archivio Mauro Staccioli

Figure 3.20: "Piramide – 38° parallelo" (Mauro Staccioli, Motta d'Affermo, Messina, Italy, 2010).
© Studio Archivio Mauro Staccioli

Figure 3.21: "Cerchio Imperfetto" (Mauro Staccioli, Parco Archeologico di Scolacium, Catanzaro, 2011)
© Studio Archivio Mauro Staccioli

Figure 3.22: "Da Sinistra a Destra" (Mauro Staccioli, Parco Archeologico di Scolacium, Catanzaro, 2011).
© Cultura Italia

Lastly, several other artists have chosen to include occasionally this material in their production (**Figure 3.23 – 3.25**) often in combination with other materials, as shown in **Figure 3.23**. For instance, Paul Shanga's artwork represents a garden sculpture made of bronze and Cor-Ten.

Figure 3.23: "Critical mass" (Paul Shanga, Vancouver, 2015).
© Paul Sangha Landscape Architects

Figure 3.24: "Hidden Landscapes" (Alex Pentek, Longford, Ireland, 2013).
© Sean O'Dowd

Figure 3.25: "Rabbit" (Alex Pentek overlooking the N2 at Ashbourne, Ireland, 2012).
© Leanne Keaney

3.4.2 Atmospheric corrosion resistance

A remarkable aspect of weathering steel is that its peculiar aesthetical features and its resistance towards atmospheric corrosion are both connected to the patina formed on the surface during its natural exposure.

Specifically, the protective and self-healing abilities of WS are related to the features of this patina, which includes mainly oxides, oxy-hydroxides of iron but also miscellaneous crystalline and amorphous substances. These constituents may be endogenous products, namely the products originated by the substrate itself, or exogenous products when they come from the atmosphere. In **Table 3.2** are listed the corrosion products found most frequently in the layers formed on WS exposed to the atmosphere. In addition, a group of Fe^{2+} / Fe^{3+} hydroxyl salts are also often detected, behind amorphous and non-

stoichiometric phases. Fe^{2+} / Fe^{3+} hydroxyl salts are also known as green rusts due to their greenblue – greyish colour [100].

Table 3.2: Chemical compounds usually found in weathering steel rust layers.

Oxides	Name	Composition
	Hematite	$\alpha\text{-}Fe_2O_3$
	Maghemite	$\gamma\text{-}Fe_2O_3$
	Magnetite	Fe_3O_4
	Ferrihydrite	$Fe_5HO_8 \cdot 4H_2O$

Hydroxides	Name	Composition
	Goethite	$\alpha\text{-}FeOOH$
	Akaganeite	$\beta\text{-}FeOOH$
	Lepidocrocite	$\gamma\text{-}FeOOH$
	Feroxyhyte	$\delta\text{-}FeOOH$

Anyway, the specific composition of patina in terms of compounds present and their relative amount depends on the environment and the time of exposure [73].

In general, patina of weathering steel is formed by two overlapping layers. The outer layer is generally loose and porous and thus sensitive to flaking; it is characterized by the presence of lepidocrocite (γ-FeOOH) while the inner layer, which appears more compact, uniform and adherent to the uncorroded metal consisting of nano-meter sized particles, is formed by goethite (α-FeOOH) [101 – 103].

The mechanism of formation of this protective layer is similar to rust formation on iron and carbon steel. During the first stage (which may take several months or even few years) the formation of lepidocrocite is predominantly dominant followed by a gradual growth of an amorphous ferric oxyhydroxide caused by the dissolution-precipitation of γ-FeOOH. The amorphous compound, after decades, slowly transforms to goethite, which is more stable form of ferric oxy-hydroxyde both electrochemically and thermodynamically speaking [10]. The schematic description of distribution and long-term changes during WS atmospheric corrosion is reported in **Figure 3.26**.
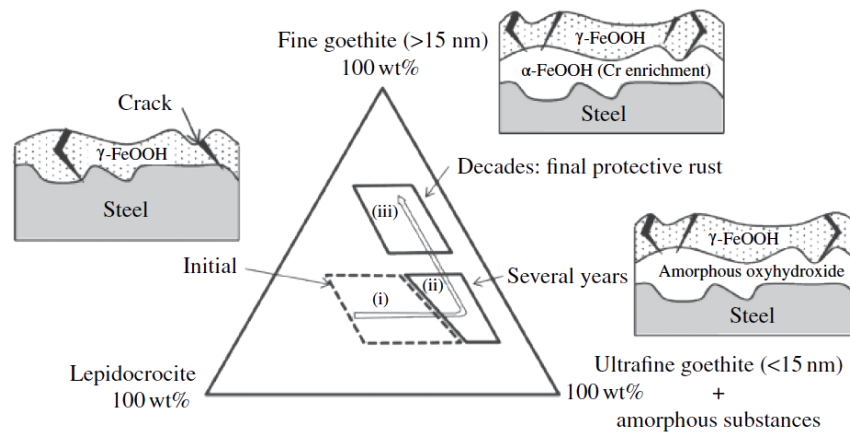
Figure 3.26: Schematic description of distribution between γ-FeOOH, amorphous ferric oxy-hydroxyde and α –FeOOH observed during different steps of atmospheric corrosion of WS [10].

Kimura et al. [104] proposed a more detailed mechanism for the autopassivation of WS. Specifically, **Figure 3.27** presents the two crystalline structure of α–FeOOH and γ-FeOOH, which are composed of FeO_6 octahedrons and intercalated hydrogen.
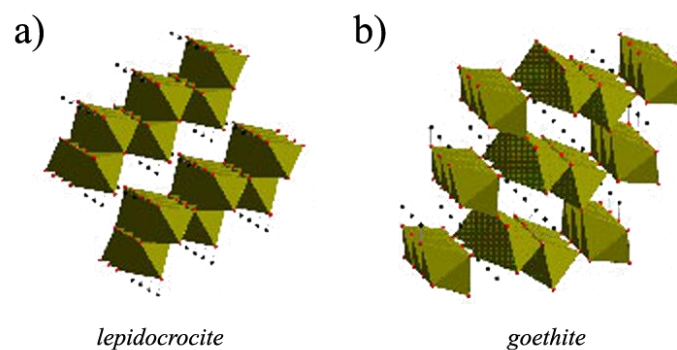
Figure 3.27: Crystalline structure of a) γ–FeOOH and b) α-FeOOH [105].

Kimura pointed out the pioneering concept of "Fe(O, OH)$_6$ network" where, during first step of corrosion and undergoing wet & dry cycle, octahedral Fe(O, OH)$_6$ unit nuclei combines with each other to arrange a network and gaining a more ordered phase, which is similar to lepidocrocite, obtaining a colloidal rust. As the corrosion progresses, the Fe(O, OH)$_6$ network may turn from lepidocrocite to goethite.

In his work, Kimura also took into account the effect of alloying elements, considering chromium addition and starting from the consideration that Cr(O, OH)$_6$ unit owns a different structure of iron network. Thus, the addition of even a small amount of elements can induce a distortion in the Fe(O, OH)$_6$ network and thus modify the evolution process

and the morphology of the rust. Specifically, chromium addition decreases the size of goethite and produces heterogeneous sites in $Fe(O, OH)_6$ network.

Yamashita et al. [106] have further extended the concept asserting that through XAFS spectra it is possible to observe a coordination of Cr^{3+} with O^{2-} to form CrO_x^{3-2x} complex anion. Chromium thus fills the vacant sites in the double chains of the $Fe(O, OH)_6$ network and causes the creation of ultrafine crystals of Cr-goethite, which are responsible of the barrier effect and of the increased cationic selectivity of the inner layer of the patina.

The presence of alloying elements, especially Cr [107] but also Cu and P, enhances the formation of goethite as well as the repetition of wet and dry cycles, actually promoting the prevalence of amorphous FeOOH respect the crystalline compound. Long-term field exposures have shown that the presence of Si in the alloy increases the amount of nanometer-sized α–FeOOH particles, while the contrary effect is achieved by the addition of Cu. Essentially, copper is the alloying element that has shown the most beneficial improvement to the corrosion resistance [9, 22]. Copper also slows down the anodic dissolution of the metal and promotes the formation of more protective ferric corrosion products through the oxidation of Fe^{2+} to Fe^{3+} worked by Cu^{2+} ions present within the aqueous layer. Lastly, the observations related to an improvement on corrosion performance even in presence of SO_2 or sulphate-containing aerosols may support the hypothesis that copper can also form relatively insoluble copper hydroxysulphates (such as $Cu_4SO_4(OH)_6$ or $Cu_3SO_4(OH)_4$) to constitute a sort of protective barriers by their precipitation on pores of rust layer.

A similar precipitation effect can be also ascribed to alloying with Ni. Generally, this element, initially added to the alloy to minimize its embrittlement [22], reduces the formation of local pores enriched by chlorides and thus it appears quite effective to reduce atmospheric corrosion, especially in marine environments.

Besides the effect of alloying, the transformation of lepidocrocite into goethite is directly related to time and atmosphere of exposure. Moreover, considering the higher stability of the goethite form, a relation between the stabilization of the patina and the relative amount of goethite and lepidocrocite present it can be postulated. Thus, Kamimura et al. [108] introduce the Protective Ability Index (PAI) calculated as the α /γ ratio to evaluate the protectiveness of the rust form on WS and its stability grade. Moreover, in order to

consider also the effect of the environment of exposure and thus the presence of atmospheric pollutants that can change the corrosion behaviour of WS (see the following section), an improved value for PAI have been introduced and calculated as:

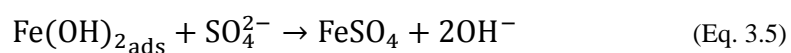$$PAI^* = \frac{\alpha}{\gamma^*} = \frac{\alpha-FeOOH}{(\gamma-FeOOH+ \beta-FeOOH+Fe_3O_4)} \qquad \text{(Eq. 3.4)}$$

An extensive effect on the corrosion process and thus on the corrosion rate in general is directly related to differences in patina composition caused by different conditions of exposure and dissimilar atmospheres as shown in **Figure 3.4**. Morcillo et al. [94] point out the discrepancy in the WS behaviour when exposed in rural or industrial/marine environment. As can be observed from the corrosion trend in **Figure 3.4**, in less aggressive environments, as represented by rural ones, patinas generally need approximately 3 ~ 5 years to achieve a stabilization; while for what concern more aggressive atmospheres, the stabilization requires more time (5 ~ 10 years for industrial atmospheres and more than 15 years for marine atmospheres) or may even not occur [109].

The effect of main atmospheric pollutants on the corrosion process of weathering steel is further described in the following section.

3.4.3 Effects of pollutants on weathering steel

Since the study carried out by Vernon [110], in which the combined effect of pollutants with humidity was expressed for the first time, many researchers have tried to figure out the SO_2 role on the atmospheric corrosion of metals.

Generally, in presence of water, SO_2 is absorbed and oxidised in the rust layer to SO_4^{2-}. The accumulation of sulphate ions occurs in particular structures called *sulphate nest* (**Figure 3.28**) and initially it develops a great number of small nests that, with the increase of exposure time, grow in dimension and consequently their distribution on the surface decrease. Anodes are located inside the sulphate nests and in this environment the anodic dissolution proceeds through:

$$Fe(OH)_{2_{ads}} + SO_4^{2-} \rightarrow FeSO_4 + 2OH^- \qquad \text{(Eq. 3.5)}$$

$$FeSO_4 \rightarrow Fe^{2+} + SO_4^{2-} \qquad \text{(Eq. 3.6)}$$

The presence of $FeSO_4$ induces a pH-regulating effect that keeps a low pH nearby the anodes. As a consequence, favourable conditions for corrosion are ensured by preventing the precipitation of iron hydroxides and the acceleration of the anodic dissolution of iron [10, 80].

This process acquired relevance on the corrosion rate only for concentrations of SO_2 higher than 20 mg $SO_2 \cdot m^{-2} \cdot day^{-1}$ [111].
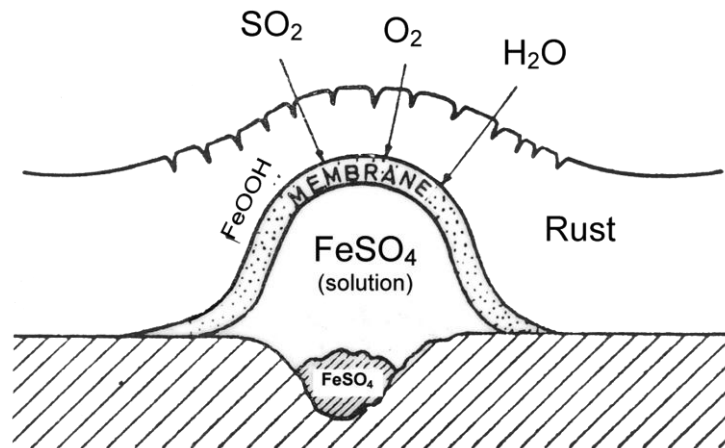
Figure 3.28: Schematic representation of a sulphate nest [94].

Ross and Calaghan [112] observed a noteworthy fact applying electron probe micro-analysis to specimens of mild steel natural aged in different seasons. When steel is exposed to atmospheres polluted by SO_2, sulphur tends to accumulate during the winter in a band at the metal-oxide interface waiting for the arrival of the summer, during which the concentration of sulphur in nests is high and then they are diffused homogenously in the rust layer.

In addition, Aramendia et al. [113] pointed out a dangerous relation between SO_2 rich atmospheres and the protective effect of dissolved nickel. Although nickel is added to WS as alloy element with the aim to increase the material resistance towards the corrosion, the presence of SO_2 induces high dissolution of metallic nickel, decreasing its protective function. Aramendia's work remarks the importance of investigate the role that atmospheric compounds can act on steel surface. As reported by Oesch [79], in fact, in humid air each single air pollutant considered (SO_2, NO_2 and O_3) plays an active role in the WS corrosion process and he also expresses the need of carrying out studies concerning the deduced interaction among pollutants.

In marine atmospheres, the higher corrosion rate of steel is related to the presence of

chlorides species. Due to their hygroscopicity, actually, they promote the formation of electrolytes even at RH% value lower than 100% and thus, they promote electrochemical corrosion.

Nevertheless, the major effect acted by chlorides on steel corrosion is related to the formation of akaganeite (β-FeOOH) and to the increase in concentration of magnetite (Fe_3O_4) [114]. While magnetite tends to be concentrated in the innermost zones of the rust layer where there is a depletion of oxygen, akaganeite tends to form in the most superficial zones of the rust layer [102].

Akaganeite is one of the polymorphous form of ferric oxyhydroxides and its formation requires the presence of halogen ions (Cl^- and F^-) in order to stabilize its crystalline structure (**Figure 3.29**). It consists of tetragonal unit cells that contain tunnels, which are stabilized by the entrance of halogen anions. Due to the presence of tunnels, akaganeite has a relatively larger volume than the initial iron and shows also a less density with the regard to the other oxyhydroxides like lepidocrocite or goethite [115]. Thus, akaganeite is characterized by an extremely porous structure, which represents both a reservoir of chlorides and an easily way to introduce chloride ions in the rust layers from outside. As a consequence, the presence of akaganeite promotes crack formation and even exfoliation [101, 116] decreasing the stability and the protective ability of the patina.
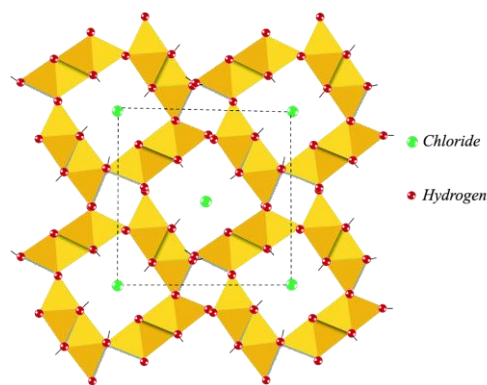
Figure 3.29: Crystalline structure of akaganeite [105].

In presence of high chloride concentration inside the aqueous layer, akaganeite formation begins with the formation of ferrous chloride and the consequently hydrolyses of water, which increases the acidity of the layer (equation 3.7) and thus enables the entry of chloride ions [117]:

$$FeCl_2 \ + \ H_2O \rightarrow FeO + 2HCl \qquad \text{(Eq. 3.7)}$$
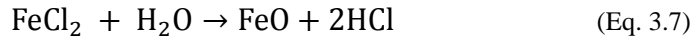
As consequence of the high chloride concentrations and of a low pH (range between 4 and 6 pH unit), precipitation of ferrous hydroxychloride (β-$Fe_2(OH)_3Cl$) occurs and promotes through its oxidation akaganeite formation. The ferrous hydroxychloride oxidation occurs in three separate steps, passing through the origin of chloride-containing green rust one – GR1 (Cl⁻) – according to equation 3.8.

$$2Fe_2(OH)_3Cl \ + \ 2H_2O \rightarrow Fe_4(OH)_8Cl + e^- + 2H^+ + Cl^- \qquad \text{(Eq. 3.8)}$$
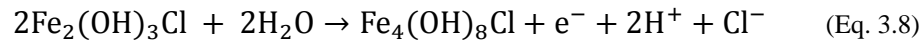
During the second stage, GR1 (Cl⁻) turns to the over-chlorinated corresponding compounds that will be indicated as (GR1 (Cl⁻)*) following by another oxidation stage that finally leads to the formation of akaganeite. Thus the entire oxidation process can be summarized as:

$$\beta Fe_2(OH)_3Cl \ \rightarrow \ GR1 \ (Cl^-) \rightarrow GR1 \ (Cl^-)^* \rightarrow \beta - FeOOH \qquad \text{(Eq. 3.9)}$$

Thus, according to the literature [113, 117, 118], atmosphere enriched by a high concentration of chlorides promote the atmospheric corrosion process due to the formation of this polymorphs of FeOOH, which shows a high-reducing capacity if compared to the other oxyhydroxides. Specifically, the following order was observed:

Akaganeite > Lepidocrocite >> Goethite

A recent study performed on WS exposed in highly aggressive atmosphere [51], highlights also the synergic effect between high levels of chlorides and SO_2. Obviously, also the relative humidity plays a significant role.

Chapter 4

Multivariate approach

Corrosion research is a highly interdisciplinary field. It involves surface science, electrochemistry, physics, materials science, metallurgy, engineering, environmental chemistry and theoretical calculations. Moreover, the complexity of the phenomena investigated requires the application of many methods to get a deeper insight.

The main aim of this work is to investigate a phenomenon which is described and affected by a several number of variables and factors that can even interact and can be influenced by each other. In the statistical field this kind of issues are called *complex problem* due to an intrinsically complexity of the experimental case itself [119]. For instance, when a complex problem is defined, one or more issues among these circumstances can occur:

- dealing with a multivariate system, such as a system characterized by an high number of variables or responses;
- considering correlation between variables and their degree of connectivity;
- lack of information, both in terms of poorness in number of samples or measures available and in terms of possible external interferences (such as instrumental noise, synergic or competitive effects).

Consequently, dealing with a system influenced by several aspects, among which, for example, the nature of the material investigated, the environmental features and surroundings in which it can be exposed or the conditions that can be used to age it in laboratory controlled situation represent undoubtedly a complex problem, since the design phase. Moreover, the high number of data collected during the experimental tests performed in this work requires necessarily a multivariate approach to explore results and thus to ensure the gathering of all the significant information. For these reason, though it is not commonly spread, the application of chemometrics to the field of environmental and cultural heritage chemistry, and also specifically to corrosion science [120], can be fruitful and extremely successful. For instance, Robbiola et al. [121] applied principal component analysis to process EDS analysis of the surfaces on several archaeological bronzes in order to investigate patinas chemical composition. Principal component analysis was also applied to explore colour measurements of patinas and coating systems

for bronzes [122] and paint dosimeters [123] exposed outdoor. Polikreti et al. [124] used multivariate statistics to study the atmospheric corrosion of bronze to provide a quantitative correlation of the corrosion products to microclimatic factors. In a previous work of the research group, principal component analysis and three-way PCA were applied to the study of outdoor long-term exposure of weathering steel [125]. Lastly, in order to estimate the corrosivity of seawater on different kind of materials (among which also carbon steel was considered), design of experiment was successfully applied [126].

In 1972, Professor Svante Wold (University of Umeå – Sweden) referred to *chemometrics* in a grant proposal with the aim to indicate the concept of the application of mathematics to chemistry in order to "*structuralize the chemical problems in mathematical terms*" [127, 128]. According to Wold's definition, this relative recent discipline does not want to be a separate branch of chemistry or to be part of mathematical science and statistics but rather an integral part of chemistry and especially of analytical chemistry. Some years later, in 1974, Wold and his colleague Professor Bruce Kowalski (University of Seattle – USA) founded the International Chemometric Society on the basis of their manifesto in which appeared the first formal definition of chemometrics. An actual and modern definition of chemometrics is [129] *"Chemometrics is the chemical discipline that uses mathematical and statistical methods, (a) to design or select optimal measurement procedures and experiments; and (b) to provide maximum chemical information by analyzing chemical data."*

As stated by Oldroyd [130], in order to build a solid arch of knowledge, scientific methodology follows two-fold pathways that lead through *synthesis* and *analysis*, as schematized in **Figure 4.1**.
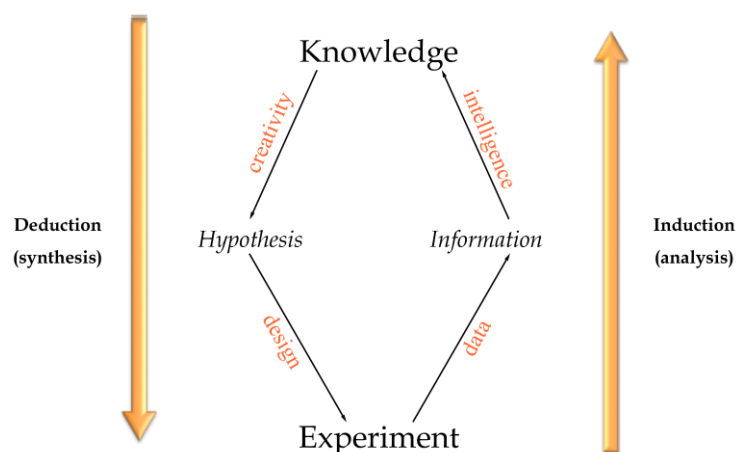
Figure 4.1: The arch of knowledge stated by Oldroyd.

(Adapted from [130])

58

During the synthesis stage, chemists define hypothesis on the basis of their former knowledge and then they need experimental data to verify the validity of assumptions made. Therefore, the first step is to decide which experiments to carry out or how to perform the sampling (*design*) in order to achieve the maximum information wasting less time and efforts. Once the experiments have been performed, the great amount of data collected needs to be explored and processed to extract new information (analysis stage) and enrich the previous knowledge. A good synergy between synthesis and analysis stage allows to obtain more data and a better quality of the information achieved and allows eventually to build a solid arch of knowledge [131]. Math and statistics applied to chemistry can help to perform this task in the best possible way. Actually, in 1982 Frank and Kowalski [132] also stated: "*Chemometric tool are vehicles that can aid chemists to move more efficiently on the path from measurements to information to knowledge*".

Chemometrics has moved far from the original vision of its founders [133] and nowadays it finds application in several fields both in the academia and in industries and a lot of specific software has been developed.

In the next paragraphs, a brief presentation about the two principal chemometric tools used in this study will be introduced.

4.1   Design of experiment (DoE)

The first chemometric tool employed in this study is Design of experiment (DoE).

In spite of the fact that the first paper published about experimental design dates back to 1935 in the work of Fisher [134], this multivariate tool is still not much applied. Nevertheless, it is well known that the traditional OVAT – *one variable at a time* approach is not the best way to perform an optimization study or even better to investigate the effect of several variables. Actually, the classical OVAT approach requires that each variable considered relevant for the system in analysis is varied individually, taking their mutual independence totally for granted and presuming that variables can not interact or be influenced by each other. Overlooking the interactions among variables allows only to obtain a local knowledge of the phenomenon and often requires more time and a much larger experimental effort.

Conversely, by means of experimental design it is possible to explore and investigate the whole experimental domain in a systematic way and thus it is also possible to achieve a mathematical model equipped moreover with predictive ability. In few words, this implies moving from a local to a global knowledge [135].

Before starting to consider and briefly describe the main features of experimental design going through each step of this methodology, let us introduce some specific terminology [131, 136], which will be used from here onwards in the next paragraphs:

- *Variables*: experimental variables that are considered relevant for the system and that can be changed independently of each other. They can be both *qualitative* and *quantitative* and both types can be considered simultaneously.

- *Levels*: the different values attributed to the variables. Despite of in everyday use the term level has a quantitative connotation, here it also represents qualitative variables (for instance, which solvent has to be tested).

- *Response factors*: the values of the experimental answers measured during the tests.

- *Experimental domain*: the experimental area investigated and circumscribed by the ranges in which the experimental variables chosen are defined. In other words, the boundaries of the experimental domain represent the extreme levels at which the variables will be studied. NB: a correct definition of boundaries and levels is essential. For instance, if boundaries are too wide often it is required to perform experiments in useless condition and this leads to insufficient precision of the model in the area investigated. Conversely, if boundaries are too narrow, the optimum can be missed.

4.1.1 Experimental plan

Formalised designs follow several steps. Specifically, five steps have to be considered:

1. Before starting the planning phase, the goal of the experiments has to be clearly defined in advance.

2. Variables, that can have an active role on the process in exam or that can have an influence on an experimental outcome, have to be identified. Sometimes, the

significant and relevant variables are not known or circumscribed; in these cases, the initial step of DoE might involve a *Plackett Burman* or partial factorial design [135] in order to screen all possible interesting variables and to reduce them to those really noteworthy.

Additionally, also response factors have to be defined.

3. Plan the experiments. Once the variables have been identified, they have to be restricted and limited in order to define an experimental domain in which the experiments are going to be performed. Obviously, the experimental domain definition is also related to the choice of the model to be applied (such as *Plackett Burman*, factorial design, central composite design or mixture design).

4. Perform the experiments according to the experimental plan defined and in a random order (except special cases, for example when memory effect can occur) to avoid the bias related to possible systematic effects.

5. Analyse and model the data obtained in order to transform data into information and produce knowledge.

It is necessary to remark that, very often, one single DoE does not lead to the final solution of the problem. Thus, in these cases, the information achieved at step 5 has to be considered as new *a priori* knowledge of the problem and has to be used to reformulate a new design going back to step 3.

As mentioned at step 3, in order to define the experimental plan to be performed, it is essential to postulate the model to be applied. In this work, a 2^3 full factorial design, described in the following section, was applied.

4.1.2 Factorial designs at two levels

In order to reduce the complexity of the problem and circumscribed the domain, the first stage of Design of Experiments is characterized by a *screening phase* in which all the significant variables of the system were considered. Generally, if the number of the variables is not large and the experimental cost is acceptable, *Full Factorial Design 2^k* turns out to be the most complete and extensive way to investigate the system. Explicitly, *Full Factorial Design 2^k* requires a number of experiments equal to 2^k, where k is the number of variables considered during the investigation. In full factorial designs, each

quantitative or qualitative variable is described by two levels, coded as -1 (to indicate the lowest level considered) and +1 (to indicate the highest one). The level 0 is in between those -1 and those +1 levels and therefore it is the centroid of the domain [135].

From a geometrical point of view, if three variables (so $k = 3$) are considered, it is possible to represent this design by means of a cube, whose corners are going to be investigated by the factorial design, as shown in **Figure 4.2**.
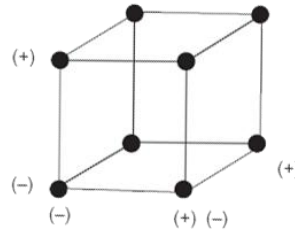
Figure 4.2: Geometrical representation of a 2^3 Factorial Design.

(Adapted from [133])

The experimental matrix for $k = 3$ can be easy built and it is reported in **Table 4.1**. As shown in **Table 4.1**, contrarily to what is done when the OVAT approach is applied, in the factorial design variable 1 is changed while variable 2 and variable 3 assume different values and vice versa. This makes DoE a suitable tool to investigate the interactions among variables.

Table 4.1: Experimental matrix of a 2^3 Factorial Design.

Experiment	Variable 1	Variable 2	Variable 3
1	-1	-1	-1
2	+1	-1	-1
3	-1	+1	-1
4	+1	+1	-1
5	-1	-1	+1
6	+1	-1	+1
7	-1	+1	+1
8	+1	+1	+1

As a consequence, by means of just eight experiments, it is possible to estimate and fit the coefficients from the second order mathematical model reported in equation 4.1:

$$y = b_0 + b_1 \cdot x_1 + b_2 \cdot x_2 + b_3 \cdot x_3 + b_{12} \cdot x_1 \cdot x_2 + b_{13} \cdot x_1 \cdot x_3 + b_{23} \cdot x_2 \cdot x_3 \qquad \text{(Eq. 4.1)}$$

where b_0 is a constant value and it is the value of the y response factor considered when the values of the three variable x_1, x_2 and x_3 are equal to 0 (at the centre of the cube

represented in **Figure 4.2**) On the other hand, b_1, b_2 and b_3 are the second order coefficients related to the individual effect of the variables x_1, x_2 and x_3 while the remaining mixed terms b_{12}, b_{13} and b_{23} are the coefficients related to the interaction terms among variables.

Actually, according to the theory [135, 137, 138], by means of eight experiments, it is possible to estimate also the three-term interaction b_{123} but in this way no degrees of freedom are available, therefore it is impossible to define a statistical significance of the coefficients. For that reason, in this work, it was made the choice of estimating only the two-term interaction.

Lastly, before the model built can be used also for prediction behind to describe the system, it has to be validated. For what concern model validation, the experimental variability plays a very important role because the higher the experimental variability, the easier it could be to validate the model. In order to validate the model, some experiments at the centre point are performed outside of the original experimental plan (related to the experimental matrix reported in **Table 4.1**). Thus, the model has been validated simply if the value measured at the level 0 correspond to the value predict by the model itself. Therefore, it is evident that if the confidence interval of the system is wide (so the experimental variability is high) then it is more probable that the value lies in the interval. Obviously, in order to perform a good experimentation, a large experimental variability is always avoidable and even more during the validation phase, where it can affect the evaluation of the models built. The precision related to the predictive ability of the model can be estimated even before performing the actual experiments of the design merely knowing *a priori* the variability associated to the system.

Moreover, to evaluate the fit of a model, values of *explained variance – R^2* and *predicted variance – Q^2* can be used. Specifically, the *explained variance* is the fraction of the total variation of the response that is explained in the model (as detailed below speaking about principal component analysis, see section 4.2.3) and here it is calculated following the equation 4.2 as the standard deviation of a regression.

$$R^2 = \frac{(SS_{tot} - SS_{resid})}{SS_{regr} + SS_{resid}} \qquad \text{(Eq. 4.2)}$$

where SS_{tot} is the sum of squares of the total variation of a selected response and corrected for the mean; SS_{tot} can be divided in two contributions resulting from the regression model (SS_{regr}) and another due to the residuals (SS_{resid}).

The predicted Q^2 corresponds to the fraction of the total variation of the response that can be predicted in the model and formally it is calculated as (equation 4.3)

$$Q^2 = \frac{(SS_{tot} - PRESS)}{SS_{tot}}$$

(Eq. 4.3)

where PRESS is the prediction residual sum of squares and is determined through cross-validation (see the following section 4.2.4) [136].

4.1.3 Response plots

After performing the experiments, by the response factors recorded it is possible to compute the model and estimate the coefficients of equation 4.1.

Moreover, once the model has been validated, it can be used to predict the value of the response factor in the entire experimental domain. Besides the evaluation of the influence of each variable and their interaction that can be achieved from the examination of the coefficients estimated, in **Figure 4.3**a – b are reported two examples of the response plots that can be obtained by the polynomial factorial design.

a)   b)
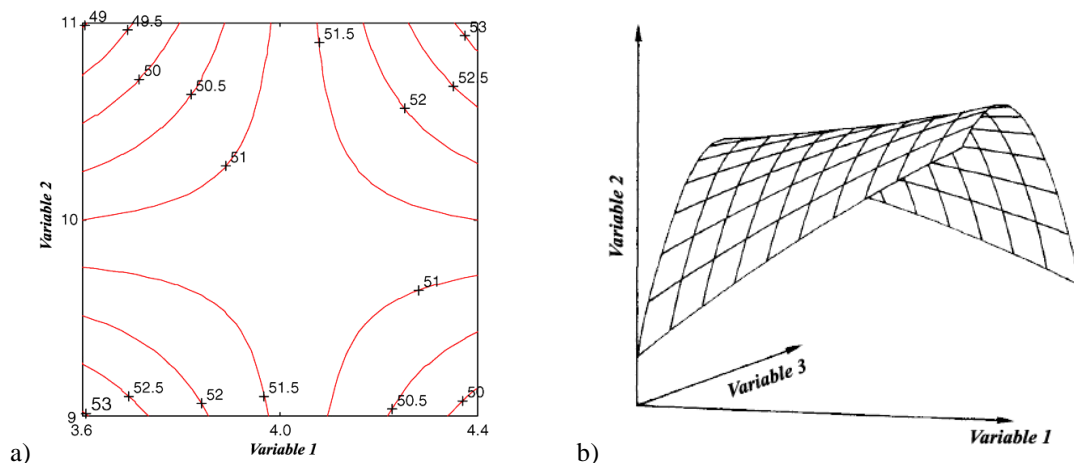
Figure 4.3: a) Isoresponse plot; b) Response surface plot.

(Adapted from [135])

Therefore, by the representation through response plots, it is possible to easily visualize and predict the trend of each response factor in every point of the experimental domain defined. Thus, conversely to the univariate approach, it is possible to achieve not only local information where the experiments have been performed but also a global

knowledge of the system investigated. Moreover, the interactions among variables can be straightforwardly identified.

4.2   Principal Component Analysis (PCA)

Each sample or, more generally, each object can be defined by a set of measurements. A graphical representation and even an exploration of object in order to find patterns or relationships among them are no longer possible when objects are characterized by more than three variables. When only two variables are used to define an object, it can be represent by means of a vector but when more than two variables are taken into account, the use of matrices is unavoidable. Moreover, quite frequently the dimensions of an object matrix can be significantly high and between variables there may be correlation that causes information to be redundant. Thus, the aim of several multivariate methods is data reduction [139].

4.2.1 Principal components

Principal component analysis (PCA) is a technique to reduce the amount of data when there is correlation, retaining yet as much as possible the variation present in the dataset. This task is achieved by transforming the original dataset (*training set*) to a new set of variables, which are uncorrelated and ordered so that the first new variables retain most of the variation present in the entire original variables [140]. These new variables are called *principal component* (PCs) and are linear combinations (Z_1, Z_2, ..., Z_n) of the original variables (X_1, X_2, ..., X_n) according to equations 4.4.

$$Z_1 = a_{11}X_1 + a_{12}X_2 + \cdots a_{1n}X_n$$

$$Z_2 = a_{21}X_1 + a_{22}X_2 + \cdots a_{2n}X_n \qquad \text{(Eq. 4.4)}$$

where the coefficients a_{11}, a_{12}, etc. are selected to make sure that the new variables, unlike the original ones, are not correlated. As linear combinations, PCs enjoy also the orthogonality property (**Figure 4.4**), so preserving the angle of the original axes.
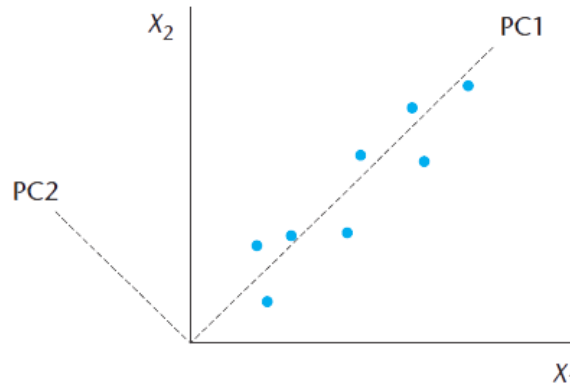
Figure 4.4: The first two principal components (PC1 vs. PC2) represented by dotted lines. Straight lines correspond to the original axes along which lie the original variables x_1 and x_2 [139].

As mentioned before, the main idea behind PCA is that the new spatial coordinates are chosen in an ordered way: the first principal component (PC1), Z_1, accounts for most of the overall dataset variation, Z_2 accounts for the next largest variation and so on. Therefore, PCA is basically equivalent to a rotation of the original axes along the directions characterised by the maximum variation. For that reason, in order to ensure the success of this method, sometimes a pretreatment of the variables is required before they have been processed. To guarantee that the results obtained about variables variance investigation are not affected by the use of different units of measurements or by the use of variables extremely different from each other, data autoscaling must be applied.

As main PCA result, data can be represented in an only two dimensions space rather than the original *n* order space. This procedure corresponds to a severe data reduction, especially if the original dataset is affected by a significant correlation among variables (**Figure 4.5**).
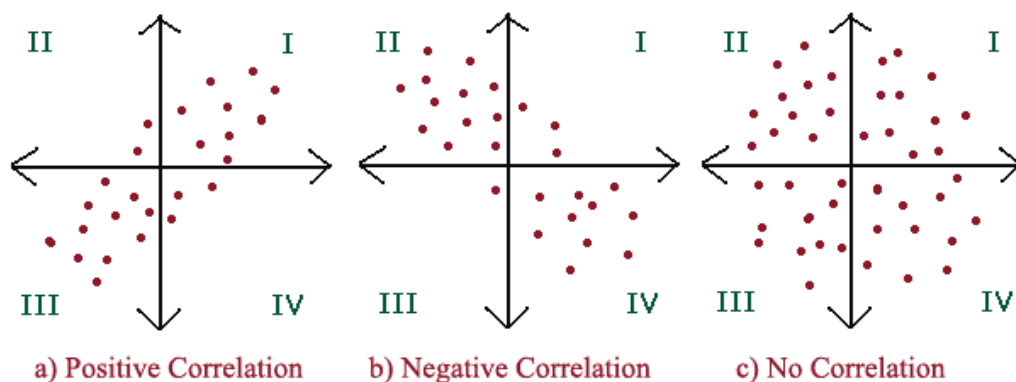
Figure 4.5: a) Positive and b) negative correlation among variables are represented. In c) no correlation is present among data. *(Modified from [141])*

66

Thus, if the original dataset is represented by a (*m* x *n*) data matrix X (with *m* corresponding to the samples or objects and *n* to the measured variables), by means of PCA is possible to decompose X following (equation 4.5):

$$
\begin{pmatrix} x_{11} & x_{12} & \cdots & x_{1n} \\ x_{21} & x_{22} & \cdots & x_{2n} \\ \cdots & \cdots & \cdots & \cdots \\ x_{m1} & x_{m2} & \cdots & x_{mn} \end{pmatrix} = \begin{pmatrix} a_{11} & \cdots & a_{1s} \\ a_{21} & \cdots & a_{2s} \\ \cdots & \cdots & \cdots \\ a_{m1} & \cdots & a_{ms} \end{pmatrix} \cdot \begin{pmatrix} f_{11} & f_{12} & \cdots & f_{1n} \\ \cdots & \cdots & \cdots & \cdots \\ \cdots & \cdots & \cdots & \cdots \\ f_{s1} & f_{s2} & \cdots & f_{sn} \end{pmatrix}
$$

$$X = A \cdot F$$

(Eq. 4.5)

where A is the matrix that contains the *loadings* of the factors (explicitly the new synthetic variables identified, F is the matrix that contains the factor *scores*, hence the dimension of matrix F is the same of the original X matrix [142].

4.2.2 Eigenanalysis

In mathematical terms the principal components are obtained from the diagonalization of the *correlation* or *covariance matrix* S, namely the matrix that contains the measures of the joint variance of all the variables of the original *m* x *n* dataset (equation 4.6).

$$diag(S) = diag\left[\frac{X_c^T X_c}{m-1}\right] \qquad \text{(Eq. 4.6)}$$

where X_c is the centered data matrix.

Therefore, from the equation 4.6 are determined two matrices:

- diagonal matrix Λ (*n* x *n*), whose diagonal elements are the eigenvalues λ_n sorted in descending order, which accounts the amount of variance explained;
- *loadings* matrix L (*n* x *N*), whose columns are the eigenvectors of the covariance matrix, nay the principal components sought and consequently the unit vectors of the new Cartesian space.

As result, it is possible to represent the original X matrix in a new space according to the following relationship (equation 4.7):

$$T = XL \qquad \text{(Eq. 4.7)}$$

where L (*n* x *N*) acts the function of a rotation matrix and T (*m* x *N*) is called *scores* matrix. If *N* is equal to *n*, the procedure illustrated corresponds only to a rotation of the original dataset without any data reduction. Otherwise, selecting a number of *N* components lower than *n* allows reducing the original data, starting from the components that carry the lowest values of information hence eigenvectors associated to small

eigenvalues. Basically, it is quite probably that small λ_n are associated to undesirable variability caused by instrumental noise or by irrelevant and correlated information.

The *rank analysis*, namely selecting the relevant number ($N < n$) of PCs is a big issue in PCA [139, 143, 144].

4.2.3 Loadings and scores plot

As expressed in the previous paragraph, L is the *loadings* matrix where the columns contain the eigenvectors of the covariance (or correlation) matrix while the rows represent the original variables (**Figure 4.6**). Loadings are linear standardized coefficients so their variance is equal to 1.
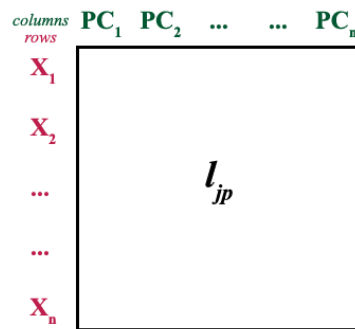
Figure 4.6: Graphical representation of L – *loadings* matrix.

The linear combination of the original variables with the loadings of the *p* component returns the *scores* that represent the new coordinates of the object in the space delimited by PCs. Unlike loadings, scores can assume any values (not necessarily included between -1 and +1).

Therefore, *loadings plot* shows the role and the weight of each variable within each component, their possible positive or negative correlation and their relevance.

On the other hand, by means of *scores plot*, PCA allows to easily visualize a multivariate dataset in a two or three dimension (**Figure 4.7**).
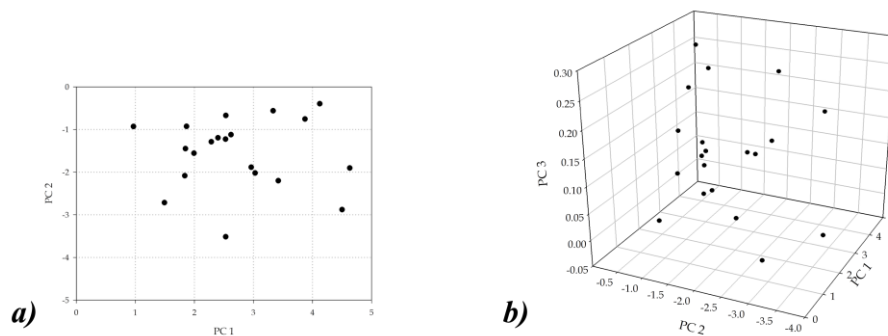
Figure 4.7: An example of *scores plot* represented in a) 2D dimension and in b) 3D dimension.

Besides a graphical representation of the multivariate objects, scores plot allows also to analyse the characteristics of objects and their similarities, the presence of potential clusters among objects or the presence of *outliers*, hence objects that follows a peculiar behaviour. Moreover, due to their mathematical derivation, there is a biunivocal correspondence between scores and loadings plots, thus they can be directly compared to identify possible relationships between objects and variables. This kind of graph is called *biplot* (**Figure 4.8**) [143, 144].
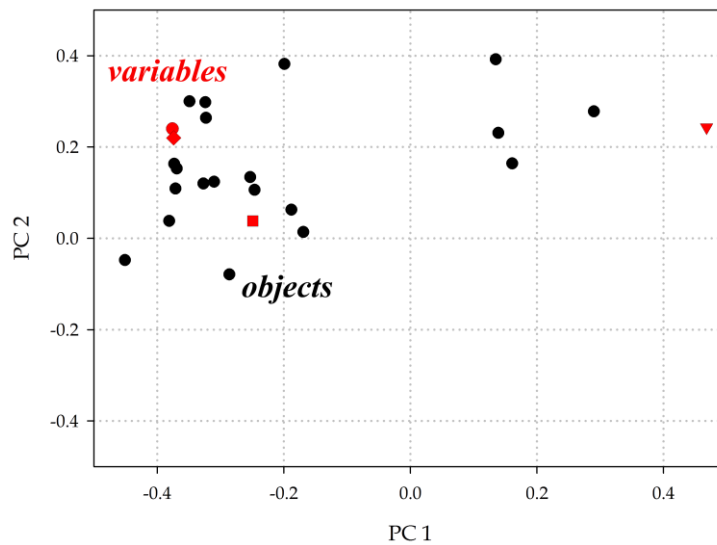
Figure 4.8: An example of *biplot*.

After performing PCA, in order to evaluate the percentage of the initial information retained in the new principal components selected, a new quantity is introduced called *percentage explained variance*; it is calculated for each kth PC according to equation 4.8.

$$EV_k\% = \frac{\lambda_k}{\sum_{m=1}^{n} \lambda_m} \cdot 100 \qquad \text{(Eq. 4.8)}$$

The fundamental property of the explained variance is that it is not only related to the performance of the model but also on the distribution of the data. In conclusion, explained variance is a useful information to certify the quality of the model built once modelling decision have been already taken rather than be used as a figure of merit during model optimization stage [145].

4.2.4 Model validation

Once PCA has been performed, to assess the overall model performance or to optimize the model built, a properly validation is required and this is another big issue of principal component analysis.

Besides the technique selected for the validation, first of all objects have to be divided between the *training set* (namely the dataset used to build the model) and an *evaluation set*, used to validate the model. The most common multivariate techniques of validation differ from each other for the criteria and the methods used to divide the objects [131]. The most conservative validation is to test the model using a representative independent test-set of sufficient size. Unfortunately, retain a reasonable amount of objects as a *test-set* is not always possible and the best alternative is to apply *cross-validation*.

By means of cross-validation the same objects are used both to estimate and test the model. Actually, a few objects are left out from the calibration data set and the model is built on the basis of the remaining objects; then, the values for the left-out objects are predicted by the model computed and the prediction residuals calculated. Several levels of validation can be considered [146]:

- *Full cross-validation* also known as *leave-one-out* method, where for *n* objects considered, *n* models are calculated excluding one object at a time from the training set and using it to predict the answer

- *Segmented cross-validation* where the calibration set is divided into segments containing a certain percentage of samples. This method is used when full cross-validation is too time-consuming or to pick out representative samples in a relatively abundant dataset.

- *Segmented cross-validation* leaves out a whole group of objects at a time.

- *Validation across categorical information about the objects*.

Chapter 5

Materials and methods

In order to investigate the effect of particulate matter and their aggressive soluble species on weathering steel corrosion, both field exposure and accelerated ageing test were performed on the material.

5.1 Description of materials

5.1.1 Weathering steel: Cor-Ten A

Commercial flat specimens of Weathering Steel (WS), of Cor-Ten A type (see section 3.4) provided by a local supplier were employed for this study. According to the UNI EN 10149 [147], their nominal composition is reported in **Table 5.1** while **Table 5.2** reports the alloy composition experimentally determined by Optical Emission Spectroscopy.

Table 5.1: Iron alloy nominal composition (weight %) of WS samples.

Element	C	Si	Mn	P	S
Weight %	0.12	0.25 – 0.75	0.20 – 0.50	0.07 – 0.15	0.035 (*max*)

Element	Cr	Ni	Cu	Fe
Weight %	0.30 – 1.25	0.65 (*max*)	0.25 – 0.55	To balance

Table 5.2: Alloy composition (weight %) found on WS samples by Optical Emission Spectroscopy.

Element	C	Si	Mn	P	S
Weight %	0.085	0.44	0.38	0.091	0.022

Element	Cr	Ni	Cu	Fe
Weight %	0.80	0.17	0.30	To balance (~ 97.71)

Moving forward to detail, $50 \times 50 \times 2$ mm samples cut from bare WS (**Figure 5.1**a) were employed for the environmental exposure while $25 \times 25 \times 2$ mm samples cut from bare WS (**Figure 5.1**b) were used for the accelerated ageing tests. To be tested through accelerated aging system, the latters were also punctured in the middle (0.2 mm as hole diameter). In both cases, specimens were degreased with acetone, washed with water and dried.
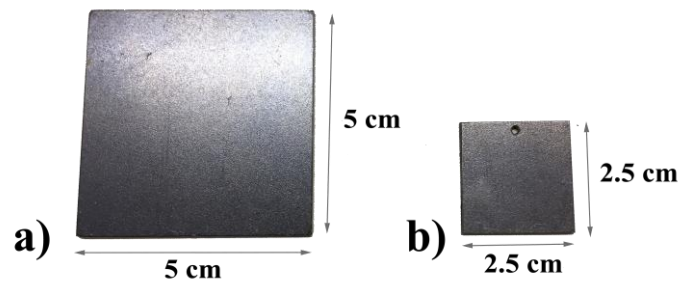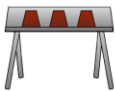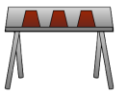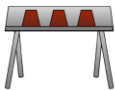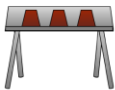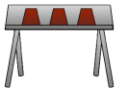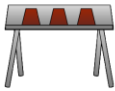
Figure 5.1: Commercial samples of bare WS for the a) environmental exposure and for b) accelerated ageing tests.

5.2 Environmental exposure

Natural field exposure were planned and performed on WS. Specifically, three one-year campaigns starting in different season (summer, winter and spring) were set (**Table 5.3**) to investigate the influence of the environmental parameters (taking into account both meteorological variables and atmospheric pollutant concentrations), especially focusing the attention to the early stage of WS atmospheric corrosion. In order to achieve a complete characterization, field exposures were performed both in sheltered and unsheltered condition.

Table 5.3: Scheme and plan of WS outdoor exposure.

Yearly exposure start season	Sample	Condition	Start of Exposure	End of Exposure
Summer	Sum_CC1		07/07/15	06/07/16
	Sum_CC2			
	Sum_CC3	Sheltered		
	Sum_CA1			
	Sum_CA2			
	Sum_CA3	Unsheltered		

Season	Sample	Condition	Start of Exposure	End of Exposure
Winter	Win_CC1		17/12/15	16/12/16
	Win_CC2			
	Win_CC3	Sheltered		
	Win_CA1			
	Win_CA2			
	Win_CA3	Unsheltered		

Season	Sample	Condition	Start of Exposure	End of Exposure
Spring	Spr_CC1		17/05/16	12/05/17
	Spr_CC2			
	Spr_CC3	Sheltered		
	Spr_CA1			
	Spr_CA2			
	Spr_CA3	Unsheltered		

5.2.1 Exposure site and conditions

The urban-coastal site of Rimini, Italy (N 44° 3' 43'', E 12° 34' 12'') was chosen for natural exposure. The test site was located at about 1.5 km from the Adriatic Sea shoreline, on the flat roof of a building in the city center (**Figure 5.2**). Three campaigns were performed starting respectively during summer, winter and spring time (as well described in paragraph 5.2.2) in order to investigate the influence of the starting time of the natural exposure of WS.
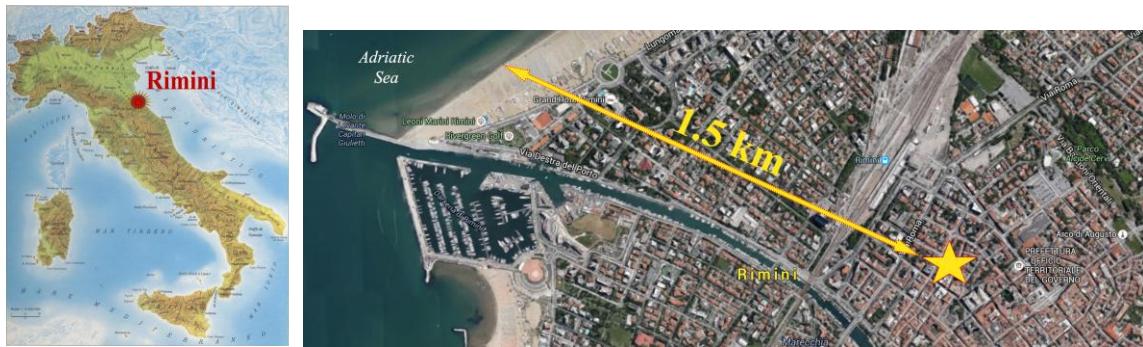
Figure 5.2: Location of the site of exposure in Rimini, Italy.

According to the ISO 8565 and ISO 9226 [148, 149], the specimens were exposed facing south and with an inclination of 45° from the horizontal.

Hourly and daily environmental data (temperature, relative humidity, time of wetness, precipitations and direction and speed of wind) and air pollutant concentrations (CO, NO_2, O_3, PM_{10} and $PM_{2.5}$) were recorded in two monitoring stations close to the site of exposure ($\sim 1 - 2$ km) and provided by the local Environmental Protection Agency (ARPA E-R, [150]). These parameters are summarized in **Table 5.4** and **Table 5.5**. A fact worthy of attention is that the pollutant SO_2 is no longer monitored in Rimini since 2008 due to its decrease in atmospheric concentration: in previous years, essentially, SO_2 showed concentrations well below the Italian law limits (daily limit of 125 µg · m^{-3} not to be exceeded more than 3 times a year [151]); specifically, from 2004 to 2007, its annual average was 2 µg · m^{-3}.

Table 5.4: Environmental data related to the exposure site of Rimini during the 3 campaigns.

Yearly exposure start season	Environmental Data							
	Annual Rainfall (mm)	Temperature (°C)		Relative Humidity (%)		Wind		TOW (h · y⁻¹), %
		Yearly Average	*Min - Max*	*Yearly Average*	*Min - Max*	*Prev. direction*	*Average speed*	
Summer jul 2015 - jul 2016	1138.5	16.4	-1.8 ~ 35.4	69	15 ~ 99	W - NW	2.00 m · s⁻¹	3092, 35%
Winter dec 2015 - dec 2016	1236.3	14.5	-1.8 ~ 32.9	72	15 ~ 99	W - NW	1.97 m · s⁻¹	2918, 33%
Spring may 2016 - may 2017	1393.0	14.9	-2.7 ~ 32.9	68	16 ~ 97	W - SW	2.17 m · s⁻¹	2165, 25%

In **Figure 5.3** the a) rainfall, b) temperature and c) relative humidity monthly trends during each seasonal campaign are shown. Overall, samples that have been exposed during summer 2015 have been exposed to the lowest amount of annual rainfall and to the highest temperature while the samples exposed during spring 2016 have been exposed to the highest amount of annual rainfall and the lowest temperature. However, taking a look to the first months of their exposure, summer samples have been exposed to a large amount of rainfall, especially during September 2015, compared to samples exposed during winter and spring. Moreover, both summer and spring samples have been exposed to high temperature during the first months of outdoor exposure. Otherwise, winter samples have been subjected to high percentages of relative humidity since the beginning of the test. The trends of rainfall, temperature and relative humidity are reported in **Figure 5.3** considering for each campaign the effective period of exposure. For instance, for all the samples that started their exposure during summer, the monthly labelled as 'Jul15' and 'Jul16' are considering the period ranging from 07/07/15 to 31/07/15 and from 01/07/16 to 06/07/16, respectively. This evaluation was made for all the campaigns, thus some monthly trend may show different values among campaigns (for instance values labelled 'Jul16' for summer and winter). The same criterion was applied to the following **Figure 5.4 – 5.7**.
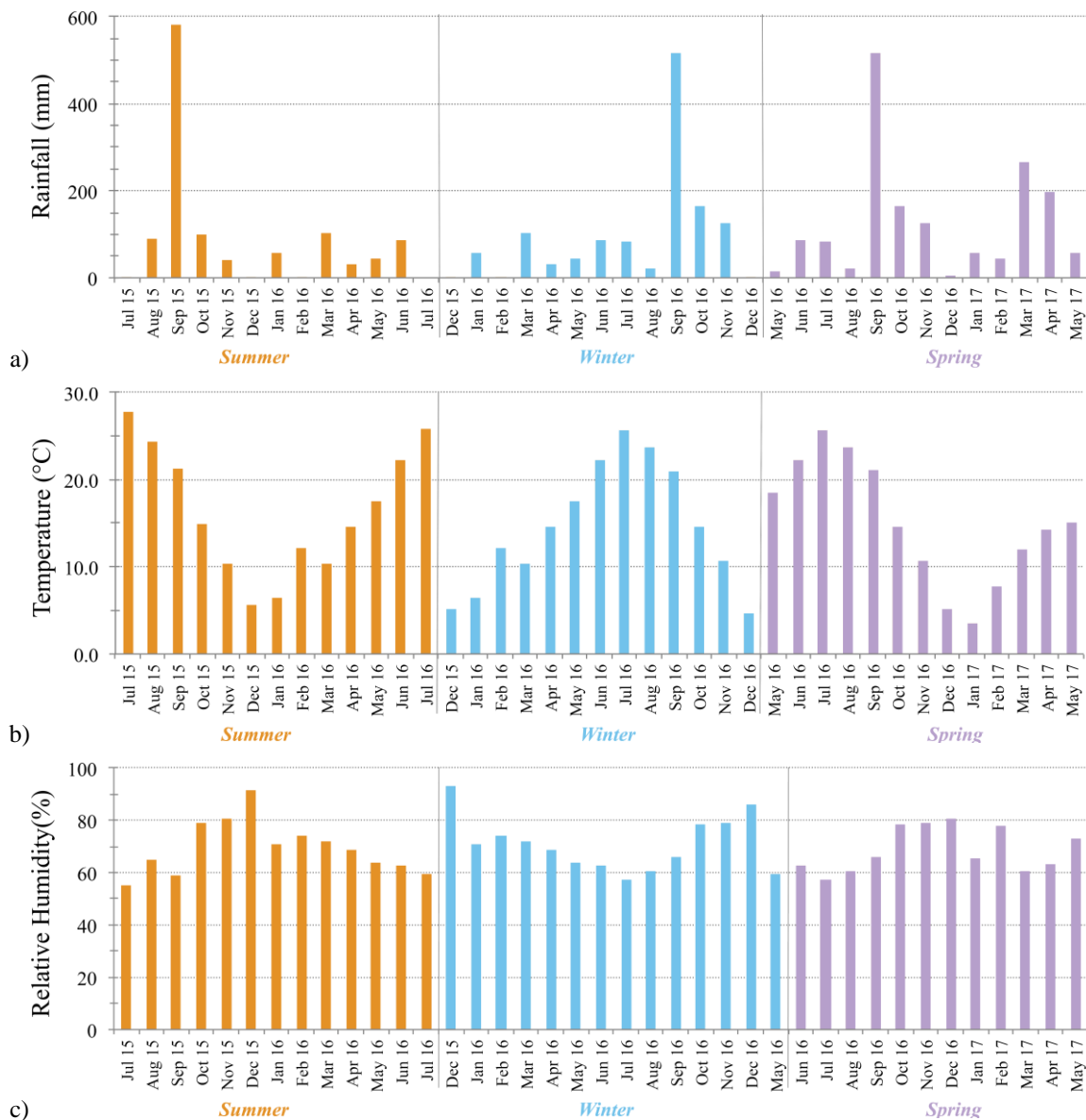
Figure 5.3: a) Rainfall, b) temperature and c) relative humidity monthly trend during each campaign with starting in: summer, winter, spring. For each campaign the effective monthly was considered. For instance, for all the samples that started their exposure during summer, the monthly labelled as 'Jul15' and 'Jul16' are considering the period ranging from 07/07/15 to 31/07/15 and from 01/07/16 to 06/07/16, respectively.

For what concern Time of Wetness (TOW) of specimens (calculated as the time in which %RH is higher than 80% and, at the same time, the temperature is higher than 0°C [12]), it ranged from 2165 to 3092 h · y^{-1}, corresponding to the 25% (for campaign started in spring) and 35% (for campaign started in summer) of the total hours of samples exposure. Considering its behaviour, wind plays an important role due to the mechanical action that it exercises on the material surfaces and also as a vector of aggressive substances, such as atmospheric pollutants and sea spray ions. In the considered site of Rimini, wind blows mainly from E – SE (sea breeze) and W – NW (land breeze). In **Figure 5.4** wind roses for each campaign considered are shown.
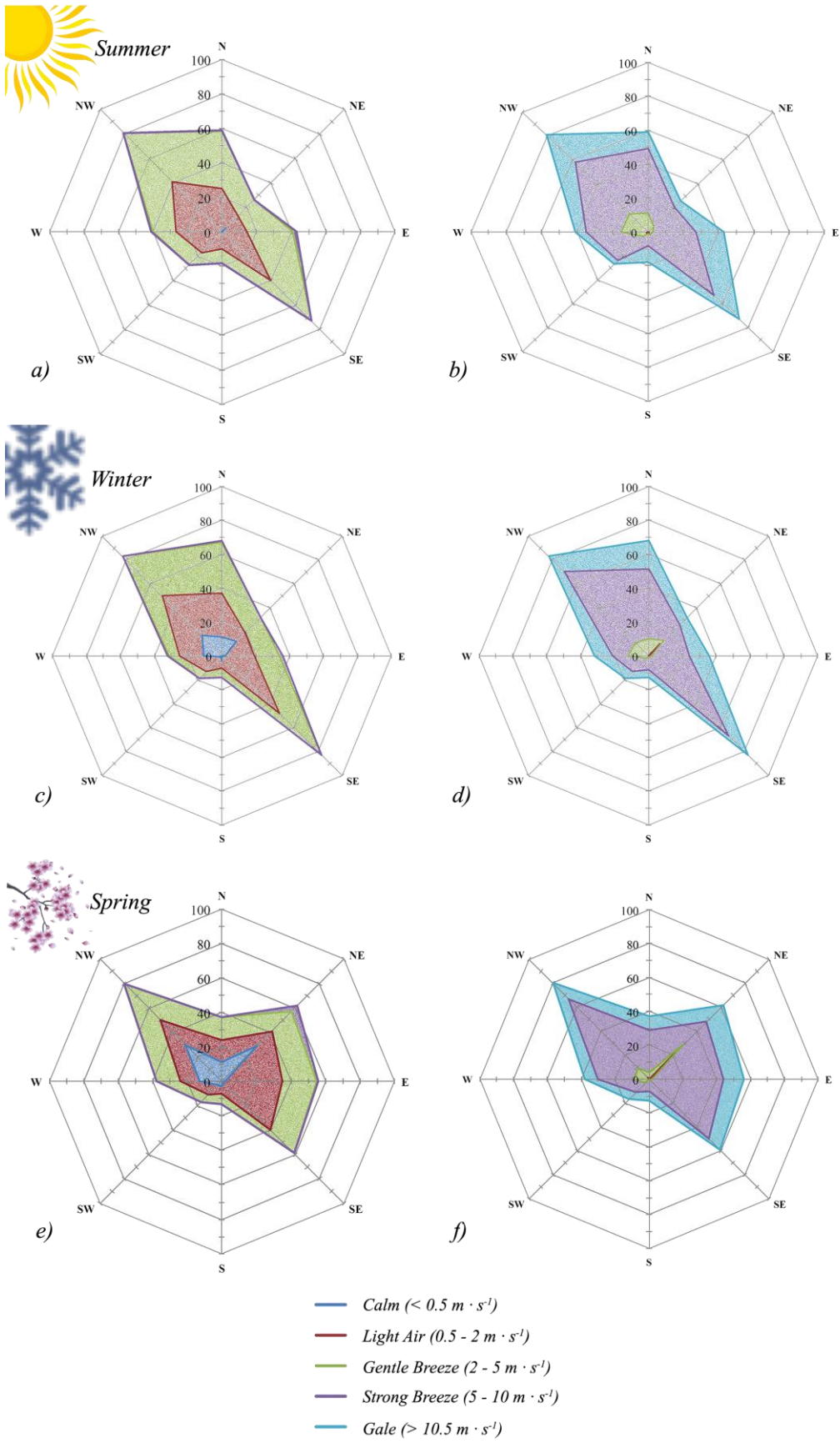
Figure 5.4: Wind roses for each campaign considered and started in summer, winter and spring. For each campaign two wind roses with mean (a, c, e) and max (b, d, f) values are reported. Intensities and directions of winds are here represented and from inside out, wind velocities are growing.

The last consideration related to the environmental features of the site of exposure is the concentration of air pollutants measured during the test. Specifically in **Table 5.5** are reported the average concentrations (annual and daily mean values) and in **Figure 5.5** are reported the monthly trend of the pollutants monitored: a) CO, b) NO_2, c) O_3, d) $PM_{2.5}$ and d) PM_{10}.

Table 5.5: Air pollutant concentrations related to the site of Rimini during the three exposure campaigns.

Yearly exposure start season	*Pollutants* $(mg\cdot m^{-3})$									
	CO		**NO_2**		**O_3**		**$PM_{2.5}$**		**PM_{10}**	
	Yearly	*Daily*	*Yearly*	*Daily*	*Yearly*	*Daily*	*Yearly*	*Daily*	*Yearly*	*Daily*
Summer *jul 2015 - jul 2016*	5911	16.2	187	0.5	394	1.1	6.8	0.02	10.2	0.03
Winter *dec 2015 - dec 2016*	6274	17.2	179	0.5	382	1.1	6.3	0.02	9.5	0.03
Spring *may 2016 - may 2017*	3728	10.4	202	0.6	391	1.1	6.9	0.02	10.2	0.03

Among the three seasonal campaigns there is no noteworthy difference regarding the annual and daily mean values of NO_2, O_3, $PM_{2.5}$ and PM_{10}, while a significant difference can be observed in the average concentrations of CO that during winter and summer campaigns is fairly higher than during spring exposure.
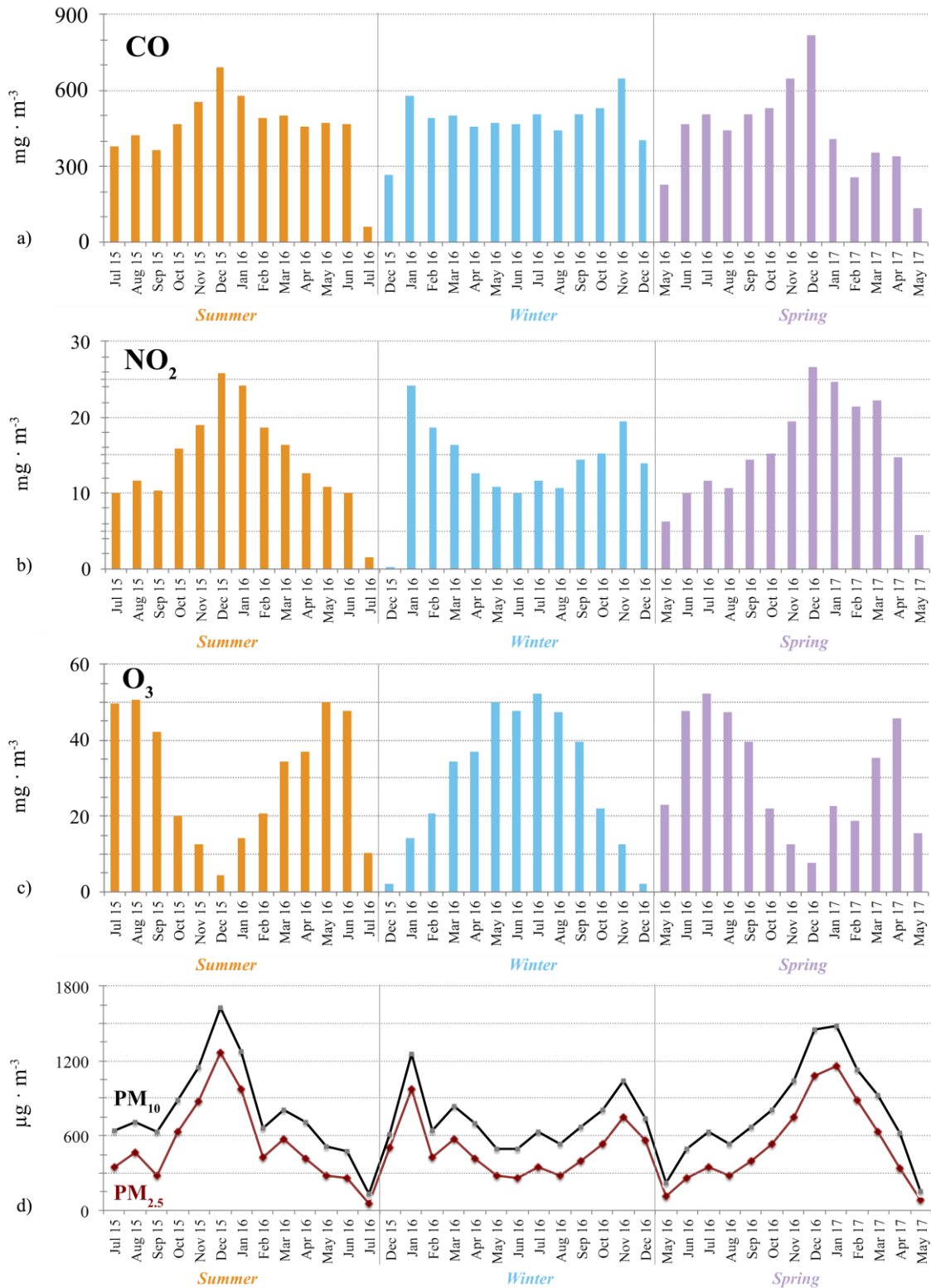
Figure 5.5: Monthly concentration of air pollutants a) CO, b) NO$_2$, c) O$_3$ (mg $\cdot$ m^{-3}) and d) PM$_{2.5}$ and PM$_{10}$ (µg $\cdot$ m^{-3}) in the exposure site of Rimini during each seasonal campaign: summer, winter, spring. For each campaign the effective monthly was considered. For instance, for all the samples that started their exposure during summer, the monthly labelled as 'Jul15' and 'Jul16' are considering the period ranging from 07/07/15 to 31/07/15 and from 01/07/16 to 06/07/16, respectively.

NO_2 and O_3 concentrations follow the normal seasonal pattern in which, during the summer months, ozone increases while nitrogen dioxide simultaneously decreases; the opposite trend is registered during winter period. Actually, during summer months (from May to August) the intensity of solar radiation reaches its highest values and promotes the reactions of ozone production, among which emerges also the reaction of NO_2 photolysis (5.1a-b).

$$NO_2 \xrightarrow{h\nu} NO + O$$

$$O + O_2 + M \rightarrow O_3 + M \qquad (5.1\text{a-b})$$
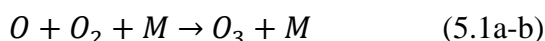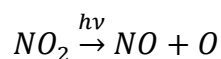
In reaction 5.1b, *M* represents a general species that can host the energy released in the reaction and thus stabilizing the ozone species.

In **Figure 5.6** is reported the monthly trend of the solar radiation during the three campaigns compared to the trend of concentrations of ozone and nitrogen oxide.
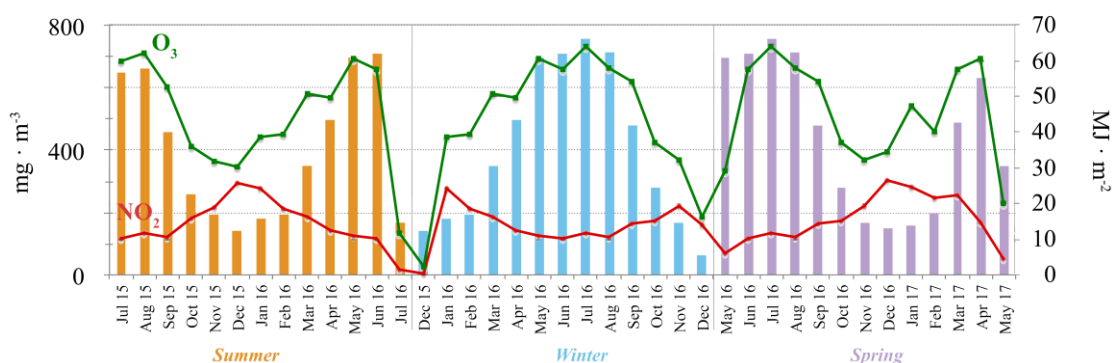
Figure 5.6: Monthly trend of the solar radiation (MJ · m^{-2}) compared to the trend of NO_2 (red) and O_3 (green) (mg · m^{-3}) during campaigns started in: summer, winter, spring. For each campaign the effective monthly was considered. For instance, for all the samples that started their exposure during summer, the monthly labelled as 'Jul15' and 'Jul16' are considering the period ranging from 07/07/15 to 31/07/15 and from 01/07/16 to 06/07/16, respectively.

A seasonal investigation especially highlights also the difference in the amount of atmospheric particulate matter that can play an active role in the corrosion process carrying hygroscopic saline compounds or acidic species, which can accelerate material decay. Commonly, $PM_{2.5}$ and PM_{10} have the same trend and their amount is higher during winter and lower during summer due to the variations in height of atmospheric boundary layer (ABL). ABL is the turbulent layer near the surface of the earth and acts a crucial role in weather, climate and especially in air quality. During colder periods the height of

ABL is smaller and thus provide less dispersion space to pollutants and consequently the height of ABL can affect the concentrations of pollutant species [152].

Moreover in **Table 5.6** are reported the concentrations of chlorides, nitrates and sulphates found out in atmospheric bulk depositions collected during the campaigns in the site of Rimini. There is no large difference in terms of sulphates annual concentration among the different campaigns. On the other hand, a marked disparity can be noticed in chlorides and nitrates annual amount: during the campaign started in spring, in fact, the content of both Cl^- and NO_3^- is much higher than the one measured during the other campaigns, especially compared to the one started in summer. Actually, the amount of nitrates registered during campaign started in spring and winter campaign is almost two times higher than that started in summer.

Table 5.6: Cl^-, NO_3^- and SO_4^{2-} contained in bulk deposition collected in the site of Rimini during the three campaigns.

Yearly exposure start season	*Bulk deposition ($\mu eq \cdot l^{-1} \cdot y^{-1}$)*		
	Cl^-	**NO_3^-**	**SO_4^{2-}**
Summer jul 2015 - jul 2016	54.3	6.3	11.4
Winter dec 2015 - dec 2016	75.9	13.6	11.9
Spring may 2016 - may 2017	80.9	12.2	11.4

Nevertheless, further relevant information can be achieved considering the monthly trends of Cl^-, NO_3^- and SO_4^{2-} (**Figure 5.7**a – c) during the three exposure campaigns. Specifically, interesting information comes from the comparison of the amount of aggressive ions during the first months of the samples exposure.
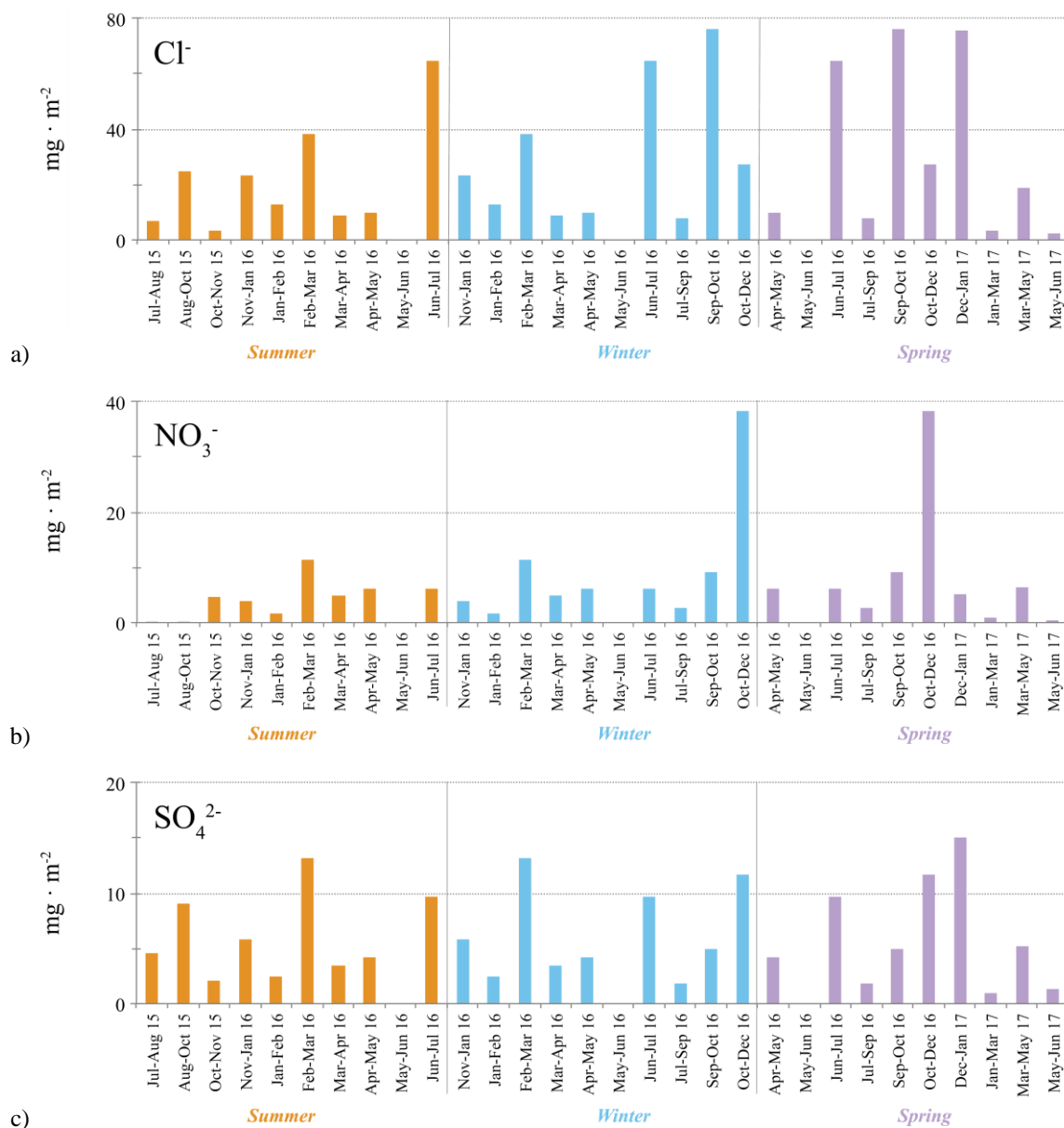
Figure 5.7: Monthly trend of concentrations (mg· m^{-2}) of a) chlorides b) nitrates and c) sulphates during the three campaigns started in: summer, winter, spring. For each campaign the effective monthly was considered. For instance, for all the samples that started their exposure during summer, the monthly labelled as 'Jul15' and 'Jul16' are considering the period ranging from 07/07/15 to 31/07/15 and from 01/07/16 to 06/07/16, respectively.

Additionally, in order to achieve a deeper understanding of the environment influence, specimens were exposed following two different geometries: sheltered and unsheltered condition with respect to the rainfall, as represented in the scheme in **Figure 5.8**.
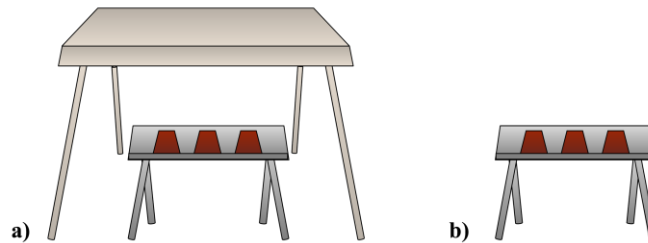
Figure 5.8: Scheme of exposure in a) sheltered and b) unsheltered condition.

5.2.2 Experimental procedure

In order to evaluate the influence of different starting time of exposure, three bare samples of WS were exposed in Rimini both in sheltered and unsheltered condition during summer, winter and spring season as reported in **Table 5.3**. In every case the exposure lasted one year.

Initially, 5 x 5 cm WS bare samples were degreased with acetone, washed with water, dried and weighted. Before starting the exposure, the side of specimen that would not have been exposed was protected by means of an insulating and protective tape and then they were labelled and weighted on analytical balance (Pioneer Ohaus PA214C, capacity 210 g, sensitivity 0.1 mg).
During the monthly sampling, each specimen was removed from the exposure site and weighted to determine mass variation after its stabilization at room temperature in laboratory.
After one year of exposure, each sample was removed and stored in dryer.

For each exposure campaign and geometry of exposition, one sample was subjected to surface analysis (specifically SEM-EDS and XRD analysis, see section 5.4.4 and 5.4.5) and cross section analysis (see section 5.4.6). While the remaining two samples were used for the boiling procedure in order to extract ions from the patina (see section 5.4.7) and subsequently they were subjected to pickling in order to determine mass loss and corrosion rates (see section 5.4.8).

5.3 Accelerated ageing

In order to achieve as much information as possible about the system investigated and to consider the individual contribution of each aggressive anion in mixture on WS corrosion, the complementary approach of accelerated ageing in laboratory condition was flanked to WS field exposures. Among the generally used systems for the laboratory ageing (see section 2.5), alternate immersion test (Wet&Dry) in solutions with opportune compositions was selected. The experimental plan was defined by applying Design of Experiment.

5.3.1 Design of experiment

In order to identify the influence of the content of chlorides, sulphates and nitrates on WS corrosion and to evaluate the possible interaction among them, a Design of Experiment was performed.

Specifically, a Full Factorial Design 2^k was applied and the Central Composite Circumscribed (CCC) quadratic model was chosen (**Figure 5.9**) considering as variables of the system (k) the amount of Cl^-, NO_3^-, SO_4^{2-}.
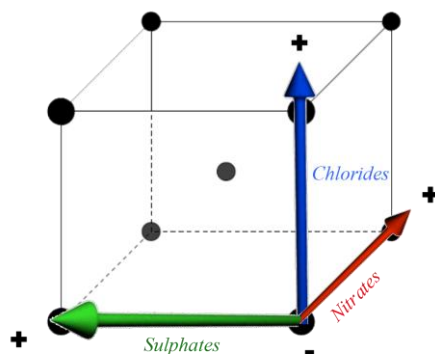
Figure 5.9: Central composite Circumscribed (CCC) model applied.

After an extensive search in literature regarding the composition of different kinds of atmospheres in terms of anions content (see section 2.3.5), the experimental domain was delimited by a lowest concentration level fixed to 1.5 ppm and an highest level fixed to 35 ppm, in order to represent both mild and quite aggressive atmospheres.

Thus, the experimental plan defined by the experimental design sketched out is reported in **Table 5.7**. Specifically, considering 3 variables ($k = 3$), the experimental plan requires the ageing of 8 (2^k) specimens in different solutions characterized by a mixture of Cl^-, NO_3^- and SO_4^{2-}, present alternately in the highest or lowest concentration level chosen,

corresponding to the vertexes of the cube represented in **Figure 5.9**, which describe the design applied. In order to validate the model, 2 additional samples were aged in the same solution prepared with Cl⁻, NO₃⁻ and SO₄²⁻ at the same concentration (20 ppm) and corresponding to the centre of the cube. As mentioned in section 4.1.1, the experiments planned were performed in a random order to avoid bias related to possible systematic effects.

Table 5.7: Experimental plan.

		Anions Concentrations		
		Cl⁻	**NO₃⁻**	**SO₄²⁻**
Specimen	*Solution*	(ppm)	(ppm)	(ppm)
1	Chl1_Nit1_Sul1	1.5	1.5	1.5
2	Chl1_Nit1_Sul3	1.5	1.5	35.0
3	Chl1_Nit3_Sul1	1.5	35.0	1.5
4	Chl1_Nit3_Sul3	1.5	35.0	35.0
5	Chl3_Nit1_Sul1	35.0	1.5	1.5
6	Chl3_Nit1_Sul3	35.0	1.5	35.0
7	Chl3_Nit3_Sul1	35.0	35.0	1.5
8	Chl3_Nit3_Sul3	35.0	35.0	35.0
9	Chl2_Nit2_Sul2	20.0	20.0	20.0
10	Chl2_Nit2_Sul2	20.0	20.0	20.0

The last two experiments planned represent two replicates of the centre point of the experimental domain defined (in other words, the centre of the cube) and they were performed in order to evaluate the experimental variance of the system and above all to validate the models that can be built through the application of DoE.

Actually, as mentioned before (see section 4.1.2), besides the contribution in the planning stage of experiments, DoE also allows to get more information during the stage of data and results elaboration. Specifically, each parameter monitored (deeply described in paragraph 5.3.4) can be considered as a *response factor* (*y*) in the equation 5.1 that describes the quadratic model applied.

$$y = b_0 + b_{Cl^-} \cdot x_{Cl^-} + b_{NO_3^-} \cdot x_{NO_3^-} + b_{SO_4^{2-}} \cdot x_{SO_4^{2-}} + b_{Cl^- NO_3^-} \cdot x_{Cl^-} \cdot x_{NO_3^-} + b_{Cl^- SO_4^{2-}} \cdot x_{Cl^-} \cdot x_{SO_4^{2-}} + b_{NO_3^- SO_4^{2-}} \cdot x_{NO_3^-}$$

(Eq. 5.1)

In equation 5.1, *y* represents the *response factor* measured, *x* terms stand for the concentration of chlorides (x_{Cl^-}), nitrates ($x_{NO_3^-}$) and sulphates ($x_{SO_4^{2-}}$), while *b* terms are

their related coefficients extrapolated by the polynomial fitting. Consequently, the remaining mixed terms (orange coloured) describe the interaction among variables: $b_{Cl^-NO_3^-}$ indicates the interaction between chlorides and nitrates, $b_{NO_3^-SO_4^{2-}}$ is related to the interaction between nitrates and sulphates and $b_{Cl^-SO_4^{2-}}$ to the interaction between chlorides and sulphates.

All the multivariate models were achieved through the interpolation of the parameters monitored and described in paragraph 5.3.4 by means of two software: the freeware software R v. 3.1.0 (GUI) and the software Modde v. 11.01 (Umetrics).

5.3.2 Weathering solutions

Weathering solutions were prepared according to the experimental design applied (see the previous section 5.3.1) and the experimental plan defined.

The solutions were prepared by dissolving in bidistilled water the proper amounts (as mentioned in the previous section, concentrations were set ranging from 1.5 ppm to 35 ppm) of Cl^-, NO_3^-, SO_4^{2-} salts, choosing for all the salts Na^+ as the same counterion. Specifically: NaCl (99%, Baker), NaNO$_3$ (99.5%, Merck) and Na$_2$SO$_4$ (99%, Merck). Na^+, which is a not particularly aggressive species regarding metal corrosion, was chosen as the same counterion for each salt used in order to not introduce a further and uncontrolled variable in the system under study.

5.3.3 Alternated immersion/emersion test (Wet&Dry)

The ageing device used consists of six glass jacketed cells and it is equipped with an automatic mobile bar to which the samples are connected by a Nylon thread. The vertical movement of each sample is related to the vertical displacement of the bar. The equipment complies with the standards ISO 11130 [153] and ASTM G44 [154]. The scheme of the device used is reported in **Figure 5.10**.

The whole duration of the test was set in 15 days. Each hourly wet and dry cycle consisted of 10 minutes of immersion and 50 minutes of emersion to ensure the complete drying of the sample. This latter parameter was fixed to 50 minutes after some preliminary test performed to investigate the required time of drying in regard to the material and the size of samples, temperature and humidity of the room.
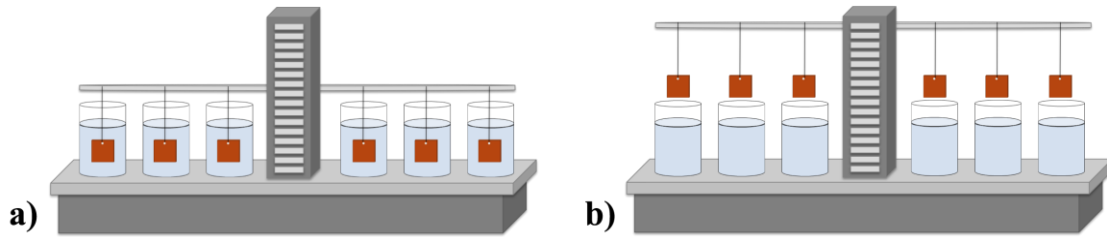
Figure 5.10: Scheme of the Wet&Dry device in a) wet and b) dry position.

Before starting the test, 2.5 x 2.5 cm WS bare samples were punctured and their dimensions were accurately determined by means of a digital calliper. Then, they were degreased with acetone, washed with water and after drying they were weighted on analytical balance (KERN AGB 210-4, capacity 210 g, sensitivity 0.1 mg).

The ageing solutions were prepared following the experimental plan established and described in the previous paragraphs (see sections 5.3.1 and 5.3.2) and each solution was replaced every week to renew the corrosive action of ageing solution. As described in the section 5.3.4, after their replacement, a portion of each solution was stored, filtered and analysed through Atomic Absorption Spectroscopy to determine their metal content (Cr, Cu, Fe, Mn, Ni).

According to the standard ISO 11130 [153], in each cell the ratio between solution volume and sample area was fixed to 32 ml $\cdot$ cm^{-2}.

The pH of each ageing solution (pH meter 211, glass pH electrode 1131b, temperature probe 7662, Hanna Instruments, accuracy – 20 °C $\pm$ 0.01 pH) and sample mass variation (KERN AGB 210-4, capacity 210 g, sensitivity 0.1 mg) were controlled each day.

5.3.4 Factors monitored

During the entire duration of the test, pH of each ageing solution and sample mass variations were monitored each day.

Secondly, metal analysis was performed on the weathering solutions collected diversifying among different fraction that contains soluble and insoluble products of corrosion (as defined by Raffo et al. [125] and described in 5.3.4.1). Additionally, after cutting specimens in half, surface analysis, mass loss and corrosion rates determination were performed on half specimens as well described in 5.3.4.2.

5.3.4.1 Analysis of weathering solutions

After replacement (at 7 days) and at the end of ageing (at 14 days), weathering solutions were collected.

Specifically, in order to determine the total fraction (TF) of the released metals, a portion of each weathering solution was acidified with nitric acid (Merck, 65% Suprapur) until reaching pH < 2, which guarantees the dissolution of all particulate and non-adherent corrosion products. TF was then stored in HDPE bottles at 4°C.

Conversely, in order to separate the metals released in the dissolved fraction (DF) from those released as particulate fraction (PF), the remaining portion of each weathering solution was filtered on cellulose acetate membrane filter (ø 47 mm, 0.45 µm pore size, Sartorius). The filtered solutions were acidified (Merck, 65% Suprapur) and stored in HDPE bottles at 4°C.

The concentrations of Cr, Cu, Fe, Mn, and Ni in filtered (DF) and non-filtered (TF) solutions were determined through AAS (see section 5.4.1).

5.3.4.2 Investigations on specimens

Once the ageing test was over, all the specimens were weighted (KERN AGB 210-4, capacity 210 g, sensitivity 0.1 mg) and stored in a dryer.

The patina formed on specimens was characterized by SEM-EDS and XRD analysis (for further details see section 5.4.4 and 5.4.5) and the α/γ protective ability index (PAI), i.e. the mass ratio of the goethite to lepidocrocite amount on WS [102], and the α/γ^* PAI, i.e. the mass ratio of the goethite to the sum of lepidocrocite, akaganeite and magnetite amount on WS [108], were calculated.

Additionally, mass loss and corrosion rates were determined for each sample (see paragraph 5.4.8).

5.4   Analytical techniques and procedures

5.4.1 Atomic Absorption Spectroscopy (AAS)

Quantification of metals in solution was performed using Atomic Absorption Spectroscopy (AAS). This technique requires the atomization of sample and consequently its irradiation with an electromagnetic radiation with specific wavelength. Then the coming out radiation is revealed by means of a detector.

For what concern sample atomization, two methods are commonly used:

- **Electrothermal Atomizer – GF-AAS** that uses a cylindrical graphite tube equipped with a platform and an injection hole (furnace); a known amount of the sample is deposited on the platform and treated with a thermal program (that includes 4 different steps: *drying*, *incineration*, *atomization*, *cleaning*). An inert gas, generally Argon, is continuously flushed in the furnace during the process. Through this atomization method is commonly possible quantify analytes in the range of $ng \cdot L^{-1}$ and $\mu g \cdot L^{-1}$.

- **Flame Atomizer – F-AAS** that uses a combination of fuel and oxidant gases (generally air/acetylene with ~ 2300 °C as flame temperature) in order to desolvate, vaporize and atomize the sample aspirated by a pneumatic nebulizer. Through this atomization method is commonly possible quantify analytes in the $mg \cdot L^{-1}$ range.

The quantification of all the metals (Cu, Cr, Fe, Mn and Ni) in solution was performed through a Perkin Elmer AAnalyst 400 and a Perkin Elmer PinnAAcle 900z Atomic Absorption Spectrometers. Considering the range of concentration of the samples, the analyses were performed predominately through GF-AAS. The instrumental condition, the graphite furnace temperature programs and the limits of detections (LoD) and quantifications (LoQ) are reported in **Table 5.8** and listed for each metal. LoDs and LoQs were determined as the metal concentrations corresponding to respectively 3 and 10 times the standard deviation of 20 replicates of a blank solution. For what concern the determination of iron content, samples with higher metal concentrations (i.e. in the $mg \cdot L^{-1}$ range) were analysed through Perkin Elmer AAnalyst 400 equipped with flame atomizer. In this case, the LoD and LoQ are 0.1 ppm and 0.4 ppm, respectively.

Furthermore, three replicate readings were performed on each sample and only values determined with a %RSD lower than 10% were considered acceptable. Values below the LoQ were set equal to ½ LoQ [131]. Quality control on multi-standard solution were performed every ten samples.

Table 5.8: Operating conditions for metal analysis in GF-AAS.

Analyte	Step	Temp (°C)	Ramp time (sec)	Hold time (sec)	Internal gas flow (mL·min^{-1})	Gas type	Wavelenght (nm)	Slit (nm)	LoD (µg/L)	LoQ (µg/L)
	1	100	1	30	250					
	2	130	15	40	250	Argon				
Cr	3	800	10	10	250		357.9	0.7	0.2	0.7
	4	2300	0	5	-	-				
	5	2450	1	3	250	Argon				

Analyte	Step	Temp (°C)	Ramp time (sec)	Hold time (sec)	Internal gas flow (mL·min^{-1})	Gas type	Wavelenght (nm)	Slit (nm)	LoD (µg/L)	LoQ (µg/L)
	1	100	1	30	250					
	2	130	15	40	250	Argon				
Cu	3	600	10	20	250		324.7	0.7	0.3	1
	4	2000	0	5	-	-				
	5	2450	1	3	250	Argon				

Analyte	Step	Temp (°C)	Ramp time (sec)	Hold time (sec)	Internal gas flow (mL·min^{-1})	Gas type	Wavelenght (nm)	Slit (nm)	LoD (µg/L)	LoQ (µg/L)
	1	100	5	20	250					
	2	140	15	15	250	Argon				
Fe	3	1400	10	20	250		248.3	1.8	0.8	2.7
	4	2400	0	5	-	-				
	5	2600	1	3	250	Argon				

Analyte	Step	Temp (°C)	Ramp time (sec)	Hold time (sec)	Internal gas flow (mL·min^{-1})	Gas type	Wavelenght (nm)	Slit (nm)	LoD (µg/L)	LoQ (µg/L)
	1	100	1	30	250					
	2	130	15	40	250	Argon				
Mn	3	600	10	20	250		279.5	0.2	0.2	0.7
	4	1900	0	5	-	-				
	5	2450	1	3	250	Argon				

Analyte	Step	Temp (°C)	Ramp time (sec)	Hold time (sec)	Internal gas flow (mL·min^{-1})	Gas type	Wavelenght (nm)	Slit (nm)	LoD (µg/L)	LoQ (µg/L)
	1	100	1	30	250					
	2	130	15	40	250	Argon				
Ni	3	600	10	20	250		232	0.2	0.6	2
	4	2300	0	5	-	-				
	5	2450	1	3	250	Argon				

5.4.2 Ion Chromatography (IC)

For the determination and the quantification of ions in solution, ion chromatography (IC) were used. This technique is based on the principle of ion-exchange: anionic or cationic species can be separated through their different affinity towards a ion-exchange resin, which acts as a stationary phase.

In this work, a Metrohm 761 Compact IC equipped with a conductivity detector was employed for the ions analysis.

Specifically, cations (Na^+, NH_4^+, K^+, Ca^{2+}, Mg^{2+}) were analysed by means of a Metrosep C4/150 column with 150.0 mm as length and 4.0 mm as internal diameter (Metrohm). The eluent phase used consists of L-(+)-Tartaric acid 4 mM (Sigma Aldrich, ACS reagent $\geq$ 99.5%), 2,6-Pyridinedicarboxilic acid (Dipicolinic acid) 1 mM (Fluka, $\geq$ 99.5%) and 0.4% of acetone (Sigma Aldrich, $\geq$ 99%). The flow rate was set to 1.2 ml $\cdot$ min^{-1} and the amount of sample injected to 20 µL.

Anions (Cl^-, NO_2^-, NO_3^-, SO_4^{2-}) analysis were performed with a Metrosep A Supp 4/5 Guard precolumn with 5 mm as length and 4.0 mm as internal diameter (Metrohm) followed by a IC SI-90 4E column with a 250 mm as length and 4.0 mm as internal diameter (Shodex) followed by a suppressor (Metrohm). The eluent phase used consists of Na_2CO_3 1.8 mM (Carlo Erba, RPE-ACS-ISO), $NaHCO_3$ 1.7 mM (Carlo Erba, RPE-ACS) and 0.4% of acetone (Sigma Aldrich, $\geq$ 99%). The flow rate was set to 1.2 ml $\cdot$ min^{-1} and the amount of sample injected to 20 µL.

Ion concentrations were determined by external standard methods using stock standard solutions (Certipur, Merck).

Limits of Quantification (LoQ) and Limit of Detection (LoD) regarding the analysed ions were calculated as the ions concentrations corresponding to respectively 3 and 10 times the standard deviation of 20 replicates of a blank solution and they are reported in **Table 5.9**.

Table 5.9: LoQ for cations (Na^+, NH_4^+, K^+, Ca^{2+}, Mg^{2+}) and anions (Cl^-, NO_2^-, NO_3^-, SO_4^{2-}).

		LoD (mg · L^{-1})	LoQ (mg · L^{-1})			LoD (mg · L^{-1})	LoQ (mg · L^{-1})
Cationi	Na^+	0.06	0.20	Anioni	Cl^-	0.02	0.06
	NH_4^+	0.05	0.20		NO_2^-	0.01	0.03
	K^+	0.09	0.30		NO_3^-	0.03	0.10
	Ca^{2+}	0.10	0.40		SO_4^{2-}	0.10	0.40
	Mg^{2+}	0.05	0.20				

5.4.3 Colour Measurements

Colour measurements were also performed on samples in order to characterize changes during the mechanism of autopassivation. According to Grassman's laws [155 – 157], three (properly selected) stimuli can match a single colour stimulus. Thus, data recorded by the instrument were elaborated in the CIE $L^*a^*b^*$ colour space (**Figure 5.11**), a three-dimensional space produced by plotting in Cartesian coordinates the following defined quantities:

- Along *z* axis, **Lightness – L***: the maximum value of L^*, equal to 100, represent the brightest white, while the minimum value, equal to 0, stands for the darkest black.

- Along *y* axis, **Red/Green ratio – a***: represents the redness on the positive side and the greenness on the negative side.

- Along *x* axis, **Yellow/Blue ratio – b***: represents the yellowness on the positive side and the blueness on the negative side.
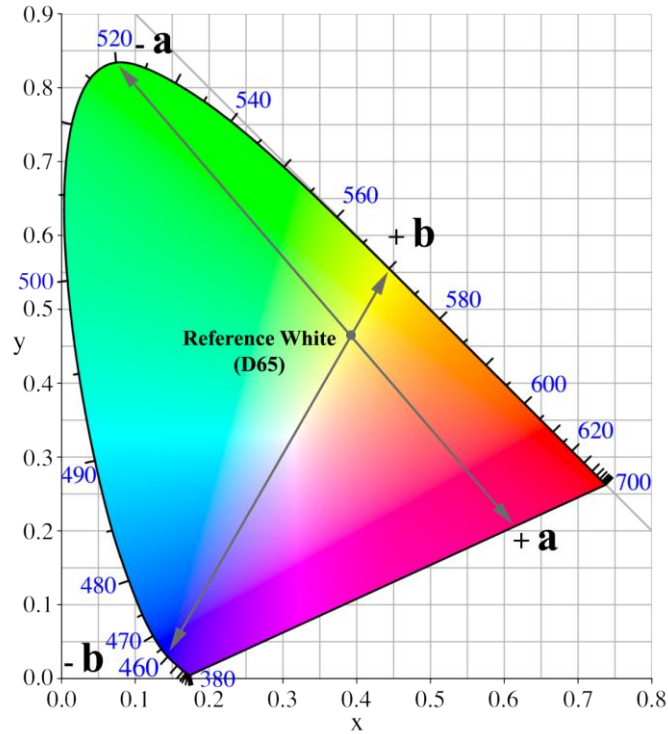
Figure 5.11: CIELAB chromaticity diagram (CIE, 1976).

Moreover, instead of specifying the colour by L^*, a^* and b^*, the quantities L^*, C_{ab}^* and h_{ab}^* expressed in polar coordinates can be used within the so-called CIELCH system. Specifically:

- **Saturation** or **Chroma – C_{ab}^***: defined as:

$$C_{ab}^* = \left(a^{*2} + b^{*2}\right)^{\frac{1}{2}} \qquad \text{(Eq. 5.2)}$$

- **Hue angle – h_{ab}^***: defined as:

$$h_{ab}^* = arc \tan\left(\frac{b^*}{a^*}\right) \qquad \text{(Eq. 5.3)}$$

Obviously, the h_{ab}^* assumes zero value along a^* axis.

The Euclidean distance in the CIELAB colour space (equation 5.4) expresses the colour-difference:

$$\Delta E_{ab}^* = \sqrt{(\Delta L^*)^2 + (\Delta a^*)^2 + (\Delta b^*)^2} \qquad \text{(Eq. 5.4)}$$

where

$$\Delta L^* = L^* - L_{reference}^*,$$
$$\Delta a^* = a^* - a_{reference}^*,$$
$$\Delta b^* = b^* - b_{reference}^*.$$

An equivalent definition of ΔE_{ab}^{*} can be expressed in terms of polar coordination (equation 5.6):

$$\Delta E_{ab}^{*} = \sqrt{(\Delta L^{*})^{2} + (\Delta C_{ab}^{*})^{2} + (\Delta H_{ab}^{*})^{2}} \qquad \text{(Eq. 5.5)}$$

Colour measurements were acquired by Datacolor D400 spectrophotometer working in alternative diffuse geometries (d/0° - total transmittance), using D illuminant with a correlated colour temperature (CCTs) of approximately 6500 K (D65) as source and the 10° observer. Both Specular Component Excluded (SCE) and Specular Component Included (SCI) were considered as measurement methods and without noticing any difference between them. According to the standard UNI-EN 15886 [158], the repeatability of the measurement was tested on 5 replicates acquired on a small area vision of 9 mm and on 6 replicates (3 for each side) on a small area vision of 6.6 mm, respectively for the natural exposed samples and the accelerated aged ones.

5.4.4 Scanning Electron Microscopy and Energy Dispersive X-Ray Spectroscopy (SEM-EDS)

Microscopy observations of the samples were performed through Scanning Electron Microscopy (SEM). By means of SEM, images of magnified (roughly between 100 and 100˙000 times) objects surface are created using a beam of electrons rather than visible light. Additionally, SEM may be also combined with energy Dispersive X-Ray Spectroscopy (SEM-EDS) in order to carry out elemental analysis and also obtain a chemical characterization of the surface of the samples.

As known from the literature, SEM-EDS analysis can provide useful information about microstructure of metals and can be used to infer corrosion products presents on metal surfaces [159]. Moreover, SEM-EDS can also help the characterization of specific shape, size and composition of particles present in the deposits of both stones [160] and surrogate surfaces [161].

Specifically, in this work, SEM-EDS analysis were performed using Hitachi S4800 high-resolution scanning electron microscope (3 nm in high vacuum mode) equipped with secondary electron and backscattered electron detectors and using Zeiss EP EVO 50 scanning electron microscope with secondary electron and backscattered electron detectors and an Oxford Instruments INCA ENERGY 350 [z > 4 (Be)]. In order to increase their conductivity, all samples observed (except cross sections) were covered by graphite.

5.4.5 X-Ray Diffraction (XRD)

Corrosion products formed on the surface of the specimens were characterised also by X-Ray Diffraction (XRD). Actually, this technique allows the identification of the structure of crystalline materials through the phenomenon of the diffraction (**Figure 5.12**) described by the Bragg's Law (equation 5.6).
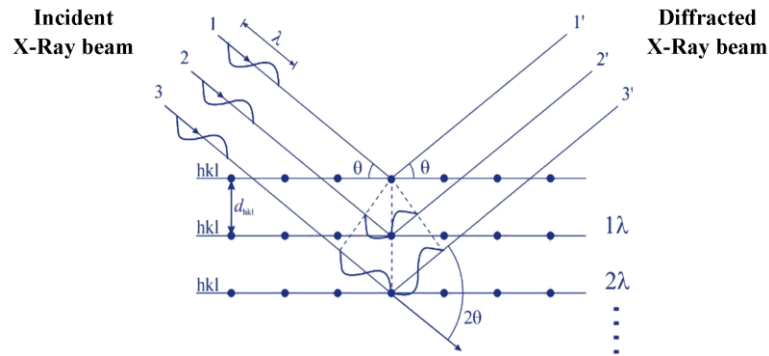
Figure 5.12: Graphical representation of the diffraction phenomenon related to the Bragg's law.

Diffraction occurs when an incident X-Ray beam strikes a material and consequently it is scattered by the atoms of the hit structure. Subsequently, the waves scattered constructively or destructively interfere with each other. The Bragg's law (equation 5.6) allows to relate the distance between crystal planes (d) and the angle (θ) at which these planes will diffract X-Rays of a determined wavelength (λ). Lastly, n is an integer.

$$n\lambda = 2d \sin \theta \qquad \text{(Eq. 5.6)}$$

The identification of an unknown sample is possible by means of a comparison of all the d-spacing values calculated through equation 5.6 with the values contained in databases [162].

For this work, XRD measurements were performed with a D8 Brukers AXS diffractometer equipped with a Cobalt X-ray tube, diffracted beam monochromator, a laser that focused on the point of the surface to be analysed (500 μm in diameter) and a LynxEye linear detector. The generator settings were 40 kV and 30 mA. XRD data were collected over a 2θ range of 10-100° with a step width of 0.03° and a counting time of 3s/step. The qualitative identification of crystalline phases present in the rust formed on specimens was performed from XRD patterns using JCPDS database (Join Committee on Powder Diffraction Standards) and software. In order to quantify crystalline phases from

XRD patterns, Rietveld method was used. By means of this method, all reflections, overlapping or not, are used in the fitting process to analyse sample overlapped patterns. Rietveld analysis allows also to overcome a problem related to the identification of akaganeite (see section 3.4.2) when it is found in a low proportion in the corrosion product layer [114].

5.4.6 Cross Sections

Corrosion layers were observed in cross section after low-speed, dry micro-cutting and cold mounting in acrylic resin (Technovit 4002 IQ, Kulzer), reinforced with silica for better edge preservation. A water-free metallographic preparation procedure was specifically developed for these samples: the polishing sequence was carried out at low speed in lubro-refrigerant oil (DiaMaxx Mono, Akasel) 9 μm to 3 μm diamond with final rinsing in 1 μm and drying with cool air. The contact with water was avoided during all the preparation sequence, so as to limit chloride leaching as much as possible. Cross-section samples were then analysed by SEM/EDS (Zeiss EVO 50 with Oxford X-Act microprobe) in order to identify the main features of the corrosion layers.

5.4.7 Extractions of ions from the patina

In order to extract and quantify the ions entrapped inside the patina of the samples after their natural exposure or accelerated ageing, a boiling method was chosen [163].
Considering the novelty of this procedure, especially towards the extraction of ions from the patina of weathering steel, the method was applied as more standardized as possible to provide for a lack in the definition of ion extracting efficiency.
First of all, for each specimen naturally aged (5 x 5 cm), the protective tape was removed from the not exposed side of the sample and the backside of the specimens was cleaned with acetone to remove all residuals of tape and glue. Then each specimen was submerged in 120 mL of bidistilled water. While, each specimen aged in laboratory (2.5 x 2.5 cm) was submerged in 20 mL of bidistilled water. All specimens were submerged inclined in order to minimize the contact with becker walls. Both kinds of specimens were successively boiled for 1 hour (temperature of the water ~ 100°C), paying attention to top up with bidistilled water where necessary (due to the water boiling) to keep specimens submerged.. Each specimen was weighted before and after the boiling process (KERN 770-60, capacity 60 g, sensitivity 0.01 mg).

The volume of the solution collected after the boiling procedure was measured and then the solutions were filtered on sterile syringe filter with cellulose acetate membrane, (Ø 25 mm, 0.45 µm pore size, GVS). A fraction of the filtered solutions was stored in PP falcon tubes at 4°C and the anions (Cl^-, NO_2^-, NO_3^-, SO_4^{2-}) and cations (Na^+, NH_4^+, K^+, Ca^{2+}, Mg^{2+}) content was quantified through ion chromatography (section 5.4.2).

5.4.8 Mass loss determination

After natural exposure or accelerated ageing test, corrosion rates – r_{corr} were measured through mass loss determination of a metallic specimen where all the corrosion products formed on the surface of the sample are removed.

According to the standard ISO 8407 [164], the chemical procedure for mass loss determination for iron and steel consists in:

1 Specimens are weighted on analytical balance (KERN 770-60, capacity 60 g, sensitivity 0.01 mg).

2 Sample are immersed in a pickling solution prepared by mixing 3.5 g of Hexamethylenetetramine (Sigma Aldrich, $\geq$ 99%) in a liter of solution of 50% HCl (Fluka, $\geq$ 37%).

3 Beakers containing pickling solutions and samples are kept in ultrasonic bath for 10 minutes.

4 At the end of each cycle in ultrasonic bath, the specimens are rinsed with distilled water for 3 times and ethanol and then dried in oven.

5 Once the samples are cooled, they are weight again.

6 In order to ensure complete removal of the corrosion products formed, the procedure is repeated from the step 3) until reaching a weight stabilization of pickled specimens.

Corrosion rate – r_{corr} can be calculated from equation 5.7.

$$r_{corr} \; (g \cdot m^{-2} \cdot y^{-1}) = \Delta m \cdot A^{-1} \cdot t^{-1} \qquad \text{(Eq. 5.7)}$$

where *A* is the surface of the pickled specimen (expressed in m^2), *t* is the exposure time (expressed in year) and Δm is the mass loss (expressed in g).

Chapter 6

Results and discussion

In order to achieve a deeper knowledge of the phenomenon investigated, both natural field exposures and accelerated ageing tests were performed as described in Chapter 5. In the two following sections the results related to environmental exposure (section 6.1) and accelerated ageing (section 6.2) are reported and discussed.

6.1 Environmental exposure

Considering that the composition, stability and therefore the protective ability of its patina are strongly influenced by several factors, including exposure conditions and environmental surroundings, natural field exposures were performed to evaluate the decay induced by the presence and the amount of contaminants on weathering steel since the beginning of its exposure. In this section the results concerning surface characterization (XRD and SEM-EDS) and destructive o semi-destructive tests (i.e. ions extraction from the patina and pickling) performed on samples collected on three different one-year campaigns in the urban-coastal site of Rimini, Italy are presented. Each campaign was planned to start in different time of the year (summer, winter and spring) in order to evaluate the influence of different condition and atmospheric compositions since the first months of exposure of the samples.

6.1.1 Colour measurements

Figure 6.1 shows the bare sample of weathering steel (5 x 5 cm) before it begins natural exposure (**Figure 6.1**a) and two samples collected after one year of exposure started during summer in the urban-coastal site of Rimini, Italy. One sample was exposed in sheltered condition (**Figure 6.1**b) and the other one in unsheltered condition (**Figure 6.1**c). As shown for instance in **Figure 6.1** concerning two samples belonging to the campaign started in summer, a slight difference in terms of colour of the patina formed is always observable between the two geometries of exposure. Moreover, even if exposed in a coastal site, samples show no sign of rust exfoliation. According to Alcántara et al. [165], rust layers formed at chloride deposition rates of less than 100 mg $Cl^- \cdot m^{-2} \cdot d^{-1}$ do not exhibit greater cracking and they are relatively compact and fairly adherent on sample

surfaces. The site of Rimini is actually characterized by chloride deposition rate ranging between 20 ~ 30 mg Cl$^-$ · m^{-2} · d^{-1} (more detailed information are reported in section 5.2.1).

Figure 6.1: a) Bare sample of WS before field exposure. Samples collected after one year of the exposure started during summer in Rimini, Italy and exposed in b) sheltered and c) unsheltered condition.

Thus, the first information about the formation and evolution of patinas on WS during its natural exposure can be achieved by means of spectrophotometric colour measurements (as described in section 5.4.3).

Results of colour measurements are reported in **Table 6.1**. In all samples a decrease in L* can be observed meaning that during the exposure all the samples tend to become darker. Otherwise, an increase in a* and b* can be observed and this implies that the patina formed on the specimens tend more to red (a*) and to yellow (b*) than bare WS.

Table 6.1: Colour coordinates in CIE L*a*b* and CIE L*C*h colour scale and colour variations (ΔE) of specimens exposed for one year in sheltered and unsheltered condition and starting their exposure in summer, winter and spring.

Yearly exposure start season		Samples	L*	a*	b*	C*	h*	ΔE
		Bare Cor-Ten A	50.1	0.3	1.8	1.8	79.5	
Summer	Sheltered	Sum_CC1	31.8	7.0	6.0	9.2	40.4	20.0
		Sum_CC2	32.0	6.5	5.5	8.5	40.0	19.5
		Sum_CC3	31.6	6.7	5.6	8.7	40.0	20.0
	Unsheltered	Sum_CA1	31.0	14.9	17.6	23.1	49.7	28.9
		Sum_CA2	31.6	13.3	14.9	20.0	48.3	26.1
		Sum_CA3	31.6	13.7	15.5	20.6	48.5	26.7
Winter	Sheltered	Win_CC1	24.1	10.3	9.9	14.3	43.7	29.0
		Win_CC2	24.7	10.1	9.6	14.0	43.6	28.4
		Win_CC3	24.3	10.8	10.1	14.8	42.9	29.1
	Unsheltered	Win_CA1	27.0	11.8	11.2	16.2	43.5	27.5
		Win_CA2	26.9	11.6	10.7	15.8	42.5	27.3
		Win_CA3	26.5	11.9	11.2	16.4	43.3	27.9
Spring	Sheltered	Spr_CC1	29.7	8.2	8.6	11.9	46.1	22.9
		Spr_CC2	29.4	8.1	7.9	11.3	44.4	23.0
		Spr_CC3	29.5	8.1	7.5	11.1	42.9	22.8
	Unsheltered	Spr_CA1	30.5	11.3	12.8	17.1	48.5	25.1
		Spr_CA2	31.1	11.3	12.9	17.2	48.7	24.7
		Spr_CA3	30.5	11.4	12.5	17.1	47.6	24.9

Moreover, results of colour measurements have been processed through multivariate analysis, specifically, by means of Principal Component Analysis in order to recognize possible differences among the samples and to identify some sample clusters. PCA was performed considering as object of the training set all the replicates acquired for each samples and L*, a* and b* as variables. Data were centered but not scaled. A full cross validation was applied. The score plot of the first model built considering also the unexposed sample as object of the dataset is reported in **Figure 6.2** and shows how naturally aged samples are distinct and separate respect to bare WS. Moreover, a preliminary clustering among samples can also be highlighted.
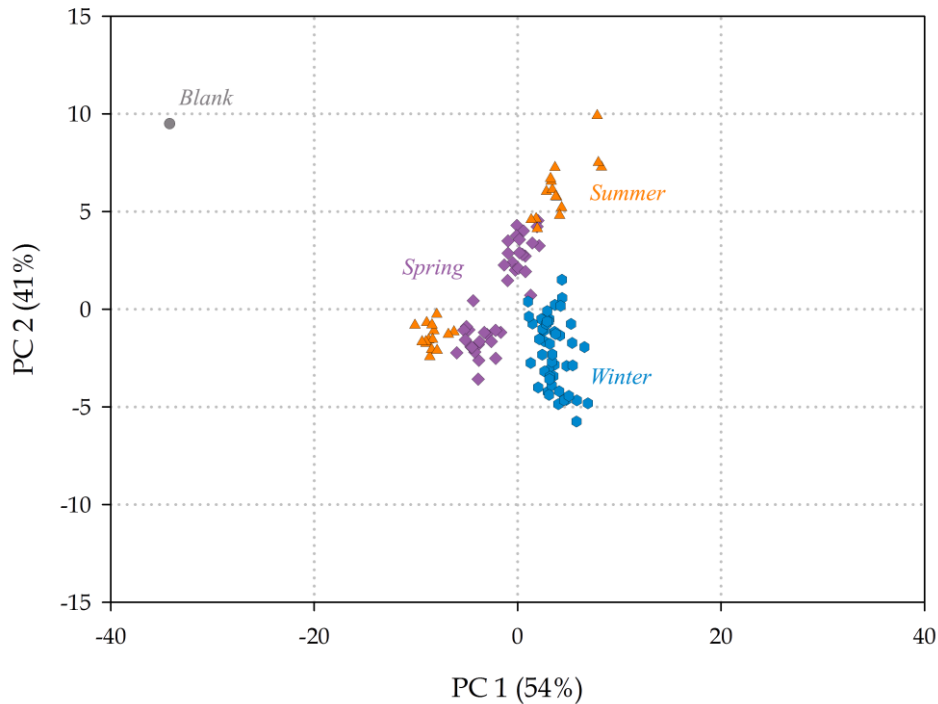
Figure 6.2: Score plot of the first component (PC1, explained variance 54%) and the second component (PC2, explained variance 41%) of the PCA model achieved on colour data reported in **Table 6.1**.

A new PCA model was created leaving out from the training set the unexposed sample to further investigate aged samples and identify possible clusters based on the "*a priori*" known classes (for instance, groups defined by their different exposure start time or samples characterized by the same geometry of exposure). The *scores plot* shown in **Figure 6.3**a highlights the presence of a clear distinction between samples exposed in sheltered (grey) and unsheltered (brown) condition while in **Figure 6.3**b is highlighted the presence of clusters related to the start exposure time of the samples (summer in orange, spring in purple and winter in light blue).
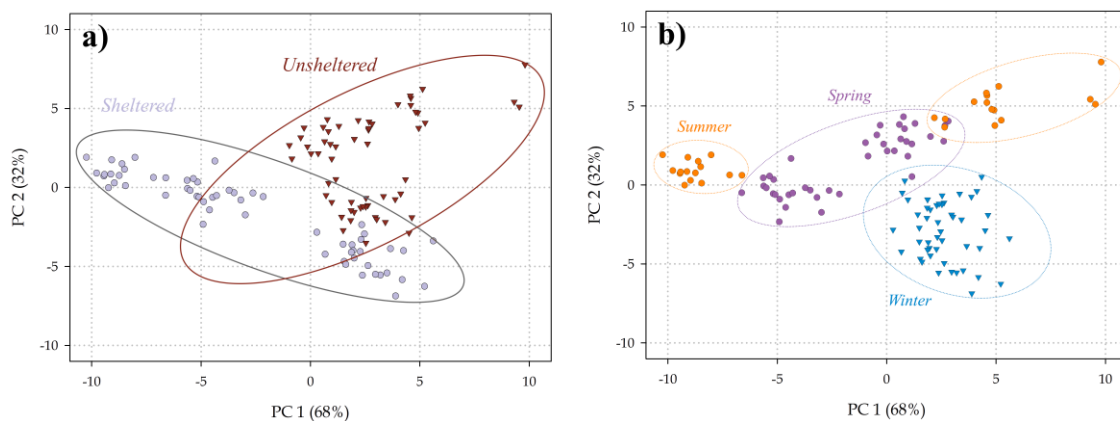
Figure 6.3: *Scores plot* of the first component (PC1, explained variance 68%) and the second component (PC2, explained variance 32%) of the PCA model achieved excluding unexposed sample.

The two scores plot also express that the distinction between sheltered and unsheltered samples is more pronounced for the samples that have been exposed in summer time following by the samples exposed during spring time while there is no clear separation among winter samples on the basis of the geometry of exposure. Considering the environmental data of the exposure site (see section 5.2.1), this observation can be related to the amount of precipitations fallen during the first 4 months of exposure (772.8 mm for samples that began their exposure in summer, while 205.2 mm for spring and lastly only 163.3 mm for samples that began their exposure in winter). Moreover, in the same period, the concentration of some pollutants (CO, NO_2, and especially $PM_{2.5}$ and PM_{10}) shows higher values for samples exposed in winter as well as relative humidity (93%). Thus, taking also into account the low temperatures (-1.8 ~ 12.2 °C) and the low intensity of the solar radiation (96.8 W · m^{-2}) that characterized the first months of the exposure, the persistence of the polluting species mentioned above on the surfaces of samples that started the field exposure in winter may have been similar for unsheltered and sheltered samples, reducing the colour difference of their patinas.

Another interesting result arises from the observation of *biplot* graph (**Figure 6.4**) in which the relation between objects and variables can be observed.
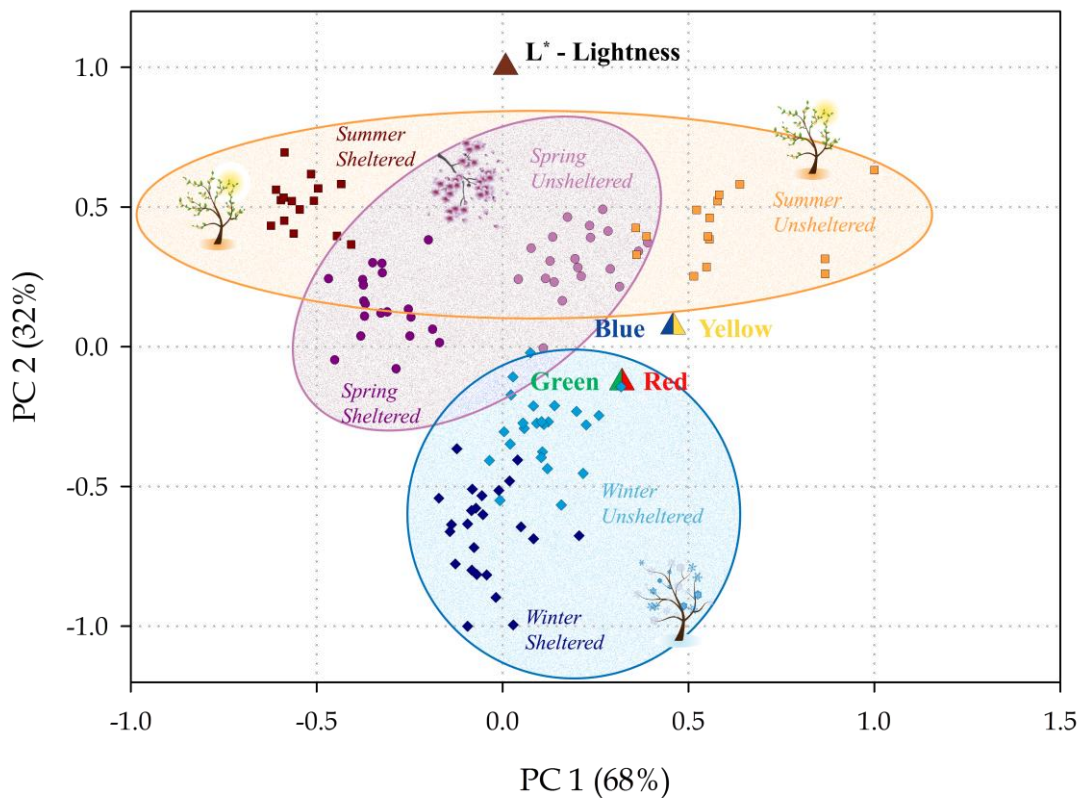
Figure 6.4: *Biplot* of the PCA model achieved excluding unexposed sample.

Specifically, **Figure 6.4** shows that the variable L^* (that is related to the lightness measured) lies along the PC 1 while the two variables a^* (Red/Green index) and b^* (Yellow/Blue index) lie along the PC 2. Therefore, it can be deduced that after the natural exposure all the samples tend to become darker and this phenomenon is particularly pronounced for winter samples. Eventually, samples exposed in sheltered condition are strongly influenced by high values of both a^* and b^* thus their patina tend to increase more in red and yellow.

6.1.2 Patina characterization

6.1.2.1 Mass variation

Preliminary information about the patina formed on each specimen exposed with two different geometries (sheltered and unsheltered) and with different starting time (summer, winter, spring) can be achieved by mass variation (MV) values (**Figure 6.5**).
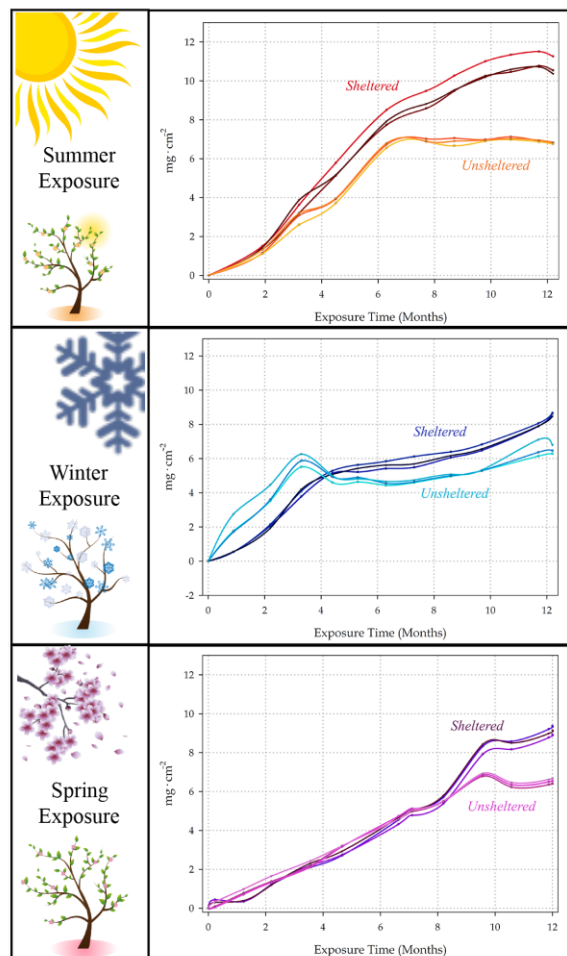
Figure 6.5: Mass variation (mg · cm^{-2}) of samples exposed in sheltered and unsheltered condition at different start time of natural exposure in Rimini.

Even though following different trends, all samples show a progressive mass increase representing the formation of corrosion products and thus to the growth of patina on the surface. Due to the action of winds, slight negative values of monthly mass variation are related to the possible loss of a fraction of non-adherent corrosion products formed and constituents the outer and porous rust layers.

The trends of mass variation are quite different among the campaigns. Specifically, as shown in **Figure 6.5**, samples that have started their exposure during spring show an almost linear trend, especially during the first months of exposure. Only after the eighth month of exposure, the trend slightly changes and a clearer distinction between sheltered and unsheltered samples can be pointed out. A sharper pattern is shown in correspondence with the monthly of "Dec16", in which an increase in concentration of CO, NO_2, $PM_{2.5}$ and PM_{10} was registered (see **Figure 5.5**).

The mass variation shown by samples that have started their exposure during summer presents a sharper trend when compared to the linear trend observed for the campaign started in spring, this trend rather follows a parabolic profile. The increase in mass variation is observed especially between the second ("Aug15") and the seventh ("Jan16") month of exposure. Also in this case the step slope of mass variation trend seems related to the increase in pollutant concentrations (see **Figure 5.5**).

Lastly, a different pattern is determined for samples that have begun the exposure in winter in which during the first months of exposure the increase of mass variation is quite sharp and above all it is sharper in unsheltered samples. A similar but milder effect can be also noticed for samples belonging to spring campaign: for the first two months the mass variation is higher in samples exposed with unsheltered geometry, suggesting for this period the presence of an alternation of wetting and drying cycles of the surfaces, which enhance corrosion product formation. Anyway, as shown by **Table 6.2** where the mass variations after one year of exposure are summarized, for each campaign, the mass variation measured after one year of exposure is higher in sheltered condition than in unsheltered condition and probably due to a more intense formation of corrosion products on sheltered surfaces, which are protected from the removal action of precipitations.

Table 6.2: The mass variations (mg · cm^{-2}) of samples after one year of exposure in different geometries (sheltered and unsheltered condition) at different start times (summer, winter and spring).

Yearly exposure start season	Total Mass Variation (mg · cm^2)		Yearly exposure start season	Total Mass Variation (mg · cm^2)		Yearly exposure start season	Total Mass Variation (mg · cm^2)	
Summer	*Sheltered*	*Unsheltered*	**Winter**	*Sheltered*	*Unsheltered*	**Spring**	*Sheltered*	*Unsheltered*
	10.54	6.80		8.64	6.29		9.37	6.41
	11.26	6.76		8.66	6.46		8.93	6.54
	10.37	6.85		8.46	6.79		9.16	6.42
Mean	10.7 ± 0.5	6.80 ± 0.04	*Mean*	8.6 ± 0.1	6.5 ± 0.3	*Mean*	9.2 ± 0.2	6.46 ± 0.07

However, examining **Table 6.2** it can be noticed that a great difference in terms of the mass variation measured after one year of exposure is present between samples exposed in sheltered and unsheltered condition and starting their exposure in summer. Conversely, the difference between sheltered and unsheltered conditions narrows considering samples belonging to the campaign started in spring and even more for those samples that began their exposure during winter season. This observation is in agreement with what has been observed in the previous section (section 6.1.1) about colour measurements, where, concerning the campaign started in winter, an unexpected behaviour of unsheltered samples is pointed out probably due to the environmental parameters related to the first months of exposure (such as high relative humidity and high concentration of CO, NO$_2$, and especially PM$_{2.5}$ and PM$_{10}$ while low rainfalls, temperatures and intensity of the solar radiation were recorded).

6.1.2.2   Patina characterization

In order to obtain a complete characterization of the corrosion products, specimen surfaces were investigated by XRD (see section 5.4.5) and SEM analysis (see section 5.4.4). Specifically, **Table 6.3** reports the quantitative estimation of crystalline phases grown on WS during its natural exposure and it also indicates the α/γ protective ability index (PAI) calculated as the mass ratio of the goethite to lepidocrocite amount [108]. In **Table 6.4**, quantitative estimation of crystalline phases is calculated by normalizing in respect to the amount of ferrihydrite in order to make possible the direct comparison of the percentages of other phases present among the samples. Ferrihydrite is actually detected when x-rays reach the uncorroded metal present under the patina. Thus, when ferrihydrite is detected the entire stratigraphy of the patina is analyzed.

Due to the presence of akaganeite, another polymorph of –FeOOH, in **Table 6.4** is also reported the α/γ^* PAI calculated as the mass ratio of the goethite to the sum of lepidocrocite and akaganeite amount [108]. The XRD spectra are later reported in **Figure 6.7**.

Table 6.3:   Summarized XRD results for natural exposed WS samples.

Yearly exposure start season	Geometry of exposure	Lepidocrocite (γ-FeOOH)	Goethite (α-FeOOH)	Akaganeite (β-FeOOH)	Ferrihydrite ($Fe_5HO_8 \cdot 4H_2O$)	α/γ
Summer	Sheltered	54.7%	19.9%	25.1%	0.31%	0.36
	Unsheltered	87.5%	12.1%	0.0%	0.38%	0.14
Winter	Sheltered	45.6%	21.5%	32.4%	0.52%	0.47
	Unsheltered	74.1%	17.0%	8.5%	0.45%	0.23
Spring	Sheltered	43.7%	21.2%	35.1%	0.00%	0.49
	Unsheltered	75.5%	12.7%	11.6%	0.18%	0.17

Table 6.4:   Summarized XRD results normalized in respect to the content of ferrihydrite.

Yearly exposure start season	Geometry of exposure	Lepidocrocite (γ-FeOOH)	Goethite (α-FeOOH)	Akaganeite (β-FeOOH)	α/γ^*
Summer	Sheltered	54.9%	20.0%	25.2%	0.24
	Unsheltered	87.9%	12.2%	0.0%	0.14
Winter	Sheltered	45.8%	21.6%	32.6%	0.28
	Unsheltered	74.4%	17.1%	8.5%	0.21
Spring	Sheltered	43.7%	21.2%	35.1%	0.27
	Unsheltered	75.6%	12.7%	11.7%	0.15

Three different morphologies were observed on the surfaces of specimens: lepidocrocite (γ-FeOOH), goethite (α-FeOOH) and also akaganeite (β-FeOOH). Lepidocrocite is always present in higher amount in the specimens that have been exposed in unsheltered condition. The opposite trend is observed for the presence of akaganeite. As known from

the literature [114], in fact, akaganeite formation requires halogen ions Cl^- and F^- in order to stabilize its crystalline structure. Thus, it is reasonable that samples exposed in sheltered condition, and therefore protected from the precipitation that wash ion species out [166], show a greater formation of this polymorph of iron oxyhydroxides. Moreover, it is reasonable that the highest percentage of akaganeite is identified on samples belonging to the campaign started in May 2016. Actually, as shown in **Figure 5.4**, they have been exposed to a large frequency of winds coming from the sea to the land (direction NE – E – SE) that can carry salts and especially chlorides species on the surfaces of samples enhancing the formation of the β-FeOOH.

Patina protective ability index (PAI, α/γ) suggests that there is a slight difference in the stability of the patinas formed especially for samples exposed during winter and spring season that show a more stable patina than summer samples. As mentioned before (see section and 3.4.3), the stability of the patina is related to its composition and specifically, the allotropic forms of iron oxyhydroxides follow Akaganeite > Lepidocrocite >> Goethite as order of electrochemical and thermodynamic stability. The transformation of lepidocrocite into goethite is a slow process related to the alternation of wet and dry cycles and consequently strictly dependent on temperatures and relative humidity. The reduced stability of patina formed on samples that started their exposure in summer could be related to the large amount of rainfalls widespread over the entire month of 'Sep15' (see **Figure 5.3**). Additionally, as reported in **Table 5.3**, samples belonging to the campaign started in summer have been also subject to the largest time of wetness (35%). Due to the meteorological conditions recorded in the early stage of their corrosion, these samples have been exposed to large wet phase without the consequent drying stage required to ensure the alternation between wet/dry cycles that lead to the formation of goethite.

On the other hand, in all the campaigns considered, patina formed on sheltered samples can be evaluated by the α/γ calculated more stable than the patina formed on unsheltered samples, highlighting a strong effect related to the geometry of exposure. However, this effect appears less sharp, especially for winter samples, if the presence of akaganeite is taking into account by means of the α/γ* index.

Additionally, comparing the *biplot* obtain from the PCA performed on colour measurements of sample surfaces, the formation of akaganeite appears to be associated to a change in the colour of the patinas: specifically, samples that contains a high amount of

akaganeite are characterized by an higher green and blue component while also a decrease in L^* - Lightness can be observed (**Figure 6.6**).
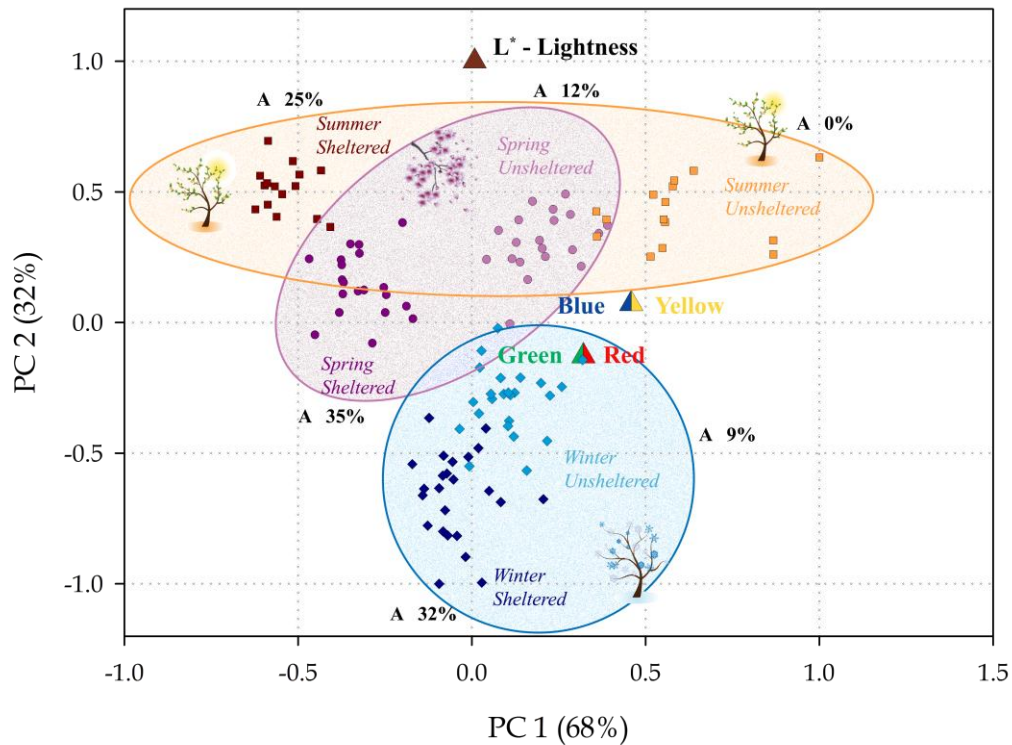

Figure 6.6: *Biplot* of the PCA model achieved processing patina colour data. The percentage content of akaganeite phase is also highlighted.

This result suggests the possibility to monitor evolution and growth of patina on samples exposed outdoors by means of spectrophotometric data processed by chemometrics, in agreement to what was developed by Luciano et al. [122] to monitor outdoor bronze patinas and protective coating systems and to what was already suggested for weathering steel in a previous work [125]. The correspondence found between the phase of iron oxides and the colour of the patina is also in agreement with what was determined by Altobelli Antunes [97]. A higher content of lepidocrocite corresponds to red coloured regions while yellow is associated to the presence of also goethite (see **Table 6.3**).

Surfaces of sample were also investigated by SEM analysis to ensure the presence of the morphologies identified through XRD analysis and to characterize the structure of the rust layer. **Figure 6.7** presents XRD spectra and some SEM images confirming the presence of lepidocrocite and goethite.
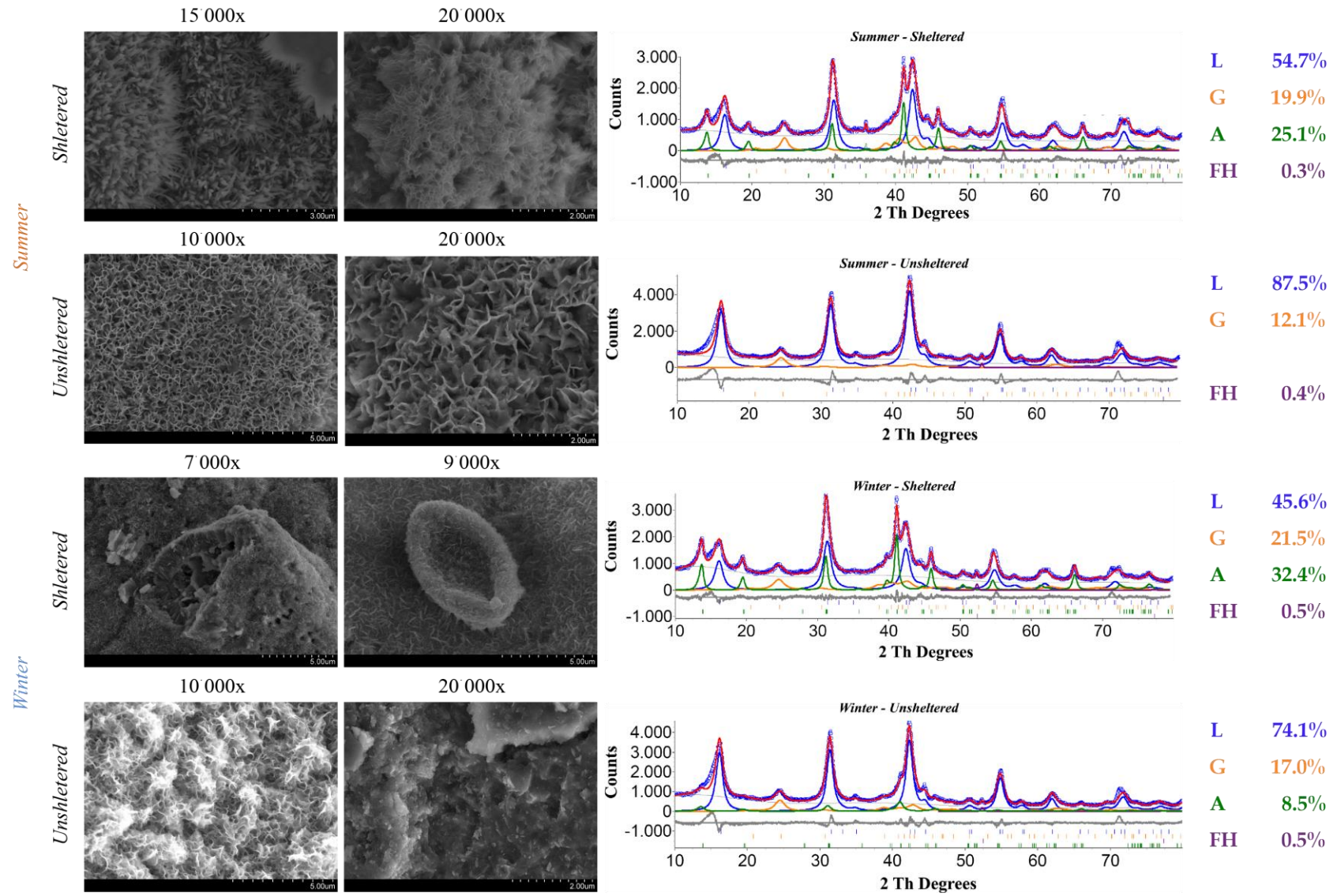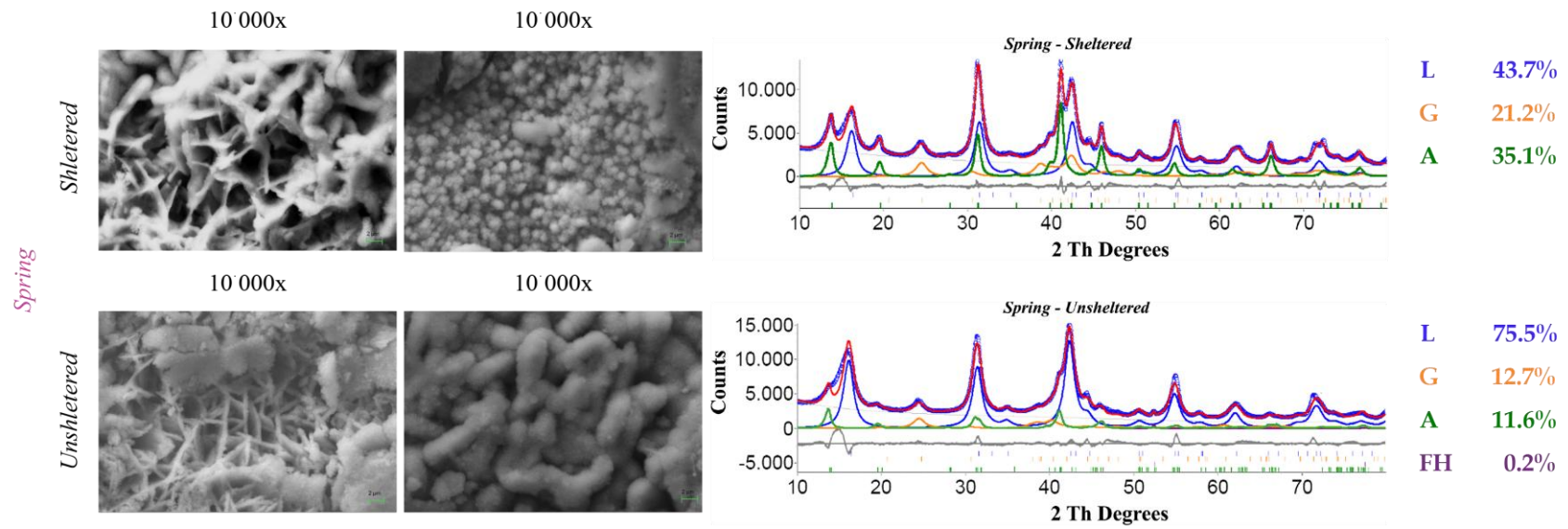
Figure 6.7: SEM images acquired and XRD spectra for each campaign and both geometries of exposure.

L stands for 'lepidocrocite', G for 'goethite', A for 'akaganeite' and FH for 'ferrihydrite'.

As observed in **Figure 6.7**, all samples present as main morphology the globular and laminar morphology of lepidocrocite. Main morphology observed here are *globular* formations of a very different kind (**Figure 6.8**a) and *bird's nest shape*, which can grow very close to each other (**Figure 6.8**b). Lepidocrocite is also present in some miscellaneous forms like clumps of grass or weeds. Tubular morphologies characterized by prismatic formations corresponding to goethite crystals can be observed (**Figure 6.8**c) [167].
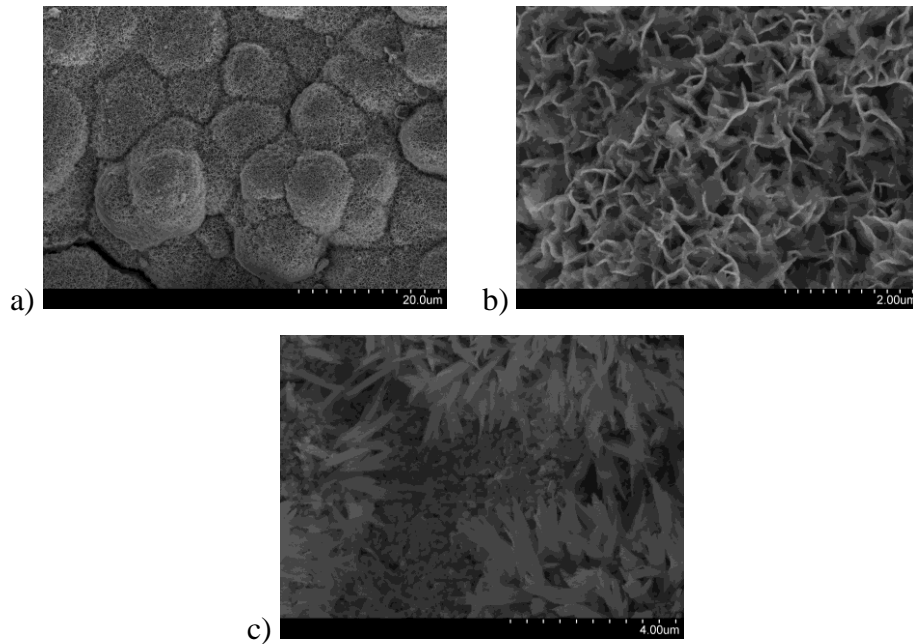

Figure 6.8: Different morphologies observed by SEM on the sample surfaces: lepidocrocite in
a) globular formations and b) bird's nest shape, c) goethite crystals.

The last morphology observed at much higher magnification (60˙000 ~ 80˙000x) is akaganeite (**Figure 6.9**). Akaganeite is constituted by tubular morphology characterized by a lattice of elongated cylinder-, tube- or cigar-shaped crystals [114, 167]. The distribution of crystals is fairly narrow and a statistical study suggest a size distribution of 100 nm < length < 200 nm and 60 nm < width < 80 nm [114, 168].
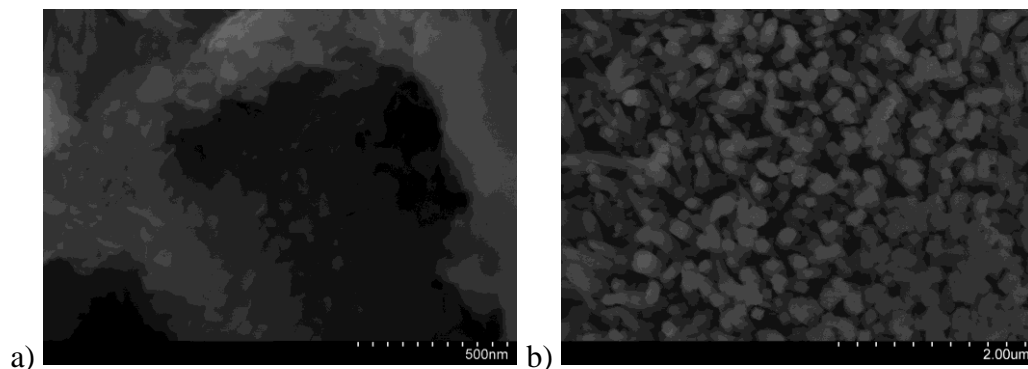
Figure 6.9: Tube- or cigar-shaped crystals of akaganeite observed at a) 80000x and b) 25000x.

Observations at high magnification show also the formation of prismatic crystallites (cigar-shaped) typical of akaganeite inside of amorphous granules, which constitute globular type formation. Actually, it can be speculated that the formation of akaganeite inside these structures may be encouraged by the entrapment of chlorides species inside the granules, once they have been formed (**Figure 6.10**).

a)   b)
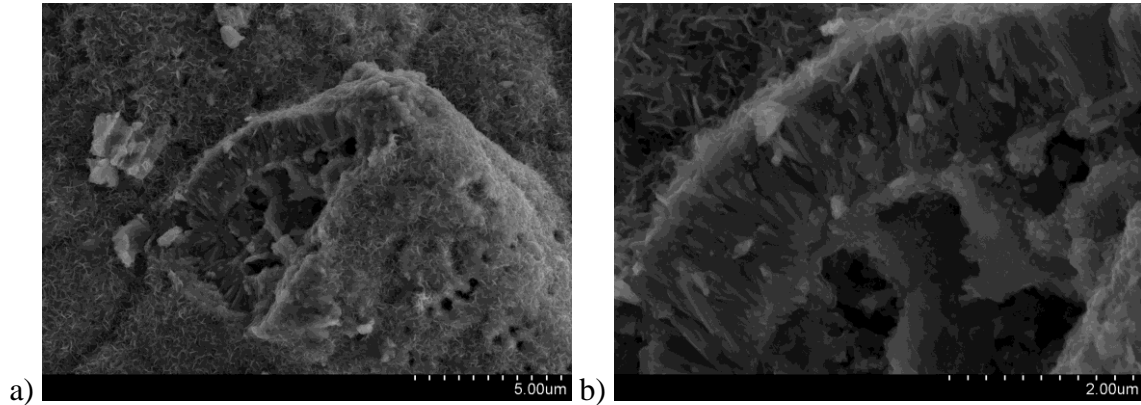
Figure 6.10: a) SEM image (7000x) of a typical globular formation that contains cigar-shaped morphology; b) Higher magnification (22000x) of the previous SEM image.

Besides its detection, another interesting result related to akaganeite morphology concerns its location in the corrosion product layer formed on steel. Actually, the preferential location of akaganeite in the steel corrosion products layer is still a controversial matter of discussion in literature [78, 169, 170]. According to many authors [171 – 173], akaganeite forms mainly in the inner part of the corrosion layer, at the interface of steel and corrosion products, where chlorides can accumulate. Conversely, akaganeite has also been detected in the outer part of thick rust layers formed on carbon steels exposed in a coastal-industrial site [101]. Lastly, Shiotani et al. [174] identified akaganeite both in the outer and inner region of the rust layer.

Actually, observations by scanning electron microscopy performed on the surfaces of samples exposed in Rimini identify the presence of akaganeite in the outer part of rust layer (**Figure 6.9**) and with a difference in terms of amount between sheltered and unsheltered geometry. As Asami and Kikuchi postulated [101], the presence of akaganeite at the surface region of samples can be probably justified considering a reactions between iron ions produced by corrosion and the atmospheric halogen ions (such as Cl^- and F^-) deposited. It can be reasonable considering the wind regime (see **Figure 5.4**) and the amount of chlorides quantified from bulk deposition in the site of

exposure of Rimini (see **Figure 5.7**a). Particularly during the first four months of exposure, a remarkable difference in the Cl⁻ concentration can be observed especially for spring and winter samples (82.45 and 83.02 mg · m^{-2} respectively) respect to summer samples (58.12 mg · m^{-2}), which indeed show also the lowest content of akaganeite both in sheltered and unsheltered condition (**Table 6.3 – 6.4**). Moreover, another correlation can be observed with the rainfall data (**Figure 5.3**a) due to the fact the both winter and spring samples have been exposed to a fewer precipitation (163.3 and 205.2 mm respectively) than summer samples (772.8 mm) during the first stage of their exposition.

Consequently, in order to achieve a deeper knowledge, it was considered important to characterize the rust layer formed on WS more in detail by means of cross section, as illustrated in the following paragraph.
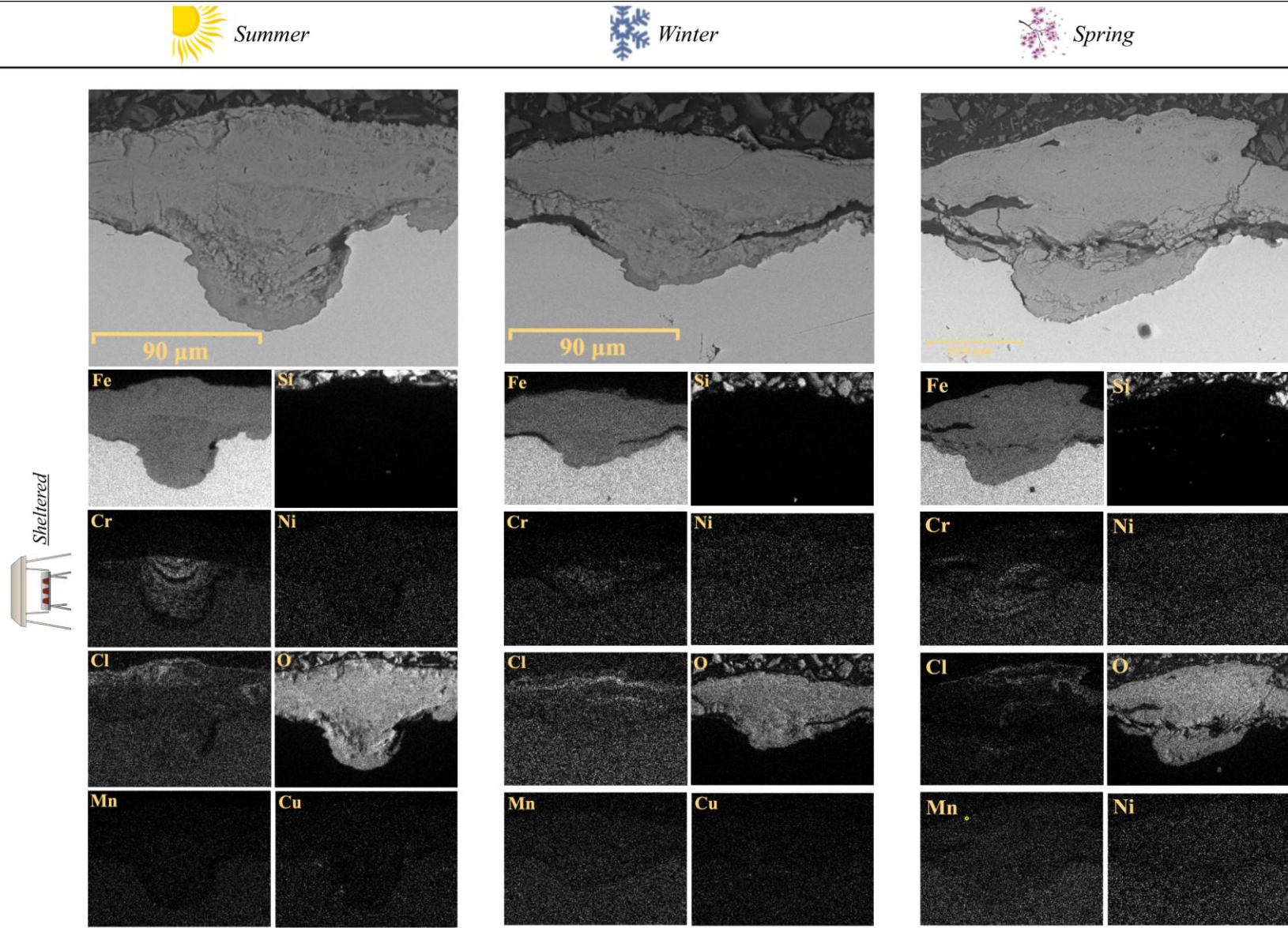
6.1.2.3 Cross section

More detailed information about the surfaces of samples were obtained by means of cross sections (see section 5.4.6) and their investigations through SEM analysis and through elemental mapping acquired by EDS analysis (**Figure 6.11 – 6.12**).

Generally, the acquired SEM images show neither a significant difference in the thickness of the layer formed nor relevant dissimilarities between the two geometries of exposure. Nevertheless, deeper corrosion pits can be observed in samples exposed during summer.

For all samples, the alloying elements Cu, Mn and Ni are equally distributed in the rust layer. On the other hand, as also reported in literature [175], Cr is preferably located in the inner part of the rust layer and Cu sometimes tends to show low concentrations.

Another interesting result can be pointed out by means of the distribution of Cl. A higher percentage of chloride is observed for samples exposed in sheltered condition and it is predominantly located in the outer part of the rust layer, as also observed in a previous work after 3 years of exposure of WS in Rimini [166]. Considering that, as mentioned before, the presence of chlorides and the depletion of oxygen can lead to the formation of akaganeite, the Cl⁻ distribution observed by EDS analysis confirms the results pointed out by the surface observation through scanning electron microscopy (see **Figure 6.7** and **Figure 6.9**). These results suggest the presence of akaganeite predominantly in the outer

rust layer. Moreover, as expected and as already supposed in a previous work [166], the fact that chloride is mainly detected on the surface of sheltered sample suggests that precipitations acting on unsheltered samples can remove Cl$^-$ ions deposited on the surfaces or enhance their penetration into the corrosion layer prompting akaganeite formation also in unsheltered sample, as confirmed by XRD result (see **Table 6.3 –6.4**).

Figure 6.11: SEM images and EDS X-Ray maps acquired on cross-section of weathering steel exposed during summer, winter and spring in sheltered condition.
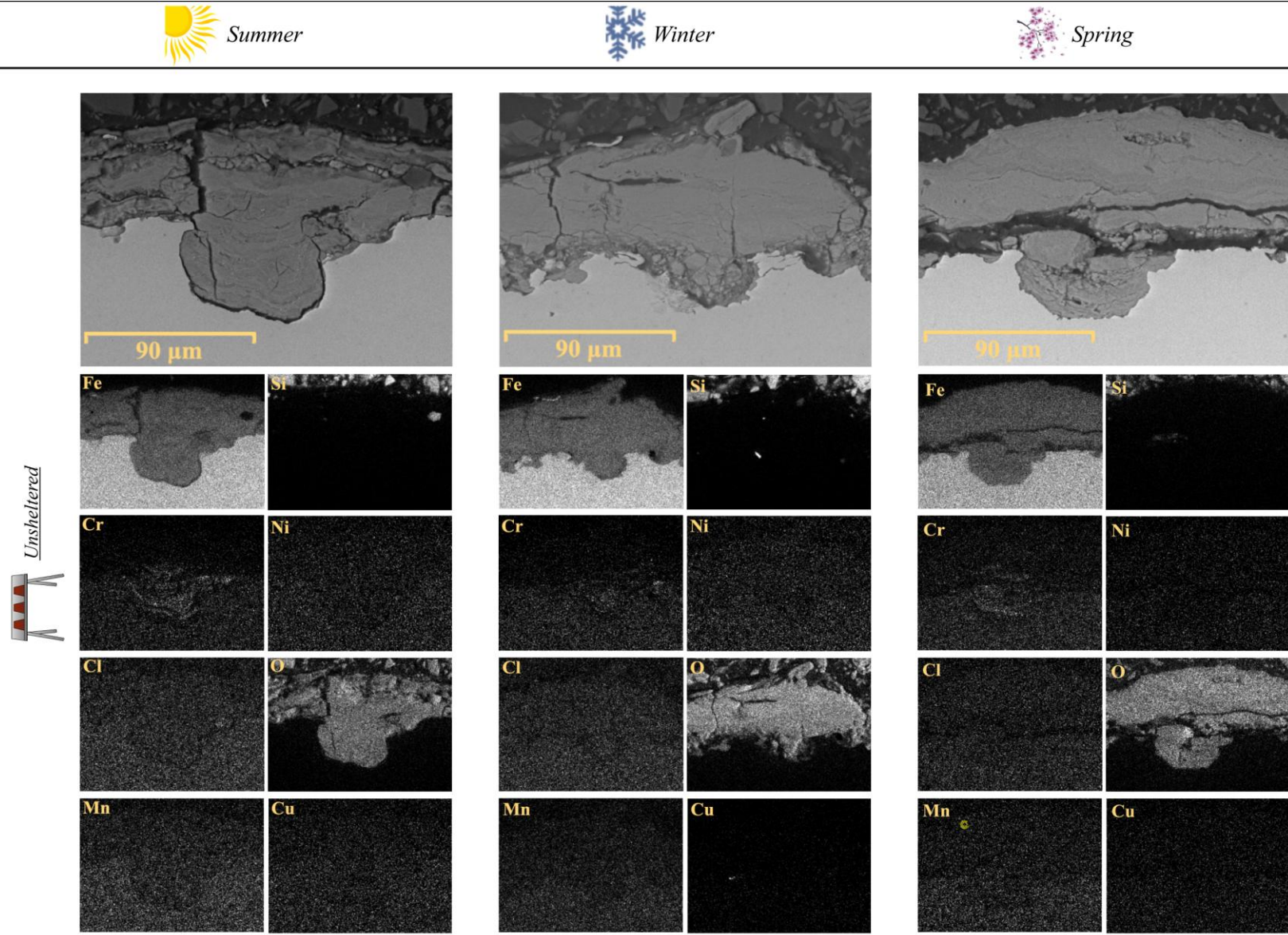
Figure 6.12: SEM images and EDS X-Ray maps acquired on cross-section of weathering steel exposed during summer, winter and spring in unsheltered condition.

Moreover, EDX analysis was carried out on four different positions of the samples (1. surface, 2. outer layer, 3. inner layer and 4. metal) and the average content of elements (%wt) found is reported in **Table 6.5**.

As expected from the alloy composition of WS, Fe and C are the elements present in the highest percentage. Concerning the elements involved in patina stabilization, Cu and Ni are not detected by EDS analysis, especially on the surfaces where also the content of Cr is decreasing, in agreement with Raffo et al. [125].

Table 6.5: Average elemental composition (%wt) obtained from EDS analysis of the cross section of each steel sample exposed in different condition.

| Yearly exposure start season	Geometry of exposure		weight% of all elements analysed and normalised															
			C	O	Na	Al	Si	P	S	Cl	K	Ca	Cr	Mn	Fe	Ni	Cu
Summer	Sheltered	1. Surface	24.29	35.39	0.41	0.16	4.63	0.00	0.00	0.54	0.00	0.09	0.14	0.11	34.24	0.00	0.00
		2. Outer layer	19.80	31.72	0.45	0.22	3.84	0.21	0.00	0.18	0.17	0.34	1.09	0.21	41.77	0.00	0.00
		3. Inner layer	20.48	36.32	0.30	0.16	4.06	0.00	0.09	0.12	0.08	0.14	0.22	0.15	37.89	0.00	0.00
		4. Metal	18.11	7.12	0.00	0.15	3.68	0.10	0.00	0.00	0.00	0.00	0.63	0.35	69.61	0.24	0.00
	Unsheltered	1. Surface	34.68	31.37	0.24	0.10	3.33	0.00	0.00	0.07	0.10	0.41	0.11	0.10	29.49	0.00	0.00
		2. Outer layer	29.75	30.96	0.22	0.09	2.85	0.00	0.08	0.00	0.00	0.38	0.20	0.21	35.27	0.00	0.00
		3. Inner layer	26.24	30.24	0.25	0.13	2.52	0.17	0.14	0.00	0.10	0.26	1.19	0.12	38.42	0.00	0.21
		4. Metal	27.29	5.67	0.16	0.11	2.53	0.10	0.00	0.00	0.00	0.17	0.61	0.30	62.64	0.19	0.22
Winter	Sheltered	1. Surface	26.13	35.26	0.23	0.12	3.61	0.00	0.00	0.34	0.06	0.00	0.15	0.16	33.94	0.00	0.00
		2. Outer layer	25.49	33.84	0.20	0.09	3.28	0.00	0.00	0.25	0.08	0.14	0.28	0.18	36.17	0.00	0.00
		3. Inner layer	22.06	32.37	0.34	0.10	3.17	0.10	0.00	0.00	0.00	0.21	0.87	0.18	40.08	0.15	0.37
		4. Metal	22.09	7.03	0.25	0.13	3.13	0.00	0.00	0.00	0.00	0.00	0.59	0.18	66.41	0.00	0.19
	Unsheltered	1. Surface	30.41	31.89	0.30	0.16	4.66	0.00	0.08	0.00	0.00	0.13	0.14	0.00	32.23	0.00	0.00
		2. Outer layer	21.88	36.21	0.22	0.14	3.89	0.00	0.20	0.00	0.00	0.08	0.38	0.00	36.84	0.00	0.15
		3. Inner layer	24.06	32.31	0.26	0.17	3.47	0.14	0.00	0.11	0.09	0.29	0.77	0.14	37.91	0.00	0.29
		4. Metal	21.07	7.63	0.30	0.12	3.65	0.09	0.00	0.00	0.00	0.00	0.65	0.31	65.96	0.00	0.23
Spring	Sheltered	1. Surface	21.14	39.19	0.25	0.20	4.18	0.00	0.11	0.40	0.00	0.00	0.15	0.15	34.23	0.00	0.00
		2. Outer layer	17.98	37.47	0.33	0.14	3.38	0.00	0.00	0.24	0.00	0.00	0.38	0.19	39.89	0.00	0.00
		3. Inner layer	16.73	30.79	0.24	0.16	2.95	0.15	0.13	0.38	0.00	0.00	1.11	0.19	47.17	0.00	0.00
		4. Metal	16.06	6.28	0.00	0.00	2.95	0.00	0.00	0.00	0.00	0.00	0.72	0.32	73.35	0.00	0.33
	Unsheltered	1. Surface	23.95	37.35	0.27	0.18	4.40	0.00	0.00	0.00	0.00	0.00	0.13	0.00	33.72	0.00	0.00
		2. Outer layer	21.11	37.19	0.25	0.20	3.81	0.00	0.13	0.07	0.00	0.00	0.13	0.00	37.11	0.00	0.00
		3. Inner layer	17.75	32.37	0.00	0.15	3.42	0.15	0.19	0.08	0.00	0.00	0.91	0.21	44.55	0.00	0.22
		4. Metal	18.24	7.81	0.00	0.22	3.44	0.00	0.00	0.00	0.00	0.00	0.63	0.27	69.08	0.00	0.32

6.1.3 Extractions of ions from the patina

Further information about the influence of environmental features on weathering steel corrosion may be achieved by means of a samples boiling procedure (see section 5.4.7) that allows extracting and recovering the environmental ions entrapped inside the patina on specimens. As described in section 5.4.7, the solutions collected by boiling were filtered and analysed by ion chromatography (see paragraph 5.4.2) in order to quantify the amount of both cations (Na^+, NH_4^+, K^+, Ca^{2+}, Mg^{2+}) and anions (Cl^-, NO_2^-, NO_3^- and SO_4^{2-}) present. **Figure 6.13** shows the amount (in mg · L^{-1}) of cations quantified in the samples. However, considering the novelty of this procedure especially towards weathering steel, a lack in terms of ion extracting efficiency definition occurred. Thus, the results obtained can be considered as trends more than exact values of concentration. The trend related to NH_4^+ is not shown because it was found below the LoD in all of the samples. Conversely, the amount of Na^+ is about one order higher than the amount of K^+ and Ca^{2+} and approximately two orders higher than Mg^{2+}.
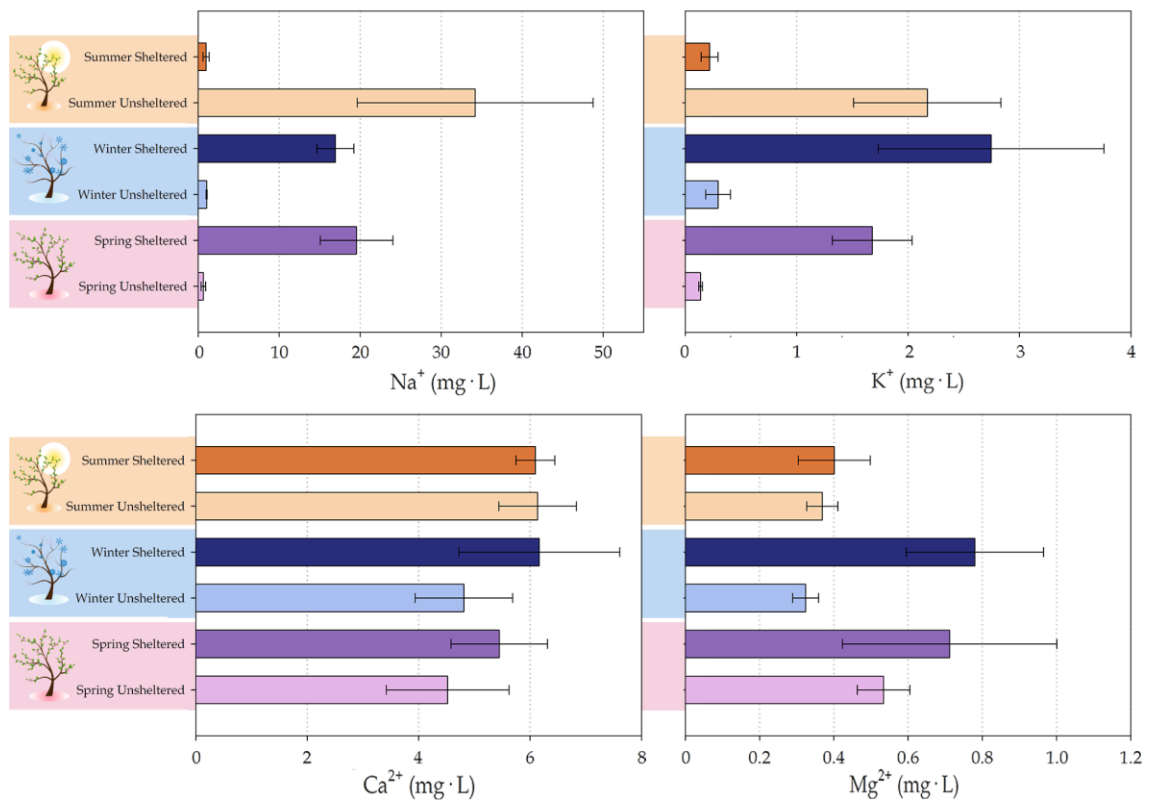
**Figure 6.13**: Concentrations (in mg · L^{-1}) of Na^+, K^+, Ca^{2+} and Mg^{2+} found in the samples after the boiling procedure.

For what concern the presence of the terrigenous elements, Ca^{2+} and Mg^{2+}, none significant difference can be observed between sheltered and unsheltered samples, only a slight tendency regarding the patina of the unsheltered samples to contain less content of Ca^{2+} and Mg^{2+}, especially for the campaigns started in winter and spring.

The same trend is recorded for Na^+ and K^+ between sheltered and unsheltered samples belonging to the campaigns started in winter and spring. These trends represent expected results considering the washing action of precipitations acting on unsheltered samples. Nevertheless, an opposite trend can be observed in samples belonging to the campaign started in summer. This unexpected result may be consistent with the results previously obtained regarding patina colour, mass variation and XRD analysis, in which the campaign started in summer shows the main and major differences in respect to other campaigns. A possible explanation for that may lie in a correlation among the environmental variables, especially between precipitation and ion deposition. Specifically, the monthly deposition of ions acting on a 45° inclined inert surfaces made by Teflon and exposed in parallel in Rimini as reference can be considered and correlated to the monthly trend of rainfalls (**Figure 5.3**). For instance, concerning the exposure begun in summer, during the month 'Sep15' characterized by large and diffuse precipitations, Na^+ deposition was relatively low (14.3 µg · cm^{-2}), especially considering the monthly average value (46.8 µg · cm^{-2}). Conversely, high peaks of Na^+ deposition were recorded in 'Apr16' and 'May16', when the rainfalls recorded were low, thus justifying the presence of Na^+ inside the patina of unsheltered samples. Supporting this hypothesis, for both the campaign started in winter and spring the highest value of Na^+ deposition was recorded between 'Sep16' – 'Dec16', which were also been the wettest months.

In **Figure 6.14** the amount (in mg · L^{-1}) of anions quantified in the samples is shown. As expected from the environmental characteristic of the exposure site (previously described in paragraph 5.2.1), chlorides are the ion species identified in greater quantity. Also for chlorides and sulphates an opposite tendency is shown for samples that have begun their exposure in summer rather than spring and winter: summer samples exposed in sheltered condition present a lower concentration of Cl^- and SO_4^{2-} in respect to those exposed in unsheltered condition. The contrary occurs for samples that have been exposed in spring and winter.
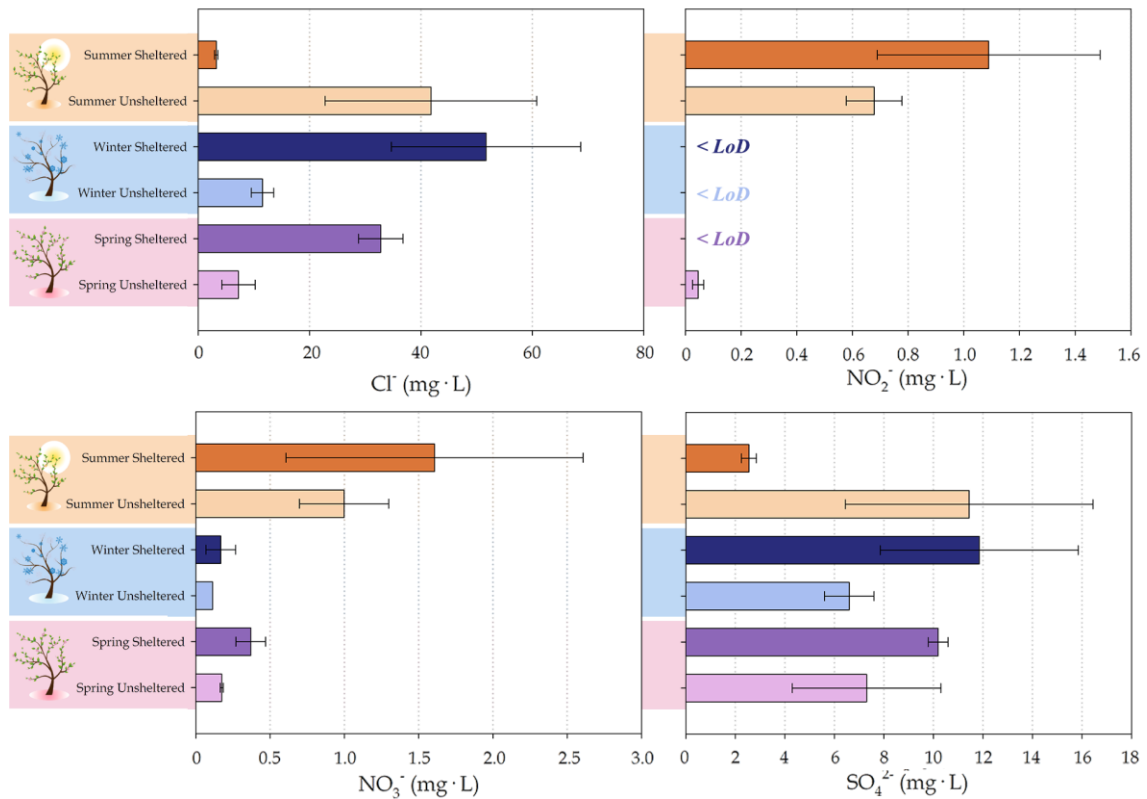
Figure 6.14: Concentrations (in mg · L) of Cl⁻, NO_2^-, NO_3^- and SO_4^{2-} found in the samples after the boiling procedure.

As regard the amount of NO_2^-, it can be detected only in summer samples, with a higher percentage in sheltered samples than unsheltered ones, and in samples exposed in unsheltered condition in spring. Finally, NO_3^- shows a concentration up to three times greater in summer samples and during all the campaign it can be noticed a common trend in which samples exposed in sheltered condition show a higher amount of nitrates than those exposed in unsheltered way. A combined effect of ions deposition and precipitation can take into account also to explain the trend observed for anionic species. Specifically, regarding the campaigns started in winter and spring, the highest peak of NO_3^- (37.8 µg · cm^{-2}, in respect to the monthly average value of 11.5 and 8.8 µg · cm^{-2}, for winter and spring respectively) was registered during the wettest month ('Sep16' – 'Dec 16'). On the contrary, concerning the campaign started in summer, the highest peak (22.7 µg · cm^{-2} in respect to the monthly average value of 8.7 µg · cm^{-2}) was registered during 'Feb16' and 'Mar16', when the rainfalls were almost absent.

Another interesting result is the acceptable correlation between the trend related to Na^+ and Cl⁻ (**Figure 6.15**), species that constitute predominant salt species in marine environment.
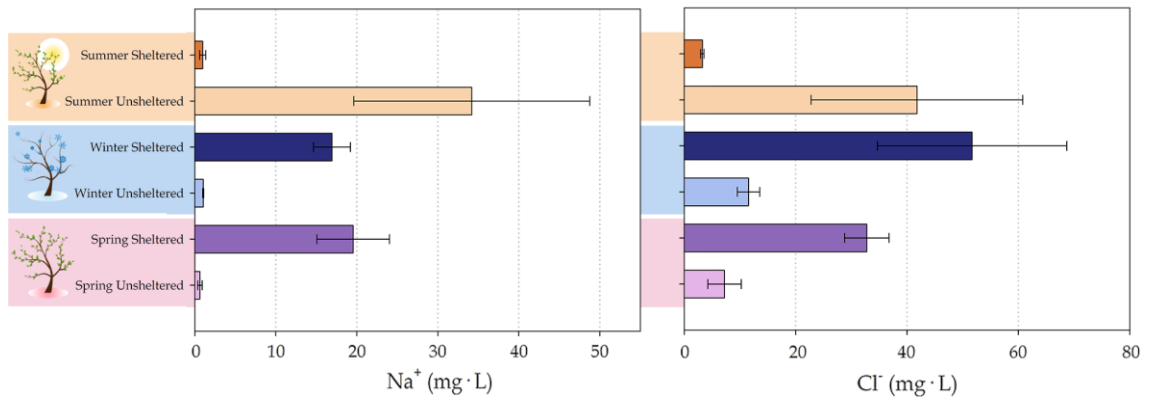
**Figure 6.15**: Comparison between the concentrations (in mg · L) of Na$^+$ and Cl$^-$ found in the samples after the boiling procedure.

6.1.4 Mass loss determination

In order to evaluate the corrosivity of the exposure conditions, mass loss determination was performed for all the samples after boiling (except one specimen for each campaign and geometry of exposure that was saved to perform surface analysis). **Figure 6.16** reports the results of mass loss determination for all the replicates considered, while in **Figure 6.17** the mean value of mass loss calculated for each campaign performed and for each geometry of exposure considered are reported. According to the equation 5.7, these values can also be directly related to corrosion rates considering that each sample was exposed for one year.
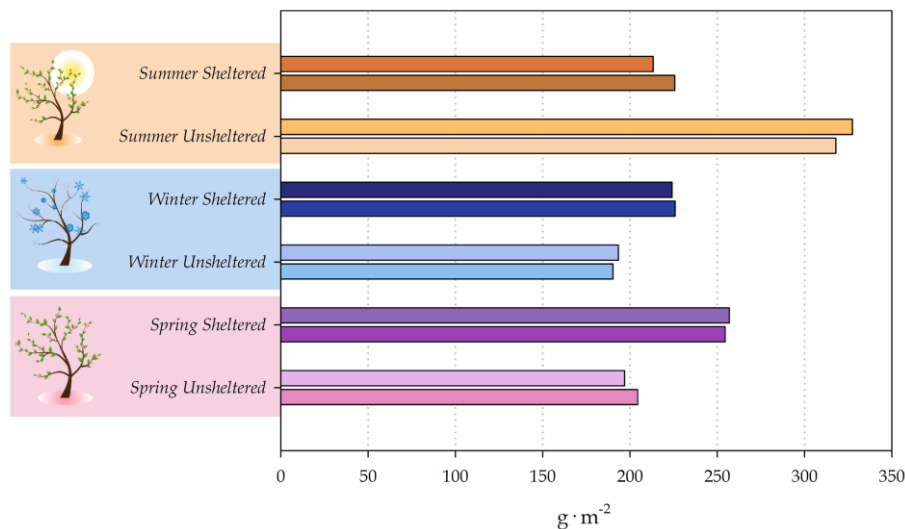
Figure 6.16: Mass loss of WS (g · m^{-2}) exposed in sheltered and unsheltered condition at different start time of natural exposure in Rimini.
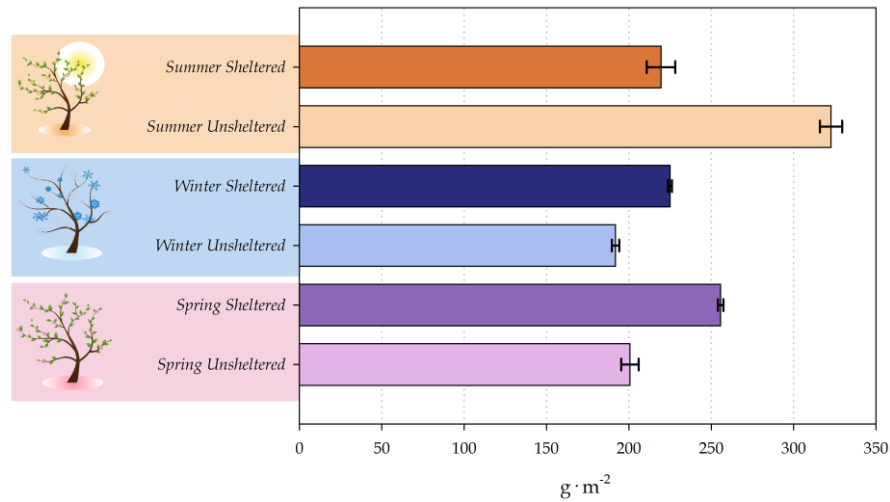
Figure 6.17: Mean values of mass loss of WS (g · m^{-2}) exposed in sheltered and unsheltered condition at different start time of natural exposure in Rimini.

All the corrosion rates determined can be categorized as a C3 atmospheric corrosivity level, according to **Table 2.4**, except for samples exposed in winter in unsheltered condition that show C2 level. The results achieved are also comparable to those determined by Ocaña [176] testing several types of WS simulating different atmosphere. According to what stated by Ocaña, the corrosion rates determined for samples that started their exposure during winter and spring are comparable to the effect of a mild marine atmosphere, while, for samples belonging to the campaign started in summer, the corrosion rates are more similar to those induced by a more aggressive marine atmosphere. The results obtained are also in agreement with the value determined by Morcillo et al. [114] related to a one-year filed study of mild steel, exposed in Cabo Villano, where the chloride deposition rate is comparable to that measured in Rimini.

The highest mass loss is observed in samples that have started their exposure during summer time in unsheltered condition. This latter result is in agreement with the results observed through XRD analysis and the PAI* index calculated. Also Kamimura et al. [108] observed the correlation between r_{corr} and PAI* index for weathering steel exposed in mild or quite aggressive atmospheres. Additionally, it may be supposed that the high r_{corr} determined for samples exposed in unsheltered condition during the campaign started in summer can be strictly related to the high content of ions extracted from the patina, especially for what concern the aggressive species of chlorides (section 6.1.3). Moreover, also the hypothesis that widespread precipitations registered during the first months of the exposure and a high TOW can have affected the patina stability of the unsheltered samples may be confirmed by the r_{corr} measured.

As expected, mass loss determined for samples belonging to the exposures started in winter and spring is higher in sheltered than in unsheltered condition, as well as the percentage of akaganeite found by XRD analysis (**Table 6.3 –6.4**). Considering apart campaigns started in winter and spring, no correlation between r_{corr} and PAI* index can be observed. A possible explanation may be that, due to the action of environmental agents, during the early stage of corrosion a quite stable layer was formed on the samples. Specifically, an alternation of the wet/dry cycles may have enhanced the transformation of lepidocrocite into goethite. This observation may be confirmed also by mass variation data (**Figure 6.4**). Actually, during the first months a greater increase of mass is measured in unsheltered more than in sheltered samples suggesting that the corrosion products formed may be the more dense allotropic form of iron oxyhydroxides (goethite and lepidocrocite). Subsequently, a tightening of environmental conditions and an increase in pollutants concentration, especially regarding the amount of chlorides, may have induced the formation of akaganeite on the stable patina previously formed, as confirmed also by the SEM observations of surfaces and cross sections, EDS and XRD analysis. Even if, the formation of akaganeite leads to a greater instability of the outer layers of the patina (as shown by low values of PAI* index), the stable inner layer previously formed can act as a protection of the uncorroded material leading to low r_{corr}.

Considering all the results achieved in this section, a strong influence of environmental parameters on WS corrosion process is highlighted, especially during the first months of its natural exposure. Specifically, as shown for samples belonging to the exposure started in summer, a marked interaction between rainfalls (or more in general, specimens wet stage) and the deposition of aggressive species (especially chlorides) is observed and it induces an inversion of the behaviour between sheltered and unsheltered samples. Actually, a larger content of ions (especially Cl^- and Na^+) and higher values of r_{corr} are shown by unsheltered more than sheltered samples. Considering also the results obtained by XRD analysis and the PAI* index calculated, a possible explanation for the behaviour observed can be related to the formation during the early stage of corrosion of a more stable patina which protect the uncorroded material and leads to lower values of r_{corr}. Thus, these results highlight the strong influence of the period in which the material begins its exposure on its corrosion and thus, in order to prevent and reduce materials decay, a deeper evaluation of the environmental features of the site of exposure is required.

6.2 Accelerated ageing tests

To achieve a better understanding of the weathering steel corrosion mechanism and specifically to investigate the effect of the main aggressive anions of particulate matter, accelerated ageing tests were performed, as described in section 5.3.

6.2.1 Colour measurements

Figure 6.18 compares bare samples of weathering steel (2.5 x 2.5 cm) before starting the test and samples collected after 14 days of accelerated ageing test.

a)   b)

Figure 6.18: a) Bare sample of weathering steel before starting the test. b) Weathering steel samples collected after 14 days of accelerated ageing test.

As described in section 5.4.3, spectrophotometric colour measurements were carried out to provide information about the growth of the patina also in samples aged by means of laboratory tests. In **Table 6.6** are reported the colour results achieved.

Table 6.6: Colour coordinates in CIE $L^*a^*b^*$ and CIE L*C*h colour scale and colour variations (ΔE) of specimens accelerating aged.

Samples	L*	a*	b*	C*	h*	ΔE
Bare Cor-Ten A	50.1	0.3	1.8	1.8	79.5	
Chl1_Nit1_Sul1	42.4	17.3	29.0	33.8	59.3	33.0
Chl1_Nit1_Sul3	48.0	16.1	26.1	30.7	58.4	29.2
Chl1_Nit3_Sul1	46.3	17.2	26.8	31.9	57.3	30.5
Chl1_Nit3_Sul3	47.4	15.9	25.4	30.0	58.1	28.5
Chl3_Nit1_Sul1	48.0	16.5	28.6	33.1	60.0	31.5
Chl3_Nit1_Sul3	48.9	15.7	25.8	30.2	58.6	28.7
Chl3_Nit3_Sul1	49.4	16.1	25.9	30.5	58.2	28.8
Chl3_Nit3_Sul3	44.6	16.6	28.1	32.6	59.6	31.5
Chl2_Nit2_Sul2	44.8	16.9	28.5	33.2	58.7	32.1
Chl2_Nit2_Sul2	45.8	16.2	26.5	31.1	59.6	29.8

Table 6.6 shows that the growth of patina on the aged samples is related to an increase of the red (a^*) and yellow (b^*) component while a more or less marked decrease in the L^* - Lightness can also be identified.

Additionally, colour measurement results have been processed through Principal Component Analysis. In **Figure 6.19** is reported the *biplot* achieved processing all replicates acquired as training set and considering L^*, a^* and b^* as variables. Data were centered but not scaled and a full cross validation was applied. PCA model obtained shows 91% as explained variance on the first component and 8% on the second component.
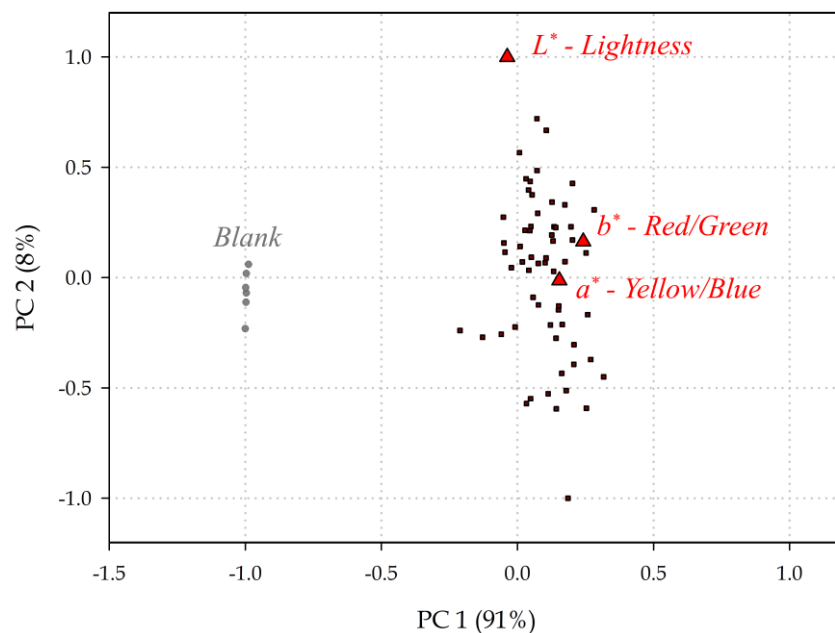
Figure 6.19: Biplot of the PCA model achieved processing colour data.

In **Figure 6.19** black squares represent the replicates of aged samples, while grey circles are the values acquired for unaged sample (blank) and the red triangles stand for the variables. Basically, there is a clear distinction from aged and unaged samples of WS but any cluster can be clearly identified among the samples.

6.2.2 Characterization of corrosion products

6.2.2.1 Mass variation

Preliminary information about the patina formed can be provided by the observations of mass variation (MV) values (mg · cm^{-2}). In **Table 6.7** are reported the mass values measured at the beginning and at the end of the test and mass variation is also calculated. Generally, **Table 6.7** shows how mass variation is strongly influenced by the presence of chlorides and sulphates. Even if MV can be considered only as indicating a phenomenon and for weathering steel MV can be affected by several reason of variability, a positive increasing of MV suggests the formation of corrosion products on the sample surfaces. Thus, MV data reported in **Table 6.7** indicates chlorides and sulphates as the most aggressive species towards weathering steel. This result is in agreement with a previous study performed on weathering steel to investigate the effect of pure solutions of chlorides, nitrates and sulphates [177]. Nevertheless, consider also the combined effect of these species in solution is an innovative perspective of this work and an additional consideration can be achieved regarding the interaction between nitrates and chlorides/sulphates. Actually, the presence of high concentrations (in ppm) of nitrates seems not to induce an increasing in the mass variation of the sample (see, for instance, MV of sample *Chl1_Nit3_Sul1*) and above all nitrates also seems to reduce the aggressive action of the other anions, as shown by the MV reported for *Chl3_Nit3_Sul1* or *Chl1_Nit3_Sul3*

Table 6.7: Values of mass at the beginning and at the end of the test and mass variation.

	Chl3_Nit3_Sul1	Chl1_Nit3_Sul1	Chl1_Nit3_Sul3	Chl1_Nit1_Sul3	Chl3_Nit1_Sul3
Initial mass (g)	6.7279	6.3960	6.9735	7.0994	6.5479
Final mass (g)	6.7486	6.4086	6.9977	7.1373	6.5780
Δ (mg·cm^{-2})	1.74	1.12	1.97	3.02	2.58

	Chl1_Nit1_Sul1	Chl3_Nit1_Sul1	Chl3_Nit3_Sul3	Chl2_Nit2_Sul2	Chl2_Nit2_Sul2
Initial mass (g)	6.9532	6.5366	6.8058	6.4415	6.4769
Final mass (g)	6.9680	6.5626	6.8495	6.4705	6.5066
Δ (mg·cm^{-2})	1.35	2.48	3.84	2.72	2.60

6.2.2.2   pH monitoring

The pH of each weathering solution was monitored every day (**Figure 6.20**).
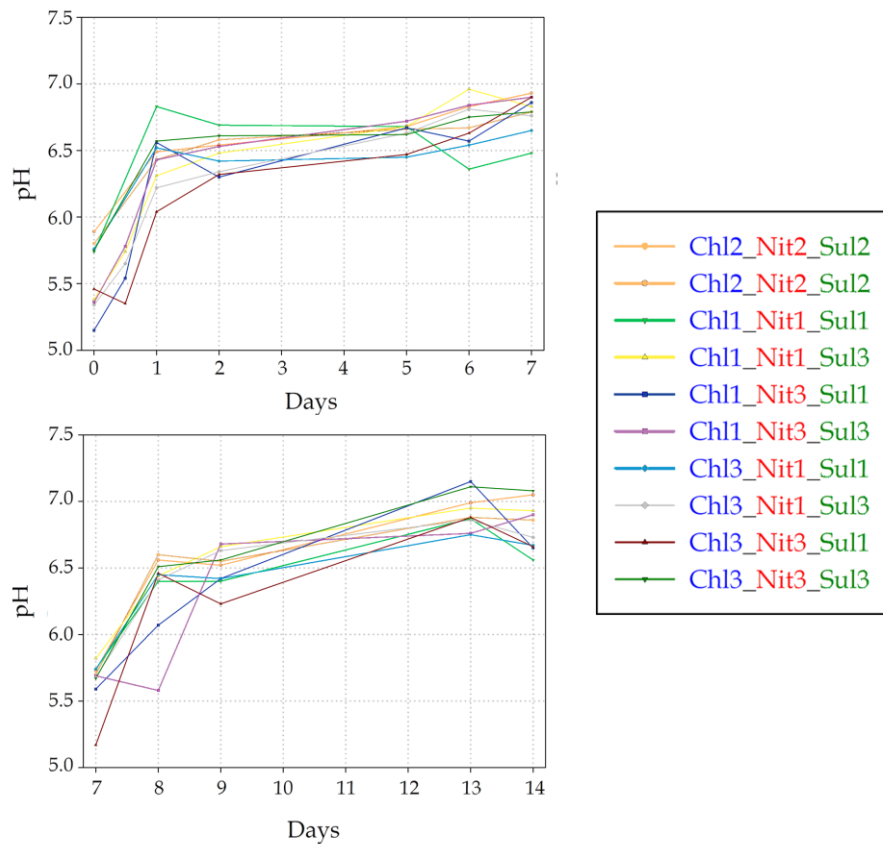
Figure 6.20: pH monitored for each weathering solution, which was renovated with fresh solution at 7 days.

To summarize, in **Table 6.8** are reported the initial value of pH of each weathering solutions and the value measured at the end of the test.

Table 6.8:   Values of pH of each weathering solutions measures at the begin and at the end of the test.

		Chl3_Nit3_Sul1	Chl1_Nit3_Sul1	Chl1_Nit3_Sul3	Chl1_Nit1_Sul3	Chl3_Nit1_Sul3
First week	Initial pH	5.46	5.15	5.36	5.38	5.34
	Final pH	6.90	6.86	6.90	6.83	6.76
	$\Delta_{1st\ week}$	1.44	1.71	1.54	1.45	1.42
Second week	Initial pH	5.17	5.59	5.69	5.82	5.68
	Final pH	6.66	6.65	6.90	6.93	6.73
	$\Delta_{1st\ week}$	1.49	1.06	1.21	1.11	1.05

		Chl1_Nit1_Sul1	Chl3_Nit1_Sul1	Chl3_Nit3_Sul3	Chl2_Nit2_Sul2	Chl2_Nit2_Sul2
First week	Initial pH	5.74	5.76	5.75	5.80	5.89
	Final pH	6.48	6.65	6.79	6.79	6.93
	$\Delta_{1st\ week}$	0.74	0.89	1.04	0.99	1.04
Second week	Initial pH	5.74	5.74	5.67	5.7	5.73
	Final pH	6.56	6.67	7.08	6.86	7.05
	$\Delta_{1st\ week}$	0.82	0.93	1.41	1.16	1.32

There is no huge difference or significant trends in pH variation among samples and between values measured after the first and the second week of the test. pH variation is always ranging between 0.74 and 1.71 pH units. It must be noticed, anyway, that reasonably the lowest values of pH variation measured (0.74 and 0.82) correspond to the least aggressive solution *Chl1_Nit1_Sul1* after the first and the second week of the test. Generally, the only trend that can be pointed out is related to solutions that contain the highest concentration of sulphates. Actually, for samples *Chl1_Nit3_Sul3*, *Chl1_Nit1_Sul3* and *Chl3_Nit1_Sul3*, the pH variation decreases between the first and the second week considered. This observation may suggest a faster aggressive action induced by sulphates and that leads to the rapid formation of corrosion products, in agreement with Raffo [177], which observed that the corrosive attack of sulphate solutions shows the highest kinetic.

6.2.2.3   Surface analysis

To achieve a complete characterization of patinas formed on WS samples during the test, XRD (see section 5.4.5) and SEM-EDS (see section 5.4.4) analysis were performed.

Table 6.9 shows the quantitative estimation of crystalline phases formed on WS during the accelerated ageing and determined through XRD analysis. Moreover, α/γ protective ability index (PAI) has been calculated as defined by the literature [108] as the mass ratio of the goethite to lepidocrocite amount. α/γ index can be considered to evaluate the protective ability of the rust layer as a patina stabilisation index.

Table 6.9: Summarized XRD results for aged WS samples.

	Lepidocrocite (γ-FeOOH)	Goethite (α-FeOOH)	Ferrihydrite ($Fe_5HO_8 \cdot 4H_2O$)	α / γ
Chl3_Nit3_Sul1	75.8%	6.4%	17.9%	0.08
Chl1_Nit3_Sul1	68.8%	6.3%	24.9%	0.09
Chl1_Nit3_Sul3	75.4%	9.8%	14.8%	0.13
Chl1_Nit1_Sul3	79.2%	13.8%	8.1%	0.17
Chl3_Nit1_Sul3	84.4%	6.7%	8.9%	0.08
Chl3_Nit1_Sul1	78.9%	11.4%	9.7%	0.14
Chl3_Nit3_Sul3	72.2%	19.0%	3.9%	0.26
Chl1_Nit1_Sul1	56.8%	12.6%	30.7%	0.22
Chl2_Nit2_Sul2	70.0%	15.2%	14.8%	0.22

Lepidocrocite (γ-FeOOH) and goethite (α-FeOOH) are always present on the surfaces of the specimens and furthermore lepidocrocite is present in all the samples in higher percentage with respect to other compounds, as also observed by SEM microscopic observations (**Figure 6.21**).
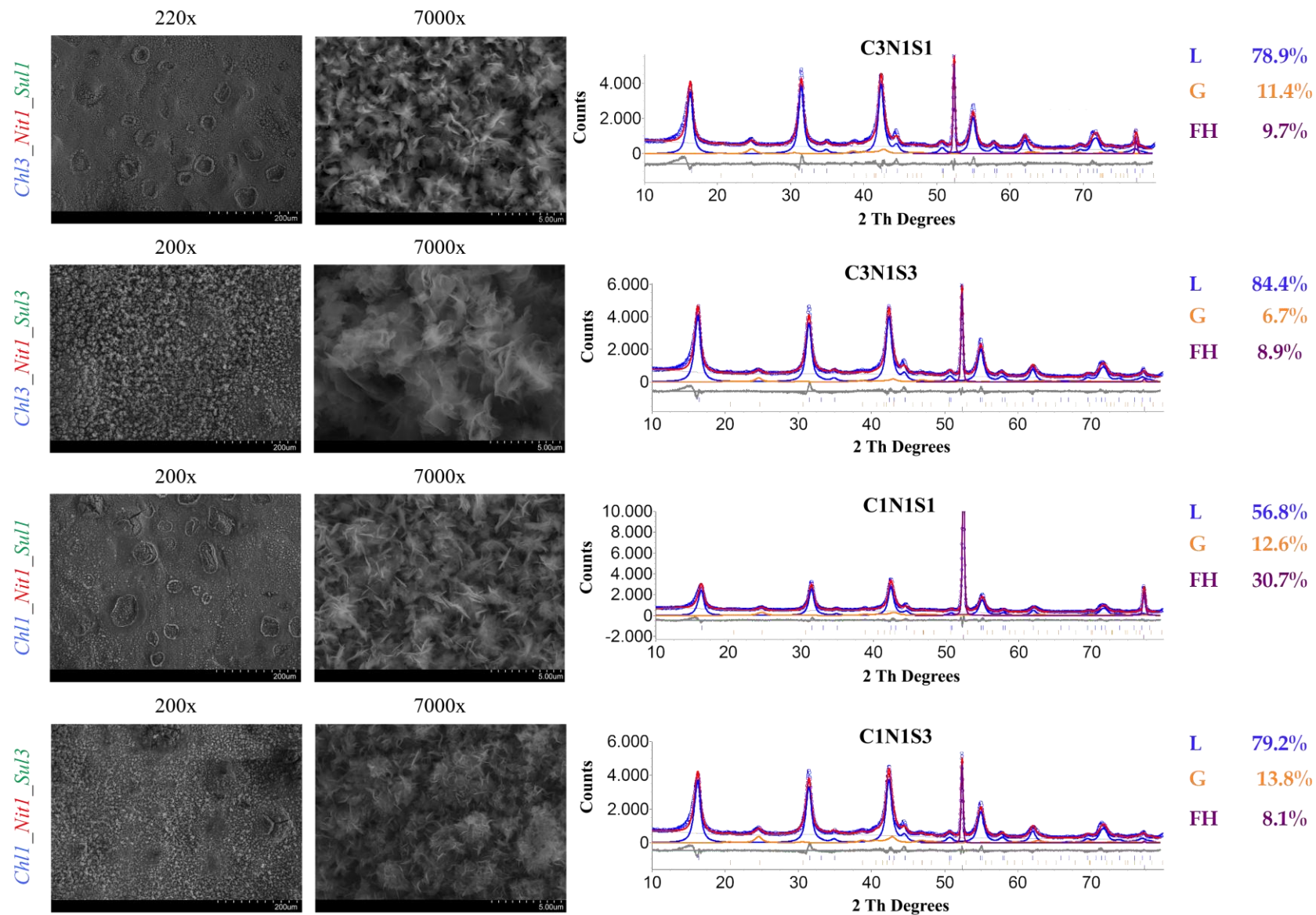
Additionally, another interesting result about the characterization of the patina comes from the observations of the percentages of ferrihydryte (FH) determined by XRD analysis. These data can be related to the thickness of the patina formed: a thin rust layer should be formed on samples, which shows large percentages of FH. Thus, it can be observed that the presence of a high content of nitrates generally leads to a thin patina. Combining this result with the PAI index calculated, it can also be affirmed that the increase in nitrates concentration also leads to the formation of an unstable patina (the lowest values of PAI index calculated are 0.08 and 0.09 related to *Chl3_Nit3_Sul1* and *Chl1_Nit3_Sul1*, respectively). Conversely, patinas with a greater thickness are obtained by ageing WS samples with solutions containing a large amount of sulphates, followed by the presence of chlorides. This latter consideration is confirmed by the mass variations measured (see section 6.2.2.1) and by Raffo [177], which suggests the following order of aggressiveness among Cl^-, NO_3^- and SO_4^{2-}:
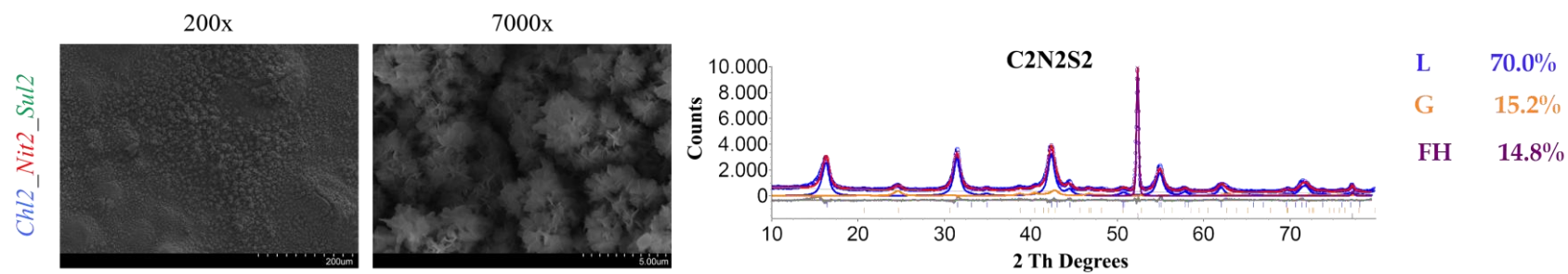
$$NO_3^- \quad < \quad Cl^- \quad < \quad SO_4^{2-}$$

Reasonably, the thickest patina formed is observed for sample *Chl3_Nit3_Sul3*, where the highest PAI value (0.26) is found. Actually, observing also the values obtained for *Chl2_Nit2_Sul2* and *Chl1_Nit1_Sul1*, patina protective ability index (PAI, α/γ) suggests that the amount of goethite, thus the stability of the patina, tends to increase for samples aged through solutions that contained the same proportion (in ppm) of Cl^-, NO_3^- and sulphates SO_4^{2-}. Moreover, according to Raffo [177], the PAI index determined for *Chl1_Nit3_Sul3* and especially for *Chl1_Nit1_Sul3* confirms the beneficial action of S-containing compounds towards passivation of corrosion layers. This effect is reduced by the presence of increasing concentration of nitrates.

C3N1S1

L	78.9%
G	11.4%
FH	9.7%

C3N1S3

L	84.4%
G	6.7%
FH	8.9%

C1N1S1

L	56.8%
G	12.6%
FH	30.7%

C1N1S3

L	79.2%
G	13.8%
FH	8.1%
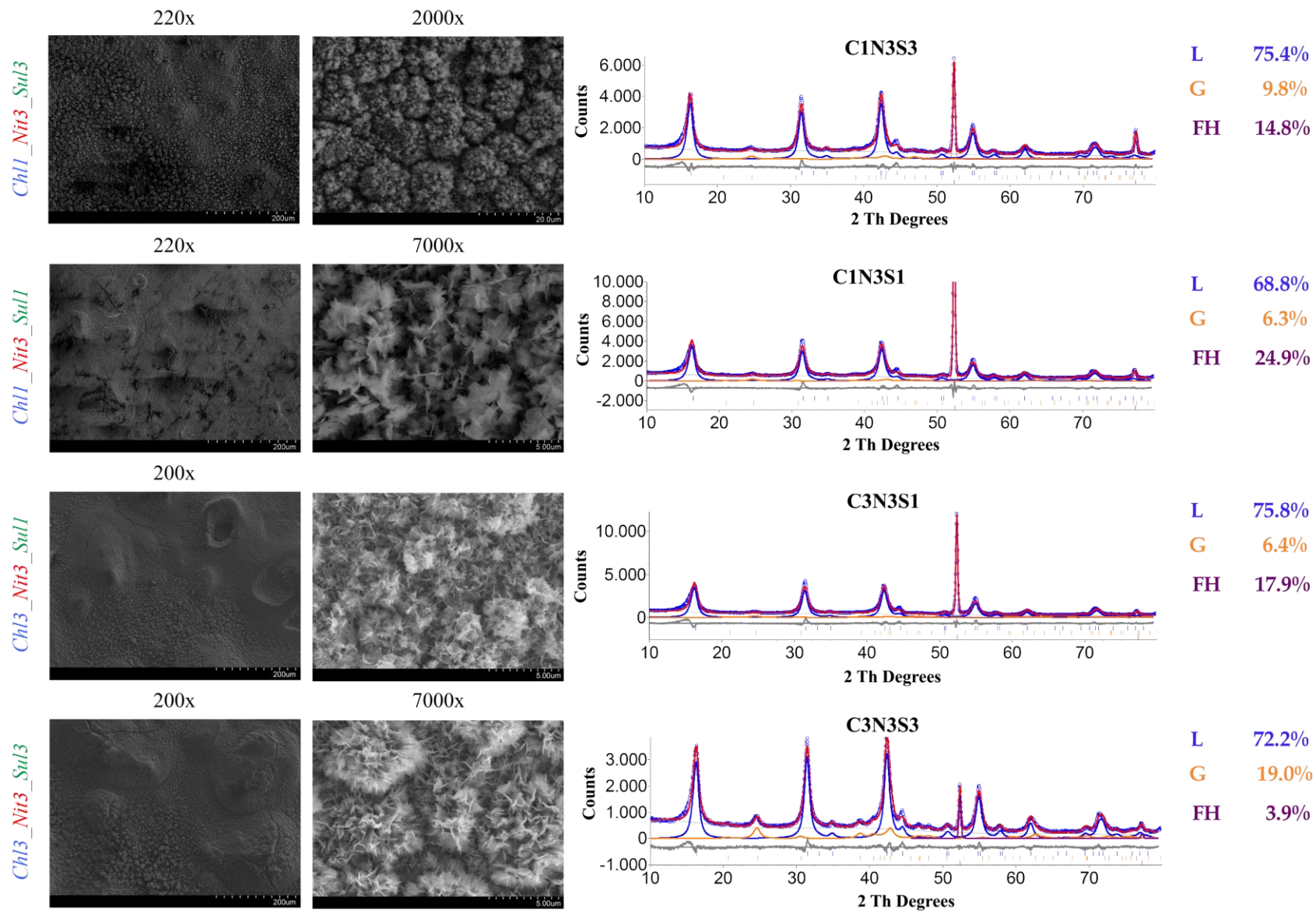
Figure 6.21: SEM images acquired at 200-220x and 7000-8000x and XRD spectra of each accelerating aged sample.
L stands for 'lepidocrocite', G for 'goethite' and FH for 'ferrihidrite'.

XRD results have been supported by the observations through SEM analysis as shown in **Figure 6.21**. In fact, all samples present, as main morphology, the laminar morphology described as "*flower petal shape*" that is characterized by flowery crystals of lepidocrocite. In some cases, the petals (laminas) can appear as plate thin laminas but they can also appear as hexagonal laminas with rounded edges.

Furthermore, some toroidal formations (rings of lepidocrocite) have been sporadically observed on the surfaces of some samples and generally these formations contain another type of morphology indicated as "*feather shape*" (**Figure 6.22**), which is very similar to the "*flower petal shape*" morphology but its corresponding Raman spectrum, as reported in previous works [166], shows some peaks attributable to lepidocrocite phase and also a shoulder peak typical of the goethite phase.


a) 20.0um **b)** 100um
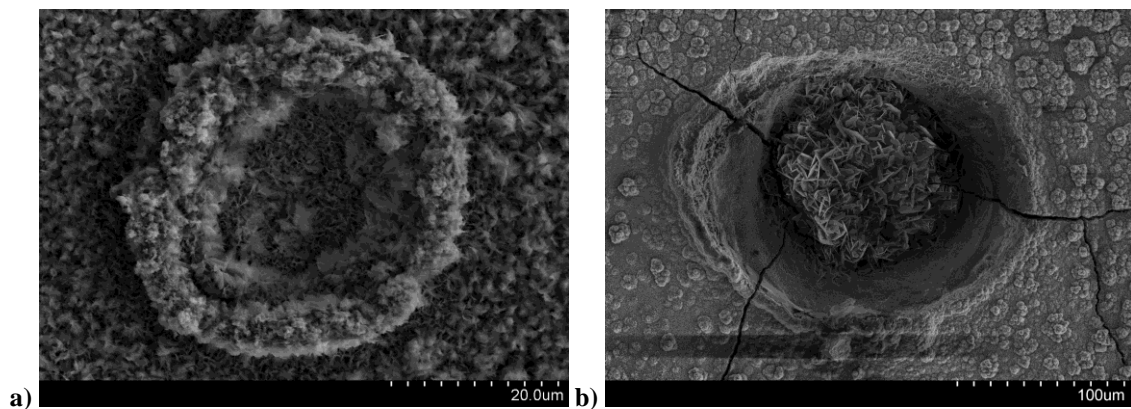
Figure 6.22: a) SEM image of a toroidal formation containing *feather shape* morphology. b) SEM image of *feather shape* morphology.

Although in different concentrations, Cl⁻ was contained in each weathering solution used to age the samples and a noteworthy fact is that the typical corrosion product formed on steel exposed to chlorine-rich environments – akaganeite [114] is not detected by both XRD and SEM analysis. The absence of β-FeOOH could be attributed to the low concentration of Cl⁻. Actually, Dunn et al. [178] stated that the formation of β-FeOOH does not occur until after 20 or more wet and dry cycles and was observed only in the increasing Cl⁻ concentration test. Refait et al. [179] suggest 2-4 mol/L, corresponding to 56-113 mg/L, as minimum concentration to observe the formation of β-FeOOH. Furthermore, the accommodation of Cl⁻ inside the crystal structure of akaganeite requires low pH. When the pH becomes slight alkaline, the hydroxide ions compete with Cl⁻ ions to occupy the crystal structural sites [180]. Thus, in agreement to Dunn et al. [178],

considering that all the weathering solution used in this test range from 5.15 to 5.89, it could be a too high pH to encourage the formation of akaganeite.

6.2.3 Metal release in solution

In order to evaluate the effect of the different weathering solutions tested containing different aggressive species in different proportion, metal analysis were performed on total (TF) and dissolved (DF) fractions (see section 5.3.4.1) collected at the middle (7 days) and at the end of the test (14 days). Releases of Cr, Cu, Fe, Mn and Ni at 7 and 14 days measured in TF and DF are shown in **Figure 6.23 – 6.27** while the cumulative releases of Cr, Cu, Fe, Mn are shown in **Figure 6.28 – 6.32**. Particulate fraction (PF) is estimated by making the difference between the TF and the DF.
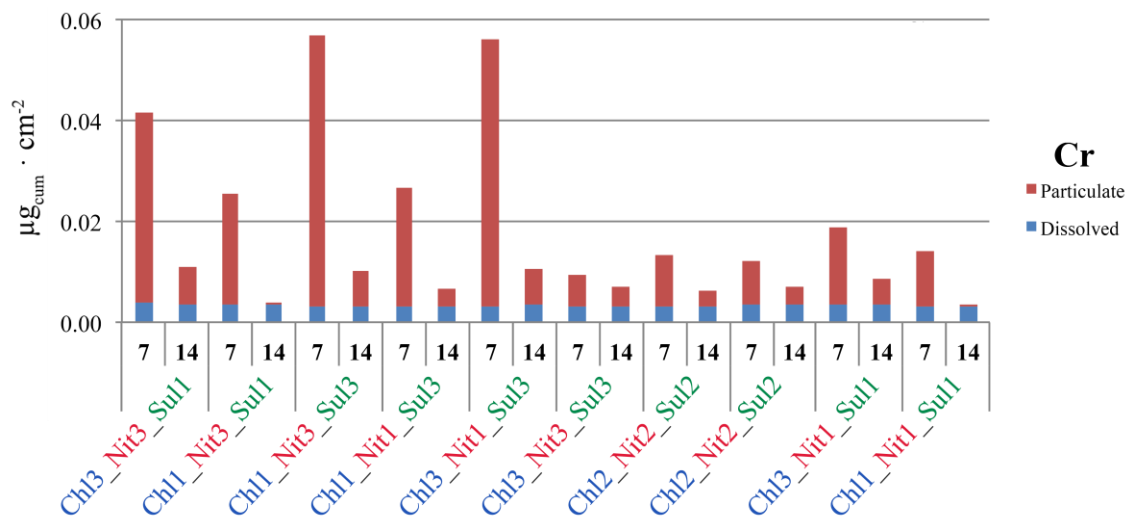
Figure 6.23: Dissolved (blue) and particulate (red) fraction of Cr released by WS aged in the different weathering solutions.

Figure 6.23 shows that the total release of Cr occurs mostly during the first week of the test. This effect is slightly more pronounced in ageing solutions where the concentrations of nitrates or sulphates are high. Conversely, as shown by the trend release of sample *Chl3_Nit3_Sul3* and the two replicates of *Chl2_Nit2_Sul2*, a competitive effect of chlorides may be observed and the total release is globally reduced and more equally distributed between the first and the second week of test.
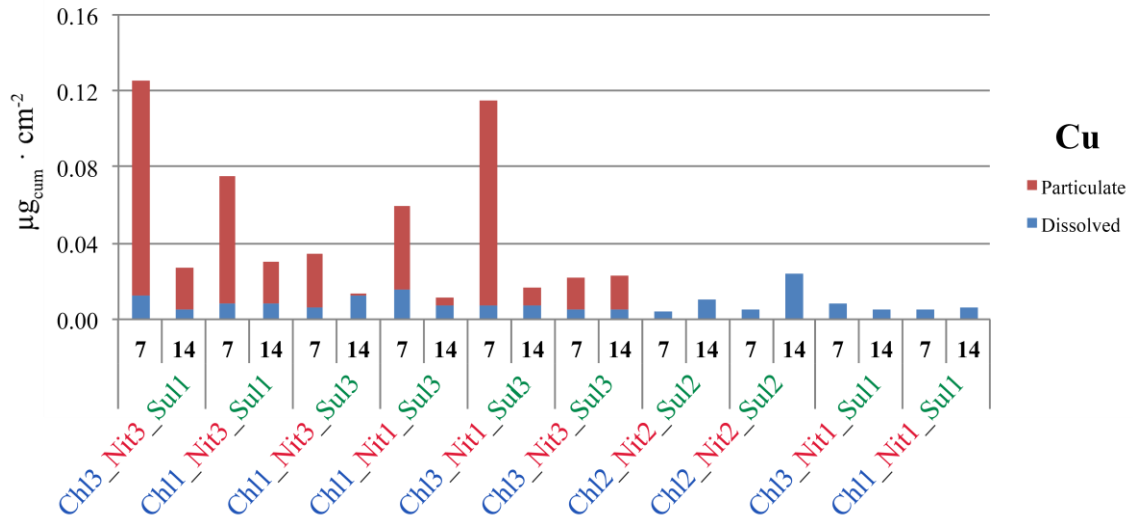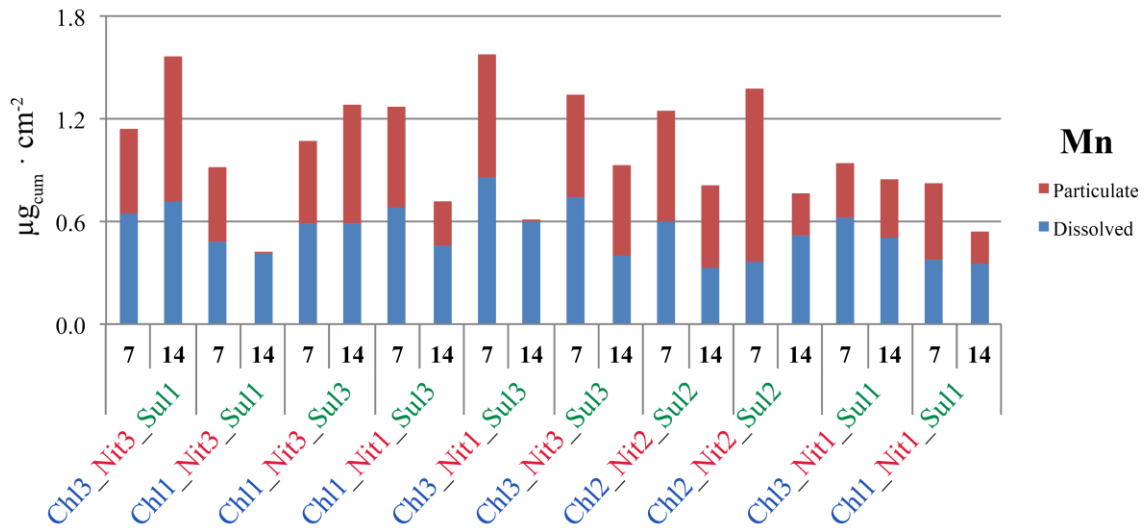
Figure 6.24: Dissolved (blue) and particulate (red) fraction of Cu released by WS aged in the different weathering solutions.

Copper, as shown in **Figure 6.24**, is also mostly released during the first week of the ageing, except for the samples aged in solutions with a low concentration of sulphates and/or nitrates and for solutions that contain the anions in the same proportion.

As reported in **Figure 6.25**, the total release of Fe shows almost the same trend for all the samples and it is mostly released during the first week. This effect is less pronounced for solution that contains a high concentration of chlorides.
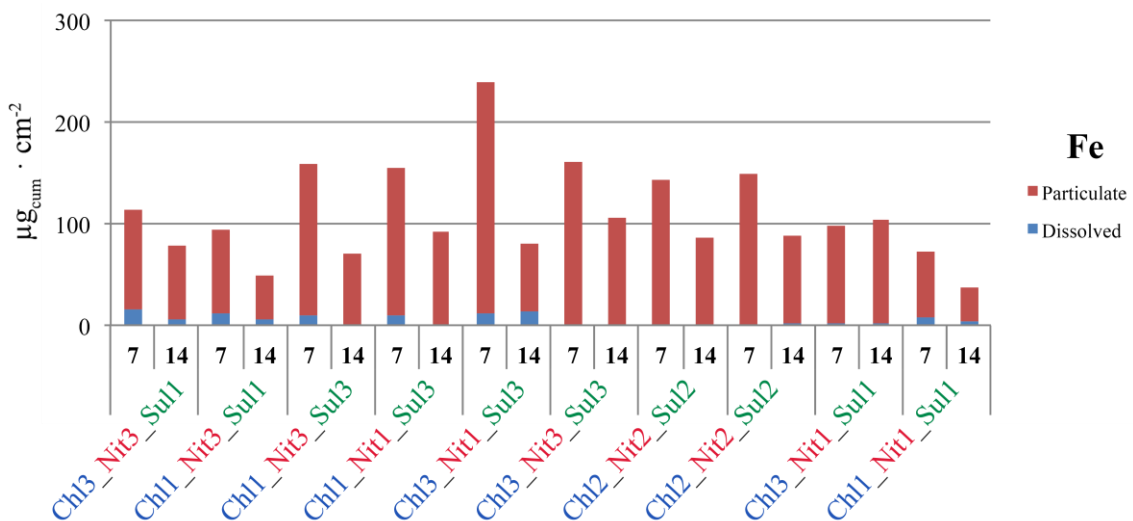
Figure 6.25: Dissolved (blue) and particulate (red) fraction of Fe released by WS aged in the different weathering solutions.
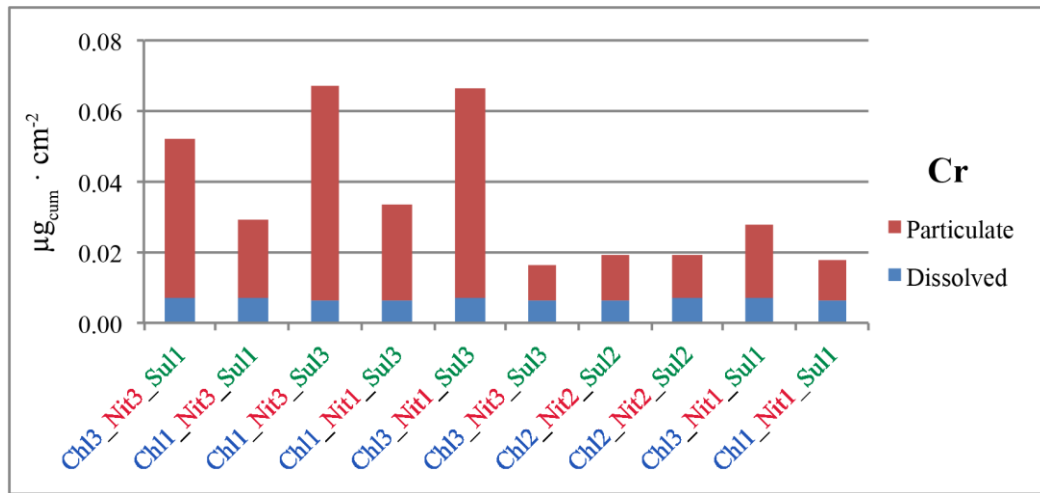
Figure 6.26: Dissolved (blue) and particulate (red) fraction of Mn released by WS aged in the different weathering solutions.
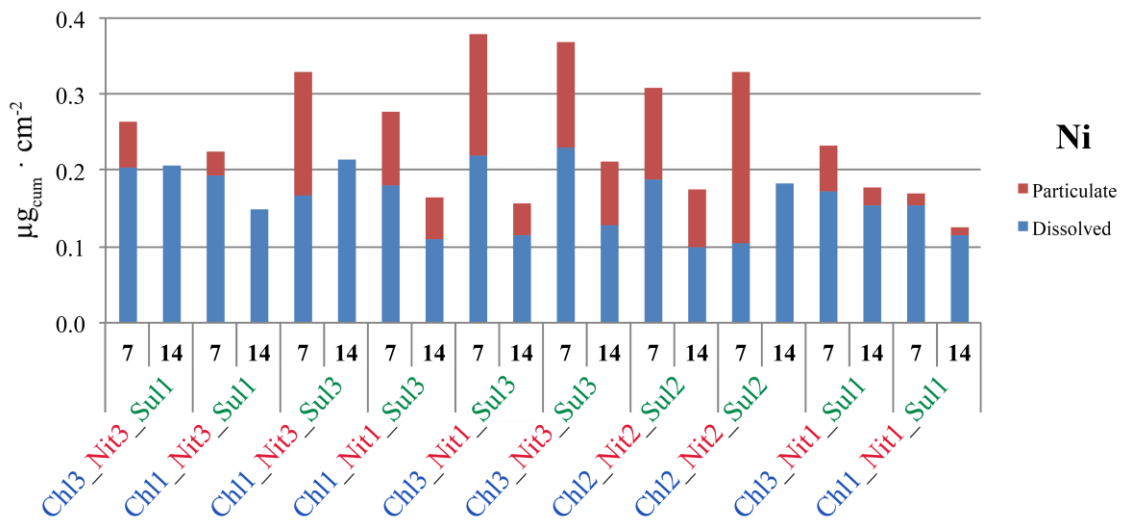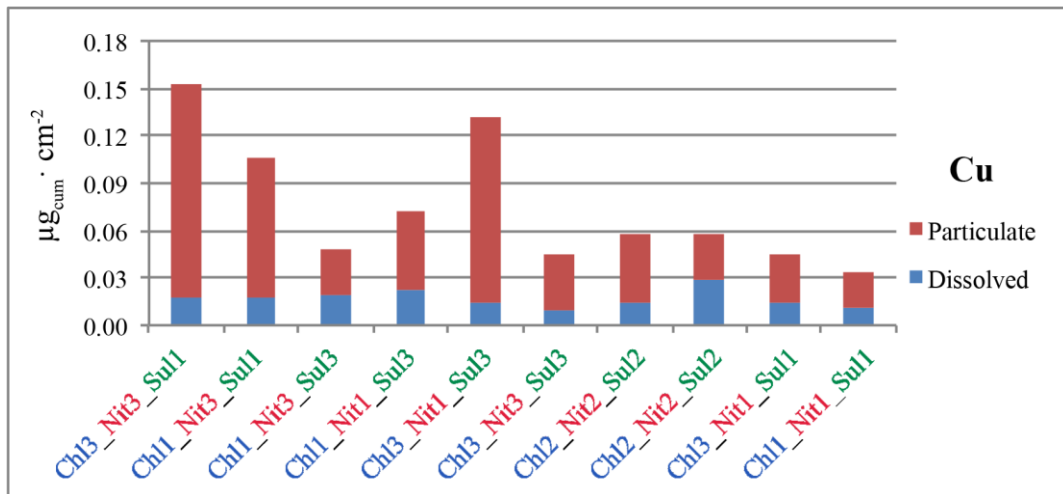

Figure 6.27: Dissolved (blue) and particulate (red) fraction of Ni released by WS aged in the different weathering solutions.

While Ni total release is always released in large quantity during the first week, Mn does not exhibit the same trend for all the solutions tested. Nevertheless, no significant correlation between the composition of the solution can be observed and related to the preference to release in DF or PF.

Figure 6.28: Dissolved (blue) and particulate (red) fraction of Cr released by WS aged in the different weathering solutions.
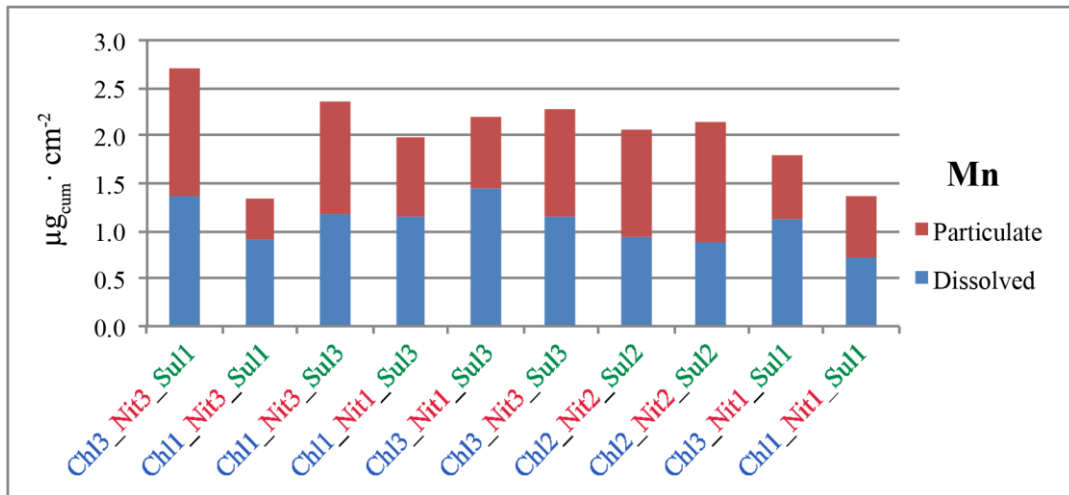

Figure 6.29: Dissolved (blue) and particulate (red) fraction of Cu released by WS aged in the different weathering solutions.
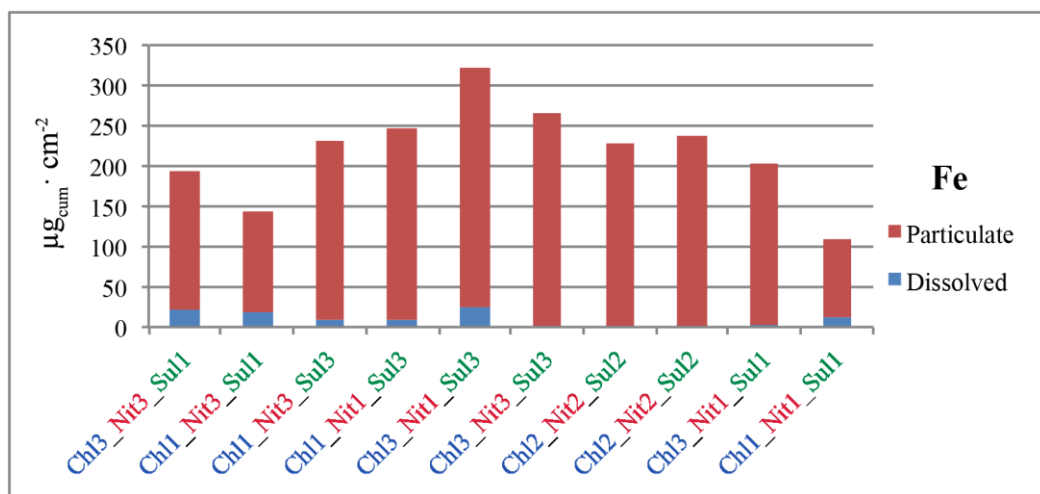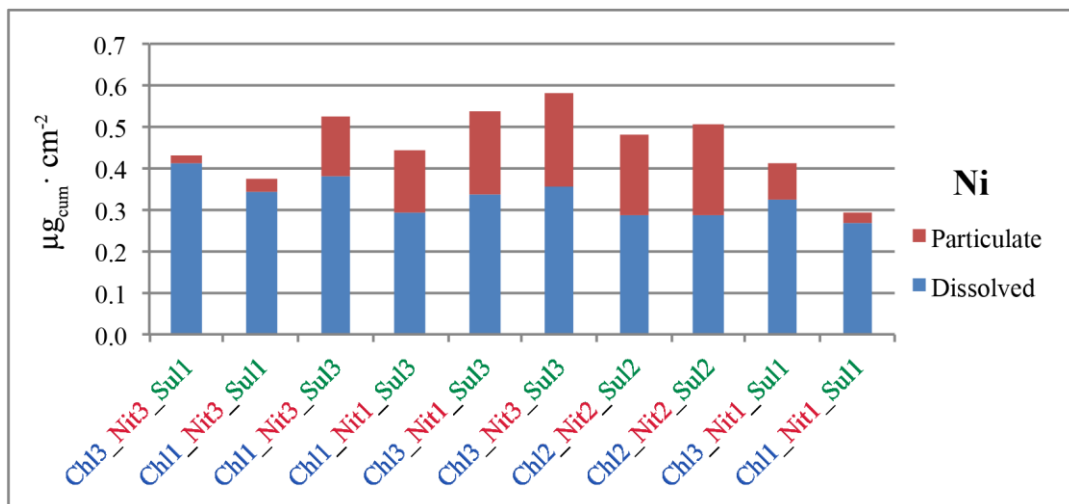

Figure 6.30: Dissolved (blue) and particulate (red) fraction of Fe released by WS aged in the different weathering solutions.

Figure 6.31: Dissolved (blue) and particulate (red) fraction of Mn released by WS aged in the different weathering solutions.

Figure 6.32: Dissolved (blue) and particulate (red) fraction of Ni released by WS aged in the different weathering solutions.

As expected from the alloy composition of WS (see section 5.1), iron is the most released metal and specifically, in all the samples, it is most released in particulate form. Iron release, appears strongly dependent on the concentration of chloride especially in the particulate fraction (PF). Otherwise a significant competitive effect of nitrates can be noticed especially towards sulphates, as observed comparing iron release of *Chl3_Nit1_Sul3*, which is greater than the release of *Chl3_Nit3_Sul3*. Another interesting result can be observed by looking to the almost absent iron release in DF of samples *Chl2_Nit2_Sul2* and *Chl3_Nit3_Sul3*, which present Cl^-, NO_3^- and SO_4^{2-} in the same concentration. Conversely, this does not occur at lower concentration, as shown by samples *Chl1_Nit1_Sul1*.

Compared to iron release, manganese release is two orders smaller and it seems quite influenced and induced by the presence of both sulphates and chlorides. For what concern both manganese and nickel, in almost all the samples, their release is above all (44% ~ 67% for Mn and 56% ~ 92% for Ni) in the DF. Specifically, Ni and Mn release in PF is strictly related to sulphates: with increasing SO_4^{2-} concentration also the percentage of metal released in PF increase. Mn release of PF is slighter affected also by the presence of chlorides. Conversely, Ni release is also related to chlorides concentration but considering the release in TF, according to a previous study of the research group about the effect of pure solution of Cl^-, NO_3^- and SO_4^{2-} on WS corrosion [177].

Chromium release in the DF is almost the same for all the solutions and it is always < LoD, while some differences are noticeable in its release in PF, where it is strictly affected by a competitive effect between nitrates and sulphates. An interesting result about Cr release in TF is that it appears to decrease when the concentrations of Cl^-, NO_3^- and SO_4^{2-} in solution are in the same proportion, as already observed also for iron release in DF. This observation confirms that, in order to reduce and control metal release (especially of elements as Cr, which may present a high toxicity if present as Cr (VI) [180]), it is necessary to take into account not only the effect of high concentrations of single species but also their possible interaction. For instance, in this case, Cr release is higher in samples *Chl1_Nit3_Sul3* and *Chl3_Nit1_Sul3* more than in *Chl3_Nit3_Sul3*.

Copper release in PF is strongly negatively dependent on the simultaneous presence of both nitrates and sulphates, too. A strong competitive effect between these two ions can be clearly noticed by observing, for instance, the Cu release of *Chl3_Nit3_Sul1* and *Chl3_Nit1_Sul3* respect to *Chl3_Nit3_Sul3*, where the concentration of Cl^- is the same and the highest value considered (35 ppm) and only the concentration of NO_3^- and SO_4^{2-} is changing. While, Cu release in the DF is almost always close to the LoD thus its release in the TF follows the same trend of the release in PF.

All these observations can be confirmed through their multivariate processing as described in section 5.3.2 and shown in the DoE model obtained and reported in the next 6.2.5.2 paragraph.

6.2.4 Mass loss determination

Mass loss determination represents an effective way to determine the amount of corroded material, thus an efficient and valuable method to directly evaluate the corrosivity of the weathering solutions tested as well as the effect and interaction of aggressive anions. Mass loss determined for each sample collected (see section 5.4.8) is reported in **Table 6.10** and its trend is shown in **Figure 6.33**.
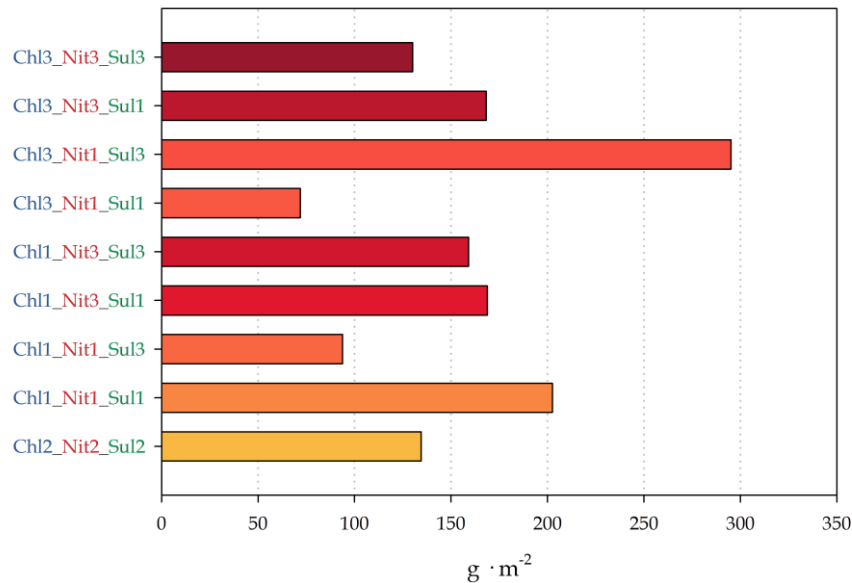
Figure 6.33: Mass loss (g · m^{-2}) of WS aged in the different weathering solutions.

Basically, the highest mass loss is observed for the sample *Chl3_Nit1_Sul3* aged in a weathering solution containing the highest concentrations considered (35 ppm) of Cl$^-$ and SO$_4$$^{2-}$ while the lowest concentration considered (1.5 ppm) of NO$_3$$^-$. Thus, first of all, by means of this observation, chlorides and sulphates are confirmed as the most aggressive species, as already observed discussing mass variation (see section 6.2.2.1) results and the release of Fe and Mn in PF (see section 6.2.3). The similar trend of aggressiveness is also in agreement with Raffo [177].

Additionally, the value of mass loss determined for samples *Chl1_Nit1_Sul1* and *Chl3_Nit3_Sul3* aged in solutions respectively with the lowest (1.5 ppm) and the highest (35 ppm) amount considered of anions confirms the competitive effect of nitrates towards chlorides and sulphates, which leads to reduce the aggressive action of Cl$^-$ and SO$_4$$^{2-}$. A competitive interaction between NO$_3$$^-$ and SO$_4$$^{2-}$ is also observed regarding the release of Fe and Cu in PF (see section 6.2.3).

Table 6.10: Mass loss (g · m^{-2} and µm) of WS samples accelerating aged.

	Mass Loss			*Mass Loss*	
	(g· m^{-2})	µm		(g· m^{-2})	µm
Chl1_Nit1_Sul1	203	25.81	Chl3_Nit1_Sul3	295	37.51
Chl1_Nit1_Sul3	94	11.95	Chl3_Nit3_Sul1	168	21.36
Chl1_Nit3_Sul1	169	21.49	Chl3_Nit3_Sul3	130	16.53
Chl1_Nit3_Sul3	159	20.22	Chl2_Nit2_Sul2	135	17.17
Chl3_Nit1_Sul1	72	9.14			

The mass losses determined are in the same order of magnitude of those determined in a previous study [176], where pure solutions of Cl$^-$, NO$_3^-$ and SO$_4^{2-}$ were evaluated by means of the accelerated ageing test CEBELCOR. Nevertheless, the noteworthy fact is that, even consider the most aggressive ageing solutions (where SO$_4^{2-}$ are present in the concentration of 25 ppm), the highest mass loss calculated by Raffo was ranging between 120 ~ 150 g · m^{-2} [177]. Thus, as expected, taking into account anions mixture as ageing solutions rather than pure solutions, a greater mass loss is generally registered, even up two times (considering the mass loss value obtained for *Chl3_Nit1_Sul3*). On the other hand, the presence of more species in solution can induce a competitive effect between them reducing their aggressive effect, as shown by sample *Chl3_Nit3_Sul3*.

Moreover, the results obtained for mass loss can be compared to those obtained by Ocaña [176] in a work where the corrosion of different types of WS was evaluated by CEBELCOR test and simulating several kinds of atmospheres. Specifically, the values determined in this study can be compared to the effect of an urban-industrial atmosphere (~ 20 µm) and a quite aggressive marine atmosphere (~ 30 µm).

6.2.5 DoE models

As mentioned before, all the parameters monitored during the test and quantified at the end of the test can be considered as response factor (*y*) in the multivariate quadratic model considered as Design of Experiment (equation 5.1). The multivariate approach is useful not only during the planning stage of the experiments but also to interpret the results and it allows to take in consideration also the interaction among the variables considered significant for the system in exam.
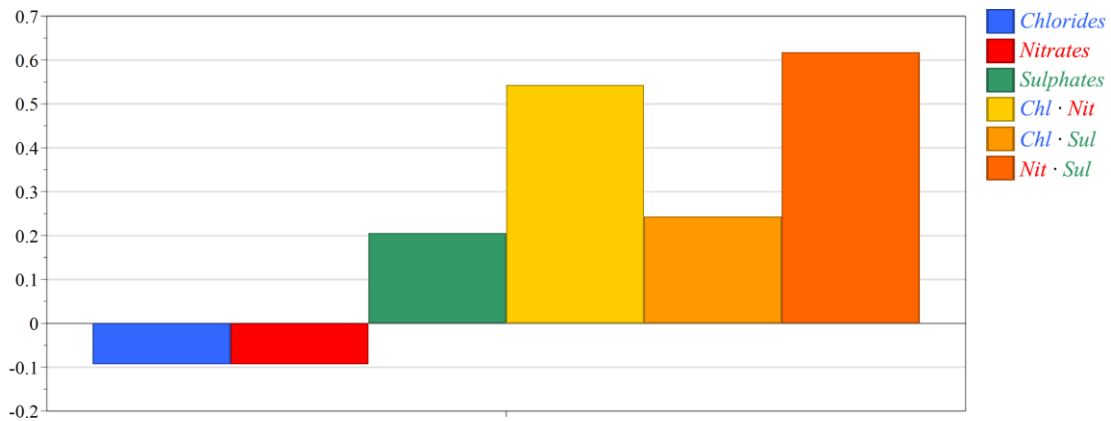
6.2.5.1   Response factor: α/γ

The first factor that was taken into account as response factor to build a multivariate model is the α/γ index calculated from the quantitative estimation of crystalline phases formed on WS during the accelerated ageing and determined through XRD analysis (section 6.2.2.3). The real coefficients calculated from the fitting are reported in **Table 6.11** while the scaled and centered coefficients are described in **Figure 6.34**.

Model was validated and it shows an R^2 of 0.910, which represent a high descriptive ability and a great robustness of the model achieved.

Table 6.11: Coefficients determined from the fitting considering the α/γ index as response factor.

| Patina Index			
Constant (b_0)	0.146		
Chlorides (b_{Cl^-})	-0.006	*Chl · Nit ($b_{Cl^-} \cdot b_{NO3^-}$)*	0.036
Nitrates (b_{NO3^-})	-0.006	*Chl · Sul ($b_{Cl^-} \cdot b_{SO4^=}$)*	0.016
Sulphates ($b_{SO4^=}$)	0.014	*Nit · Sul ($b_{NO3^-} \cdot b_{SO4^=}$)*	0.041

The σ of coefficient is 0.019, thus some coefficients (especially b_{Cl^-} and b_{NO3^-}) appears statistically not significant. Anyway, the statistical evaluation does not affect the meaning of the coefficients or their relationship.

Figure 6.34: Coefficients scaled and centered determined from the fitting considering the α/γ index as response factor.

Moreover, in order to easily visualize the response factor considered and to predict its value in the entire experimental domain, the fitted polynomial can be plotted (**Figure 6.35**a – c) to obtain a response surfaces for each couple of variables considered.
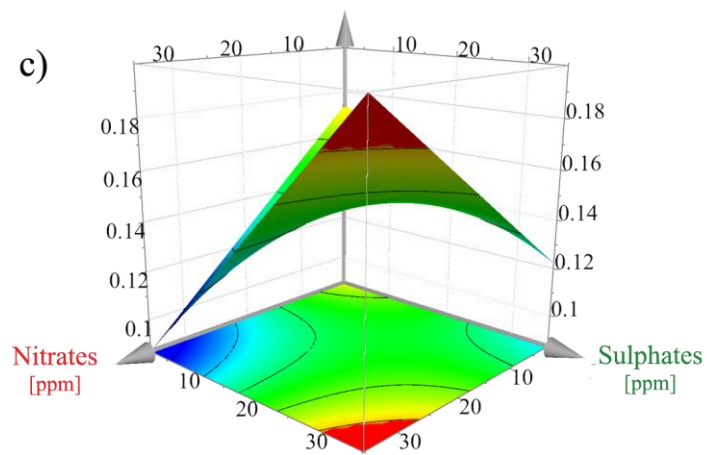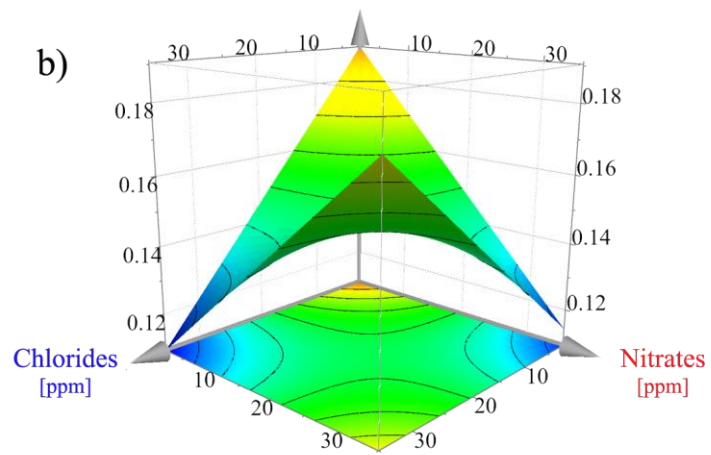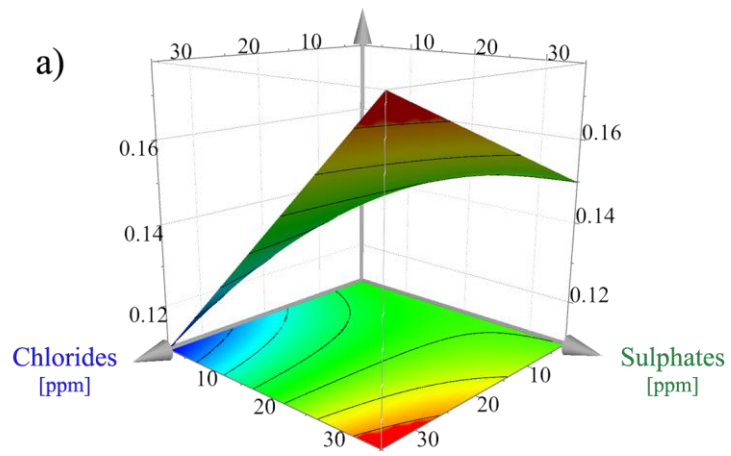
Figure 6.35: Response surfaces plot obtained by the polynomial fit regarding α/γ index as response factor and considering the interaction between a) chlorides and nitrates, b) chlorides and sulphates and c) nitrates and sulphates.

As already suggested by the coefficients, the response surfaces suggest the presence of synergic interactions among ions, especially between $Cl^- \cdot NO_3^-$ and $NO_3^- \cdot SO_4^{2-}$. Therefore, when the ions are present in the same proportion (in ppm), patina tends to be stabilized, as already deduced in paragraph 6.2.2.3 by observing the calculated PAI index. The multivariate model built also confirms that as highest is the content of $Cl^- \cdot SO_4^{2-}$ and/or $NO_3^- \cdot SO_4^{2-}$ as highest is the stability that can be reached by the patina.

6.2.5.2   Response factor: metal release

As well as it was done for the α/γ index, total metal release was employed as response factor to build a model according to equation 5.1. **Table 6.12** contains the real coefficients calculated and the model built, after being validated, shows 0.921 as R^2, thus, also considering metal release as response factor, a robust method with high descriptive ability is obtained.

Table 6.12: Coefficients determined from the fitting considering the total metal release as response factor.

Total Metal Release			
Constant (b$_0$)	216.402		
Chlorides (b$_{Cl-}$)	31.737	*Chl · Nit (b$_{Cl-}$ · b$_{NO3-}$)*	-10.254
Nitrates (b$_{NO3-}$)	-5.799	*Chl · Sul (b$_{Cl-}$ · b$_{SO4=}$)*	-22.612
Sulphates (b$_{SO4=}$)	34.144	*Nit · Sul (b$_{NO3-}$ · b$_{SO4=}$)*	-30.174

After fitting the polynomial, it can be plotted in the experimental domain considered (**Figure 6.36**a – c).
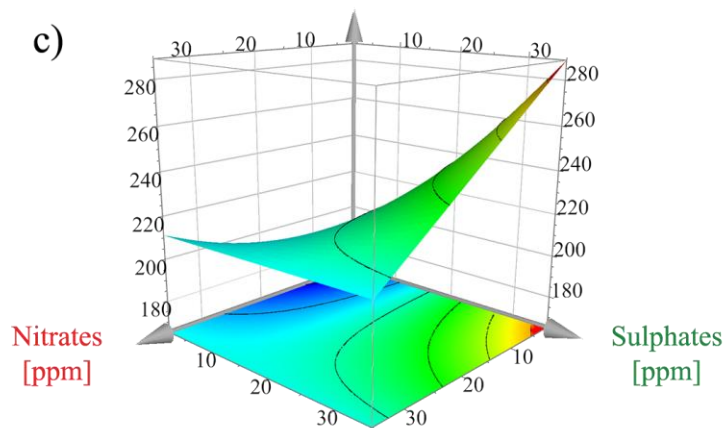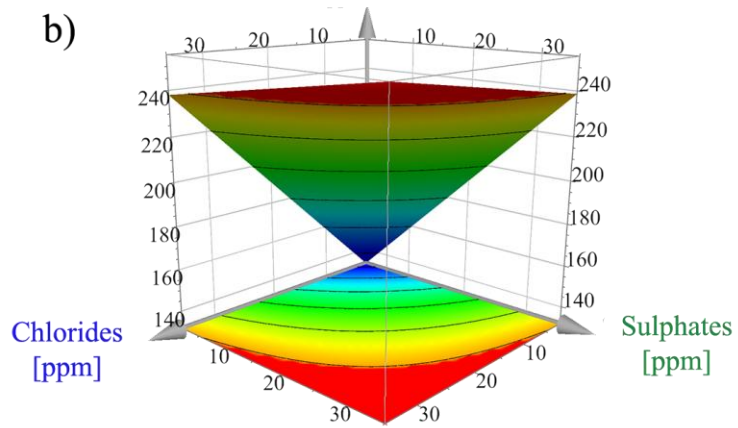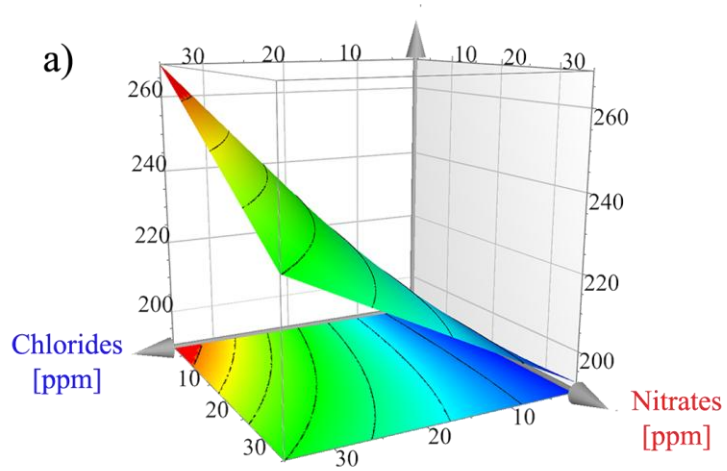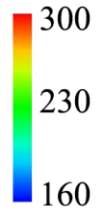
Figure 6.36: Response surfaces plot obtained by the polynomial fit regarding total metal release as response factor and considering the interaction between a) chlorides and nitrates, b) chlorides and sulphates and c) nitrates and sulphates.

The model built expresses and confirms the observed negative influence of nitrates, both in pure solution and in mixtures. Specifically, it shows a significant competitive effect in respect to sulphates. Thus, as observed in the previous section, in presence of increasing values of nitrates, the aggressive action of sulphates towards metal release is reduced. Conversely, a slight effect is observed due to the interaction between $Cl^- \cdot NO_3^-$ and $Cl^- \cdot SO_4^{2-}$. Additionally, as found out in a previous work [177], sulphates appear to be the most aggressive species followed by chlorides, as observed by mass variation data, Fe, Cu and Mn release (especially in PF) results presented in the previous section.

6.2.5.3   Response factor: corrosion rates

Lastly, also corrosion rates were considered as response factor and the coefficient calculated are reported in **Table 6.13**. Model was validated and its R^2 is 0.511, therefore it must be considered that the model achieved is less robust. Generally, in order to improve the robustness of a model and thus to achieve better performance also in predictive ability, the number of experiments to be performed according to the experimental plan can be extend, for instance considering as a model the Central Composite Face-Centered design (CCD).

Table 6.13: Coefficients determined from the fitting considering the corrosion rates as response factor.

Corrosion Rates			
Constant (b_0)	3923.780		
Chlorides (b_{Cl^-})	125.024	*Chl · Nit ($b_{Cl^-} \cdot b_{NO3^-}$)*	-305.100
Nitrates (b_{NO3^-})	-112.800	*Chl · Sul ($b_{Cl^-} \cdot b_{SO4=}$)*	923.525
Sulphates ($b_{SO4=}$)	202.725	*Nit · Sul ($b_{NO3^-} \cdot b_{SO4=}$)*	-493.749

Figure 6.37 shows the response surfaces regarding the variables considered.
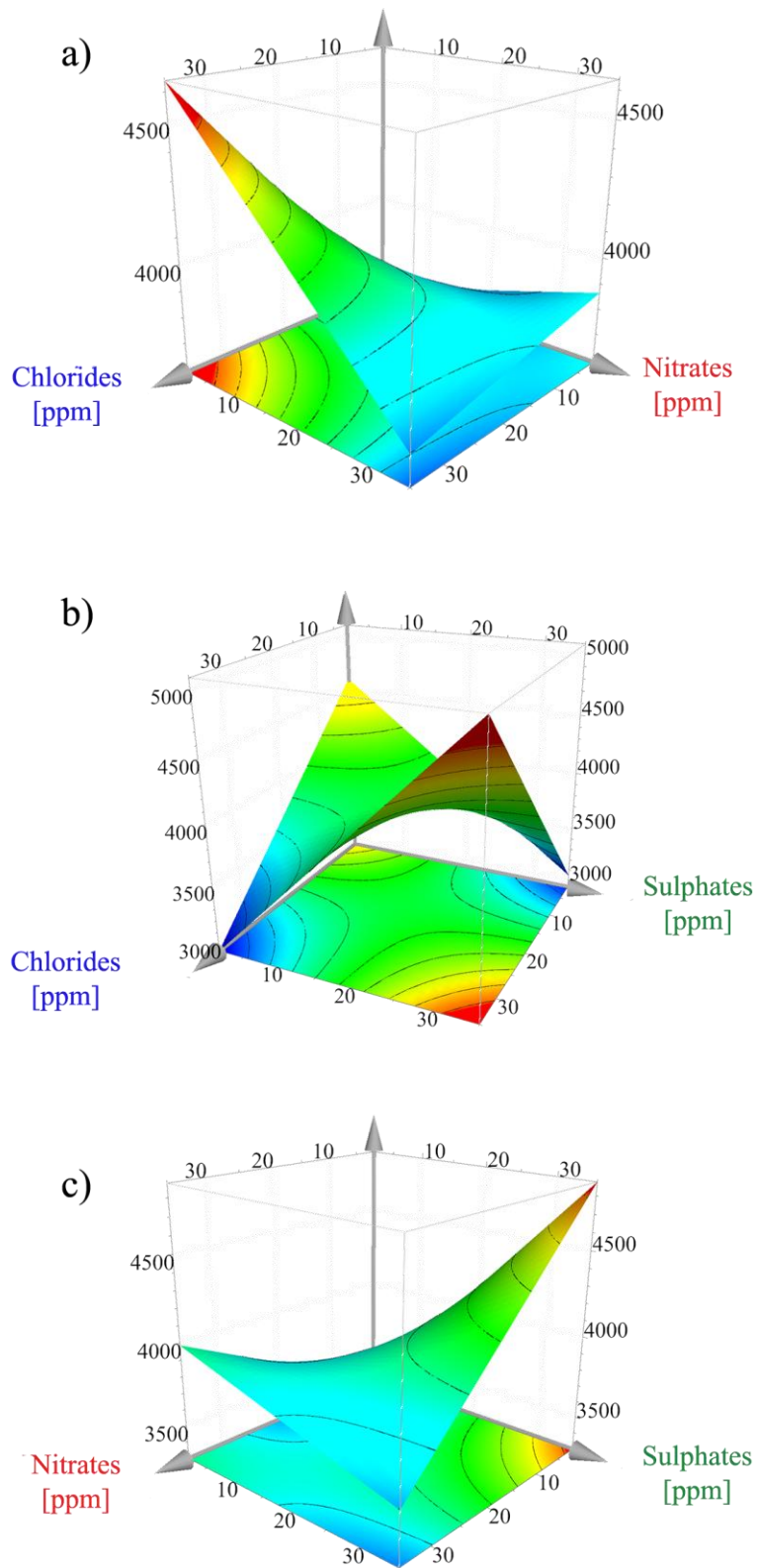
Figure 6.37: Response surfaces plot obtained by the polynomial fit regarding corrosion rates as response factor and considering the interaction between a) chlorides and nitrates, b) chlorides and sulphates and c) nitrates and sulphates.

The presence of nitrates and Cl^- or SO_4^{2-} in mixture in the ageing solutions remarkably reduces the corrosion rate of weathering steel. Otherwise, the interaction between chlorides and sulphates is strongly synergic. Thus, besides confirming the results achieved for pure solutions by Raffo [177], the results obtained in this work highlights the presence of a further contribution to the increasing of corrosion rates related to the synergic interaction between chlorides and sulphates. Therefore, in order to reduce its corrosion and prevent its decay, WS outdoor exposures under atmospheres particularly polluted in terms of sulphates and chloride should be avoided. On the other hand, atmospheres rich in terms of nitrates appears to be less aggressive, both for the low aggressiveness behaviour of pure solutions of NO_3^- and also for the competitive effect shown towards Cl^- and SO_4^{2-} considering metal release and corrosion rates. Moreover, the model obtained considering as response factor the PAI index confirms a slight synergic effect of NO_3^- towards the formation of goethite and thus regarding patina stabilization.

Additionally, a noteworthy fact to keep in mind is that all models obtained from the application of DoE are representatives of an experimental domain that considers and characterizes different possible changes in the concentration of pollutants of growing interest. Thus, achieve robust method can help to predict and evaluate the trend of a factor of interest (for instance, corrosion rate) inside a range of concentration ad to evaluate the effect of a change in the amount of Cl^-, NO_3^- or SO_4^{2-} measured.

Chapter 7

Conclusions

The main aim of this PhD research study was to further investigate the issue of atmospheric corrosion, focusing the attention on the effect that pollutants of growing interest could have on corrosion process. To better understand the mechanisms acting, weathering steel, a low-alloyed carbon steel, was investigated both by field exposures and accelerated ageing test.

Specifically, environmental conditions and pollutants concentrations can play an active role in the formation of corrosion products on weathering steel, especially in the early stage of its exposure. Moreover, the decay process of the material can be affected by the atmospheric composition and thus by the presence of a specific combination of aggressive ions, inducing an effect on alloying metal release, stability of the patina formed and eventually on corrosion rates.

The main conclusions achieved in this work are summarized here below.

Considering the results obtained from the natural exposures, which started in different period of the year (summer, winter and spring), a strong influence of environmental parameters is observed. A strong correlation between the precipitations and the deposition of aggressive species occurs, especially during the first months of exposure when the material starts to corrode. Specifically, samples that started their exposure during summer exhibit a different behaviour in respect to the samples belonging to other campaigns showing for unsheltered samples a larger content of ions (especially Na^+ and Cl^-) inside the patina formed and thus higher values of corrosion rates.

A possible explanation for this unexpected observation may be highlighted considering also the surface analysis performed in order to characterize and evaluate the composition of the patina formed. XRD results and the PAI* index calculated seem to suggest that, due to the persistent rainfalls of the first months of exposure, a lack in the circumstances necessary to transform lepidocrocite in to more stable goethite occurs. Due to the long wet phase that samples are subjected, the almost absence of an alternation of wet and dry cycles induces instability in the patina formed, which leads to a high corrosion rate.

Moreover, corrosion rate is further increased by the formation on the surface of the specimens of akaganeite (as determined by XRD analysis and SEM observations of the surfaces and the cross sections of the sample) due to the large chloride deposition, which occurred during the next month characterized by low precipitations.

On the contrary, due to the action of environmental agents, in the early stage of corrosion on samples that begun their exposure during winter and spring, a quite stable layer is formed, due to the formation of akaganeite, as supported also by the positive values of mass variation measured. This stable inner layer acts as a protection of the uncorroded material leading to low values of corrosion rate. Subsequently, a tightening of environmental conditions and an increasing in pollutants concentration induces the formation of an outer rust layer composed by akaganeite, which also justifies the low values of PAI* index calculated and the absence of correlation between corrosion rates and the patina protective ability index. As expected, mass loss determined for these samples is higher in sheltered than in unsheltered condition, as well as the percentage of akaganeite found by XRD analysis. This latter result is actually related to the action of chlorides, which can be deposited mostly on the surface of sheltered samples that are not exposed to the washing effect of rainfalls.

In order to further investigate the effect of the main aggressive anions (Cl^-, NO_3^- and SO_4^{2-}) and to evaluate possible interaction among them, a design of experiment was used to plan the accelerated ageing tests on weathering steel.

As main result, total metal release and corrosion rate of weathering steel are remarkably reduced by the presence of NO_3^- and Cl^- or SO_4^{2-} in mixture. Moreover, a slight synergistic effect of NO_3^- and SO_4^{2-} towards the formation of goethite is observed by the XRD analysis, leading to a stabilization of the patina formed on samples. The PAI index calculated also suggests that solutions in which Cl^-, NO_3^- and SO_4^{2-} are present in the same proportion are related to the formation of a patina characterized by a high stability, especially when greater concentration of the species is reached.

On the other hand, the accelerated ageing tests performed show a strong synergistic interaction between Cl^- and SO_4^{2-}, enhancing the aggressiveness of the single anion

towards corrosion rates and regarding the release of iron, copper and manganese, especially in particulate fraction.

Therefore, keeping in mind that the experimental domain considered to perform this investigation was selected in order to represent changing in pollutant concentrations, the results obtained suggest that atmospheres characterized by high concentration of nitrates may be less aggressive towards decay material and also the effect of the more aggressive species of Cl^- and SO_4^{2-} can be attenuated. Moreover, a more accurate evaluation of a factor of interest can be provided through Design of Experiment. For instance, even considering a change in anions concentrations, metal release can be monitored and predicted by the validated models. Specifically, each different contribution can be evaluated processing the releases measured for each different metals in each fraction considered (dissolved or particulate fraction). Remarkably, particulate fraction represents the patina that, loosely bound to the metal surface, is lost during the corrosion process. Thus, a deep characterization of particulate fraction is really important in order to both evaluate the progress of corrosion and consider the environmental impact of WS. In fact, this part of corrosion products is lost in the environment and consequently it can interact with soil and superficial water behaving itself as a polluting species.

Then, in order to rapidly monitor the entire progress of corrosion process, also corrosion rates can be considered as response factor in modelling. This last result can be placed at the service of the conservation science and become a really powerful tool for prevention and for cultural heritage protection. Particularly, this methodology could be very useful towards the conservation of contemporary art, which is still a challenge and where Ws is mainly employed.

To conclude, the innovative approach pursued in this work allows to deep investigate the effects induced by a changing in atmospheric composition and to clarify the corrosion mechanism related to pollutant of growing interest. Due to technical/sampling problems to overcome, these pollutant are also the species less studied in literature in relation to corrosion. For this reason in Appedix A are also reported the main results of the validation of a new sampler developed by the research group of Professor Bolzacchini (University of Milano Bicocca) called "*Deposition Box*". The aim of this device is to collect representative and reproducible deposits of particulate matter and thus enrich the knowledge about its effect on materials corrosion.

Appendix A

Validation of *"Deposition Box"*

A.1   Introduction

The study of the decay of material is a very complex issue and it is even more intricate if the role of particulate matter (PM) on the process is taken into account considering its wet and dry deposition.

Due to its chemical composition and its variety, PM represents a matrix as complex to investigate as dangerous towards the corrosion of metallic surface. The hygroscopic characteristics of the salt contained in deposited PM keep materials moist for longer periods of time, prompting the corrosion process and preventing the occurrence of dry conditions necessary for the protective patina formation [181].

Moreover, as deeply described in the section 2.3.5, PM is increasing its relative concentration in European atmosphere in respect to other main pollutants (such as SO_2 or NO_x). However, even if the role of PM in some decay process (such as the formation of black crust) was clarified [182, 183], aerosol dry deposition on urban surface has been not yet well described by the literature, especially concerning dry deposits on building materials and vertical surface [184].

This lack of knowledge is mainly caused by the difference in estimate deposition fluxes arising in dependence of the sampler geometry and the sampling surface features and above all, by the difficulties in sampling dry depositions [185, 186].

Actually, dry deposition occurs with several mechanisms like *turbulent diffusion*, *sedimentation*, *Brownian diffusion*, *interception*, *inertial forces*, *electrical migration*, *thermophoresis* and *diffusiophoresis*. All these mechanisms, due to their inner nature, can not be standardised. Deposition rates are governed by meteorological factors (wind velocity, relative humidity), particle characteristics (size and shape), and surface characteristics (friction velocity, microscale roughness, and temperature).

Anyway, to properly perform a whatever study about effect of PM on cultural heritage, both to study material corrosion or to test a conservation treatments, it is essential to deposit PM directly on the material surface and to guarantee that the properties of deposed PM can be determined with accuracy. Therefore, the need of repeatable, homogenous dry deposition measurements arises.

Therefore, a new sampler designed and developed by the research group of Professor E. Bolzacchini from the University of Milano Bicocca was investigated in order to prove its use as an alternative and validate method to obtain reproducible samples of dry PM deposits.

A.1.1 "Deposition box"

"Deposition box" is a new sampler designed and built to fill the gap in the field of PM dry deposition sampling [187].

In order to standardize the methodology and to collect reliable samples of atmospheric PM directly deposited on a substrate, "Deposition box" was developed so that to avoid any particle removal mechanisms. It is composed by a 50x50x20 cm^3 box covered by a white pitched roof (overall dimension: 70x70x55 cm^3), necessary to avoid rainfall and wind variability together with the overheating within the structure in conditions of high solar radiation (**Figure A.1**).

a)   **b)**
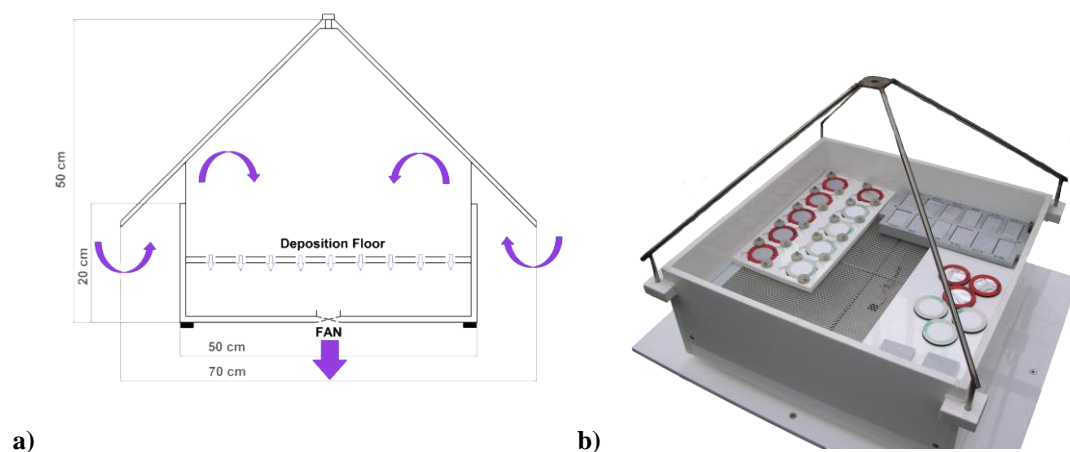
Figure A.1: a) Scheme of the alternative sampler developed; b) real picture of the "Deposition box" without the covering roof [187].

One of the main advantages of this sampler is that it can house each kind of specimens, both surrogate surface (like filters or aluminium foils) and real substrates (for instance, stone, polymeric or metallic specimens). Specimens can be placed on a punctured stainless steel exposure floor located 150 mm from the air intake level.

Then, a fan (Sunon DR MagLev DC fan; flow of 1.5 m^3 h^{-1}) housed in the bottom of the box guarantees air exchange inside the sampler and, in addition, it provides a standardised useful air exchange rate of 30 h^{-1} leading, at the same time, a negligible

linear air speed through the exposed surface: 0.002 m sec^{-1}. This air speed is lower than any ambient wind speed at which specimens can be exposed in natural field test.

Additionally, the number size distribution of atmospheric PM inside and outside "Deposition box" was measured during a validation test by means of two Optical Particles Counters (OPCs, Grimm model 1.107) to prove the efficacy of the "Deposition box" and, on the other hand, to exclude any dimensional artefacts in the particle size distribution of the PM collected inside the box.

Lastly, a further noteworthy fact is that "Deposition box" is a system characterized by low construction and operating costs. Thus, "Deposition box" seems to have all the characteristics to be suitable as innovative and reliable sampling method.

A.2 Materials and methods

A.2.1 Specimens and sampling campaigns

In order to validate Deposition box as an alternative sampling tool to achieve reproducible and representative deposit samples and to investigate the unlike answers of different materials towards PM dry deposition, both surrogate and real stone surfaces were exposed in two sites of the urban area of Milan during several sampling campaigns planned and carried out by the University of Milano Bicocca.

As mentioned in section A.1, Deposition box can house any kind of material. Specifically, in this work different substrates were chosen to represent different properties in terms of surface roughness and porosity. Thus, two different surrogate surfaces were chosen:

- **PTFE** – PTFE membrane filters (ø 47 mm, 0.2 µm, PALL).

- **Alu** – Punched discs from aluminium foils with ø 47 mm.

The latter was chosen in order to mimic and investigate the behaviour towards dry deposited PM of a metallic surface (more familiar and similar to WS) while PTFE was basically chosen for its assumed inertia against PM deposits.

Additionally, also a real stone material (5 x 3 x 1 cm specimens cut from quarries blocks of **Carrara marble**) was exposed. Carrara marble is a metamorphic stone essentially composed of calcium carbonate ($<$ 98%) with a crystalline structure and an open porosity ~2% [188]. Stone specimens were prepared according to UNI 10921 [189] and the effective are for the deposition was 15.00 cm^2.

Aluminium discs were washed in bidistilled water and acetone before their exposure while no pre-treatment was required for PTFE filters. The mass of both was determined by means of an analytical balance (Sartorius SE2, capacity 2 g, sensitivity 0.1 µg) after 24 hours drying in dessicator. Then, PTFE and Alu were placed in a suitable filter-older ring, giving back 11.94 cm^2 as effective area of deposition. In turn, filter-older rings were housed and fixed to an inert PTFE plate to avoid a possible accidental overthrow.

The surfaces of Carrara marble were polished with FEPA 180 (82 µm) sandpaper and immersed in bidistilled water for 20 minutes in order to remove any soluble substance present. Then, stone specimens were dried at 60°C in oven and weighted by analytical

balance (sensitivity 0.1 mg). As well as surrogate surfaces, also stones were placed in a suitable inert sampler holder to be laid down in "Deposition box".

Two sites in the urban area of Milan were selected for performing two parallel campaigns (**Figure A.2**):

- ▪ Torre Sarca – TS (45° 31' 19'' N, 9° 12' 46'' E): it is placed in correspondence of one of the busiest way of access to the centre of the city so it can be considered as a traffic site.

- ▪ Villa Necchi Campiglio – VN (45° 28' 08'' N, 9° 12' 08'' E): this place is an heritage property of FAI (Fondo Ambiente Italiano; (www.visitfai.it/villanecchi/) located inside the Low Emission Zone of Milan, named "Area C" [190].
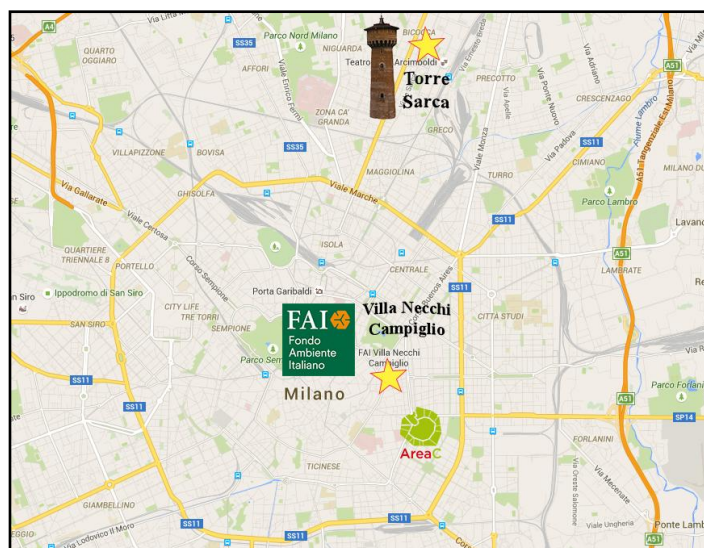
Figure A.2: The two site of sampling shown in the map of the center of Milan.
(Modified from www.google.it/maps/)

Once the two "Deposition boxes" were placed (**Figure A.3**), several parallel sampling campaigns were carried out. A summary scheme of these campaigns is reported in **Table A.1**. For each sampling campaign and for each specimen or surrogate surface considered, a minimum of three samples was exposed.

Figure A.3: "Deposition box" placement in the Torre Sarca (on the left) and Villa Necchi (on the right) site.

(Modified from www.google.it/maps/)

Table A.1: Summary scheme of the campaigns carried out in parallel in TS and VN.

	ID	Start	End	Materials
Torre Sarca (TS)	Sum13	03/07/13	01/10/13	Al, PTFE, Carrara Marble
	Win14	23/12/13	26/03/14	Al, PTFE, Carrara Marble
	Sum14	30/05/14	01/10/14	Al, PTFE, Carrara Marble
	16m	23/12/13	05/05/15	Al, PTFE, Carrara Marble
	ID	Start	End	Materials
Villa Necchi Campiglio (VN)	Win14	23/12/13	26/03/14	Al, PTFE, Carrara Marble
	Sum14	30/05/14	01/10/14	Al, PTFE, Carrara Marble
	16m	23/12/13	05/05/15	Al, PTFE, Carrara Marble

Before the validation work described in the following sections was carried out, the research group of Professor Bolzacchini performed also the chemical characterization through ionic chromatography of all the samples collected during the different campaigns in TS and VN.

A.2.2 Determination of the size-distribution of the deposited PM

With the aim of validating the alternative sampling method used, once the samples were recovered, they were analysed through the acquisition of Variable Pressure Scanning Electron Microscopy (VP-SEM, see section 5.4.4) images and processing them with the freeware software ImageJ (v. 1.51i, NIH).

Specifically, SEM images were acquired at different magnifications (from 100x to 10000x) through a VP-SEM Zeiss EP EVO 50 working in low vacuum mode (p = 80 Pa, E = 20 keV and 7 – 9 mm as working distance) and acquiring images both in backscattered and secondary electron mode. In order to represent the whole sample, several images were recorded in different spots of each specimens following the mapping grid illustrate in **Figure A.4**. Besides, according to the interest of comparing samples achieved in Torre Sarca and Villa Necchi, specifically homogenous deposit areas were selected for the investigation by avoiding the contribution of giant biogenic particles coming from a *Tilia* tree located near the "Deposition box" placed in Villa Necchi.
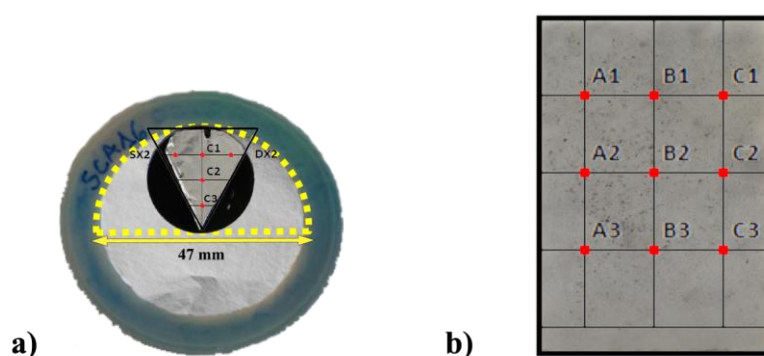
Figure A.4: Mapping grid defined for a) Alu samples and b) Carrara marble samples.

All the images collected by VP-SEM had 1024 pixels of width, 672 pixels of height and a resolution of 72 ppi. Images were processed through the freely available ImageJ software to separate particles deposited from the matrix below. This process shown in **Figure A.5**a − b was carried out selecting a suitably brightness threshold value. Then, to identify and count the isolated particles as a function of the area of their visible side, the "*analyse particle*" plug-in was applied (**Figure A.5**c) on three images for each sample.
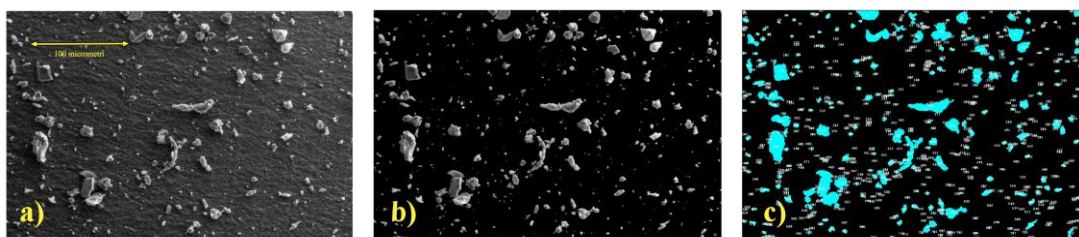
Figure A.5: Application of the plug-in "*Analyze Particle*" to a) SEM images of Alu filter (500x). b) Isolation of deposited particles from the matrix below. c) Identification and count of the isolated particles.

Whereas, after a preliminary investigation, aluminium turned out to be the optimal support for this kind of analysis, images collected for PTFE filters were not processed. Actually, PTFE matrix does not allow the identification of small particles deposited on it due to its fibrous structure, as shown in **Figure A.6** and reported by Casuccio et al. [191].
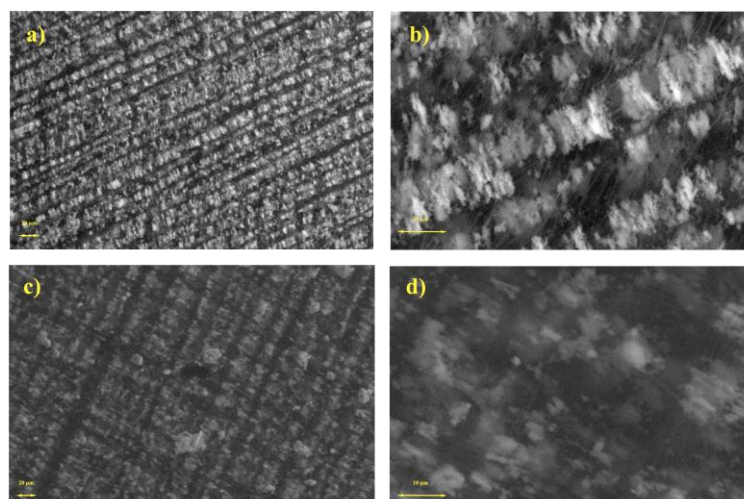
Figure A.6: SEM images of blank PTFE filter at a) 1000x and b) 5000x. SEM images of deposited PTFE filter at c) 1000x and d) 5000x.

Eventually, also Carrara marble samples were not processed through ImageJ because, in this case, in agreement to what reported by Telloli et al. [192], observed deposits were mainly constituted by complex amorphous agglomerates rather than single particles. Therefore, two ALU discs exposed in Torre Sarca and two exposed in Villa Necchi during sum14 and win14 were chosen to investigate the size-distribution of the deposited PM. Otherwise, Carrara marbles were taken into account for the determination of the covering grade of the material described in the next section.

Another remarkable fact is that the distributional results obtained through this kind of elaboration were expressed in terms of area of the visible side of the particles rather than

of geometrical equivalent diameter. This choice was related to the various and irregular shape of the particles found.

A.2.3 Determination of the covering grade of the material

Besides acquiring SEM images, punctual EDS analysis at 1000x and elementary maps at 500x were also acquired on exposed and not exposed (blank reference) samples by means of an Oxford Instruments INCA ENERGY 350 [z > 4 (Be)].

EDS maps were thus used to estimate the 2D covering grade of Alu and Carrara marbles. Specifically, a new method was developed considering the decrease in terms of atomic percentage of the main constituents elements (so obviously Al for Alu and the sum of Ca and Mg for marble samples) related to the dry deposition on surfaces. This procedure was carried out considering the amount of the elements considered basically negligible in the deposits with respect to the percentage found in the corresponding blank specimens.

Therefore, according to these premises, a Covering Grade Index (CGI, expressed in percentage) was defined (equation A.1):

$$CGI = \frac{(at\%X_{blank} - at\%X_{sample})}{at\%X_{blank}} \cdot 100 \qquad\text{(Eq. A.1)}$$

where *at%* is the atomic percentage, *X* represents the element considered (so Al for Alu and the sum of Ca and Mg for marbles), *blank* and *sample* subscripts refer to not exposed and exposed surfaces respectively.

A.3 Results

A.3.1 Determination of the size-distribution of the deposited PM

Deposits characterization performed by SEM analysis allows to evaluate the particle size distribution.

Particularly, the biggest single particle was observed on a samples coming from the site of Torre Sarca and exposed during sum14. This particle shows a visible area of 1081 μm^2. Otherwise, the smallest particle that was possible to identify has a visible area of 0.4 μm^2. Particles with this area were observed on all the samples investigated, independently from the site and the sampling period. Furthermore, even if the area of 0.4 μm^2 represents the instrumental detection limit related to the resolution of the SEM images acquired, it also represents an important result to validate the device as an alternative PM sampling method demonstrating that also fine particles may deposit and be collected through "Deposition box".

Areas of the smallest and the biggest particles, and the estimated number of particles/agglomerates per surface unit (Num · mm^2) determined for each Alu sample are reported in **Table A.2**.

Table A.2: Dimensional results obtained for each Alu sample analyzed.

		Torre Sarca (TS)		Villa Necchi Campiglio (VN)	
		win14	sum14	win14	sum14
Visible area of	Smallest single particle (μm^2)	0.4	0.4	0.4	0.4
	Biggest single particle (μm^2)	643	1081	983	991
Particles/Agglomerates per surface unit (Num/mm^2)		5870	4330	4150	5150

Another important result in order to validate "Deposition box" arises from the comparison of the size distribution obtained (**Figure A.7**).
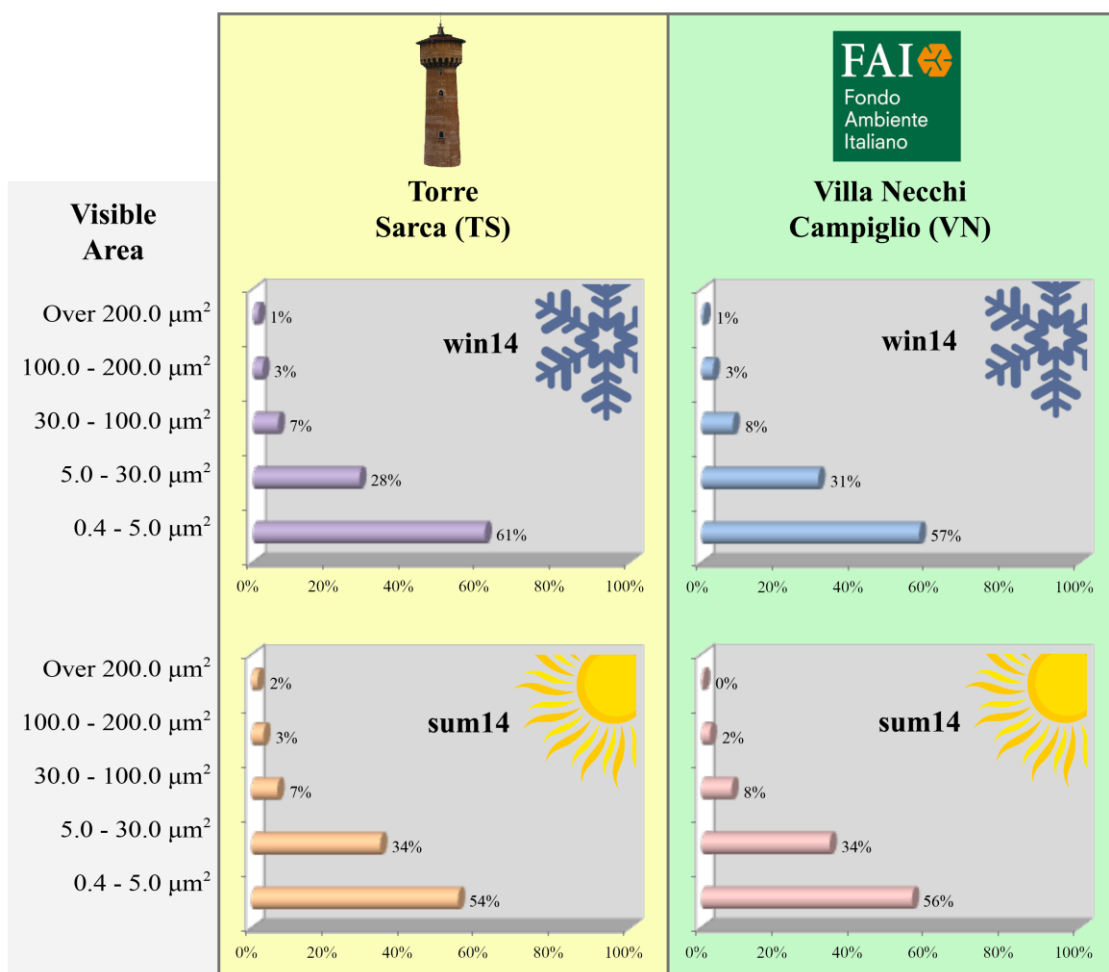
Figure A.7: Size distribution obtained for Alu samples investigated.

Figure A.7 shows that the dimensional distribution follows a common trend for all the samples. The dominant dimensional class is represented by particles/agglomerates (55-60%) with a visible area between 0.4 and 5 μm^2; about 30% falls in the range of 5 – 30 μm^2 and then, as the visible area increase, the number of particles continues to progressively decrease. Lastly, less than 3% of total particles are particles/agglomerates with area > 200 μm^2.

A.3.2 Determination of the covering grade of the material

EDS maps acquired at 500x (**Figure A.8**) were used to estimate the 2D covering grade for both Alu discs and Carrara marble.
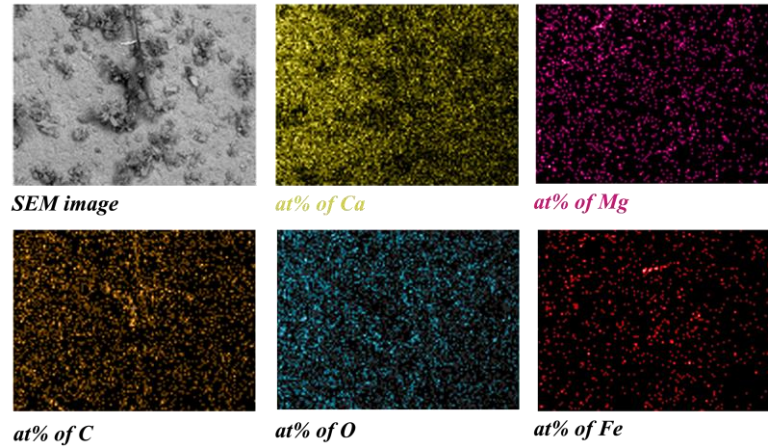
Figure A.8: Example of the EDS maps acquired at 500x for a marble sample.

For what concern Alu discs, the Al *at%* found in blank specimen is 99.3% (σ = 0.007) thus, according to equation A.1, the Covering Grade Index was calculated for all Alu specimens and the values are reported in **Table A.3**.

As regards Carrara marble, the sum of the Ca and Mg *at%* found in blank specimen is 19.2% (σ = 0.1). CGI_s calculated for marble specimens (two specimens exposed in VN in sum14 and sum14+win14, so 4 and 10 months respectively; three specimens exposed in TS during sum14, sum14+win14 and 16m) are also reported in **Table A.3**; they range between 12% and 37% and they increase as the exposed time increases, therefore CGI determined on marble allows to evaluate the time increasing tendency of deposits to spread over the surface.

Table A.3: CGI_s calculated for all the samples analyzed.

Material	Torre Sarca (TS)				Villa Necchi (VN)	
	❄ win14	☀ sum14			❄ win14	☀ sum14
Alu	25%	47%			21%	23%
	☀ sum14	☀ sum14+win14 ❄	16m		☀ sum14	☀ sum14+win14 ❄
Marble	12%	13%	37%		19%	30%

A.4   Conclusions

In order to achieve a standardised method to sample dry deposition of atmospheric particulate matter, a new exposure method was developed, designing a sampler able to avoid any particles removal mechanism.

Once ensured the absence of particles artefacts, "Deposition box" was validated investigating deposits samples obtained from different seasonal campaigns and in two different site of exposure by means of SEM images processed through the freeware software ImageJ. Thus, their size particles distribution was determined.

Even if both surrogate and real materials were exposed, the best substrate for the validation procedure was aluminium, while PTFE filters were excluded from the ImageJ processing, due to their fibrous structure that prevents the separation of the matrix below from the particles deposited.

For what concern aluminium samples, the smallest particle identified on each sample is the smallest particle detectable by the methodology (representing the LoD) and it has an area of 0.4 μm^2. Therefore, as first result, the possibility of sampling through deposition box even fine particles is confirmed. Then, observing the size distribution obtained for each sample, it can be pointed out that each samples shows a similar trend in distribution, although significant difference between sites and seasons are detected. Thus, this result constitutes a further proof of the reproducibility achievable by "Deposition box".

Secondly, using EDS maps acquired for both marble and aluminium sample, an estimate of the 2D covering grade is expressed from the element atomic percentages found in the specimens respect to those measured for blank samples. Covering grade index represents a simple parameter suitable to quickly indicate sample covering.

To conclude, "Deposition box" allows to obtain repeatable samples and appears to be a suitable alternative method to fill the gap in the field of dry PM deposition sampling. Therefore, this innovative sampler paves the way for new possible investigation on particulate matter and especially to the study of the role of its dry depositions on the corrosion process of any kind of material.

References

1. ISO 8044, "*Corrosion of metals and alloys*", Geneva, Switzerland: ISO, 2015.

2. Bardal E., *Corrosion and protection*, Springer, pp. 1 – 315, 2004.

3. Schweitzer P. A., *Fundamentals of metallic corrosion – Atmospheric and media corrosion of metals*, 2ⁿᵈ ed., CRC Press, pp. 1 – 727, 2007.

4. Pedeferri P., *Corrosione e protezione dei materiali*, Ed. Polipress, pp. 1 – 441, 2007.

5. Marcus P., *Corrosion mechanisms in theory and practice*, 3ʳᵈ ed., CRC Press, pp. 1 – 929, 2011.

6. Revie R. W. and Uhlig H. H., *Corrosion and corrosion control – An introduction to corrosion science and engineering*, 4ᵗʰ ed., Wiley, pp. 1 – 490, 2008.

7. Koch G. H., Bronger M. P. H., Thompson N. G., Virmani Y. P. and Payer J. H., "*Corrosion Costs and Preventive Strategies in the United States, Supplement to Materials Performance*," NACE Int., pp. 1 – 12, 2002.

8. Albrecht P. and Hall T. T., "Atmospheric Corrosion Resistance of Structural Steels", *Journal of materials in civil engineering*, **15** (1), pp. 2 – 24, 2003.

9. Revie R. W., *Uhlig's corrosion handbook*, 3ʳᵈ ed., Wiley, pp. 1 – 1253, 2011.

10. Leygraf C., Wallinder I. O., Tidblad J. and Graedel T., *Atmospheric Corrosion,* 2ⁿᵈ ed., Wiley, pp. 1 – 374, 2016.

11. Stratmann M., Bohnenkamp K. and Ramchandran T., "The influence of copper upon the atmospheric corrosion of iron", *Corrosion science*, **27** (9), pp. 905 – 926, 1987.

12. Schindelholz E., Kelly R. G., Cole I. S., Ganther W. D. and Muster T. H., "Comparability and accuracy of time of wetness sensing methods relevant for atmospheric corrosion", *Corrosion science*, **67**, pp. 233 – 241, 2013.

13. Corvo F., Pérez T., Martin Y, Reyes J., Dzib L. R., González-Sánchez J. and Castañeda A., "Time of wetness in tropical climate: considerations on the estimation of TOW according to ISO 9223 standard", *Corrosion science*, **50**, pp. 206 – 219, 2008.

14. Wang X., Li X. and Tian X., "Influence of Temperature and Relative Humidity on the Atmospheric Corrosion of Zinc in Field Exposures and Laboratory Environments by Atmospheric Corrosion Monitor", *International journal of electrochemical science*, **10**, pp. 8361 – 8373, 2015.

15. ISO 9223, "*Corrosion of metals and alloys - Corrosivity of atmospheres – Classification*", Geneva, Switzerland: ISO, 2012.

16. Henriksen J. F. and Mikhailov A. A., "Atmospheric corrosion tests of metals in SO_2-polluted cold atmosphere in northern Norway and along its border with Russia", *Protection of metals*, **38** (6), pp. 579 – 589, 2002.

17. Tidblad J., Mikhailov A. A. and Kucera V., "Model for prediction of the time of wetness from average annual data on relative air humidity and air temperature", *Protection of metals*, **36** (6), pp. 533 – 540, 2000.

18. Veleva L., Acosta M. and Meraz E., "Atmospheric corrosion of zinc induced by runoff", *Corrosion science*, **51**, pp. 2055 – 2062, 2009.

19. Schumann U., *Atmospheric Physics – Background, methods, trends*, Springer, pp. 1 – 877, 2012.

20. Putaud J. P., Raes F., Dingenen R. V., Brüggemann E., Facchini M. C., Decesari S., Fuzzi S., Gehrig R., Hüglin C., Laj P., Lorbeer G., Maenhaut W., Mihalopoulos N., Müller K., Querol X., Rodriguez S., Schneider J., Spindler G., Brink H. T., Tørseth K. and Wiedensohler A. "A European aerosol phenomenology—2: chemical characteristics of particulate matter at kerbside, urban, rural and background sites in Europe", *Atmospheric environment*, **38**, pp. 2579 – 2595, 2004.

21. Larssen, S., Sluyter, R., Helmis, C., "*Criteria for EUROAIRNET, the EEA air quality monitoring and information network*", 1999. http://reports.eea.eu.int/TEC12/en

22. Cramer S. D. and Covino B. S., *ASM handbook* – Volume 13B – Corrosion: materials, ASM international, pp. 1 – 704, 2005.

23. https://www.epa.gov/air-trends/sulfur-dioxide-trends

24. EEA, "*Air quality in Europe – 2016 report*", EEA, pp. 1 – 88, 2016.

25. Directive 2008/50/EC on *ambient air quality and cleaner air for Europe*, 2008.

26. http://www.eea.europa.eu/themes/air/interactive/so2

27. Tomasi C., Fuzzi S. and Kokhanowsky, *Atmospheric aerosols - Life Cycles and Effects on Air Quality and Climate*, Wiley, pp. 1 – 680, 2017.

28. Tidblad J., Kucera V., Ferm M., Kreislova K., Brüggerhoff S., Doytchinov S., Screpanti A., Grøntoft T., Yates T., De la Fuente D., Roots O., Lombardo T., Simon S., Faller M., Kwiatkowski L., Kobus J., Varotsos C., Tzanis C., Krage L., Schreiner M., Melcher M., Grancharov I. and Karmanova N., "Effects of Air Pollution on Materials and Cultural Heritage: ICPMaterials Celebrates 25 Years of Research", *International Journal of Corrosion*, pp. 1 – 16, 2012.

29. Akimoto H., *Atmospheric reaction chemistry*, Springer, pp. 1 – 433, 2016.

30. WHO, *"Air quality guidelines for particulate matter, ozone, nitrogen dioxide and sulfur dioxide*", WHO, pp. 1 – 20, 2006.

31. Screpanti A. and De Marco A., "Corrosion on cultural heritage buildings in Italy: A role for ozone?", *Environmental pollution*, **157**, pp. 1513 – 1520, 2009.

32. Arpav, "*A proposito di ozono*", Agenzia regionale per la prevenzione e protezione ambientale del Veneto, 2nd ed., pp. 1 – 16, 2015.

33. Monks P. S., Archibald A. T., Colette A., Cooper O., Coyle M., Derwent R., Fowler D., Granier C., Law K. S., Mills G. E., Stevenson D.S., Tarasova O., Thouret V., Von Schneidemesser E., Sommariva R., Wild O. and Williams M. L., "Tropospheric ozone and its precursors from the urban to the global scale from air quality to short-lived climate forcer", *Atmospheric chemistry and physics*, **15**, pp. 8889 – 8973, 2015.

34. Morcillo M., Chico B., Mariaca L. and Otero E., "Salinity in marine atmospheric corrosion: its dependence on the wind regime existing in the site", *Corrosion science*, **42**, pp. 91 – 104, 2000.

35. ASTM International G140, "Standard Test Method for Determining Atmospheric Chloride Deposition Rate by Wet Candle Method", pp. 1 – 4, 2002.

36. Galvele J. R., "Transport process and the mechanism of pitting of metals", *Journal of Electrochemical Society*, **123** (4), pp. 464 – 474, 1976.

37. Burstein G. T. and Pistorius P. C., "Surface roughness and the metastable pitting of stainless steel in chloride solutions", *Corrosion*, **51** (5), pp. 380 – 385, 1995.

38. http://www.civilengineeringforum.me/chloride-induced-corrosion-mechanism/

39. Bensalah N., *Pitting corrosion*, InTech, pp. 1 – 178, 2012.

40. Seinfeld J. H. and Pandis S. N., *Atmospheric chemistry and physics: From air pollution to Climate Change*, 2nd ed., Wiley, 2006.

41. Harrison R. M. and Hester R. E., *Airborne Particulate Matter - Sources, Atmospheric Processes and Health*, RCS, pp. 1 – 387, 2016.

42. Vernon W. H. J., "Second experimental report to the Atmospheric Corrosion Research Committee (British Non-Ferrous Metals Research Association)", *Transaction of the Faraday Society*, **23**, pp. 113 – 183, 1927.

43. WHO, *"Air quality guidelines for Europe"*, 2nd ed., WHO, pp. 1 – 273, 2000.

44. Perrone M. G., Larsen B., Ferrero L., Sangiorgi G., De Gennaro G., Udisti R., Zangrando R., Gambaro A. and Bolzacchini E., "Sources of High PM2.5 Concentrations in Milan, Northern Italy: Molecular Marker Data and CMB Modelling", *Science of the total environment*, **414**, pp. 343 – 355, 2012.

45. Nastos P. T., Alexakis D., Kanellopoulou H. A. and & Kelepertsis A. E., "Chemical composition of wet deposition in a Mediterranean site Athens, Greece related to the origin of air masses", *Journal of atmospheric chemistry*, **58**, pp. 167 – 179, 2007.

46. Tositti L., Pieri L, Brattich E., Parmeggiani S. and Ventura F., "Chemical characteristics of atmospheric bulk deposition in a semi-rural area of the Po Valley (Italy)", *Journal of atmospheric chemistry,* **74**, pp. 1 – 25, 2017.

47. Goidanich S., Brunk J., Herting G., Arenas M. A. and Odnevall Wallinder I., "Atmospheric corrosion of brass in outdoor applications – Patina evolution, metal release and aesthetic appearance at urban exposure conditions", *Science of the total environment*, pp. 46 – 57, 2011.

48. Yi L., Xiaolan Y., Hongbing C., Weili L., Jie T. and Shufeng W., "Chemical characteristics of precipitation at three Chinese regional background stations from 2006 to 2007", *Atmospheric research*, **96**, pp. 173 – 183, 2010.

49. Sakihama H., Ishiki M. and Tokuyama A., "Chemical characteristics of precipitation in Okinawa Island, Japan", *Atmospheric environment*, **42**, pp. 2320 – 2335, 2008.

50. Huston R., Chan Y. C., Chapman H., Gardner T. and Shaw G., "Source apportionment of heavy metals and ionic contaminants in rainwater tanks in a subtropical urban area in Australia", *Water research*, **46**, pp. 1121 – 1132, 2012.

51. Nishimura T., "Rust formation mechanism on low alloy steels after exposure test in high Cl⁻ and high SO_x environment", *Materials*, **10** (199), pp. 1 – 11, 2017.

52. Amodio M., Catino S., Dambruoso P. R., De Gennaro G., Di Gilio A., Giungato P., Laiola E., Marzocca A., Mazzone A., Sardaro A. and Tutino M., "Atmospheric Deposition: Sampling Procedures, Analytical Methods, and Main Recent Findings from the Scientific Literature", *Advances in meteorology*, pp. 1 – 27, 2014.

53. Ebert M., Inerle-Hof M. and Weinbruch S., "Environmental scanning electron microscopy as a new technique to determine the hygroscopic behaviour of individual aerosol particles", *Atmospheric environment*, **36**, pp. 5909 – 5916, 2002.

54. Duncan J. R. and Balance J. A., "Marine Salts Contribution to Atmospheric Corrosion," *Degradation of Metals in the Atmosphere*, American Society for Testing and Materials, Philadelphia, PA, pp. 316–326, 1988.

55. Knotkova D. and Kreislova K., "Corrosivity of atmospheres – derivation and use information, Chapter 3 in Transactions on State of the Art in Science and Engineering, Vol. 28, WIT Press, pp. 73 – 105, 2007.

56. Surnam B. Y. R. and Oleti C. V., "Determining the Corrosivity of Atmospheres, Through the Weight Loss Method, According to ISO 9223", *Advanced materials research*, pp. 975 – 982, 2012.

57. Morales J., Díaz F., Hernández-Borges J., González S. and Cano V., "Atmospheric corrosion in subtropical areas: Statistic study of the corrosion of zinc plates exposed to several atmospheres in the province of Santa Cruz de Tenerife (Canary Islands, Spain)", *Corrosion science*, **49** (2), pp. 526 – 541, 2007.

58. Wang Z., Liu J., Wu L., Han R. and Sun Y., "Study of the corrosion behaviour of weathering steels in atmospheric environments", *Corrosion science*, **67**, pp. 1 – 10, 2013.

59. Bard A. J., Stratmann M. and Frenkel G.S., "*Corrosion and oxide films*", Wiley, pp. 1 – 755, 2003.

60. Wang J., Wang Z. Y. and Ke W., "A study of the evolution of rust on weathering steel submitted to the Qinghai salt lake atmospheric corrosion", *Materials chemistry and physics*, **139**, pp. 225 - 232, 2013.

61. Leuenberger-Minger A. U., Buchmann B., Faller M., Richner P. and Zöbeli M., "Dose-response functions for weathering steel, copper and zinc obtained from a four-year exposure programme in Switzerland", *Corrosion science*, **44**, pp. 675 – 687, 2002.

62. Damian L. and Fako R., "Weathering structural steels corrosion in atmospheres of various degrees of pollution in Romania", *Materials and corrosion*, **51**, pp. 574 – 578, 2000.

63. Oh S. J., Cook D. C. and Townsend H. E., "Atmospheric corrosion of different steels in marine, rural and industrial environments", *Corrosion science*, **41**, pp. 1687 – 1702, 1999.

64. Jaén J. A. and Iglesias J., "Corrosion study of steels exposed over five years to the humid tropical atmosphere of Panama", *Hyperfine interact*, **238** (37), pp. 1 – 10, 2017.

65. Cano H., Neff D., Morcillo M., Dillmann P., Díaz I. and De la Fuente D., "Characterization of corrosion products formed on Ni 2.4 wt% - Cu 0.5 wt% - Cr 0.5 wt% weathering steel exposed in marine atmospheres", *Corrosion science*, **87**, pp. 438 – 451, 2014.

66. Dhaiveegan P., Elangovan N., Nishimura T. and Rajendran N., "Weathering steel in industrial-marine environment: field study", *Materials transactions*, **57** (2), pp. 148 – 155, 2016.

67. Christodoulakis J., Tzanis C.G., Varotsos C .A., Ferm M. and Tidblad J., "Impact of air pollution and climate on materials in Athens, Greece", *Atmospheric chemistry and physics*, **17**, pp. 439 – 448, 2017.

68. Liu B., Wang D. W., Guo H., Ling Z. H and Cheung K., "Metallic corrosion in the polluted urban atmosphere of Hong Kong", *Environmental monitoring and assessment*, **187** (4112), pp. 1 – 11, 2015.

69. Urban V., Krivy V. and Kreislova K., "The development of corrosion processes on weathering steel bridges", *Procedia engineering*, **114**, pp. 546 – 554, 2015.

70. Karaca F., "Mapping the corrosion impact of air pollution on the historical peninsula of Istambul", *Journal of cultural heritage*, **14**, pp. 129 – 137, 2013.

71. Krivy V., Kubzova M., Kreislova K. and Urban V., "Characterization of corrosion products on weathering steel bridges influenced by chloride deposition", *Metals*, **7** (336), pp. 1 – 16, 2017.

72. Aramendia J., Gomez-Nubla L., Arrizabalaga I., Prieto-Taboada N., Castro K. and Madariaga J. M., "Multianalytical approach to study the dissolution process of weathering steel: the role of urban pollution", *Corrosion science*, **76**, pp. 154 – 162, 2013.

73. Morcillo M., Díaz I., Chico B., Cano H. and De La Fuente D., "Weathering steels: From empirical development to scientific design. A review", *Corrosion science*, **83**, pp. 6 – 31, 2014.

74. Zakipour S., Tidblad J. and Leygraf C., "Atmospheric corrosion effects of SO_2, NO_2 and O_3 – A comparison of laboratory and field exposed nickel", *Journal of electrochemical society*, **144** (10), pp. 3513 – 3517, 1997.

75. Pourbaix M., Van Muylder J. and Pourbaix A., "Application of an electrochemical wet and dry method for atmospheric corrosion testing", *Cebelcor RT*, **259**, 1980.

76. Calero J., Alcántara J., Chico B., Díaz I., Simancas J., De La Fuente D. and Morcillo M., "Wet/dry accelerated laboratory test to simulate the formation of multi-layered rust on carbon steel in marine atmosphere", *Corrosion engineering, science and technology*, pp. 1 – 10, 2017.

77. Garcìa K. E., Morales A. L., Barrero C. A. and Greneche J. M., "On the rust products formed on weathering and carbon steels exposed to chloride in dry-wet cyclical processes", *Hyperfine interactions*, **161**, pp. 127 – 137, 2005.

78. Xiao H., Ye W., Song X., Ma Y. and Li Y., "Evolution of akaganeite in rust layers formed on steel submitted to wet/dry cyclic tests", *Materials*, **10** (1262), pp. 1 – 14, 2017.

79. Oesch S., "The effect of SO_2, NO_2, NO and O_3 on the corrosion of unalloyed carbon steel and weathering steel-the results of laboratory exposures", *Corrosion science*, **38** (8), pp. 1357 – 1368, 1996.

80. Marco J. F., "On the mechanisms of the corrosion of weathering steel by SO2 in laboratory studies: influence of the environmental parameters", *Hyperfine interaction*, **238** (51), pp. 1 – 21, 2017.

81. Montoya P., Díaz I., Granizo N., De la Fuente D. and Morcillo M., "An study on accelerated corrosion testing of weathering steel", *Materials chemistry and physics*, **142**, pp. 220 – 228, 2013.

82. Cheng Q. E., Tian Y. W., Li X. G. and Zhou C., "Corrosion behaviour of nickel-containing weathering steel in simulated marine atmospheric environment", *Materials and corrosion*, **65** (10), pp. 1033 – 1037, 2014.

83. Chiavari C., Benrardi E., Martini C., Passarini F., Motori A. and Bignozzi M.C., "Atmospheric corrosion of Cor-Ten steel with different surface finish: accelerated ageing and metal release", *Materials chemistry and physics*, **136**, pp. 477 – 486, 2012.

84. Callister W. D. and Rethwisch D. G., *Materials science and engineering – An introduction*, 9th ed., Wiley, pp. 1 – 960, 2014.

85. Verhoeven J. D., *Steel metallurgy for the non metallurgist*, ASM International, pp. 1 – 225, 2007.

86. Hosford W. F., *Iron and steel*, Cambridge University press, pp. 1 – 298, 2012.

87. Davis J. R., *Alloying – Understanding the basics*, ASM International, pp. 1 – 647, 2001.

88. Gandy D., *Carbon steel handbook*, EPRI, pp. 1 – 172, 2007.

89. ASTM Standard A690, High-Strength Low-Alloy Nickel, Copper, Phosphorus Steel H-Piles and Sheet Piling with Atmospheric Corrosion Resistance for Use in Marine Environments", pp. 1 – 3, 2006.

90. ASTM Standard A242, "High-Strength Low-Alloy Structural Steel", pp. 6 – 11, 2001.

91. ASTM International A588, "High-Strength Low-Alloy Structural Steel, up to 50 ksi [345 MPa] Minimum Yield Point, with Atmospheric Corrosion Resistance", pp. 1 – 3, 2001.

92. ASTM Standard A606, "Steel, Sheet and Strip, High-Strength, Low-Alloy, Hot-Rolled and Cold-Rolled, with Improved Atmospheric Corrosion Resistance", pp. 1 – 4, 2009.

93. ASTM Standard A633, "Normalized High-Strength Low-Alloy Structural Steel Plates", pp. 1 – 3, 2006.

94. Morcillo M., Chico B., Díaz I., Cano H. and De La Fuente D., "Atmospheric corrosion data of weathering steels. A review", *Corrosion science*, **77**, pp. 6 – 24, 2013.

95. Blanc A., *Architecture and Construction in Steel*, Taylor & Francis, pp. 1 – 640, 1993.

96. Thompson P. D. and Ford K. M., *Estimating life expectancies of highway assets, volume 2: final report*, The National Academies Press, pp. 1 – 242, 2012.

97. Altobelli Antunes R., Uchida Ichikawa R., Gallego Martinez L. and Costa I., "Characterization of corrosion products on carbon steel exposed to natural weathering and to accelerated corrosion tests", *International journal of corrosion*, pp. 1 – 9, 2014.

98. Dal Co F., "Il rivestimento e il decadere del senso delle cose. Perchè gli architetti prediligono il Cor-Ten", *Casabella*, **807**, pp. 2 – 4, 2011.

99. http://www.nssmc.com

100. Schwertmann U. and Corneil R. M., *Iron oxides in the laboratory: preparation and characterization*, VCH, pp. 1 – 1806, 1991.

101. Asami K. and Kikuchi M., "In-depth distribution of rusts on a plain carbon steel and weathering steels exposed to coastal–industrial atmosphere for 17 years", *Corrosion science*, **45**, pp. 2671 – 2688, 2003.

102. Yamashita M., Miyukl H., Matsuda Y., Nagano H. and Misawa T., "The long term growth of the protective rust layer formed on weathering steel by atmospheric corrosion during a quarter of a century", *Corrosion science*, **36** (2), pp. 283 – 299, 1994.

103. Cook D. C., Oh S. J., Balasubramanian R. and Yamashita M., "The role of goethite in the formation of the protective corrosion layer on steels", *Hyperfine interactions*, **122**, pp. 59 – 70, 1999.

104. Kimura M., Suzuki T., Shigesato G., Kihira H. and Suxuki S., "Characterization of Nanostructure of Rusts Formed on weathering steel", *ISIJ International*, **42** (12), pp. 1534 – 1540, 2002.

105. https://geoweb.princeton.edu

106. Yamashita M., Konishi H., Mizuki J. and Uchida H., "Nanostructure of Protective Rust Layer on Weathering Steel Examined Using Synchrotron Radiation X-rays", *Materials transactions*, **45** (6), pp. 1920 – 1924, 2004.

107. Qian Y. H., Niu D., Xu J. J. and Li M. S., "The influence of chromium content on the electrochemical behaviour of weathering steels", *Corrosion science*, **71**, pp. 72 – 77, 2013.

108. Kamimura T., Hara S., Miyuki H., Yamashita M. and Uchida H., "Composition and protective ability of rust layer formed on weathering steel exposed to various environments", *Corrosion science*, **48**, pp. 2799 – 2812, 2006.

109. Díaz I., Cano H., Chico B., De la Fuente D. and Morcillo M., "Some clarifications regarding literature on atmospheric corrosion of weathering steels", *International journal of corrosion*, pp. 1 – 9, 2012.

110. Vernon W. H. J., "A laboratory study of the atmospheric corrosion of metals. Part II. Iron: the primary oxide film. Part III. The secondary product or rust (influence of sulphur dioxide, carbon dioxide, and suspended particles on the rusting of iron)", *Transaction of the Faraday Society,* **31**, pp. 1668 – 1700, 1935.

111. Morcillo M., De la Fuente D., Díaz I. and Cano H., "Atmospheric corrosion of mild steel", *Revista de metalurgia*, **47** (5), pp. 426 – 444, 2011.

112. Ross T. K. and Callaghan B. G., "The seasonal distribution of ferrous sulphate formed during the atmospheric rusting of mild steel", *Corrosion science*, **6** (7), pp. 341 – 343, 1966.

113. Aramendia J., Gómez-Nubla L., Castro K. and Madariaga J. M., "Spectroscopic speciation and thermodynamic modeling to explain the degradation of weathering steel surfaces in SO2 rich urban atmospheres", *Microchemical journal*, **115**, pp. 138 – 145, 2014.

114. Morcillo M., González-Calbet J. M., Jiménez J. A., Díaz I., Alcántara J., Chico B., Mazarío-Fernández A., Gómez-Herrero A., Llorente I. and De la Fuente D., "Environmental Conditions for Akaganeite Formation in Marine Atmosphere Mild Steel Corrosion Products and Its Characterization", *Corrosion*, pp. 872 – 886, 2015.

115. Alcántara J., De la Fuente D., Chico B., Simancas J., Díaz I. and Morcillo M., "Marine Atmospheric Corrosion of Carbon Steel: A Review", *Materials*, **10** (406), pp. 2 – 67, 2017.

116. Morcillo M., Chico B., De la Fuente D., Alcántara J., Odnevall Wallinder I. and Leygraf C., "On the mechanism of rust exfoliation in marine environments", *Journal of the electrochemical society*, **164** (2), pp. C8 – C16, 2017.

117. Antony H., Legrand L., Maréchal L., Perrin S., Dillmann Ph. and Chaussé A., "Study of lepidocrocite γ-FeOOH electrochemical reduction in neutral and slightly alkaline solutions at 25 °C", *Electrochimica Acta*, **51** (4), pp. 745 – 753, 2005.

118. Antony H., Lair V., Legrand L. and Chaussé A., "Electrochemical reduction of ferric corrosion products and evaluation of galvanic coupling with iron", *Corrosion science*, **48** (8), pp. 2050 – 2063, 2006.

119. Frensch P. A. and Funke J., *Complex problem solving – The European perspective*. Psychology Press, pp. 1 – 360, 2014.

120. Luciano G., Traverso P. and Letardi P., "Applications of chemometric tools in corrosion studies", *Corrosion science*, **52**, pp. 2750 – 2757, 2010.

121. Robbiola L., Blengino J. M. and Fiaud C., "Morphology and mechanisms of formation of natural patinas on archaeological Cu-Sn alloys", *Corrosion science*, **12**, pp. 2083 – 2111, 1998.

122. Luciano G., Leardi R. and Letardi P., "Principal component analysis of colour measurements of patinas and coating systems for outdoor bronze monuments", *Journal of cultural heritage*, **10**, pp. 331 – 337, 2009.

123. Herrera A., Ballabio D., Navas N., Todeschini R. and Cardell C., "Principal Component Analysis to interpret changes in chromatic parameters on paint dosimeters ezposed long-term to urban air", *Chemometrics and intelligent laboratory systems*. **167**, pp. 113 – 122, 2017.

124. Polikreti K., Argyropoulos V., Charalambous D., Vossou A., Perdikatsis V. and Apostolaki C., "Tracing correlations of corrosion products and microclimate data on outdoor bronze monuments by principal component analysis", *Corrosion science*, **51**, pp. 2416 – 2422, 2009.

125. Raffo S., Vassura I., Chiavari C., Martini C., Bignozzi M. C., Passarini F., Bernardi E., "Weathering steel as a potential source for metal contamination: Metal dissolution during 3-year of field exposure in a urban coastal site", *Environmental Pollution*, **213**, pp. 571 – 584, 2016.

126. Hajeeh M., "Estimating corrosion: a statistical approach", *Materials and design*, **24**, pp. 509 – 518, 2003.

127. Wold S., "Chemometrics; what do we mean with it, and what do we want from it?", *Chemometrics and intelligent laboratory systems*, **30**, pp. 109 – 115, 1995.

128. Brown S. D., "The chemometrics revolution re-examined", *Journal of Chemometrics*, **31** (1), pp. 1 – 23, 2016.

129. Massart D. L., Vandeginste B. G. M., Buydens L. M. C., De Jong s., Lewi P. J. and Semyers-Verbeke J., *Data handling in science and technology*, vol. 20 – Handbook of Chemometrics and Qualimetrics: Part B. Elsevier Science, pp. 1 – 713, 1998.

130. Oldroyd D., *The arch of knowledge*, Methuen, pp. 1 – 413, 1986.

131. Massart D. L., Vandeginste B. G. M., Buydens L. M. C., De Jong s., Lewi P. J. and Semyers-Verbeke J., *Data handling in science and technology*, vol. 20 – Handbook of Chemometrics and Qualimetrics: Part A, Elsevier Science, pp. 1 – 867, 1998.

132. Frank I. E. and Kowalski B. R., "Chemometrics", *Analytical chemistry*, **54** (5), pp. 232 – 243, 1982.

133. Brereton R. G., "The evolution of chemometrics, *Analytical methods*, **5**, pp. 3785 – 3789, 2013.

134. Fisher R. A., *The design of experiments*, Haffner press, pp. 1 – 26, 1935.

135. Leardi R., *Data handling in science and technology*, vol. 28 – Chemometrics in food chemistry, Chapter 2 – Experimental design, Elsevier Science, pp. 9 – 53, 1998.

136. Lundstedt T., Seifert E., Abramo L., Thelin B., Nyström Å., Pettersen J. and Bergman R., "Experimental design and optimization", *Chemometrics and intelligent laboratory systems*, **42**, pp. 3 – 40, 1998.

137. Box G. E. P., Hunter J. S. and Hunter W. G., *Statistics for experiments – Design, innovation, and discovery*, Wiley, 2nd ed., pp. 1 – 633, 2005.

138. Leardi R., "Experimental design in chemistry", *Analytica chimica acta*, **652**, pp. 161 – 172, 2009.

139. Miller J. N. and Miller J. C., *Statistics and chemometrics for analytical chemistry*, Pearson, 5th ed., pp. 1 – 268, 2005.

140. Jolliffe I.T., *Principal component analysis*, Springer, 2nd ed., pp. 1 – 488, 2002.

141. http://facweb.cs.depaul.edu

142. Einax J.W., Zwanzinger H.W., Geiss S., *Chemometrics in environmental analysis*, VCH, pp. 1 – 384, 1997.

143. Todeschini R., *Introduzione alla chemiometria*, EdiSES, pp. 1 – 417, 1998.

144. Wold S., "Principal component analysis", *Chemometrics and Intelligent Laboratory Systems*, **2**, pp. 37 – 52, 1987.

145. Kjeldahl K. and Bro R., "Some common misunderstandings in chemometrics", *Journal of chemometrics*, **24**, pp. 558 – 564, 2010.

146. Esbensen K. H., Guyot D., Westad F. and Houmøller L. P, *Multivariate data analysis – in practice*, CAMO Software, 5th ed., pp. 1 – 597, 2010.

147. UNI EN 10149, "*Prodotti piani laminati a caldo di acciai ad alto limite snervamento per formatura a freddo*", Italia, 2013.

148. ISO 8565, "*Metals and alloys -- Atmospheric corrosion testing -- General requirements*", Geneva, Switzerland: ISO, 2011.

149. ISO 9226, "*Corrosion of metals and alloys -- Corrosivity of atmospheres -- Determination of corrosion rate of standard specimens for the evaluation of corrosivity*", Geneva, Switzerland: ISO, 2012.

150. http://www.arpa.emr.it

151. D. Lgs. 155/2010, "*Attuazione della direttiva 2008/50/CE relativa alla qualita' dell'aria ambiente e per un'aria piu' pulita in Europa*".

152. Wang W., Mao F., Gong W., Pan Z. and Du L., "Evaluating the Governing Factors of Variability in Nocturnal Boundary Layer Height Based on Elastic Lidar in Wuhan", *International Journal of Environmental Research and Public Health*, **13** (11), pp. 1 – 12, 2016.

153. ISO 11130, "*Corrosion of metals and alloys -- Alternate immersion test in salt solution*", Geneva, Switzerland: ISO, 2010.

154. ASTM Standard G44, "*Standard Practice for Exposure of Metals and Alloys by Alternate Immersion in Neutral 3.5 % Sodium Chloride Solution*", pp. 1 – 5, 2013.

155. Malacara D., *Color Vision and Colorimetry - Theory and Applications*, 2nd ed., SPIE Press, pp. 1 – 176, 2011.

156. Shanda J., *Colorimetry – Understanding the CIE system,* Wiley, pp. 1 – 467, 2007.

157. CIE, *Technical report: Colorimetry*, 3rd ed., CIE 15, 2004.

158. UNI-EN 15886, "*Conservazione dei Beni Culturali - Metodi di prova - Misura del colore delle superfici*", Ente italiano di normazione, Italia, 2010.

159. Stuart B. H., *Analytical Techniques in Materials Conservation*, Wiley, pp. 1 – 444, 2007.

160. Graue B., Siegesmund S., Oyhantcabal P., Naumann R., Licha T., Simon K., "The effect of air pollution on stone decay: the decay of the Drachenfels trachyte in industrial, urban, and rural environments - a case study of the Cologne, Altenberg and Xanten cathedrals", *Environmental earth science*, **69**, pp. 1095 – 1124, 2013.

161. Pipal A. S. and Satsangi P. G., "Study of carbonaceous species, morphology and sources of fine ($PM_{2.5}$) and coarse (PM_{10}) particles along with their climatic nature in India", *Atmospheric research*, **154**, pp. 103 – 115, 2015.

162. Lifshin E., *X-ray Characterization of Materials*, Wiley, pp. 1 – 277, 2008.

163. FHWA, *"Methodology for Analysis of Soluble Salts From Steel Substrates"*, Federal Highway Administration Research and Technology, pp. 1 – 32, 2014.

164. ISO 8407, "*Corrosion of metals and alloys -- Removal of corrosion products from corrosion test specimens*", Geneva, Switzerland: ISO, 2009.

165. Alcántara J., Chico B., Díaz I., De la Fuente D., Morcillo M., "Airborne chloride deposit and its effect on marine atmospheric corrosion of mild steel", *Corrosion science*, **97**, pp. 74 88, 2015.

166. Bernardi E., Raffo S., Chiavari C., Martini C., Nobili L., Bignozzi M. C., Vassura I., "Cor-Ten in marine atmosphere: the influence of the environment on corrosion" in 31° Congress on science and cultural heritage – Metalli in Architettura: conoscenza, conservazione e innovazione, pp. 113 – 122, Arcadia ricerche s.r.l., Bressanone (Italy), 2015.

167. Alcántara J., Chico B., Simancas J., Díaz I., De la Fuente D., Morcillo M., "An attempt to classify the morphologies presented by different rust phases formed during the exposure of carbon steel to marine atmospheres", *Materials characterization*, **118**, pp. 65 – 78, 2016.

168. Luna C., Ilyn M., Vega V., Prida V. M., González J. and Mendoza-Reséndez R., "Size distribution and frustrated antiferromagnetic coupling effects on the magnetic behaviour of ultrafine akaganeite (β-FeOOH) nanoparticles", *The journal of physical chemistry*, **118**, pp. 21128 – 21139, 2014.

169. Remazeilles C. and Refait Ph., "On the formation of β-FeOOH (akaganeite) in chloride-containing environments", *Materials science*, **49** (2), pp. 844 – 857, 2007.

170. Asami K. and Kikuchi M., "Characterization of Rust Layers on Weathering Steels Air-Exposed for a long period*", *Materials transactions*, **43** (11), pp. 2818 – 2825, 2002.

171. Dillmann Ph., Mazaudier F. and Hoerlé S., "Advances in understanding atmospheric corrosion of iron. I. Rust characterisation of ancient ferrous artefacts exposed to indoor atmospheric corrosion", *Corrosion science*, **46**, pp. 1401 – 1429, 2004.

172. Neff D., Dillmann Ph., Bellot-Gurlet L. and Beranger G., "Corrosion of iron archaeological artefacts in soil: characterisation of the corrosion system", *Corrosion science*, **47**, pp. 515 – 535, 2005.

173. Selwyn L.S., Sirois P.I. and Argyropoulos V., "The corrosion of excavated archaeological iron with details on weeping and akaganéite", *Studies in conservation*, **44** (4), pp. 217 – 232, 1999.

174. Shiotani K., Tanimoto W., Maeda C., Kawabata F. and Amano K., "Analysis for structure of rust layer formed on weathering steel bridge for bare use exposed in coastal industrial zone for 27 years", *Zairyo-to-Kankyo*, **49**, pp. 67 – 71, 2000.

175. Li q. X., Wang Z. Y., Han W., Han E. H., "Characterization of the rust formed on weathering steel exposed to Qinghai salt lake atmosphere", *Corrosion science*, **50**, pp. 365 – 371, 2008.

176. "Corrosión atmosférica de aceros patinables de nueva generación", Ph.D. Dissertation by Díaz I., Ph.D., Universidad complutense de Madrid, pp. 1 – 258, 2012.

177. "The influence of the environment on the atmospheric corrosion of weathering steel: field and laboratory studies", Ph.D. Dissertation by Raffo S., Ph.D., University of Bologna, pp. 1 – 243, 2016.

178. Dunn D. S., Bogart M. B., Brossia C. S. and Cragnolino G. A., "Corrosion of iron under alternating wet and dry conditions", *Corrosion*, **56** (5), pp. 470 – 481, 2000.

179. Refait P. and Genin M. R., "The mechanism of oxidation of ferrous hydroxychloride in aqueous solution: the formation of akaganeite vs goethite", *Corrosion science*, **39**, pp. 539 – 553, 1997.

180. Merian E., Anke M., Inhat M. and Stoeppler M., *Elements and their compound in the environment: occurrence, analysis and biological relevance*, 2nd ed., Wiley, pp. 1 – 15, 2008.

181. Aramendia J., Gomez-Nubla L., Castro K. and Madariaga J. M., "Structural and chemical analyzer system for the analysis of deposited airborne particles and degradation compounds present on the surface of outdoor weathering steel objects", *Microchemical journal*, **123**, pp. 267 – 275, 2015.

182. Bugini R., Laurenzi Tabasso M. and Realini M., "Rate of formation of black crusts on marble. A case study", *Journal of cultural heritage*, **1**, pp. 111 – 116, 2000.

183. Brimblecombe P., *The effects of air pollution on the built environment*, Imperial College Press, pp. 1 – 448, 2003.

184. Maro D., Connan O., Flori J. P., Hébert D., Mestayer P., Olive F. and Solier L. "Aerosol Dry Deposition in the Urban Environment: Assessment of Deposition Velocity on Building Facades", *Journal of Aerosol Science*, **69**, pp. 113 – 131, 2014.

185. Ferm M., Watt J., O'Hanlon S., De Santis F. and Varotsos C., "Deposition measurement of particulate matter in connection with corrosion studies", *Analytical bioanalytical chemistry*, **384**, pp. 1320 – 1330, 2006.

186. López-García P., Gelado-Caballero M. D., Santana-Castellano D., Suárez de Tangil M., Collado-Sánchez C. and Hernández-Brito J. J., "A three-year time-series of dust deposition flux measurements in Gran Canaria, Spain: A comparison of wet and dry surface deposition samplers", *Atmospheric environment*, **79**, pp. 689 – 694, 2013.

187. "Interactions between atmospheric particulate matter and stone surfaces by means of laboratory and in field studies", Ph.D. Dissertation by Casati M., Ph.D., University of Milano-Bicocca, pp. 1 – 175, 2014.

188. Poli T., Toniolo L. and Chiantore O., "The protection of different Italian marbles with two partially flourinated acrylic copolymers", *Applied Physics A: Materials Science & Processing*, **79** (2), pp. 347–351, 2004.

189. UNI 10921, "*Beni culturali - Materiali lapidei naturali ed artificiali - Prodotti idrorepellenti - Applicazione su provini e determinazione in laboratorio delle loro caratteristiche*," Italia, 2001.

190. http://www.comune.milano.it/wps/portal/ist/it/servizi/mobilita/Area_C

191. Casuccio G. S., Schlaegle S. F., Lersch T. L., Huffman G. P., Chen Y., Shah N., "Measurement of fine particulate matter using electron microscopy techniques", *Fuel processing technology*, **85**, pp. 763 – 779, 2004.

192. Telloli C., Malaguti A., Mircea M., Tassinari R., Vaccaro C. and Berico M., "Properties of agricultural aerosol released during wheat harvest threshing, plowing and sowing", *Journal of environmental sciences*, **26**, pp. 1903 – 1912, 2014.